

Theoretische Physik

**Self-interaction corrections to
density-functional theory for solids,
surfaces, and nanotubes**

Inaugural-Dissertation
zur Erlangung des Doktorgrades
der Naturwissenschaften im Fachbereich Physik
der Mathematisch-Naturwissenschaftlichen Fakultät
der Westfälischen Wilhelms-Universität Münster

vorgelegt von
Björn Baumeier
aus Münster

– 2009 –

Dekan: Prof. Dr. Johannes Wessels
1. Gutachter: Prof. Dr. Johannes Pollmann
2. Gutachter: Prof. Dr. Peter Krüger
Tag der mündlichen Prüfung:
Tag der Promotion:

Publications

Significant parts of this thesis have already been published in the following references:

- **B. Baumeier, P. Krüger, and J. Pollmann**
Self-interaction-corrected pseudopotentials for silicon carbide
Phys. Rev. B **73**, 195205 (2006).
- **B. Baumeier, P. Krüger, and J. Pollmann**
Atomic and electronic structure of BeO and the BeO(10 $\bar{1}$ 0) surface: An ab initio investigation
Phys. Rev. B **75**, 045323 (2007).
- **B. Baumeier, P. Krüger, and J. Pollmann**
Structural, elastic, and electronic properties of SiC, BN, and BeO nanotubes
Phys. Rev. B **76**, 085407 (2007).
- **B. Baumeier, P. Krüger, and J. Pollmann**
Bulk and surface electronic structures of alkaline-earth metal oxides: Bound surface and image-potential states from first principles
Phys. Rev. B **76**, 205404 (2007).
- **P. Krüger, B. Baumeier, and J. Pollmann**
First-principles investigation of an epitaxial silicon oxynitride layer on a 6H-SiC(0001) surface
Phys. Rev. B **77**, 085329 (2008).
- **B. Baumeier, P. Krüger, J. Pollmann, and G. V. Vajenine**
Electronic structure of alkali-metal fluorides, oxides, and nitrides: Density-functional calculations including self-interaction corrections
Phys. Rev. B **78**, 125111 (2008).
- **B. Baumeier, P. Krüger, and J. Pollmann**
First-principles investigation of the atomic and electronic structure of the 4H-SiC(1 $\bar{1}$ 02)-c(2 \times 2) surface
Phys. Rev. B **78**, 245318 (2008).

Note: This version of the dissertation includes corrections for spelling and grammatical errors. B.B. January 26, 2009

Contents

Introduction	7
1. Concepts of solid state theory	13
1.1. Born-Oppenheimer Approximation	13
1.2. Density-functional theory: Kohn-Sham Equations	14
1.3. Local-density approximation	17
2. Practical realization of density-functional theory calculations	19
2.1. Solving the Kohn-Sham equations	19
2.2. Norm-conserving pseudopotentials	22
2.3. Self-consistent electronic structure calculations	25
2.4. Total energy calculations	28
2.5. Atomic forces and optimization of the atomic structure	29
3. Self-interaction corrections to density-functional theory	33
3.1. The self-interaction error	33
3.2. Self-interaction corrections in atoms: The Perdew-Zunger approach	35
3.3. Self-interaction corrections for solids: First approaches	38
3.4. Self-interaction-corrected pseudopotentials	40
3.5. Structural properties of cubic and hexagonal bulk silicon carbide	52
3.6. Electronic structure of 2H-, 4H-, and 6H-SiC	53
3.7. Summary	58
4. Properties of (110) and (001) surfaces of 3C-SiC	59
4.1. The nonpolar 3C-SiC(110)-(1x1) surface	60
4.2. The polar 3C-SiC(001) surface	64
4.3. Summary	75
5. Properties of (10$\bar{1}$0) and (1$\bar{1}$02)-c(2x2) surfaces of 4H-SiC	77
5.1. The 4H-SiC(10 $\bar{1}$ 0) surface	77
5.2. The 4H-SiC(1 $\bar{1}$ 02)-c(2x2) surface	94
5.3. Summary	114
6. Bulk and surface properties of alkaline-earth metal oxides	117
6.1. Atomic and electronic structure of BeO and the BeO(10 $\bar{1}$ 0) surface	117
6.2. Bound surface and image potential states of alkaline-earth metal oxides	131

7. Structural, elastic and electronic properties of SiC, BN and BeO nanotubes	151
7.1. Graphitic monolayers	152
7.2. Nanotubes	158
7.3. Summary	179
8. Electronic structure of alkali-metal fluorides, oxides and nitrides	181
8.1. Atomic term values	182
8.2. Bulk electronic properties	183
8.3. Bulk structural properties	192
8.4. Summary	195
9. Conclusions and Outlook	197
Summary	203
Appendix	207
A. Explicit forms of Pulay-, Hellmann-Feynman- and Madelung forces . . .	207
B. Pseudopotentials including semicore states	209
C. Decay constants for Gaussian orbitals	210
Bibliography	211
Zusammenfassung	227

Introduction

The initial formulation of density-functional theory (DFT) in the middle of the twentieth century [1, 2] has unlocked the door to developing practical independent-particle approaches for the ab-initio study of structural and electronic properties of solids. Simple proofs show that many properties of a system of interacting particles can be derived from their ground state density $\rho(\mathbf{r})$. As the DFT is a formally exact theory for correlated many-body systems, $\rho(\mathbf{r})$ contains all the information about the ground state and also all excited states. However, no exact expression for the functional is known for more than a single-electron system.

Despite their simplicity, approximate functionals for the exchange-correlation (XC) energy within the Kohn-Sham approach based on the solution of the homogenous electron gas, like the local-density approximation (LDA) or the generalized-gradient approximation (GGA), have turned out to be remarkably successful in studying the fundamental properties of many-body systems, including bulk crystals, clean and adsorbate-covered surfaces as well as more complicated nanostructures. There are, however, some significant drawbacks: firstly, the energetics of highly correlated electrons, like localized (semicore) *d*-electrons, are underestimated. Secondly, and more importantly, the fundamental energy gap between occupied and empty bands in semiconductors and insulators is systematically underestimated by about 50%. In order to illustrate this problem Fig. 0.1 shows the theoretical band gaps as resulting from standard LDA calculations for the bulk crystals that will be studied in this work against their respective experimental values, as far as they are known.

Many approaches have been made to rectify this problem. For example, quasiparticle approaches based on the *GW* approximation [3, 4] (GWA), which treat one-particle excitations using electron Green functions, have been particularly successful in this regard [5–8]. Compared to standard LDA, however, the numerical effort for GWA calculations is considerably higher. This is particularly true when systems with broken translational symmetry are described by large unit cells containing many atoms. In such cases GWA calculations become extraordinarily demanding computationally.

Other approaches concentrate on improving the functionals themselves. Various generalized-gradient approximations have been developed, which take not only the local charge density but also its gradient into account evaluating the XC potential and energy, respectively. Others try to account for non-local contributions leading to the average density

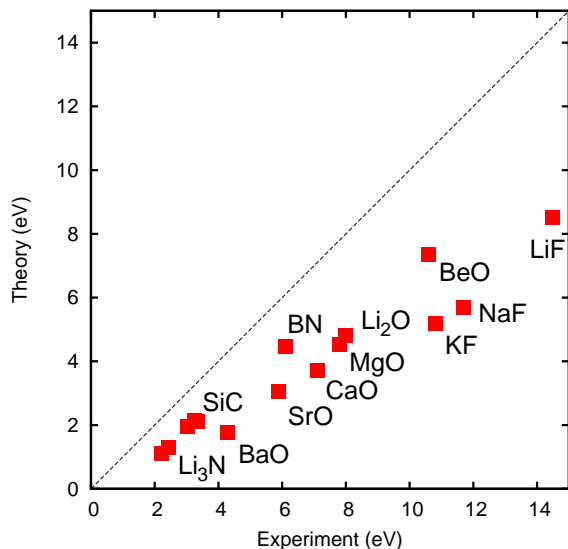


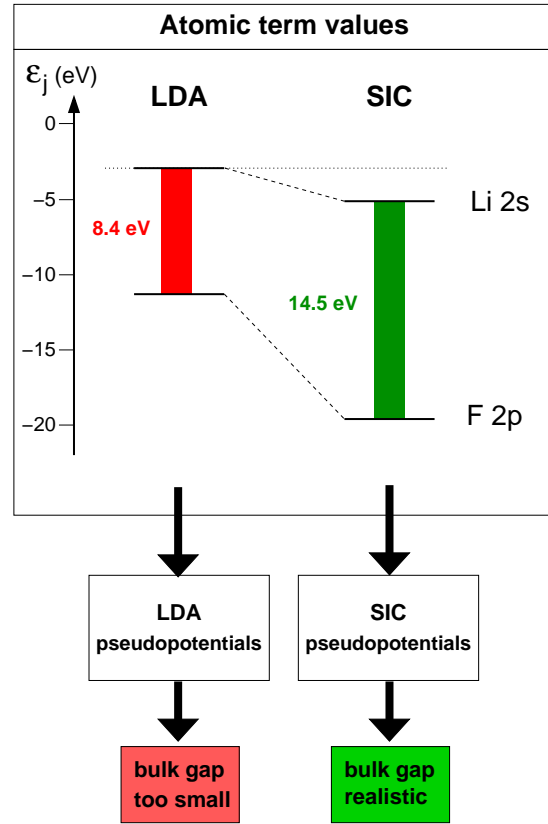
Figure 0.1: Calculated band gap energies of materials studied in this work as resulting from standard LDA calculations compared to their respective experimental values.

(ADA) and weighted density approximations (WDA) [9]. Optimized effective potential (OEP) techniques introduce orbital-dependent functionals. The energy is defined as a functional of the potential V instead of the particle density n . Notably, the particular application of the OEP to the Hartree-Fock exchange leads to the so called exact exchange (EXX) functional. Such can be used, for instance, in hybrid functionals, which are widely used by chemists. They are a combination of orbital-dependent Hartree-Fock and an explicit density functional [10–12].

These numerous approaches are of different quality but all that go beyond LDA or GGA share a common significant drawback. From a computational point of view, the numerical effort to evaluate these functionals is higher than in LDA/GGA, often even considerably so. This fact limits their applicability to comparatively small systems. This is all the more critical as the scientific interest focuses on configurations that are modeled using large unit cells containing a large number of atoms, e.g. in studies of surfaces, nanostructures, or defects. Technological applications usually exploit the properties of these structures making them particularly interesting and relevant. It is therefore vital to describe them most accurately from a theoretical point of view. Due to the high calculational demands of the methods mentioned above, these properties are not accessible by them except for isolated cases.

In this work a different approximate treatment of the electronic structure shall be employed. Perdew and Zunger [13] have very early realized that in the case for isolated atoms the errors in the electronic structure arise from spurious self-interactions inherent in the LDA functional. They heuristically defined a self-interaction correction (SIC) for such systems leading to an orbital-dependent formulation of the energy functional. As it turns out, the use of these corrections massively improves the agreement between calculated term values and experimental binding energies for free atoms. The direct appli-

Figure 0.2: The idea of constructing SIC pseudopotentials illustrated for LiF. On the left hand side, a standard LDA calculation underestimates term values of the free atoms leading to a too small level distance in the combined spectrum. Accordingly constructed pseudopotentials carry this error into the solid and the bulk gap results too small. An atomic SIC calculation in contrast yields a much improved combined spectrum and – via an appropriate pseudopotential construction – a realistic bulk band gap.



cation of the SIC functional in calculations for solids is difficult for many reasons as will be discussed later (cf. Chapter 3). Among some other intricacies, the orbital-dependence renders it computationally very demanding, as well.

The approach in this work tries to bridge this gap and transfer the well-defined *atomic* corrections to the solid using the pseudopotential approach. The idea of using self-interaction corrected pseudopotentials has been proposed previously and has been used in different modifications [14–20]. Its fundamental idea is illustrated in Fig. 0.2 for the case of LiF. On the left hand side, the two highest occupied term values of lithium (cation) and fluorine (anion) are shown as calculated within LDA. Due to the self-interaction error, the level positions are too high and their distance results too small. When standard LDA pseudopotentials are constructed based on these results, this term value distance translates into the bad gap in LiF, which results too small compared to experiment. On the right hand side of Fig. 0.2, the effect of SIC on the atomic term values is shown. As a result of the self-interaction correction, both term values of the free atoms are found lower in energy as compared to LDA. Most importantly, the level distance is increased. If it is now possible to construct pseudopotentials based on this improved spectrum, one can transfer the atomic SIC effect to the solid without any additional computational costs. This approximate SIC has mostly been applied to bulk solids with strongly-localized valence states,

e.g. *semicore* d -states, before. The aim of this work is twofold: Firstly, the applicability of the SIC pseudopotential approach to usual sp -bonded solids shall be scrutinized. An important aspect in this regard is also the performance of such calculations for systems with reduced periodicity, most notably surfaces. Therefore, in this work, the structural and electronic properties of a multitude of bulk crystals, surfaces, and related nanostructured matter will be investigated using self-interaction corrected pseudopotentials. In particular, selected non-polar and polar surfaces of silicon carbide (SiC) will be studied. SiC is a compound semiconductor of large application potential for the use in micro- and optoelectronic devices. Compared to silicon it has many advantageous features such as high possible operating temperatures combined with high mechanical strength, a higher electric breakdown field, higher thermal conductivity, lower intrinsic carrier concentration, and a larger saturated electron drift velocity, among others. These can be exploited, for instance, in MOSFETs where the use of silicon carbide instead of silicon offers increased switching speeds and lower losses. In addition to its technological relevance, SiC is also interesting from a more fundamental point of view. The compound exists in a large number of different polytypes, ranging from purely cubic to purely hexagonal ones with various mixed stacking sequences in between. This offers a variety of qualitatively different geometries that can be studied. As SiC is a highly reactive material, it represents a workhorse for a number of fundamental studies with regards to surface reconstructions, adsorption properties etc. The availability of experimental and beyond-LDA reference data for selected surfaces of the cubic modification 3C-SiC allows for a sound assessment of the SIC pseudopotential approach for such systems. Of particular interest in this regard is the effect on surfaces on which higher reconstructions lead to characteristic differences in the electronic structure between bulk and surface, e.g. by dimer formation.

Another class of materials that shall be studied in this work are the alkaline-earth metal oxides BeO, MgO, CaO, SrO, and BaO. For these highly ionic compounds, the SIC pseudopotential method can be expected to work extremely well. Such a study is motivated by the technological relevance of these oxides, e.g. as supports in catalysis, on the one hand, and by more fundamental aspects on the other hand. Going from beryllium to barium in the second group of the periodic table of elements the chemical properties change considerably. For the heavier cations in the oxide compounds, the energy separation between the valence $(N)s$ and core $(N-1)p$ electrons decreases in such a fashion that the derived bands reside close to the oxygen valence bands in the solid. Such *semicore* p -bands of filled inner shells are very important to account for and should be influenced by self-interaction corrections as well. Quasiparticle calculations and experimental reference will serve to assess the results of SIC calculations of the bulk crystals. In case of the respective (001) surfaces, a quasiparticle calculation [21] reported the occurrence of loosely bound image potential states (IPS) at the MgO(001) surface. It will be investigated whether the SIC pseudopotential approach yields an accurate description of such states and whether IPS

also occur on the other alkaline-earth metal oxide surfaces.

Since the initial discovery of carbon-based nanotubes in the early 1990s [22], there has been an ever growing interest in studies of such one-dimensional systems. An interesting feature of these tubular structures is that they can be formed in different helicities spanning a significant range of diameters from about 4 to possibly several hundred angstroms. For the use in microelectronic devices knowledge of their electronic structure is vital. It can easily be fathomed that the electronic structure is intimately related to geometric properties such as the helicity and the diameter. An investigation of the band gap progression in silicon carbide nanotubes based on standard LDA [23] has found that for small diameters the gap of so-called zigzag nanotubes vanishes. In this work, the structural and electronic properties of a significant number of nanotubes based on silicon carbide, boron nitride, and beryllium oxide will be studied using SIC pseudopotentials. The aim, in particular, is to monitor the progression of the respective band gaps in the diameter range of four to 25 Å and to discuss the band gap collapse reported in earlier studies.

Finally, a comprehensive study of nine bulk alkaline-metal fluorides, oxides, and nitrides is performed. Sparked by the only recent synthesis of sodium nitride [24, 25], a standard LDA study predicts a negative gap for this ionic compound, which is in disagreement with experimental observations. SIC pseudopotentials will be used to study the electronic structure of this and eight related compounds aiming at reconciling theoretical and experimental results.

Therefore, this work is structured as follows: In the first chapter, the basic concepts of solid state theory used in this work, i.e. density-functional theory and the local-density approximation, are presented. Chapter 2 deals with some details of the practical realization of the calculations, including short descriptions of norm-conserving pseudopotentials, the self-consistent procedure, and geometry optimization. The self-interaction error and the subsequent attempts of self-interaction corrections are presented in detail in Chapter 3. In particular, the SIC pseudopotential approach used in this work is motivated and discussed instructively in application to the bulk solids of 3C-, 2H-, 4H-, and 6H-SiC. The method will then be used in Chapter 4 to investigate the structural and electronic properties of 3C-SiC(110)-(1×1) and the (2×1) and c(2×2) reconstructions of the carbon-terminated 3C-SiC(001) surface. In the following chapter, the results of respective studies of 4H-SiC(10 $\bar{1}$ 0) and 4H-SiC(1 $\bar{1}$ 02)-c(2×2) will be presented. Bulk and surface properties of alkaline-earth metal oxides will be discussed in Chapter 6, while Chapter 7 focuses on the structural, elastic, and electronic properties of different nanotubes. Finally, Chapter 8 deals with the electronic structure of alkali-metal fluorides, oxides, and nitrides before an Outlook and a Summary conclude this work.

Chapter 1.

Concepts of solid state theory

The quantum-mechanical treatment of electronic and structural properties of solids is based on Schrödinger's equation for many-particles. For only a handful of systems, this equation can be solved analytically, which necessitates the use of numerical procedures combined with suitable approximations.

This section begins with the description of the decoupling of ionic and electronic systems in the framework of the Born-Oppenheimer approximation. Later, density-functional theory in local-density approximation is presented as method of choice for solving the electronic problem.

1.1. Born-Oppenheimer Approximation

The solid under investigation shall consist of N_K atomic cores localized at the spatial coordinates \mathbf{R}_λ carrying the charges Z_λ and N_e electrons with the coordinates \mathbf{r}_i . In the CGS system, the associated Hamiltonian reads

$$\begin{aligned}\hat{H} &= \sum_{\lambda=1}^{N_K} \frac{\hat{\mathbf{P}}_\lambda^2}{2M_\lambda} + \frac{1}{2} \sum_{\lambda=1}^{N_K} \sum_{\substack{\eta=1 \\ \eta \neq \lambda}}^{N_K} \frac{Z_\lambda Z_\eta e^2}{|\mathbf{R}_\lambda - \mathbf{R}_\eta|} \\ &+ \sum_{i=1}^{N_e} \frac{\hat{\mathbf{p}}_i^2}{2m_i} + \frac{1}{2} \sum_{i=1}^{N_e} \sum_{\substack{j=1 \\ j \neq i}}^{N_e} \frac{e^2}{|\mathbf{r}_i - \mathbf{r}_j|} - \sum_{i=1}^{N_e} \sum_{\lambda=1}^{N_K} \frac{Z_\lambda e^2}{|\mathbf{r}_i - \mathbf{R}_\lambda|} \\ &= \underbrace{\hat{T}_K + \hat{V}_{KK}}_{\hat{H}^K} + \underbrace{\hat{T}_e + \hat{V}_{ee} + \hat{V}_{eK}}_{\hat{H}^{el}} .\end{aligned}\tag{1.1}$$

Here, \hat{T}_K is the kinetic energy of the nuclei and \hat{T}_e that of the electrons. Coulomb interaction is repulsive for electrons (\hat{V}_{ee}) and nuclei (\hat{V}_{KK}) among themselves, respectively, as well as attractive (\hat{V}_{eK}) among each other.

Using the Born-Oppenheimer approximation [26] the motion of nuclei and electrons can

be decoupled. Due to the relation of masses $\frac{m_e}{M_K}$, which is of the order $10^{-4} - 10^{-5}$ depending on the particular element, one can assume as a first approximation that the electrons always move within a rigid lattice of nuclear cores. The nuclear coordinates are no longer regarded as dynamic variables but as parameters of the Hamiltonian for the electronic system.

An expansion of the wave functions of the total system in terms of the eigenstates of the electronic system under omission of transitions between electronic states (electron-phonon coupling) leads to two separate equations. First, the dynamics of the electrons is treated within a rigid nuclear lattice. Using atomic units, the Hamiltonian of the electronic system that shall be solved in the following reads

$$\begin{aligned} \hat{H} &= \sum_i^{N_e} -\hat{\nabla}_{\mathbf{r}_i}^2 - \sum_{i=1}^{N_e} \sum_{\lambda=1}^{N_K} \frac{2Z_\lambda}{|\mathbf{r}_i - \mathbf{R}_\lambda|} + \sum_{i=1}^{N_e} \sum_{\substack{j=1 \\ j \neq i}}^{N_e} \frac{1}{|\mathbf{r}_i - \mathbf{r}_j|} \\ &= \hat{T}_e + \hat{V}_{ek} + \hat{V}_{ee} . \end{aligned} \quad (1.2)$$

All lengths that enter this Hamiltonian are scaled in multiples of Bohr's radius $a_B = 0.529 \text{ \AA}$, energies are measured in Rydbergs.

Then, the collective oscillations of the nuclei in the effective potential

$$V_{\text{eff}}(\mathbf{R}) = \frac{1}{2} \sum_{\lambda=1}^{N_K} \sum_{\substack{\eta=1 \\ \eta \neq \lambda}}^{N_K} \frac{Z_\lambda Z_\eta e^2}{|\mathbf{R}_\lambda - \mathbf{R}_\eta|} + E_n^{\text{el}}(\mathbf{R}) , \quad (1.3)$$

with $E_n^{\text{el}}(\mathbf{R})$ being the electronic energies associated to the Hamiltonian of Eq. (1.2) are calculated according to

$$\left(\sum_{\lambda=1}^{N_K} \frac{\hat{\mathbf{P}}_\lambda^2}{2M_\lambda} + V_{\text{eff}}(\mathbf{R}) \right) \Phi_{\alpha,n}(\mathbf{R}) = E_\alpha \Phi_{\alpha,n}(\mathbf{R}) . \quad (1.4)$$

1.2. Density-functional theory: Kohn-Sham Equations

Two theorems by Hohenberg and Kohn [1] constitute the fundamental basis of density functional theory:

- (1) The ground state ψ_0 of a system consisting of spin-free, identical fermions is a one-to-one functional of the particle density $\varrho(\mathbf{r})$.

(2) The functional

$$\begin{aligned}
 E[n] &= \int V_{\text{ext}}(\mathbf{r})n(\mathbf{r}) d^3r + \langle \psi | \hat{T} + \hat{V}_{\text{ee}} | \psi \rangle \\
 &= \int V_{\text{ext}}(\mathbf{r})n(\mathbf{r}) d^3r + F[n(\mathbf{r})] \ ,
 \end{aligned}
 \tag{1.5}$$

obeys a variational principle with respect to the particle density $n(\mathbf{r})$ and is minimal for the density of the ground state ρ :

$$E_0 = E[\rho] \leq E[n] \ . \tag{1.6}$$

\hat{T} and \hat{V}_{ee} are the operators of the kinetic energy and the electron-electron interaction, respectively. The functional $F[n]$ also is a unique functional of the particle density. However, it is independent of the external nuclear potential V_{ext} . Proofs of these theorems can be found, e.g. in chapter 6.2 of Ref. [10].

The determination of the correct ground state energy results from Theorem (2) by a variation of the total energy with respect to the density n . The variation of the particle density $n(\mathbf{r})$ at fixed particle number N has to be performed for the respective external potential $V_{\text{ext}}(\mathbf{r})$. To do so, Kohn and Sham [2] replaced the kinetic energy T of the interacting particles with that of the non-interacting electron gas T_0 at density n . The classic Coulomb energy is separated and all non-classical effects, like exchange and correlation, are incorporated into the energy E_{xc} . No exact expression for this XC-energy is known.

Within the approach of Kohn and Sham, the energy functional reads:

$$\begin{aligned}
 E[n] &= T_0[n] + \int V_{\text{ext}}(\mathbf{r})n(\mathbf{r}) d^3r + \int \int \frac{n(\mathbf{r})n(\mathbf{r}')}{|\mathbf{r} - \mathbf{r}'|} d^3r' d^3r + E_{\text{xc}}[n] \\
 &= E_{\text{kin}} + E_{\text{ext}} + E_{\text{H}} + E_{\text{xc}} \ .
 \end{aligned}
 \tag{1.7}$$

This functional has to be varied with respect to the charge density $n(\mathbf{r})$. Further representing the charge density $n(\mathbf{r})$ using single-particle orbitals ϕ_i , i.e.

$$n(\mathbf{r}) = \sum_{i=1}^{N_e} |\phi_i(\mathbf{r})|^2 \ , \tag{1.8}$$

as a sum of single-particle densities, the system of N_e interacting particles is transformed to a system of N_e effectively non-interacting particles. The kinetic energy

$$T_0[n] = \sum_{i=1}^{N_e} \int \phi_i^*(\mathbf{r})(-\nabla^2)\phi_i(\mathbf{r}) d^3r \ . \tag{1.9}$$

and the effective potential

$$V_{\text{eff}}([n], \mathbf{r}) = V_{\text{ext}}(\mathbf{r}) + \int \frac{2n(\mathbf{r}')}{|\mathbf{r} - \mathbf{r}'|} d^3r' + \frac{\delta E_{\text{xc}}[n]}{\delta n(\mathbf{r})} , \quad (1.10)$$

in which the external potential V_{ext} is formed by the interaction of electrons with the nuclear potentials, do not explicitly contain the particle density $n(\mathbf{r})$. Instead the single-particle wave functions $\phi_i(\mathbf{r})$ appear. It is convenient to replace the functional derivative with respect to the particle density to one with respect to the single-particle wave functions. The normalization of the $\phi_i(\mathbf{r})$ remains as a constraint, which is accounted for by a Lagrange parameter ϵ_i . The variation then finally leads to the Euler equations of a system of non-interacting particles, the *Kohn-Sham equations*:

$$\{-\nabla^2 + V_{\text{eff}}([\varrho], \mathbf{r})\} \phi_i(\mathbf{r}) = \epsilon_i \phi_i(\mathbf{r}) . \quad (1.11)$$

Hereby, the original many-particle equation is transformed to a system of N single-particle equations. Due to the dependence of the effective potential on the charge density, the solution of these equations has to be calculated self-consistently.

One should note at this point that the aforementioned eigenvalues ϵ_i - which have been formally introduced as Lagrange parameters in the variation and are thus only a mathematical tool - are often interpreted as single-particle energies. Strictly, there is no formal justification for this.

Multiplying $\phi_i^*(\mathbf{r})$ with Eq. (1.11) and subsequent integration over \mathbf{r} and summation of all N_e leads to

$$\sum_i^{N_e} \epsilon_i = T_0[n] + \int V_{\text{ext}}(\mathbf{r})n(\mathbf{r}) d^3r + \int \int \frac{2n(\mathbf{r})n(\mathbf{r}')}{|\mathbf{r} - \mathbf{r}'|} d^3r' d^3r + \int V_{\text{xc}}([n], \mathbf{r})n(\mathbf{r}) d^3r . \quad (1.12)$$

Solving this equation for $T_0[n]$ and substituting the result into the energy functional (1.7) yields an expression for the ground state energy ($n(\mathbf{r}) = \varrho(\mathbf{r})$):

$$E[\varrho] = \sum_{i=1}^{N_e} \epsilon_i - \int \int \frac{\varrho(\mathbf{r})\varrho(\mathbf{r}')}{|\mathbf{r} - \mathbf{r}'|} d^3r' d^3r + E_{\text{xc}}[\varrho] - \int V_{\text{xc}}([\varrho], \mathbf{r})\varrho(\mathbf{r}) d^3r . \quad (1.13)$$

In order to determine the total energy of the solid, the repulsion of the nuclei among themselves must be considered additionally:

$$E_{\text{tot}} = E[\varrho] + \sum_{\lambda=1}^{N_K} \sum_{\substack{\eta=1 \\ \eta \neq \lambda}}^{N_K} \frac{Z_\lambda Z_\eta}{|\mathbf{R}_\lambda - \mathbf{R}_\eta|} . \quad (1.14)$$

1.3. Local-density approximation

In the Kohn-Sham equations, all many-body effects are incorporated into the XC-energy $E_{xc}[n]$, for which no exact expression is known. The motivation of the *local-density approximation* is that as long as the particle density of the inhomogeneous electron gas is not too structured, it can be considered as locally constant. Hence, one approximates the density of the inhomogeneous electron gas locally by that of the homogenous one.

Let $\epsilon_{xc}(n(\mathbf{r}))$ be the exchange-correlation energy per electron of the homogenous electron gas for the density $n(\mathbf{r})$. Then, the XC-energy of the inhomogeneous electron gas can be written in the framework of the LDA as

$$E_{xc}[n] = \int n(\mathbf{r})\epsilon_{xc}(n(\mathbf{r})) d^3r. \quad (1.15)$$

The exchange-correlation potential then reads

$$V_{xc}([n], \mathbf{r}) = \frac{\delta E_{xc}[n]}{\delta n(\mathbf{r})} = \epsilon_{xc}(n(\mathbf{r})) + n(\mathbf{r}) \frac{d\epsilon_{xc}(n)}{dn} = V_{xc}^{LDA}(n(\mathbf{r})) \quad (1.16)$$

Ceperley and Alder [27] determined numerical values for the homogenous electron gas using Monte-Carlo methods. Perdew and Zunger [13] parametrized their results as follows:

$$\epsilon_{xc} = \epsilon_x + \epsilon_c \quad (1.17)$$

$$\epsilon_x = -\frac{0.9164}{r_s} \quad (1.18)$$

$$\epsilon_c = \begin{cases} -0.2846/(1 + 1.0529\sqrt{r_s} + 0.3334r_s) & \text{for } r_s \geq 1 \\ -0.0960 + 0.0622 \ln r_s - 0.0232r_s + 0.0040r_s \ln r_s & \text{for } r_s < 1 \end{cases} \quad (1.19)$$

$$r_s = \left(\frac{3}{4\pi n} \right)^{1/3} \quad (1.20)$$

$$V_{xc} = \epsilon_{xc} - \frac{r_s}{3} \frac{d}{dr_s} \epsilon_{xc} \quad (1.21)$$

Chapter 2.

Practical realization of density-functional theory calculations

Chapter 1 dealt with the fundamental aspects of density-functional theory within the local-density approximation for a general many-electron system. On this basis, the practical realization of DFT calculations which aim at the determination of structural and electronic properties of solids will be discussed below.

In the following section, a basis consisting of Gaussian orbitals is introduced, which is used to solve the Kohn-Sham equations numerically. The self-consistent procedure and the determination of the total energy is discussed in detail.

2.1. Solving the Kohn-Sham equations

According to Bloch's Theorem, the eigenvalues and eigenfunctions of a 3D-periodic bulk crystal can be classified by the wave vector \mathbf{k} and the band index n . The Kohn-Sham equations read:

$$\hat{H}\psi_{n,\mathbf{k}}(\mathbf{r}) = E_n(\mathbf{k})\psi_{n,\mathbf{k}}(\mathbf{r}) \quad , \quad (2.1)$$

with the Hamiltonian

$$\hat{H} = -\nabla^2 + V_{\text{eff}}([\varrho], \mathbf{r}) \quad . \quad (2.2)$$

Above equations constitute an eigenvalue problem. Within the pseudopotential approach only the valence electrons contribute to the effective potential, which can be written as

$$V_{\text{eff}}([\varrho], \mathbf{r}) = V_{\text{ion}}^{\text{ps}}(\mathbf{r}) + V_{\text{H}}([\varrho], \mathbf{r}) + V_{\text{xc}}([\varrho], \mathbf{r}). \quad (2.3)$$

Here, $\varrho(\mathbf{r})$ is the charge density of the valence electrons.

Using Bloch's Theorem, the wave function $\psi_{n,\mathbf{k}}(\mathbf{r})$ can be represented by a product of a

plane wave and a lattice periodic function $u_n(\mathbf{k}, \mathbf{r})$:

$$\psi_{n,\mathbf{k}}(\mathbf{r}) = e^{i\mathbf{k}\mathbf{r}} u_n(\mathbf{k}, \mathbf{r}) . \quad (2.4)$$

In this work, the wave functions $\psi_{n,\mathbf{k}}(\mathbf{r})$ are constructed using a finite set of lattice-periodic Bloch functions and read as:

$$\psi_{n,\mathbf{k}}(\mathbf{r}) = \sum_{\alpha,\nu} c_{n\alpha\nu}(\mathbf{k}) \chi_{\alpha\nu}(\mathbf{k}, \mathbf{r}) , \quad (2.5)$$

with

$$\chi_{\alpha\nu}(\mathbf{k}, \mathbf{r}) = \frac{1}{\sqrt{N_0}} \sum_{\mathbf{R}_j} e^{i\mathbf{k}(\mathbf{R}_j + \boldsymbol{\tau}_\nu)} \phi_{\alpha\nu}(\mathbf{r} - \mathbf{R}_j - \boldsymbol{\tau}_\nu) . \quad (2.6)$$

Here, the $\{\mathbf{R}_j\}$ are the vectors of the Bravais lattice and $\boldsymbol{\tau}_\nu$ is a vector of the non-primitive basis associated with the atom ν of the unit cell.

As ansatz functions $\phi_{\alpha\nu}(\mathbf{r})$, atom-centered Gaussian orbitals are employed, which can be expressed as

$$\phi_{\alpha\nu}(\mathbf{r}) = N_{lm,\gamma} r^l Y_{lm}(\vartheta, \varphi) e^{-\gamma_{\alpha\nu} r^2} \quad (2.7)$$

Due to their localization at the atomic positions, they are obviously dependent on the $\boldsymbol{\tau}_\nu$. The angular components of the orbitals are described by spherical harmonics $Y_{lm}(\vartheta, \varphi)$, while Gaussian functions with decay constants $\gamma_{\alpha\nu}$ constitute the radial components. The factor $N_{lm,\gamma}$ ensures the normalization of the functions. Associated with the different $\alpha \hat{=} (lm)$ are different symmetries of the orbitals. Typically, one considers the following symmetry types:

$$\alpha \hat{=} (lm) \hat{=} s, p_x, p_y, p_z, d_{zx}, d_{yz}, d_{xy}, d_{3z^2-r^2}, d_{x^2-y^2}, s^* . \quad (2.8)$$

The peculiar orbital $s^* = r^2 \cdot s$ serves to describe energetically higher states with spherical symmetry.

Using these Gaussian orbitals, the secular equation for the eigenvalue problem follows as

$$\sum_{\alpha'\nu'} c_{\alpha'\nu'}^{n,\mathbf{k}} \{ H_{\alpha\nu\alpha'\nu'}^{\mathbf{k}} - \epsilon_{n,\mathbf{k}} S_{\alpha\nu\alpha'\nu'}^{\mathbf{k}} \} = 0 . \quad (2.9)$$

The elements of the matrix of the Hamiltonian are calculated as

$$H_{\alpha\nu\alpha'\nu'}^{\mathbf{k}} = \sum_{\mathbf{R}_j} e^{i\mathbf{k}(\mathbf{R}_j - \boldsymbol{\tau}_\nu + \boldsymbol{\tau}_{\nu'})} \int \phi_{\alpha\nu}^*(\mathbf{r} - \boldsymbol{\tau}_\nu) \hat{H} \phi_{\alpha'\nu'}(\mathbf{r} - \mathbf{R}_j - \boldsymbol{\tau}_{\nu'}) d^3r \quad (2.10)$$

and those of the overlap matrix as

$$S_{\alpha\nu\alpha'\nu'}^{\mathbf{k}} = \sum_{\mathbf{R}_j} e^{i\mathbf{k}(\mathbf{R}_j - \boldsymbol{\tau}_\nu + \boldsymbol{\tau}_{\nu'})} \int \phi_{\alpha\nu}^*(\mathbf{r} - \boldsymbol{\tau}_\nu) \phi_{\alpha'\nu'}(\mathbf{r} - \mathbf{R}_j - \boldsymbol{\tau}_{\nu'}) d^3r \quad , \quad (2.11)$$

respectively. These matrix elements can be determined analytically in real space for the given $\phi_{\alpha\nu}(\mathbf{r})$. For explicit forms of the orbitals $\phi_{\alpha\nu}(\mathbf{r})$ as well as the matrix elements $H_{\alpha\nu\alpha'\nu'}^{\mathbf{k}}$ and $S_{\alpha\nu\alpha'\nu'}^{\mathbf{k}}$, see appendix B of Ref. [20] and Ref. [28] for possible improvements. Standard methods can be used to solve the secular equation for any given \mathbf{k} point numerically. This yields the required eigenvalues $\epsilon_{n,\mathbf{k}}$ together with the associated expansion coefficients $c_{\alpha\nu}^{n,\mathbf{k}}$, which can be used to finally construct the wave functions $\psi_{n,\mathbf{k}}(\mathbf{r})$. The electronic charge density of the considered system is a vital magnitude for the self-consistent calculation. With the use of Bloch functions, it is calculated according to

$$\varrho(\mathbf{r}) = 2 \cdot \sum_{n_{\text{occ}}} \sum_{\mathbf{k}} |\psi_{n,\mathbf{k}}(\mathbf{r})|^2 \quad (2.12)$$

as a sum over all occupied bands n_{occ} and over all \mathbf{k} points within the Brillouin zone. The factor 2 appears due to the spin degeneracy of the occupied bands.

Performing the sum over all \mathbf{k} is numerically impossible due to the discrete nature of a \mathbf{k} -point sampling. Still, one could simply take a high number of discrete and uniformly distributed points within the Brillouin zone to calculate the charge density. This poses an unjustified computational effort. Instead, it is much more commendable to make use of more efficient methods. These methods rely on the limitation of the sum to *special points* located within the irreducible wedge of the Brillouin zone. Consequently, these special points have to be determined based on the symmetry of the crystal at hand. A weight w_s is associated with each special point \mathbf{k}_s , which basically stands for the number of unique points within the full Brillouin zone that can be generated applying the symmetry operations of the Bravais lattice on the special points. The charge density (as well as all other properties that rely on Brillouin zone integration) can then be calculated according to

$$\varrho(\mathbf{r}) = 2 \cdot \sum_{n_{\text{occ}}} \left\{ \sum_s w_s \sum_{P \in M(\mathbf{k}_s)} |\psi_{n,P\mathbf{k}_s}(\mathbf{r})|^2 \right\} . \quad (2.13)$$

Here, the sum over the symmetry operations P that generate the star $M(\mathbf{k}_s)$ appear. The generated wave functions can be written using the transformation matrices $D_{\alpha\alpha'}^{(P)}$ of the symmetry group as

$$\psi_{n,P\mathbf{k}_s}(\mathbf{r}) = \sum_{\alpha\nu} \left\{ \sum_{\alpha'} D_{\alpha\alpha'}^{(P)} c_{\alpha'\nu}^{n,\mathbf{k}} \right\} \chi_{\alpha\nu}(P\mathbf{k}, \mathbf{r}) . \quad (2.14)$$

There are different methods for constructing the special points \mathbf{k}_s within the irreducible wedge of the Brillouin zone. Most commonly used are point schemes by Chadi and Cohen [29] or Monkhorst and Pack [30].

2.2. Norm-conserving pseudopotentials

The effective potential that enters the Kohn-Sham equations (1.11) consists of three contributions: the external potential of the nuclei $V_{\text{ext}}(\mathbf{r})$, the Hartree potential $V_{\text{H}}([\varrho], \mathbf{r})$ and exchange-correlation potential $V_{\text{xc}}([\varrho], \mathbf{r})$ of the electrons. Hitherto, all electrons within the unit cell of the crystal have been treated on equal footing. It is well known, however, that electrons from closed, inner shells of the atoms interact only weakly with their environment and thus hardly contribute to chemical bonding. On the one hand this is due to the stronger localization of such electrons close to the nucleus, on the other hand their respective energies are also much lower than the Fermi level, near which the characteristics of the chemical bond are determined. This suggests that it might be beneficial to limit the density-functional calculations to valence electrons and to incorporate the effects of the core electrons into an *ionic pseudopotential* $V_{\text{ion}}^{\text{ps}}(\mathbf{r})$. The Kohn-Sham equations in the pseudopotential approach then read

$$\{-\nabla^2 + V_{\text{eff}}^{\text{ps}}([\varrho^{\text{ps}}], \mathbf{r})\} \phi_i^{\text{ps}}(\mathbf{r}) = \epsilon_i \phi_i^{\text{ps}}(\mathbf{r}) \quad , \quad (2.15)$$

where the ϕ_i^{ps} are the associated pseudo wave-functions. With the respective pseudo charge-density

$$\varrho^{\text{ps}}(\mathbf{r}) = \sum_i^{\text{occ}} |\phi_i^{\text{ps}}(\mathbf{r})|^2 \quad (2.16)$$

the effective, screened pseudopotential is written as

$$V_{\text{eff}}^{\text{ps}}([\varrho^{\text{ps}}], \mathbf{r}) = V_{\text{ion}}^{\text{ps}}(\mathbf{r}) + V_{\text{H}}^{\text{ps}}([\varrho^{\text{ps}}], \mathbf{r}) + V_{\text{xc}}^{\text{ps}}([\varrho^{\text{ps}}], \mathbf{r}) \quad . \quad (2.17)$$

Such a pseudopotential does not exhibit the typical $1/r$ divergence of the standard Hartree potential and can consequently be described using a reduced basis set for the solution of the Kohn-Sham equations. A number of different kinds of pseudopotentials has been explored. Earlier calculations relied on *empirical* or *semi-empirical* pseudopotentials in which either the complete effective potential or its ionic component are fitted to empirical data. However, such pseudopotentials are problematic when being used in chemical environments different to those they were originally constructed for.

In contrast, so called *norm-conserving ab-initio* pseudopotentials do not rely on any reference data for the investigated system. They are constructed based on atomic all-electron calculations and have to fulfill a number of conditions that ensure accuracy and transfer-

ability. Details of these conditions and the construction process can be found in section 2 of Ref. [20] and references therein. The result of this process is a *semi-local* effective potential $V_{\text{eff},l}^{\text{ps}}(\mathbf{r})$, i.e. one that depends on the angular momentum l . The ionic pseudopotential is generated by unscreening this effective potential according to

$$V_{\text{ion},l}^{\text{ps}}(\mathbf{r}) = V_{\text{eff},l}^{\text{ps}}([\varrho^{\text{ps}}], \mathbf{r}) - V_{\text{H}}^{\text{ps}}([\varrho^{\text{ps}}], \mathbf{r}) - V_{\text{xc}}^{\text{ps}}([\varrho^{\text{ps}}], \mathbf{r}) \quad (2.18)$$

and can be split into a local component and a non-local one

$$\begin{aligned} V_{\text{ion}}^{\text{ps}} &= V_{\text{ion,loc}}^{\text{ps}}(\mathbf{r}) + V_{\text{ion,nloc}}^{\text{ps}} \\ &= V_{\text{ion,loc}}^{\text{ps}}(\mathbf{r}) + \sum_l \Delta V_l^{\text{ps}}(r) \sum_m |lm\rangle \langle lm| . \end{aligned} \quad (2.19)$$

This is possible because the nonlocality is limited to a core region, defined by radii $r_{c,l}$. The exact choice of the local component within that core region is arbitrary, in principle. In practical calculations, the local part can be treated in Fourier space, while the non-local part has to be determined in real space. Using the basis set of Gaussian orbitals to represent the Bloch functions, the calculation of matrix elements of the pseudopotential as given in Eq. (2.19) is highly demanding. Kleinman and Bylander [31] therefore developed a scheme to transform the non-local pseudopotential into a fully separable form. In that context the choice of the local part within the core region becomes relevant. Usually, this is set to be the component of the highest angular momentum l_{max} so that $\Delta V_{l_{\text{max}}}^{\text{ps}} = 0$. Then, the remaining non-local part of the pseudopotential operator follows in Kleinman-Bylander form as

$$\hat{V}_{\text{ion,nloc}}^{\text{KB}} = \sum_{lm} \frac{|\Delta V_l^{\text{ps}}(r)\phi_{lm}^{\text{ps}}\rangle \langle \Delta V_l^{\text{ps}}(r)\phi_{lm}^{\text{ps}}|}{\langle \phi_{lm}^{\text{ps}} | \Delta V_l^{\text{ps}}(r) | \phi_{lm}^{\text{ps}} \rangle} . \quad (2.20)$$

A suitable parametrization of the local and non-local part of the pseudopotential can be found in chapter 2 of Ref. [20].

2.2.1. Non-linear core corrections

The unscreening of the effective pseudopotential in Eq. (2.18) is achieved by subtracting the Hartree- and XC-potential based on the pseudo valence charge density $\varrho_{\text{val}} = \varrho^{\text{ps}}$. Any interaction between the valence charge and the core charge ϱ_{core} is neglected. This is correct for the Hartree potential as it is linear in the charge density. The XC-potential, in contrast, is not linear in the charge density and consequently the procedure defined in Eq. (2.18) is only an approximation. As long as there is no significant overlap between ϱ_{val} and ϱ_{core} , this approximation is well justified. There are, however, cases in which

this no longer holds. This affects the calculated total energy and the respective derived properties, like lattice constants, bulk moduli or atomic forces, in particular.

Louie *et al.* [32] proposed to use the combined charge density $\varrho_{\text{val}} + \varrho_{\text{core}}$ when calculating the XC-potential in the solid. Therefore, during unscreening of the pseudopotential the effective potential is evaluated as:

$$V_{\text{ion},l}^{\text{ps}}(\mathbf{r}) = V_{\text{eff},l}^{\text{ps}}([\varrho_{\text{val}}], \mathbf{r}) - V_{\text{H}}^{\text{ps}}([\varrho_{\text{val}}], \mathbf{r}) - V_{\text{xc}}^{\text{ps}}([\varrho_{\text{val}} + \varrho_{\text{core}}], \mathbf{r}) \quad (2.21)$$

The use of such non-linear core corrected (NLCC) pseudopotentials in calculations for solids requires the the atomic core charge density as additional input as it has to be added to the valence charge density when evaluating the XC-potential and energy. This poses an increased numerical demand as the core charge density of atoms is usually very structured and localized close to the nucleus. However, the error resulting from the pseudopotential construction in Eq. (2.18) mainly originates from the spatial regions in which both ϱ_{val} and ϱ_{core} are of similar magnitude. In Ref. [32] it was also shown that it is hence possible to smooth the core charge density in proximity of the nucleus, i.e. for radii smaller than a predefined radius r_0 , and use a partial core charge defined by

$$\tilde{\varrho}_{\text{core}}(r) = \begin{cases} \frac{A}{r} \sin(Br) & r \leq r_0 \\ \varrho_{\text{core}}(r) & r > r_0 \end{cases}. \quad (2.22)$$

The radius r_0 is typically determined as being the radius, at which the core charge density is larger than the valence charge density by a factor of 1 to 2. The remaining two parameters A and B must fulfill the conditions that

$$\tilde{\varrho}_{\text{core}}(r_0) = \varrho_{\text{core}}(r_0) \quad (2.23)$$

$$\left. \frac{d\tilde{\varrho}_{\text{core}}(r)}{dr} \right|_{r=r_0} = \left. \frac{d\varrho_{\text{core}}(r)}{dr} \right|_{r=r_0}, \quad (2.24)$$

so that the resulting partial density is continuously differentiable. Due to the explicit form given in Eq. (2.22), the slope of the full charge density must be negative at r_0 . In order to generate a node-free partial core density, it must also be ensured that $0 < B < \frac{\pi}{\varrho_0}$.

It turns out that the use of non-linear core corrected pseudopotentials as defined by Eq. (2.21) improves the calculated total energies as well as lattice constants etc. significantly (cf Refs. [32–35]).

2.3. Self-consistent electronic structure calculations

In the course of a self-consistent solution of the Kohn-Sham equations it is necessary to calculate for every iteration N the new output potential $V_{\text{out}}^N(\mathbf{r})$ based on the respective charge density. The complete effective potential is composed of a local (here already in Fourier representation) and a non-local part as was shown in the previous section:

$$V_{\text{eff}}^N(\mathbf{r}) = V_{\text{ion,nloc}}^{\text{KB}}(\mathbf{r}) + \sum_{\mathbf{G}_l} V_{\text{out}}^N(\mathbf{G}_l) e^{-i\mathbf{G}_l \mathbf{r}} , \quad (2.25)$$

where:

$$V_{\text{out}}^N(\mathbf{G}_l) = V_{\text{ion,loc}}^{\text{KB}}(\mathbf{G}_l) + V_{\text{H}}^N(\mathbf{G}_l) + V_{\text{xc}}^N(\mathbf{G}_l) . \quad (2.26)$$

The local component $V_{\text{ion,loc}}^{\text{KB}}(\mathbf{G}_l)$ of the pseudopotential remains unchanged during the procedure, just as the non-local component $V_{\text{ion,nloc}}^{\text{KB}}(\mathbf{r})$. Apparently, it is sufficient to calculate these two contributions once at the beginning of the procedure.

The Fourier transform $V_{\text{ion,loc}}^{\text{KB},\mu}(\mathbf{G}_l)$ of the local part of the pseudopotential in the parameterized Kleinman-Bylander form (cf. Sec. 2 of Ref. [20]) follows as:

$$\begin{aligned} V_{\text{ion,loc}}^{\text{KB},\mu}(\mathbf{G}_l) = & -\frac{4\pi}{\Omega_0} \frac{Z_\mu}{\mathbf{G}_l^2} \sum_i A_{\mu,i} e^{-\frac{\mathbf{G}_l^2}{4\alpha_{\mu,i}}} \\ & + \frac{1}{\Omega_0} \sum_{j=1}^n \left(\frac{\pi}{\beta_{\mu,j}} \right)^{3/2} \left\{ B_{\mu,j} + B_{\mu,j+n} \left(\frac{3}{2\beta_{\mu,j}} - \frac{\mathbf{G}_l^2}{4\beta_{\mu,j}^2} \right) \right\} e^{-\frac{\mathbf{G}_l^2}{4\beta_{\mu,j}}} . \end{aligned} \quad (2.27)$$

As one can see, this expression diverges for $\mathbf{G}_l = \mathbf{0}$. During the setup of the secular equation, this term is omitted as will be discussed in more detail when one considers the total energy.

The Fourier coefficients of the Hartree potential can be determined by transforming the Poisson equation into Fourier space, resulting in

$$V_{\text{H}}(\mathbf{G}_l) = \frac{8\pi}{\mathbf{G}_l^2} \varrho(\mathbf{G}_l) . \quad (2.28)$$

This term also diverges for $\mathbf{G}_l = \mathbf{0}$ and is consequently omitted as well during the setup of the potential matrix. The two divergent terms $V_{\text{ion,loc}}^{\text{KB}}(\mathbf{G}_l = \mathbf{0})$ and $V_{\text{H}}(\mathbf{G}_l = \mathbf{0})$ compensate each other [36].

The exchange-correlation potential $V_{\text{xc}}^N(\mathbf{r})$ is determined in real space according to Eq. (1.21) and is subsequently transformed into Fourier space using a Fast-Fourier-Transform

(FFT). Since both the Hartree- and XC-potential depend on the actual charge density, these parts of the total potential have to be updated in each iteration of the self-consistent procedure.

However, the output potential of the N -th iteration that is given by

$$V_{\text{out}}^N(\mathbf{G}_l) = V_{\text{ion,loc}}^{\text{KB}}(\mathbf{G}_l) + V_{\text{H}}^N(\mathbf{G}_l) + V_{\text{xc}}^N(\mathbf{G}_l) \quad (2.29)$$

is hardly suitable to be used as input potential $V_{\text{in}}^{N+1}(\mathbf{G}_l)$ for iteration $N + 1$. In actual calculations, such a choice often leads to difficulties with the convergence of the solution. Assuming that convergence is reached when the input potentials of two successive iterations do not differ, meaning that the squared difference

$$\sum_{\mathbf{G}} |V_{\text{in}}^{N+1}(\mathbf{G}) - V_{\text{in}}^N(\mathbf{G})|^2 < m_0 \quad (2.30)$$

is lower than a certain convergence limit m_0 . A typical value for this limit is

$$m_0 = 10^{-9} \text{ Ryd}^2 \quad (2.31)$$

In order to avoid the aforementioned difficulties in finding a convergent solution and to achieve a significantly faster convergence, the input potential $V_{\text{in}}^{N+1}(\mathbf{G}_l)$ is determined by mixing potentials of previous iterations. Some techniques defining the mixing functional \mathcal{E} are described in appendix C of Ref. [20].

Figure 2.1 schematically shows the sequence of a self-consistent calculation.

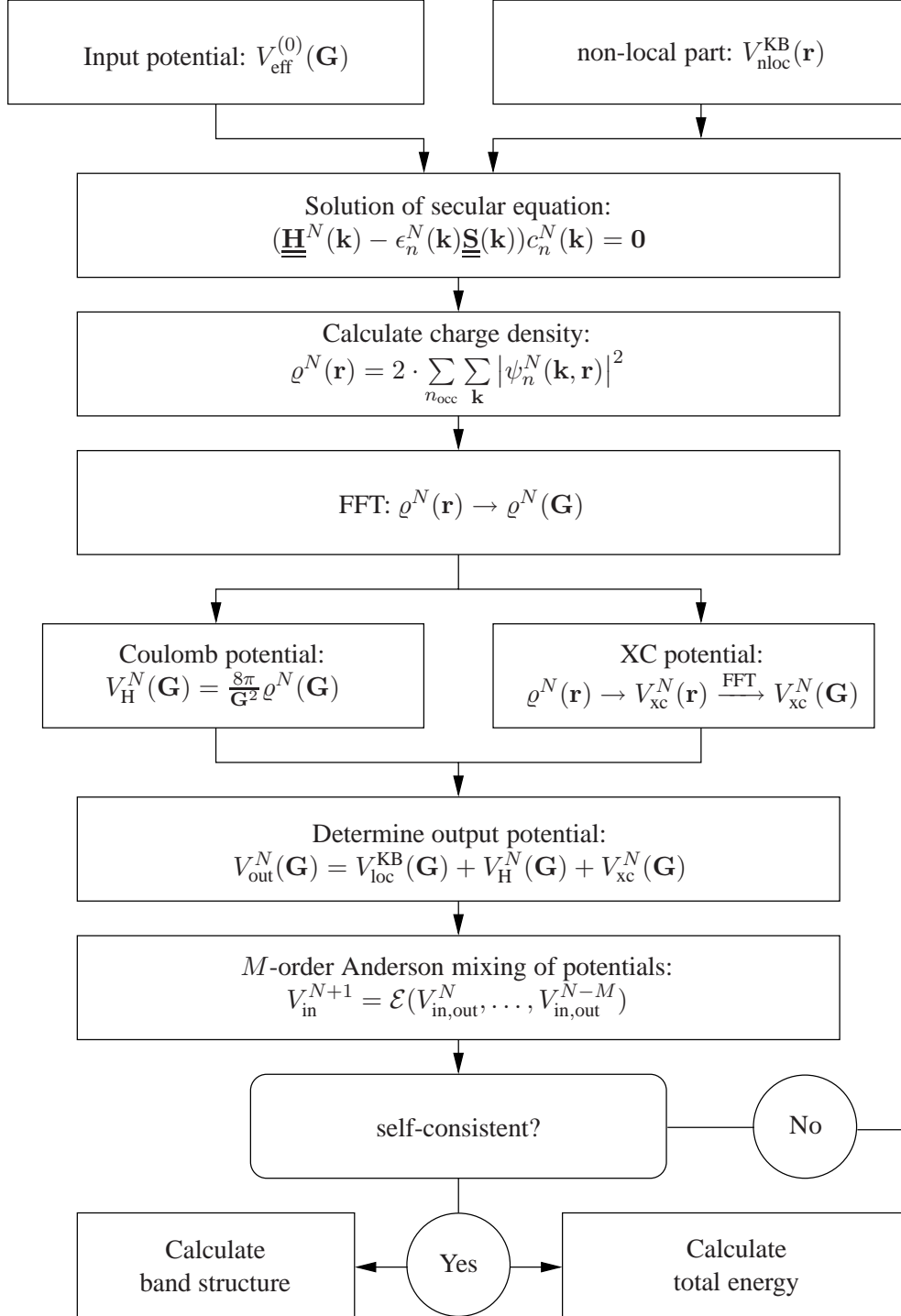


Figure 2.1: Flow chart of the electronic self-consistent procedure.

2.4. Total energy calculations

According to Hohenberg and Kohn [1], the total energy of a solid can be determined exactly for its ground state within DFT. As one has to resort to the use of approximations, e.g. the LDA, for the unknown exchange-correlation energy and potential, respectively, and by using pseudopotentials, one can only approximate the true total energy. This magnitude is of vital importance for the determination of geometric (atomic) structure of solids as bulk crystals, surfaces (with or without adsorbates) and lower-dimensional systems.

As in (1.14), the total energy per unit cell (of volume Ω_0) of a solid reads within DFT-LDA:

$$\begin{aligned}
 E_{\text{tot}} &= 2 \sum_{n_{\text{occ}}, \mathbf{k}} \epsilon_n(\mathbf{k}) - \iint_{\Omega_0} \frac{\varrho(\mathbf{r}')\varrho(\mathbf{r})}{|\mathbf{r}' - \mathbf{r}|} d^3r' d^3r \\
 &+ \int_{\Omega_0} (\epsilon_{\text{xc}}(\varrho(\mathbf{r})) - V_{\text{xc}}(r))\varrho(\mathbf{r}) d^3r + \sum_{\substack{\{j,\nu\} \neq \{j_0,\mu\}}} \frac{Z_\nu Z_\mu}{|\mathbf{R}_{j,\nu} - \mathbf{R}_{j_0,\mu}|} \\
 &= E_{\text{bs}} - E_{\text{H}} + E_{\text{xc}} + E_{\text{Mad}} .
 \end{aligned} \tag{2.32}$$

Here, the vector $\mathbf{R}_{j,\nu}$ stands for the position of the nuclei $\mathbf{R}_j + \boldsymbol{\tau}_\nu$, while it shall hold that $\mathbf{R}_{j_0,\mu} = \boldsymbol{\tau}_\mu$. The sum over n_{occ} shall run over all occupied bands.

In the previous section it has already been mentioned that the divergent terms of the local part of the pseudopotential and the Hartree potential are omitted when setting up the secular equation. This can be done as the total Fourier component of $\mathbf{G}_l = \mathbf{0}$ equals the mean total potential within the unit cell and thus only acts as a constant shift to the calculated energy spectrum. This of course only holds as long as no divergency remains in the respective components. Obviously, for a total energy calculation, one needs the definition of an absolute energy scale and hence, one cannot omit the contributions from $\mathbf{G}_l = \mathbf{0}$ to the total energy.

In Ref. [36] a thorough discussion of how these terms are treated is given. Firstly using the pseudopotential parametrization they are separated into non-divergent and divergent components. Then it is shown in quite some detail that the latter compensate each other so that, in effect, no divergency remains in the total energy.

Finally, the total energy of the solid per unit cell is calculated according to:

$$\begin{aligned}
 E_{\text{tot}} &= \frac{2}{n_s} \sum_{\mathbf{k}, n}^{\text{occ}} \epsilon_n^0(\mathbf{k}) + \Omega_0 \sum_{\mathbf{G}} [\epsilon_{\text{xc}}(\mathbf{G}) - V_{\text{xc}}(\mathbf{G})] \varrho^*(\mathbf{G}) \\
 &- \Omega_0 \sum_{\mathbf{G} \neq \mathbf{0}} \frac{4\pi}{G^2} |\varrho(\mathbf{G})|^2 + E_{\text{Mad}} + Z \sum_{\mu} a_{\mu} .
 \end{aligned} \tag{2.33}$$

2.5. Atomic forces and optimization of the atomic structure

So far, the determination of the electronic structure for a fixed atomic geometry has been analyzed. The converged solution of Eq. (2.9) yields the ground state energy for this geometry. However, it is well possible that for a different set of atomic positions, a lower total energy might result. The total energy is therefore dependent on the atomic configuration. If one optimizes the atomic structure of a given system – usually when the three-dimensional symmetry of translation is broken, i.e. at a surface of the crystal – one is looking for a minimum of the associated total energy hypersurface.

Obviously, one has to look at the derivatives of the total energy with respect to the atomic positions. This is, however, nothing else than the negative of the forces on the atoms. More explicitly, the force on the atom located at the position τ_ν follows as

$$\mathbf{F}_\nu = -\nabla_{\tau_\nu} E_{\text{tot}}. \quad (2.34)$$

In order to evaluate (2.34), Eq. (1.14) is used in a slightly different form

$$\begin{aligned} E_{\text{tot}} &= \frac{2}{N_0} \sum_{n,\mathbf{k}}^{\text{occ}} \int_{V_0} \psi_{n,\mathbf{k}}^*(\mathbf{r}) \left(-\Delta + \frac{1}{2}V_{\text{H}}(\mathbf{r}) + \epsilon_{\text{xc}}(\mathbf{r}) + V_{\text{ext}}(\mathbf{r}) \right) \psi_{n,\mathbf{k}}(\mathbf{r}) d^3r + E_{\text{Mad}} \\ &= \left\langle \Psi \left| -\Delta + \frac{1}{2}V_{\text{H}} + \epsilon_{\text{xc}} + V_{\text{ext}} \right| \Psi \right\rangle + E_{\text{Mad}} \end{aligned} \quad (2.35)$$

The bracket form has been introduced in order to ease the following discussion. Let us now first consider an arbitrary hermitian operator \hat{O} . Its derivative with respect to the atomic positions can be written as

$$\begin{aligned} \nabla_\nu \langle \Psi | \hat{O} | \Psi \rangle &= \langle \nabla_\nu \Psi | \hat{O} | \Psi \rangle + \langle \Psi | \nabla_\nu \hat{O} | \Psi \rangle + \langle \Psi | \hat{O} | \nabla_\nu \Psi \rangle \\ &= 2\text{Re} \langle \Psi | \hat{O} | \nabla_\nu \Psi \rangle + \langle \Psi | \nabla_\nu \hat{O} | \Psi \rangle. \end{aligned} \quad (2.36)$$

Identifying $\hat{O} = \langle \Psi | -\Delta + \frac{1}{2}V_{\text{H}} + \epsilon_{\text{xc}} + V_{\text{ext}} | \Psi \rangle$, one can make use of this relation and analyze the dependence of V_{H} and ϵ_{xc} on the atomic positions. As the associated operators are local and multiplicative, the wave functions Ψ can be combined in the charge density $\varrho(\mathbf{r})$. After some calculations, one finds that

$$\langle \Psi | \nabla_\nu V_{\text{H}} | \Psi \rangle = \int_{V_0} \varrho(\mathbf{r}) \nabla_\nu V_{\text{H}}(\mathbf{r}) d^3r = \dots = 2\text{Re} \langle \Psi | V_{\text{H}} | \nabla_\nu \Psi \rangle \quad (2.37)$$

and

$$\langle \Psi | \nabla_\nu \epsilon_{xc} | \Psi \rangle = \int_{V_0} \varrho(\mathbf{r}) \nabla_\nu \epsilon_{xc}(\mathbf{r}) d^3r = \dots = 2\text{Re} \langle \Psi | V_{xc} - \epsilon_{xc} | \nabla_\nu \Psi \rangle, \quad (2.38)$$

respectively. Now, the derivative of the total energy follows as

$$\begin{aligned} \nabla_\nu E_{\text{tot}} &= 2\text{Re} \langle \Psi | -\Delta + \frac{1}{2}V_H + \epsilon_{xc} + V_{\text{ext}} | \nabla_\nu \Psi \rangle + \langle \Psi | \nabla_\nu (\frac{1}{2}V_H + \epsilon_{xc}) | \Psi \rangle \\ &\quad + \langle \Psi | \nabla_\nu V_{\text{ext}} | \Psi \rangle + \nabla_\nu E_{\text{Mad}} \\ &= 2\text{Re} \langle \Psi | -\Delta + V_H + V_{xc} + V_{\text{ext}} | \nabla_\nu \Psi \rangle + \langle \Psi | \nabla_\nu V_{\text{ext}} | \Psi \rangle + \nabla_\nu E_{\text{Mad}}. \end{aligned} \quad (2.39)$$

So, finally, one can identify three separate contributions to the forces that have to be calculated. Identifying $-\Delta + V_H + V_{xc} + V_{\text{ext}}$ as the Kohn-Sham Hamiltonian, the force on the ν -th atom reads

$$\mathbf{F}_\nu = -\nabla_\nu E_{\text{tot}} = \underbrace{-2\text{Re} \langle \Psi | \hat{H} | \nabla_\nu \Psi \rangle}_{:=\mathbf{F}_\nu^{\text{Pul}}} - \underbrace{\langle \Psi | \nabla_\nu V_{\text{ext}} | \Psi \rangle}_{:=\mathbf{F}_\nu^{\text{HF}}} - \underbrace{\nabla_\nu E_{\text{Mad}}}_{:=\mathbf{F}_\nu^{\text{Mad}}}. \quad (2.40)$$

The first term $\mathbf{F}_\nu^{\text{Pul}}$ is the *Pulay force*, which only occurs for an incomplete or τ -dependent basis. Using a plane wave basis, this force vanishes as $\nabla_\nu \Psi = \mathbf{0}$. The *Hellmann-Feynman force* $\mathbf{F}_\nu^{\text{HF}}$ is in contrast connected to the change of the physical system, in which electrons reside as the external potential changes. Both of these terms can be treated using the *Hellmann-Feynman theorem*. In appendix A explicit expressions for these three forces based on the use of a localized basis are presented in detail.

The intention of calculating forces is to find an optimized atomic configuration, for which the total energy of the system reaches a local minimum and the forces vanish. Just as in the case of finding a self-consistent solution of the Kohn-Sham equations for a fixed geometry, this can be achieved by an iterative process.

This process is schematically depicted in Fig. 2.2. Based on an input configuration of the atomic geometry $\tau^{(N)}$ in the N -th step of the iteration, the associated effective potential $V_{\text{in}}^{(N)}$ is used to start an electronic self-consistent procedure as was described in section 2.3. This leads to a converged effective potential $V_{\text{out}}^{(N)}$ and the total energy $E_{\text{tot}}(\tau^{(N)})$, from which the atomic forces $\mathbf{F}^{(N)}$ are calculated. If the total force is lower than a certain threshold, a local minimum of the total energy hypersurface is assumed to be found. If it is not, a new atomic configuration is determined based on the calculated forces. Just as in the case of the electronic self-consistent calculation, it is appropriate to use a mixing scheme to find this updated configuration. Instead of simply moving the ions in the direction of the respective forces on them, results from previous iterations are considered as well, analogous to the mixing of effective potentials that was mentioned in section 2.3.

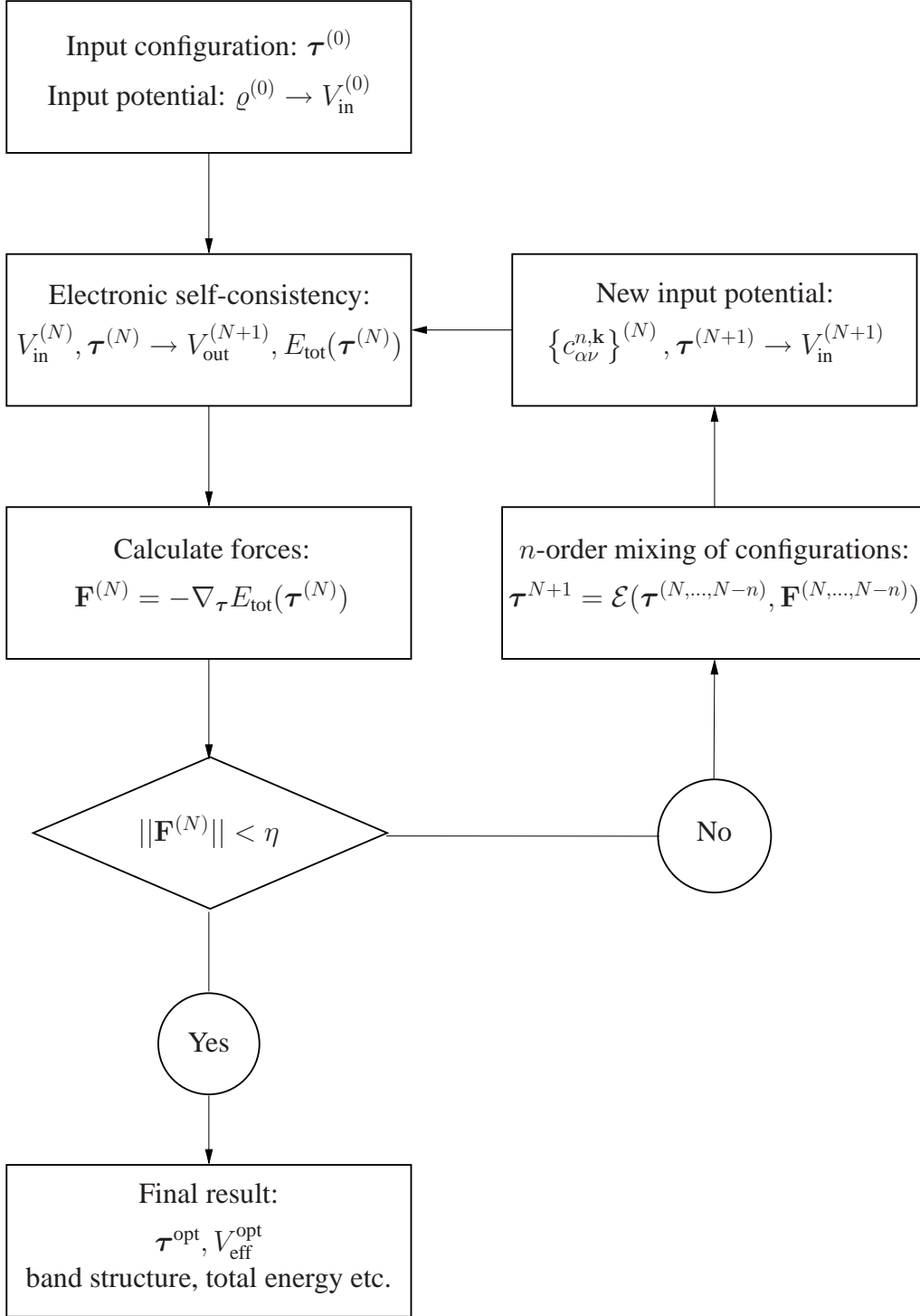


Figure 2.2: Flow chart of the geometry optimization.

Chapter 3.

Self-interaction corrections to density-functional theory

For applications of a solid in opto- and microelectronic devices a precise knowledge of its electronic properties is essential. From a theoretical point of view, density-functional theory using the local-density approximation has been established as an extremely useful *ab-initio* method to calculate these properties. However, standard LDA calculations typically underestimate critical band structure data, like the band gap or the valence band width.

The systematic deviations of DFT-LDA results from experimental data can be traced back to unphysical self-interactions inherent in LDA, as has been shown by Perdew and Zunger [13]. The authors applied a self-interaction correction (SIC) to atomic systems and were able to overcome the shortcomings of the LDA to a large extent.

In this chapter, a short summary of Perdew and Zunger's fundamental findings for atomic systems will be given. There will be a review of previous related attempts to apply self-interaction-correction schemes to solids before the approach to construct self-interaction-corrected pseudopotentials followed in this work will be presented in detail. The *s, p*-bonded compound semiconductor silicon carbide will serve as a prototypical example in this regard.

3.1. The self-interaction error

As mentioned before, Perdew and Zunger [13] attributed the errors of DFT-LDA in atomic systems to unphysical self-interactions due to the use of the LDA. They also proposed a simple method to remove this self-interaction error (SIE) from the energy functional and the associated effective potential. The hydrogen atom constitutes a very instructive example for the discussion of the SIE and the self-interaction correction.

Density-functional theory as presented up to this point needs to be modified when spin-

polarization is significant for the system under investigation¹. This is usually the case in metal compounds with respect to magnetism and in isolated atoms like hydrogen. The needed modification is achieved by partitioning the total charge density $n(\mathbf{r})$ in the individual contributions of spin-up and spin-down electrons, respectively:

$$n(\mathbf{r}) = n^\uparrow(\mathbf{r}) + n^\downarrow(\mathbf{r}) . \quad (3.1)$$

In analogy to the spin-less case the variation of the energy functional

$$E[n^\uparrow, n^\downarrow] = T_0[n] + \int V_{\text{ext}}(\mathbf{r})n(\mathbf{r}) d^3r + \int \int \frac{n(\mathbf{r})n(\mathbf{r}')}{|\mathbf{r} - \mathbf{r}'|} d^3r' d^3r + E_{\text{xc}}^\sigma[n^\uparrow, n^\downarrow] , \quad (3.2)$$

with respect to the single-particle wave functions fulfilling the norm constraint $\phi_i^\sigma(\mathbf{r})$ leads to the spin-polarized Kohn-Sham equations for the ground state ($n(\mathbf{r}) = \varrho(\mathbf{r})$):

$$\{-\nabla^2 + V_{\text{ext}}(\mathbf{r}) + V_{\text{H}}([\varrho], \mathbf{r}) + V_{\text{xc}}([\varrho^\uparrow, \varrho^\downarrow], \mathbf{r})\} \phi_i^\sigma(\mathbf{r}) = \epsilon_i^\sigma \phi_i^\sigma(\mathbf{r}) . \quad (3.3)$$

Within the local-spin-density approximation (LSDA), numerical results of the homogeneous electron gas are used to parameterize the XC-energy and the XC-potential, respectively.

The electronic ground state of the hydrogen atom is now treated within the framework of the LSDA. The energy functional solely depends on the $1s$ wave function and reads:

$$\begin{aligned} E^{\text{LSDA}}[\varrho_{1s}] &= T_0[\varrho_{1s}] + \int V_{\text{ext}}(\mathbf{r})\varrho_{1s}(\mathbf{r}) d^3r + E_{\text{H}}[\varrho_{1s}] + E_{\text{xc}}^{\text{LSDA}}[\varrho_{1s}, 0] \\ &= -13.6 \text{ eV} + 8.5 \text{ eV} - 7.9 \text{ eV} \\ &= -13.0 \text{ eV} . \end{aligned}$$

Obviously, the total energy of the hydrogen atom as calculated within LSDA deviates by +0.6 eV from the exact solution. As there is only one single electron in the system, the contributions from the Hartree energy E_{H} and from the exchange-correlation energy E_{xc} should cancel each other. The LSDA is not exact, however, and contains a non-vanishing repulsive electron-electron interaction leading to a total energy that is too high by roughly 5%. The presence of a single electron directly shows that this net electron-electron interaction can only stem from the interaction of the $1s$ electron with itself. This unphysical *self-interaction* is an immediate consequence of the use of the LSDA.

The SIE is even more severe for the calculated eigenvalues of the Kohn-Sham equations:

$$\begin{aligned} \epsilon_{1s}^{\text{LSDA}} &= \langle \phi_{1s} | -\nabla^2 - \frac{2}{r} | \phi_{1s} \rangle + \langle \phi_{1s} | V_{\text{H}}[\varrho_{1s}] + V_{\text{xc}}^{\text{LSDA}}[\varrho_{1s}, 0] | \phi_{1s} \rangle \\ &= -13.6 \text{ eV} + 6.3 \text{ eV} \\ &= -7.3 \text{ eV} . \end{aligned}$$

¹Spin-polarization is only introduced here to better visualize the error and the later corrective approach in the isolated atom. Any subsequent calculation is performed within the unpolarized regime of the LDA.

Relying on the common interpretation of these eigenvalues as single-particle excitation energies yields a binding energy of the $1s$ electron that deviates by a massive 6.3 eV or 46% from the exact values. Such deviations of the calculated properties in the framework of L(S)DA (total energy by roughly 5% and the difference of highest occupied and lowest unoccupied eigenvalues, i.e. the gap in semiconductors, by 40%) from experimental reference data are also found for almost all many-electron systems and can be primarily traced back to the unphysical self-interaction inherent in the used approximation.

3.2. Self-interaction corrections in atoms: The Perdew-Zunger approach

Considering the analysis of the SIE in the previous section, a simple way to compensate this error in the hydrogen atom is to subtract the terms originating from the net electron-electron interaction from the energy functional and the potential, respectively:

$$\begin{aligned} E^{\text{LSDA}}[\varrho_{1s}] &= T_0[\varrho_{1s}] + \int V_{\text{ext}}(\mathbf{r})\varrho_{1s}(\mathbf{r}) d^3r + E_{\text{H}}[\varrho_{1s}] + E_{\text{xc}}^{\text{LSDA}}[\varrho_{1s}, 0] \\ &\quad - E_{\text{H}}[\varrho_{1s}] - E_{\text{xc}}^{\text{LSDA}}[\varrho_{1s}, 0] \\ &= -13.6 \text{ eV} , \end{aligned}$$

and

$$\begin{aligned} \epsilon_{1s}^{\text{LSDA}} &= \langle \phi_{1s} | -\nabla^2 - \frac{2}{r} | \phi_{1s} \rangle + \langle \phi_{1s} | V_{\text{H}}[\varrho_{1s}] + V_{\text{xc}}^{\text{LSDA}}[\varrho_{1s}, 0] | \phi_{1s} \rangle \\ &\quad - \langle \phi_{1s} | V_{\text{H}}[\varrho_{1s}] - V_{\text{xc}}^{\text{LSDA}}[\varrho_{1s}, 0] | \phi_{1s} \rangle \\ &= -13.6 \text{ eV} . \end{aligned}$$

Obviously, this simple approach leads to an agreement between the LSDA and the exact results. Perdew and Zunger [13] transferred this approach to many-electron atoms defining a *self-interaction-corrected* energy functional that reads as:

$$E^{\text{approx,SIC}} = E^{\text{approx}} - \sum_{\alpha}^{\text{occ}} \{ E_{\text{H}}[\varrho_{\alpha}] + E_{\text{xc}}^{\text{approx}}[\varrho_{\alpha}] \} . \quad (3.4)$$

Here, the LSDA energy functional is replaced by a more general expression E^{approx} indicating that the same can be done – in principle – for any approximative XC-potential that solely depends on the single-particle charge density $\varrho(\mathbf{r})$ such as LDA or GGA. A variation of this SIC-functional again yields a set of effective single-particle wave functions

$$\{ -\nabla^2 + V_{\alpha,\text{eff}}^{\text{SIC}}(\mathbf{r}) \} \phi_{\alpha}^{\text{SIC}}(\mathbf{r}) = \epsilon_{\alpha}^{\text{SIC}} \phi_{\alpha}^{\text{SIC}}(\mathbf{r}) , \quad (3.5)$$

with the effective potential:

$$V_{\alpha,\text{eff}}^{\text{SIC}}([\varrho], \mathbf{r}) = V_{\text{eff}}([\varrho], \mathbf{r}) - \{V_{\text{H}}([\varrho_{\alpha}], \mathbf{r}) + V_{\text{xc}}^{\text{approx}}([\varrho_{\alpha}, 0], \mathbf{r})\} \quad (3.6)$$

$$= V_{\text{eff}}([\varrho], \mathbf{r}) - V_{\alpha}^{\text{SIC}}(\mathbf{r}) . \quad (3.7)$$

The SIC energy functional (3.4) and the SIC equations (3.5) constitute what will from now on be referred to as the PZ-SIC approach. Apparently the state-dependence of the energy functional directly results in a state-dependent effective potential $V_{\alpha,\text{eff}}^{\text{SIC}}([\varrho], \mathbf{r})$. Actually, the variation of Eq. 3.4 is not as straightforward as in the usual Kohn-Sham case. For instance, the calculated orbitals $\phi_{\alpha}^{\text{SIC}}(\mathbf{r})$ are no longer strictly orthogonal. The introduction of non-diagonal Lagrangian parameters can solve this problem but is neglected for the sake of simplicity. A more detailed discussion of these and related difficulties with the PZ-SIC approach will be given at a later stage of this work.

The effective potential $V_{\text{eff}}(\mathbf{r})$ within the L(S)DA or GGA vanishes for large r due to the complete screening of the Coulomb potential of the nucleus. As the exchange-correlation potential is only locally dependent on the charge density, it also goes to zero in the same condition. The SIC potential $V_{\alpha}^{\text{SIC}}(\mathbf{r})$, however, runs asymptotically as $\frac{2}{r}$, which translates into a $-\frac{2}{r}$ tail of the effective SIC potential $V_{\alpha,\text{eff}}^{\text{SIC}}([\varrho], \mathbf{r})$. For the occupied states, this is the correct asymptotic dependence of a single-particle potential.

As pointed out above, the SIC energy functional (3.4) results in an exact description of the hydrogen atom. One has to keep the fact in mind that this only constitutes a heuristic approximation for more general many-electron systems. Yet, the results of the respective SIC calculations are highly convincing that this approximation is justified. As was pointed out above, the deviation of LSDA results with regards to the total energy are in the order of 5%. It turns out that the L(S)DA yields total-energy derived physical properties of solids that are in good agreement with experimental results, for instance lattice constants or bulk moduli (cf. Ref. [10] and references therein). These bonding characteristics are intimately related to the charge density distribution and accordingly to the single-particle wave functions. Consequently, these properties should only exhibit minimal changes after inclusion of SIC. A respective comparison of the wave functions of free atoms indeed shows that the changes are only minor. The total energy is typically lowered and deviates by about 0.5% from experimental results. Due to the additional attractive potential the electronic wave functions show a tendency to slightly localize with respect to the L(S)DA reference.

In contrast, the spectrum of the associated Kohn-Sham eigenvalues is more significantly altered. In Table 3.1, the atomic term values as resulting from non-spinpolarized LDA and PZ-SIC calculations as well as experimentally determined ionization energies are shown for the variety of chemical elements that will be addressed later in this work. The results indicate that the interpretation of the eigenvalues as ionization energies of the free atoms

3.2. Self-interaction corrections in atoms: The Perdew-Zunger approach

	non-spin-polarized		spin-polarized		Exp.
	$\epsilon_{\alpha}^{\text{LDA}}$	$\epsilon_{\alpha}^{\text{SIC}}$	$\epsilon_{\alpha}^{\text{LDA}}$	$\epsilon_{\alpha}^{\text{SIC}}$	E_b^a
Alkali metals					
Li $2s$	-2.90	-5.10	-3.13	-5.33	-5.39
Na $3s$	-2.82	-4.92	-3.02	-5.12	-5.14
K $4s$	-2.42	-4.06	-2.57	-4.21	-4.34
Alkaline earth metals					
Be $2s$	-5.60	-9.03	-6.28	-9.71	-9.32
Mg $3s$	-4.79	-7.54	-5.30	-8.05	-7.65
Ca $4s$	-3.88	-5.95	-4.24	-6.31	-6.11
Sr $5s$	-3.64	-5.55	-3.96	-5.87	-5.69
Ba $6s$	-3.35	-5.02	-3.62	-5.29	-5.21
Metalloids					
B $2s$	-9.39	-13.92	-10.32	-14.85	
B $2p$	-3.72	-7.78	-3.97	-8.03	-8.30
Si $3s$	-10.88	-15.01	-11.59	-15.72	
Si $3p$	-4.17	-7.36	-4.61	-7.80	-8.15
Non-metals					
C $2s$	-13.65	-19.66	-14.78	-20.79	
C $2p$	-5.42	-11.05	-6.19	-11.82	-11.26
N $2s$	-18.41	-25.06	-19.61	-26.26	
N $2p$	-7.24	-13.47	-8.50	-14.24	-14.53
O $2s$	-23.74	-31.38	-25.03	-32.67	
O $2p$	-9.20	-16.48	-6.50	-13.78	-13.62
Halogens					
F $2s$	-29.63	-38.28	-30.99	-39.64	
F $2p$	-11.29	-19.60	-9.78	-18.09	-17.42

^afrom Ref. [37]

Table 3.1: Atomic term values (in eV) of the valence shell levels for various free atoms as resulting from non-spinpolarized LDA and PZ-SIC calculations. For reference, spinpolarized values (see text for details) and the experimental ionization energies E_b for the respective levels as given in Ref. [37] are listed, as well.

is hugely more justified when PZ-SIC is applied. While pure L(S)DA eigenvalues exhibit deviations of roughly 40% from experimental reference values, the inclusion of the PZ-SIC improves the respective agreement massively. The spinpolarized eigenvalues given in Table 3.1 result from adding the spin-polarization effect on the binding energies (from Δ SCF calculations) defined as $\delta E^{\text{spin}} = E_b^{\text{LDA}} - E_b^{\text{LSDA}}$ to the non-spinpolarized values.

3.3. Self-interaction corrections for solids: First approaches

As was shown in the preceding section, the PZ-SIC approach for atomic systems has resulted in a significantly improved agreement between calculated atomic term values and the ionization energies as determined experimentally for the free atoms. It has been pointed out before that the treatment of solids within the framework of DFT-LDA is problematic with respect to the calculated electronic properties. In particular, the fundamental band gap in semiconductors and insulators is often underestimated by about 50% when being derived from the calculated Kohn-Sham eigenvalues. The success of the PZ-SIC in atomic systems indicates that self-interaction errors in solids can conceptually be overcome applying the very same PZ-SIC approach.

It has turned out, however, that such an approach is not straightforward but holds some significant intricacies. As the respective corrections are state dependent a direct transfer of the PZ-SIC approach to bulk solids is computationally very demanding. This stems from the fact that the corrected energy functional (3.4) as proposed by Perdew and Zunger lacks an invariance with respect to an unitary transformation of the occupied orbitals. This has the most peculiar consequence that for the in principle infinitely extended Bloch wave functions, the PZ-SIC vanishes. However, this does not imply that the DFT functional in Eq. (1.7) is free of self-interaction errors in such a case. In literature, this is often discussed in the context of *canonical* and *localized* single particle orbitals [38]. The PZ-SIC is heuristically defined for many-electron atoms and the respective canonical orbitals in this case are localized so that both are identical. In periodic systems, however, canonical orbitals are defined as the usual eigenstates of the Hamiltonian showing Bloch symmetry. It can be rationalized that such orbitals do not fit to the original idea of the PZ-SIC in the first place. So instead of treating the solid in terms of the canonical Bloch wave functions, it might be more appropriate to switch over to a description of the respective wave functions at least partially based on localized functions.

As the SIC functional (3.4) is not invariant with respect to a unitary transformation, not only one but several local minima exist. The trivial one is the one belonging to the Bloch functions and the resulting vanishing SIC, i.e. the DFT-LDA ground state is also – but not exclusively – a minimum of the SIC functional. Besides the complementary case when

all functions are Wannier-like, several mixed situations may exist, as well.

Svane and Gunnarsson [39] and later also Szotek, Temmerman, and Winter [40] developed a fully self-consistent SIC scheme within a Linear Muffin-Tin Orbital (LMTO) implementation and applied it to transition metals. In view of the variational procedure, they argued that the solution leading to the lowest local minimum of the SIC energy functional is the true SIC solution. However, when this turns out to be one of the mixed localized-delocalized solutions mentioned above, several interpretational problems (size-consistency, sphericalization) arise that have been discussed in Ref. [41].

The usual choice for localized functions within a crystal are Wannier functions $w_{n,\mathbf{R}}$ which are periodic within a Born-von-Karman unit cell

$$w_{n,\mathbf{R}}(\mathbf{r}) = w_{n,\mathbf{0}}(\mathbf{r} - \mathbf{R}) \quad (3.8)$$

and can in principle be constructed from the Bloch eigenfunctions $\psi_{n,\mathbf{k}}$ via a unitary transformation

$$w_{n,\mathbf{R}}(\mathbf{r}) = \frac{1}{N_{\text{BvK}}} \sum_{\mathbf{k}} \psi_{n,\mathbf{k}}(\mathbf{r}) e^{-i\mathbf{k}\mathbf{R}} . \quad (3.9)$$

However, the Bloch orbitals themselves are only uniquely defined except from a phase factor. This can be chosen for each band n and each \mathbf{k} to define a new linear combination of the eigenstates

$$\tilde{\psi}_{n,\mathbf{k}}(\mathbf{r}) = \sum_m \psi_{m,\mathbf{k}}(\mathbf{r}) U_{mn}^{(\mathbf{k})} , \quad (3.10)$$

which leaves the many-particle wave function unchanged. If one considers this degree of freedom, the transformation of Bloch functions to Wannier functions reads

$$w_{n,\mathbf{R}} = \frac{1}{N_{\text{BvK}}} \sum_{\mathbf{k}} \sum_m \psi_{n,\mathbf{k}}(\mathbf{r}) e^{-i\mathbf{k}\mathbf{R}} U_{mn}^{(\mathbf{k})} =: \frac{1}{N_{\text{BvK}}} \sum_{\mathbf{k}} \sum_m \psi_{n,\mathbf{k}}(\mathbf{r}) \tilde{U}_{mn}^{(\mathbf{k})} . \quad (3.11)$$

Eq. (3.11) again constitutes an unitary transformation $\tilde{\mathbf{U}}^{(\mathbf{k})}$ whose actual form is subject to physical motivation. It should be stressed that such a transformation leaves the physical properties of the DFT functional, i.e. the ground state properties, unaffected.

Heaton *et al.* [42] have been the first to apply a Wannier-function based scheme to the SIC functional in Eq. (3.4). They defined the unitary transformation as the one yielding the variational minimum of that functional. The approach, however, was practically based on approximative Wannier functions after introducing a unified Hamiltonian by means of band projections. Nevertheless, considerable improvements of the calculated band structures could be achieved for solid Ar, LiCl and LiF [43].

Very often, the unitary transformation from Bloch to Wannier functions is chosen to min-

imize the magnitude Ω , defined as

$$\Omega = \sum_n [\langle w_{n,\mathbf{0}} | \mathbf{r}^2 | w_{n,\mathbf{0}} \rangle - \langle w_{n,\mathbf{0}} | \mathbf{r} | w_{n,\mathbf{0}} \rangle^2] , \quad (3.12)$$

which inversely quantifies the localization of the Wannier functions. Wannier functions with minimal Ω are maximally localized and hence called *maximally localized Wannier functions* (MLWF). Bylaska and coworkers [44] derived a self-consistent SIC scheme based on MLWF and applied it to a number of oxide crystals (SiO_2 , Al_2O_3 , TiO_2) as well as to covalently bonded Si and Ge. While the approach turned out to be conceptually working, quantitative agreement with experimental data on the fundamental band gaps of the oxides could only be achieved by substantially scaling the correction by a factor of 0.4. For silicon and germanium, this still led to an overcorrection as the band gaps resulted as 2.3 eV (Si, Exp: 1.2 eV) and 1.2 eV (Ge, Exp: 0.8 eV), respectively.

More recently, Stengel and Spaldin [38] also implemented a fully self-consistent SIC scheme for solids based on Wannier functions. In contrast to Bylaska *et al.*, however, they returned to the original idea of Heaton and coworkers with regard to the choice of the unitary transformation. It was found as well that such an approach massively overcorrects the band gaps in the case of Silicon (4.5 eV) and MgO (11.6 eV). This is in line with the results obtained in Ref. [44] and corroborates the idea that a scaling of the PZ-SIC, probably connected to dielectric screening, is necessary in solids.

3.4. Self-interaction-corrected pseudopotentials

Basically all of the aforementioned studies point to two significant properties of the PZ-SIC applied to solids, namely that the SIC is highly localized and that a scaling, i.e. a weakening, of the PZ-SIC is necessary.

Based on these findings, a simplified approach to SIC in solids shall be scrutinized in this work. The idea is best rationalized within the framework of the Linear Combination of Atomic Orbitals (LCAO). In Fig. 3.1 the formation of energy bands in a polar sp^3 -bonded solid is presented schematically. At first isolated atoms with uniquely defined atomic s and p levels with the energies ϵ_s and ϵ_p exist independently, e.g. at a sufficiently large mutual distance of the atoms. The first step towards energy bands in a solid is the formation of sp^3 hybrids, which are a linear combination of the atomic orbitals and yield the energy $\epsilon_{sp^3} = (\epsilon_s + 3\epsilon_p)/4$. As the solid is supposed to be polar, the hybrid energy of the cation $\epsilon_{sp^3}^c$ (red) is higher than the respective energy of the anion hybrid $\epsilon_{sp^3}^a$ (blue). Their energy difference is twice the so called *hybrid polar energy* $2E_p = \epsilon_{sp^3}^c - \epsilon_{sp^3}^a$. Now, when two atoms with such hybrids are brought together, they form bonding and antibonding orbitals as in molecular bonds. The energy separation now amounts to $2E_{mb} = 2\sqrt{E_p^2 + E_c^2}$,

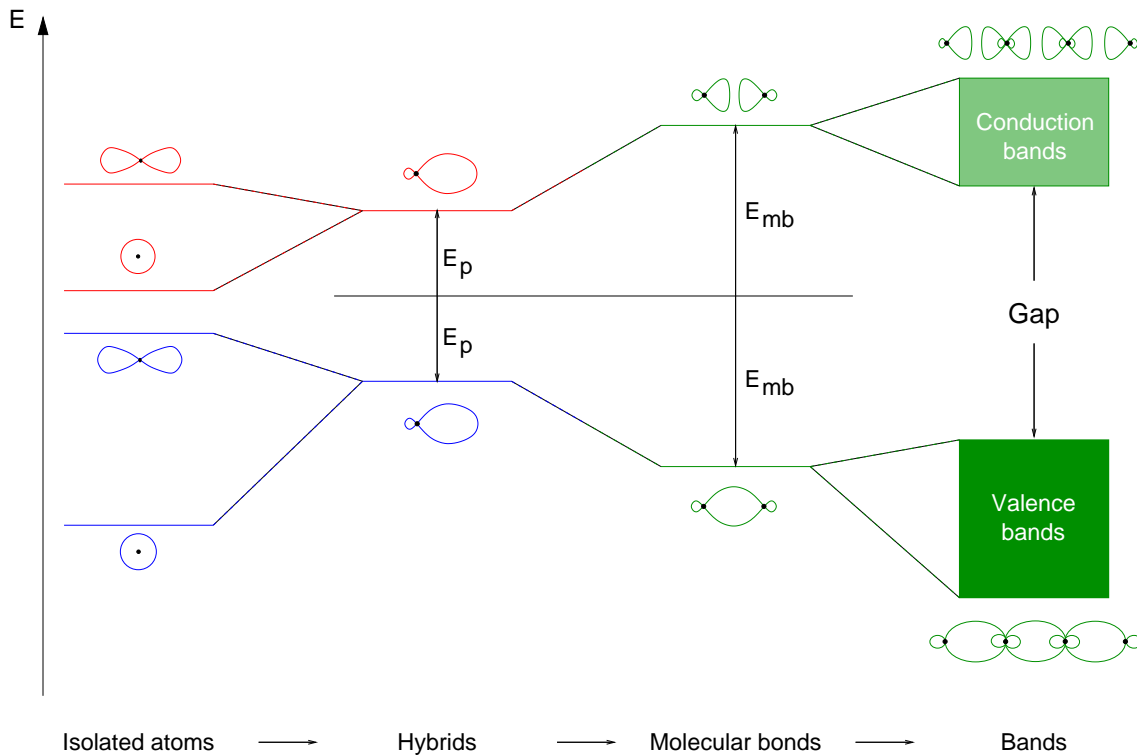


Figure 3.1: Schematic transformation of atomic orbitals to band states in a sp^3 bonded solid.

where E_c is the *hybrid covalent energy*, which can be approximated as only a function of the bond lengths d according to $E_c = 4.37\hbar/(md^2)$. When more of these molecular bonds are combined to a crystal, the formation of bands is determined by the magnitude of the *metallic energy*, which defines the interaction between different hybrids and is a function of the atomic energies of the involved atoms. Certainly, this is a very simplified model and a more detailed derivation of the respective energies and a deeper discussion of the band formation is found in Ref. [45]. Still, in spite of its simplicity, this models very nicely illustrates that basically the nature of the electronic structure of solids can be traced back to the respective energy spectrum of the constituting isolated atoms. As explained previously DFT calculations for solids are often performed using ionic pseudopotentials that reproduce the LDA eigenvalues of the full atomic calculation for the valence electrons. These atomic eigenvalues do not agree with experimental reference data (see Sec. 3.2) and consequently, the energy spectrum of the constituting atoms that enters the calculation of the properties of solids at the first step is incorrect. It is not surprising that under such conditions, the calculated properties show the same systematic errors as those determined for the atoms.

This finding leads one to expect that the introduction of *atomic* and hence localized self-interaction corrections into nonlocal, norm-conserving pseudopotentials will approximate

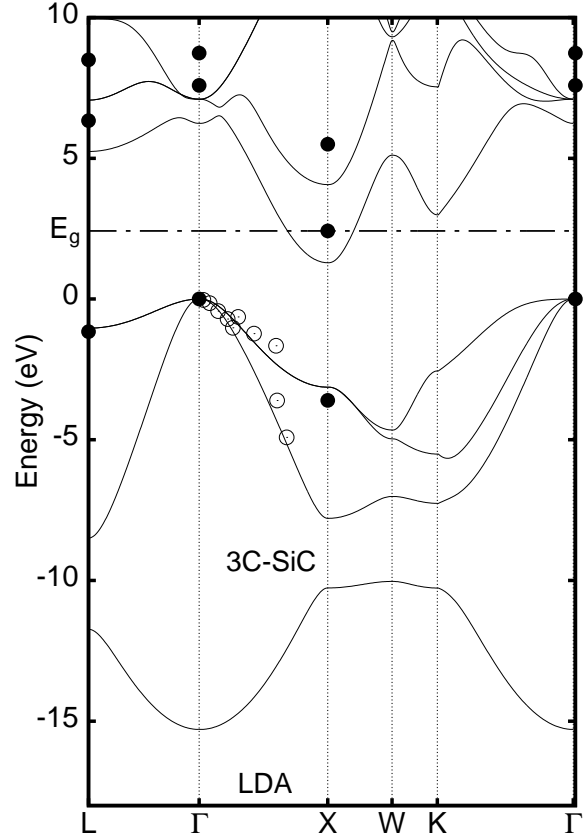
the results of full SIC calculations at least to a significant extent. The idea of incorporating corrections for self-interaction approximately has previously been implemented by various groups in different approaches. First, Rieger and Vogl [14] have reported respective calculations for bulk Si, Ge, Sn and GaAs. While the authors found significant effects in the description of strongly bound core levels, improvements obtained for the gaps of these s, p bonded semiconductors have only been marginal. Later on, Vogel and coworkers [16–18] have successfully applied an alternative approach to II-VI semiconductors and group-III nitrides accounting for self-interaction and relaxation corrections (SIRC) in a solid by modified atomic SIC and SIRC pseudopotentials. In the latter work [18], the relaxation corrections turned out to be of particular importance for the semi-core d -bands in these compounds. Inspired by this previous work, Filippetti and Spaldin [19] have more recently extended and modified the approach and applied it not only to a II-VI compound and a group-III nitride but also to a number of transition metal and manganese oxides. Their pseudo-SIC approach turned out to work satisfyingly for the latter materials, as well. The materials, studied by Vogel *et al.* [16–18] and Filippetti and Spaldin [19] are all characterized by localized semi-core d -states on which SIC (and SIRC) have a very pronounced effect.

In the following, the procedure of constructing self-interaction-corrected pseudopotentials (SICPP) is demonstrated for the ionic compound semiconductor silicon carbide as a prototype. Since SiC is a s, p bonded semiconductor and does not have highly localized semi-core d -states, the application of SICPP to this kind of material cannot *a priori* be expected to yield an improved description of the electronic properties of a variety of SiC polytypes. The results will hence also assist in assessing the usefulness of these self-interaction-corrected pseudopotentials in more general terms².

In the following construction and first exemplary application of SIC pseudopotentials 3C-SiC is used as a reference. This cubic modification of SiC crystallizes in the zinc-blende structure, with a lattice constant of 4.36 Å. A standard LDA calculation using the non-local, norm-conserving *ab-initio* pseudopotentials as described in Sec. 2.2 is performed with a basis set of Gaussian orbitals with the decay constants of 0.18, 0.50, 1.00 and 0.25, 1.00, 2.86 (in atomic units) for Si and C, respectively. The obtained standard LDA band structure is shown in Fig. 3.2 in direct comparison with a number of experimental data points. It exhibits a heteropolar or ionic band gap between the lowest C $2s$ -derived band and the three higher s, p -like valence bands as is typical for an ionic compound semiconductor. The total width of the LDA valence bands is 15.29 eV. 3C-SiC has an indirect optical gap between the Γ - and the X -point. The calculated LDA gap energy of 1.29 eV underestimates the experimental value [46] of 2.42 eV by about 45%, as is typical for standard LDA. In addition, the calculated conduction bands show significant \mathbf{k} -dependent

²Relaxation corrections have only a very minor influence on the band structure of the polytypes and have been ignored, therefore, for simplicity of the approach.

Figure 3.2: LDA band structure of 3C-SiC along high-symmetry lines of the Brillouin zone. The dashed line indicates the experimental gap of 2.42 eV [46]. Open circles show wave-vector-resolved photoemission data from Ref. [47]. The full dots are derived from optical data. For the respective references, see Table 3.3.



deviations from the data points. Presently there are no experimental data available in the literature on the low-lying C $2s$ band.

The LDA shortcomings of the band structure in Fig. 3.2 occur in spite of the fact that the employed standard pseudopotentials reproduce by construction the atomic all-electron LDA term values exactly as is shown in Table 3.2, where both the all-electron and the pseudopotential eigenvalues are given. As was discussed before, if one interprets the eigenvalues $\epsilon_{\alpha}^{\text{LDA}}$ as excitation energies, it becomes obvious that they deviate strongly by some 50% from the experimental data. In particular, the measured energy difference between the C $2p$ and Si $3p$ term values of 3.2 eV is strongly underestimated by the respective energy difference of the LDA term values amounting to 1.2 eV, only.

Within the pseudopotential framework the orbital-dependent self-interaction corrected effective potential as given in Eq. (3.7) reads

$$V_{\alpha,\text{eff}}^{\text{SIC}}([\varrho], [\varrho_{\alpha}], \mathbf{r}) = V_{\alpha}^{\text{PS}} + V_{\text{H}}([\varrho], \mathbf{r}) + V_{\text{xc}}^{\text{LDA}}([\varrho], \mathbf{r}) + V_{\alpha}^{\text{SIC}}([\varrho_{\alpha}], \mathbf{r}) \quad (3.13)$$

and

$$V_{\alpha}^{\text{SIC}}([\varrho_{\alpha}], \mathbf{r}) = -V_{\text{H}}([\varrho_{\alpha}], \mathbf{r}) - V_{\text{xc}}^{\text{LDA}}([\varrho_{\alpha}], \mathbf{r}) . \quad (3.14)$$

Here ϱ and ϱ_{α} are the atomic valence and orbital charge densities, respectively. The so-

	E_{α}^{exp}	$\epsilon_{\alpha}^{\text{ae,LDA}}$	$\epsilon_{\alpha}^{\text{ps,LDA}}$	$\epsilon_{\alpha}^{\text{ps,SIC}}$	$\Delta\epsilon_{\alpha}$
C 2s	—	-13.7	-13.7	-19.7	-6.0
C 2p	-11.3 ^a	-5.4	-5.4	-11.1	-5.7
Si 3s	—	-10.9	-10.9	-15.0	-4.1
Si 3p	-8.1 ^a	-4.2	-4.2	-7.4	-3.2

^afrom Ref. [48]

Table 3.2: Atomic term values (in eV) for C and Si atoms as resulting from non-spinpolarized LDA and SIC calculations. For reference both the all-electron and pseudopotential term values resulting in LDA are shown, as well as the energy shifts $\Delta\epsilon_{\alpha} = \epsilon_{\alpha}^{\text{ps,SIC}} - \epsilon_{\alpha}^{\text{ps,LDA}}$ of the eigenvalues due to self-interaction correction.

lution of Eq. (3.5) for Si and C pseudoatoms yields the SIC term values $\epsilon_{\alpha}^{\text{ps,SIC}}$ given in Table 3.2. While there is no exact agreement between the SIC term values and the experimental ionization energies, the deviations from the latter have been reduced dramatically. For example, the energy difference between the C 2p and Si 3p term values resulting from the SIC calculation as 3.7 eV is in much closer agreement with the experimental value of 3.2 eV than the energy difference between the respective LDA term values of 1.2 eV. Exact agreement was not to be expected, anyway, since Eq. (3.5) is solved without including spin polarization because it is insignificant for the SiC solid, to be addressed below. Comparing the term values resulting from the all-electron or pseudopotential LDA calculations with those resulting from the pseudopotential SIC calculations, one first notes a pronounced absolute shift of the SIC term values with respect to the LDA term values. Much more importantly, however, the term values resulting from the SIC calculations show prominent relative shifts with respect to one another as compared to the LDA term values. These have very significant bearing on the outcome of electronic structure calculations for solids since the atomic SIC term values of the interacting atoms in the solid occur at largely different relative positions from the start, as compared to the respective LDA term values. So the solid state interaction of the different atoms is strongly influenced thereby giving rise to changes in the energy positions and dispersions of the bulk bands.

The *atomic* SIC pseudopotentials for Si and C ions are defined according to Eq. (3.13) by

$$V_{\alpha}^{\text{ps,SIC}}([\varrho_{\alpha}], \mathbf{r}) := V_{\alpha}^{\text{ps}}(\mathbf{r}) + V_{\alpha}^{\text{SIC}}([\varrho_{\alpha}], \mathbf{r}) . \quad (3.15)$$

When such atomic self-interaction corrected pseudopotentials as in Eq. (3.15) are applied to the 3C-SiC solid, a band structure as shown in Fig. 3.3 results. It is quite obvious that this band structure is rather unphysical. Compared to the LDA band structure in Fig. 3.2 the total valence band width is increased by about 10 eV, all band dispersions are

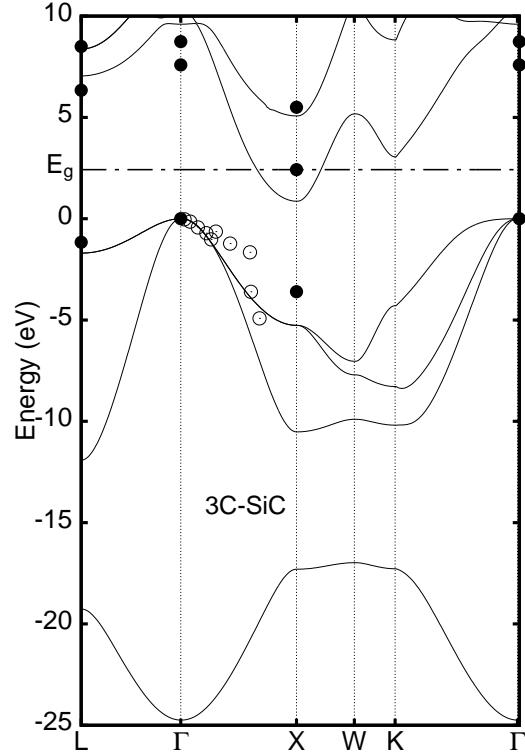


Figure 3.3: Band structure of 3C-SiC along high-symmetry lines of the Brillouin zone as resulting from unmodified SIC. For further details, see caption of Fig. 3.2.

significantly enlarged. The intricate features of the conduction bands are modified to the worse, as well.

This strongly suggests that one has to modify the atomic SIC pseudopotentials of Eq. (3.15) such that they can meaningfully be applied to solids. A fully detailed analysis of the necessity for the modifications and conceptual details can be found in Refs. [17, 20]. The problems as evident in the band structure in Fig. 3.3 are intimately related to the atomic characteristics of the used potentials. They feature an asymptotic $-2/r$ tail originating from the Coulomb potential $V_{\alpha}^{\text{SIC}}([\varrho_{\alpha}], \mathbf{r})$. Such long-range tails cause an unphysical overlap of the SIC potential contributions – which are introduced as truly atomic properties in this approach, after all – from different atomic sites.

Another aspect that adds to the observed unphysical band structure in Fig. 3.3 is the fact that in their present form, the corrective potentials $V_{\alpha}^{\text{SIC}}([\varrho_{\alpha}], \mathbf{r})$ also induce self-interaction corrections for all states which are derived from the occupied atomic levels. This in particular includes the Si $3p$ level, which significantly contributes to conduction band states in the bulk crystal. As such, these states are unoccupied and hence free of self-interaction errors (see, e.g., Refs. [39–41, 49–53]). Transferring the atomic corrections to the solid without further modifications leads to unphysical overlap of the self-interaction corrections from different atomic sites on the one hand, and to a spurious correction of unoccupied bands on the other hand. Apparently, the $V_{\alpha}^{\text{SIC}}([\varrho_{\alpha}], \mathbf{r})$ need to be appropriately modified before they can be used in solid state calculations.

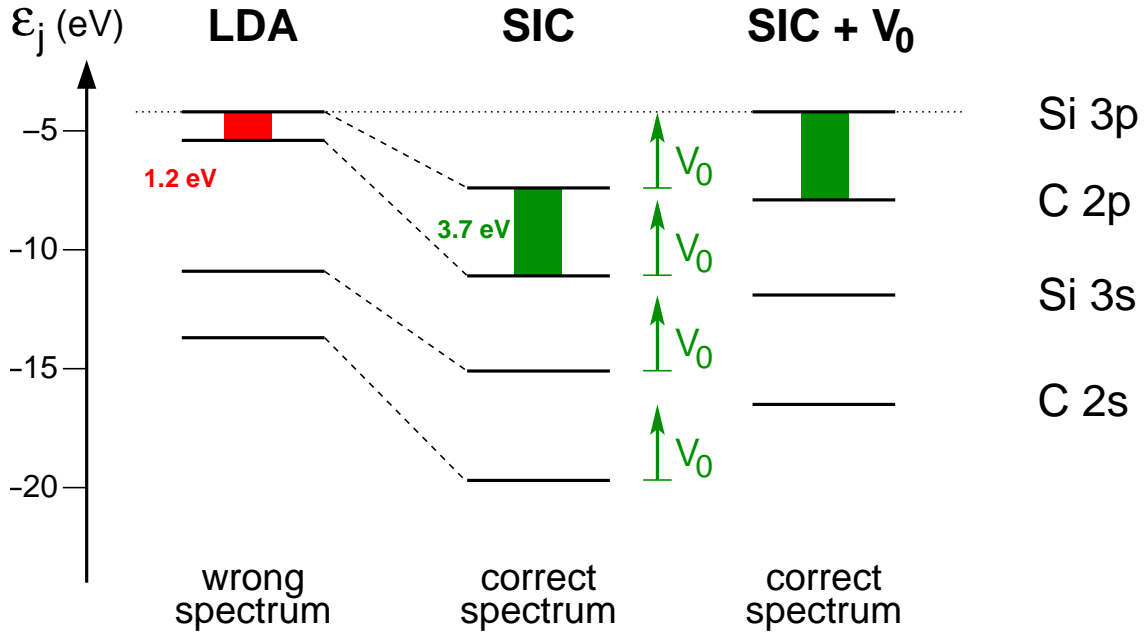


Figure 3.4: Illustration of the effect of the SIC modification procedure on the combined atomic eigenvalue spectra of isolated silicon and carbon atoms.

In this work, the following two-step modification procedure to reduce the overlap of the final correction potentials in the solid is employed. On the one hand, all correction potentials are referred relative to the energetically highest atomic state of the atoms constituting the solid. On the other hand, the remaining $-2/r$ tails are cut off appropriately.

Fig. 3.4 illustrates the effects of this modification procedure on the combined term value spectrum of silicon and carbon atoms. On the left, the spectrum resulting from the standard LDA calculation is shown. The energy difference between the Si 3p and C 2p levels amounts to 1.2 eV only. In contrast, the difference of the experimental binding energies is 3.2 eV, so the LDA spectrum is essentially incorrect. As has been shown above, a SIC calculation shown in the middle leads to a significantly improved spectrum (if one ignores spin-polarization effects). In the LCAO picture of Fig. 3.1, this improved energy spectrum should enter the calculation for the solid. Any modification to the SIC potentials should conserve this improved spectrum and at the same time guarantee that the problems with respect to the SIC overlap and the spurious correction of unoccupied bulk states are avoided.

If one further assumes that the energetically highest atomic state, i.e. Si 3p in SiC, dominantly contributes to these conduction bands (which turns out to be a good assumption for a number of polar solids), one can rigidly shift all correction potentials by the same value $V_0 := \epsilon_{\text{Si}3p}^{\text{LDA}} - \epsilon_{\text{Si}3p}^{\text{SIC}} = 3.2 \text{ eV}$ (see $\Delta\epsilon_\alpha$ for Si 3p in Table 3.2). Apparently, this does not change the relative distances between the atomic SIC levels but reduces the overlap

by reducing the strength of the final potentials in the solid substantially (see, e.g., Fig. 3 in Ref. [17]). By this modification, the influence of the Si $3p$ self-interaction correction is reduced to a large extent in accord with the fact that delocalized conduction-band states themselves do not experience a significant self-interaction. The changes in the band structure are predominantly brought about by the SIC contributions to the C $2s$, C $2p$ and Si $3s$ pseudopotentials. The $-2/r$ tails of the radial components of the correction terms $V_\alpha^{\text{SIC}}([\varrho_\alpha], \mathbf{r})$ are then cut off at suitable radii r_α defined by the condition that the pseudopotentials with the SIC contributions cut off at r_α reproduce the atomic SIC term values within 10^{-2} Ry. For the valence states of the Si and C atoms the above criterion yields the radii 3.84 and 4.36 a.u. for C $2s$ and $2p$, and 4.72 and 5.87 a.u. for Si $3s$ and $3p$, respectively. The cut-off is actually achieved on a short length scale by multiplying the correction terms with the smooth function $f(x_\alpha) = \exp(-x_\alpha^7)$ with $x_\alpha = r/r_\alpha$ to avoid problems in their Fourier representation.

The respectively modified self-interaction correction contributions can now be used in the calculations for the solid. For the valence states of a given ion they are uniquely specified by the angular momentum quantum number l . They can therefore be written as $V_l^{\text{SIC}}(r) + V_0$ multiplied by the projector on the angular momentum eigenstates and by the above cut-off function and can simply be added to the nonlocal part of the usual pseudopotentials

$$\hat{V}^{\text{ps,SIC}} = \hat{V}_{\text{loc}}^{\text{ps}} + \hat{V}_{\text{nlc}}^{\text{ps,SIC}} \quad (3.16)$$

with

$$\begin{aligned} \hat{V}_{\text{nlc}}^{\text{ps,SIC}} &= \hat{V}_{\text{nlc}}^{\text{ps}} + \hat{V}_{\text{nlc}}^{\text{SIC}} \\ &= \sum_l \Delta V_l^{\text{ps}} \hat{P}_l + \sum_l \Delta V_l^{\text{SIC}} \hat{P}_l \end{aligned} \quad (3.17)$$

and

$$\Delta V_l^{\text{SIC}}(r) = \{V_l^{\text{SIC}}(r) + V_0\} f(x_l) \quad (3.18)$$

with $x_l = r/r_l \equiv r/r_\alpha$.

The nonlocal SIC contributions to the ionic pseudopotentials can now be represented in the fully separable Kleinman-Bylander form

$$\hat{V}_{\text{nlc}}^{\text{SIC}} = \sum_{l,m} \frac{|\phi_{l,m}^{\text{SIC}} \Delta V_l^{\text{SIC}}\rangle \langle \phi_{l,m}^{\text{SIC}} \Delta V_l^{\text{SIC}}|}{\langle \phi_{l,m}^{\text{SIC}} | \Delta V_l^{\text{SIC}} | \phi_{l,m}^{\text{SIC}} \rangle} \quad (3.19)$$

just as ordinary nonlocal pseudopotentials. The l, m values entering Eq. (3.19) are uniquely defined by the orbital indices α for each ion.

The SIC pseudopotentials according to Eqs. (3.16)-(3.19) for the silicon carbide solid can now readily be employed in a usual LDA code causing no additional computational effort

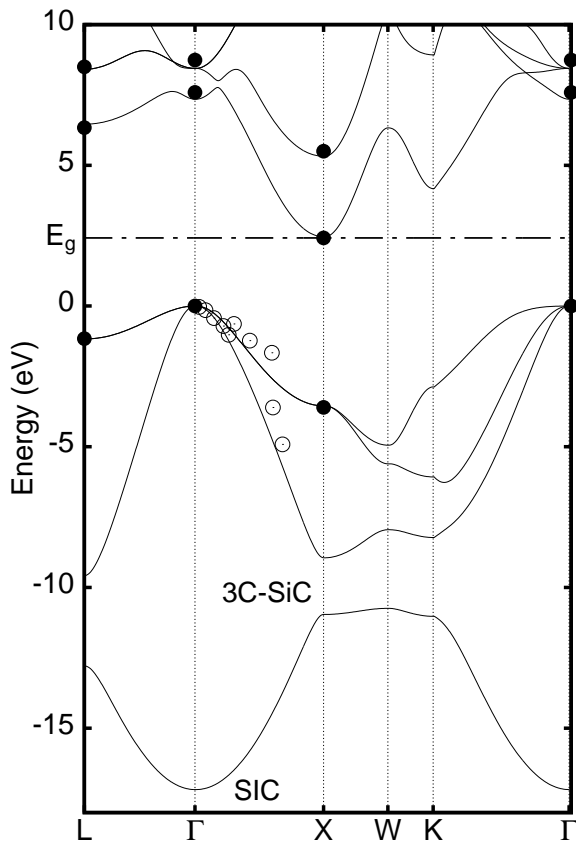


Figure 3.5: SIC band structure of 3C-SiC along high-symmetry lines of the Brillouin zone. For further details, see caption of Fig. 3.2.

as compared to a standard LDA calculation³. Employing these pseudopotentials for Si and C the SIC band structure shown in Fig. 3.5 is obtained. Compared to the LDA band structure, the fundamental band gap has increased to 2.46 eV and is now in very gratifying agreement with experiment. At the same time, the total width of the valence bands has increased to 17.18 eV. The broadening of the SIC valence bands, as compared to the LDA valence bands, mainly originates from the lowering of the C $2s$ band relative to the higher s, p valence bands due to its stronger self-interaction correction, as already evidenced by the $\Delta\epsilon_\alpha$ value in Table 3.2 which is largest for C $2s$. The dispersion of the measured valence bands along the Γ - X line is very well described. In particular, the energy of the highest occupied X_{5v} state, which is observed at -3.60 eV in experiment [55], is much more accurately described in SIC than in standard LDA (cf. Fig. 3.2). Most importantly, the SIC approach does not only yield a very good description of the valence bands and the band gap but also a very accurate description of the experimental data for the conduction bands.

In Table 3.3 a summary of band-structure energies for 3C-SiC resulting from LDA and

³From now on, if not explicitly stated otherwise, the abbreviation SIC refers to the self-interaction-corrected pseudopotential approach as has been presented above, for the sake of simplicity. Any formulation like "the SIC calculations yield" shall not imply any undue preference of this approach over another.

3C	LDA	SIC	QPR	QPW	Exp
Γ_{1v}	-15.29	-17.18	-16.44	-17.31	—
Γ_{15v}	0.00	0.00	0.00	0.00	0.00
Γ_{1c}	6.25	7.35	7.35	8.29	7.59 ^a
Γ_{15c}	7.10	8.45	8.35	9.09	8.74 ^a
X_{1v}	-10.25	-10.96	-11.24	-11.82	—
X_{3v}	-7.79	-8.95	-8.64	-8.53	—
X_{5v}	-3.13	-3.55	-3.62	-3.49	-3.60 ^b
X_{1c}	1.29	2.46	2.34	2.59	2.42 ^c
X_{3c}	4.07	5.32	5.59	5.77	5.50 ^b
L_{1v}	-11.72	-12.79	-12.75	-13.39	—
L_{1v}	-8.49	-9.58	-9.42	-9.39	—
L_{3v}	-1.04	-1.17	-1.21	-1.13	-1.16 ^b
L_{1c}	5.24	6.46	6.53	7.22	6.34 ^d
L_{3c}	7.07	8.41	8.57	8.94	8.50 ^b

^afrom Ref. [54]

^bfrom Ref. [55]

^cfrom Ref. [46]

^dfrom Ref. [56]

Table 3.3: Calculated band-structure energies (in eV) at high-symmetry points for 3C-SiC in comparison with the results of quasiparticle calculations by Rohlfing *et al.* [7] (QPR) and Wenzien *et al.* [8] (QPW) and experiment.

SIC calculations is given, as well as theoretical results from two different GWA calculations [7, 8] and experimental results [46, 54–56] for 3C-SiC. The LDA results show the typical shortcomings discussed above underestimating all conduction-band energies considerably. The SIC results are in very good agreement with the majority of the experimental data. The LDA band-gap problem seems to have largely been overcome by including SIC, at least in this case of 3C-SiC. The overall width of the valence bands resulting from the SIC calculation is larger than that resulting from the GWA calculations of Rohlfing *et al.* [7] but is close to that in the GWA results of Wenzien *et al.* [8]. To date there are no experimental data on the total valence band width to compare with. Comparing the GWA results of Wenzien *et al.* [8] with the SIC results, the GWA results from Ref. [7] and the experimental data it appears that the former band-structure energies result in the upper conduction bands significantly higher than all other values.

To further evidence the above difference, critical point transition energies as resulting from the different calculations in comparison with experimental data are summarized in Table 3.4. As is most obvious, the LDA values fall far short of all measured transition

3C	LDA	SIC	QPR	QPW	Exp ^a	Exp ^b
$\Gamma_{1c} - \Gamma_{15v}$	6.25	7.35	7.35	8.29	7.59	7.4
$\Gamma_{15c} - \Gamma_{15v}$	7.10	8.45	8.35	9.09	8.74	9.0±0.2
$X_{1c} - X_{5v}$	4.42	6.05	5.96	6.08	6.02	5.8
$X_{3c} - X_{5v}$	7.21	8.91	9.21	9.26	9.10	8.3±0.1
$L_{1c} - L_{3v}$	6.29	7.63	7.74	8.35	7.50	7.5
$L_{3c} - L_{3v}$	8.11	9.58	9.78	10.07	9.66	9.4

^aderived from the experimental data in Table 3.3

^bfrom Ref. [56]

Table 3.4: Calculated critical point transition energies (in eV) in 3C-SiC in comparison with respective results of quasiparticle calculations by Rohlfing *et al.* [7] (QPR) and Wenzien *et al.* [8] (QPW) and with various values derived from experimental data.

energies due to the LDA band-gap problem. On the contrary, most of the SIC results and the quasiparticle results from Ref. [7] are in very good accord with the experimental data. The quasiparticle results from Ref. [8] overestimate the transition energies for the reason mentioned above whenever final states in the higher conduction bands are involved.

Self-interaction-corrected structural properties: Total Energy

In order to judge the usefulness of the pseudopotentials, it is vital to check whether they yield reasonable results not only for the electronic structure but also for structural parameters, like the lattice constant or the bulk modulus. To determine these parameters one has to calculate the total energy of the system which is a ground-state property. The SIC pseudopotentials allow for an accurate description of the occupied valence bands, as noted above, and should lead to very good total energies, therefore. In the framework of pseudopotential theory the total energy within the full SIC-LDA approach [see Eq. (3.4)] can be written as:

$$E^{\text{SIC}} = \sum_{\alpha}^{\text{occ}} \epsilon_{\alpha}^{\text{SIC}} + \Delta E_1 + \Delta E_2 + E_{\text{ion}} \quad , \quad (3.20)$$

with

$$\Delta E_1 = \int \left(-\frac{1}{2} V_{\text{H}}([\tilde{\varrho}], \mathbf{r}) + \epsilon_{\text{xc}}^{\text{LDA}}([\tilde{\varrho}], \mathbf{r}) - V_{\text{xc}}^{\text{LDA}}([\tilde{\varrho}], \mathbf{r}) \right) \tilde{\varrho}(\mathbf{r}) d^3r \quad (3.21)$$

and

$$\Delta E_2 = \sum_{\alpha}^{\text{occ}} \int \left(\frac{1}{2} V_{\text{H}}([\tilde{\varrho}_{\alpha}], \mathbf{r}) - \epsilon_{\text{xc}}^{\text{LDA}}([\tilde{\varrho}_{\alpha}], \mathbf{r}) + V_{\text{xc}}^{\text{LDA}}([\tilde{\varrho}_{\alpha}], \mathbf{r}) \right) \tilde{\varrho}_{\alpha}(\mathbf{r}) d^3r . \quad (3.22)$$

Here, $\tilde{\varrho}$ and $\tilde{\varrho}_{\alpha}$ are the valence and orbital charge densities in the solid, respectively, and E_{ion} is the ion-ion interaction energy. The terms $\Delta E_1 + \Delta E_2$ account for double counting that occurs when the SIC eigenvalues $\epsilon_{\alpha}^{\text{SIC}}$ are simply summed up. The term ΔE_1 is the usual term accounting for double counting within standard LDA.

In order to evaluate the term ΔE_2 , it can be rewritten as

$$\begin{aligned} \Delta E_2 &= \sum_{\alpha}^{\text{occ}} \int (V_{\text{H}}([\tilde{\varrho}_{\alpha}], \mathbf{r}) + V_{\text{xc}}^{\text{LDA}}([\tilde{\varrho}_{\alpha}], \mathbf{r})) \tilde{\varrho}_{\alpha}(\mathbf{r}) d^3r \\ &\quad - \sum_{\alpha}^{\text{occ}} \int \left(\frac{1}{2} V_{\text{H}}([\tilde{\varrho}_{\alpha}], \mathbf{r}) + \epsilon_{\text{xc}}^{\text{LDA}}([\tilde{\varrho}_{\alpha}], \mathbf{r}) \right) \tilde{\varrho}_{\alpha}(\mathbf{r}) d^3r . \end{aligned} \quad (3.23)$$

Except for the sign, the term in parentheses in the first line is the solid state analog to the SIC contribution in the atomic effective potential of the Kohn-Sham equations as defined in Eq. (3.14) while the integral in the second line is the Hartree exchange-correlation energy $E_{\text{HXC}}[\tilde{\varrho}_{\alpha}]$ of the orbital charge density $\tilde{\varrho}_{\alpha}$. ΔE_2 then reads

$$\Delta E_2 = - \sum_{\alpha}^{\text{occ}} \int V_{\alpha}^{\text{SIC}}([\tilde{\varrho}_{\alpha}], \mathbf{r}) \tilde{\varrho}_{\alpha}(\mathbf{r}) d^3r - \sum_{\alpha}^{\text{occ}} E_{\text{HXC}}[\tilde{\varrho}_{\alpha}] . \quad (3.24)$$

In the SIC pseudopotential approach, only the valence charge densities $\tilde{\varrho}(\mathbf{r})$ are calculated for the solid by solving the Kohn-Sham-Equations but not the orbital charge densities $\tilde{\varrho}_{\alpha}$. Therefore, as in the construction of the SIC pseudopotentials, one resorts to the modified SIC pseudopotentials $\Delta V_{\alpha}^{\text{SIC}}$ as defined in Eq. (3.18) and E_{HXC} as functions of the atomic charge densities ϱ_{α} and approximates ΔE_2 correspondingly. Projecting the solid-state wave functions onto the localized atomic one-particle orbitals $\phi_{\alpha}^{\text{SIC}}$, ΔE_2 can be approximated by [17]

$$\Delta E_2 \approx - \sum_{n,\mathbf{k}} \left\langle \psi_{n,\mathbf{k}} \left| \hat{V}_{\text{nloc}}^{\text{SIC}} \right| \psi_{n,\mathbf{k}} \right\rangle - \sum_{\alpha}^{\text{occ}} E_{\text{HXC}}[\varrho_{\alpha}] \quad (3.25)$$

with $\hat{V}_{\text{nloc}}^{\text{SIC}}$ according to Eq. (3.17).

$E_{\text{HXC}}[\varrho_{\alpha}]$ is then an atomic property which is constant in the solid and drops out when derivatives of the total energy are calculated.

Using Eq. (3.20) with the above approximation for ΔE_2 it is possible to evaluate the total energy of the investigated systems for a number of unit cell volumes around its minimum and determine the lattice constants and bulk moduli.

		LDA	SIC	Exp
3C	<i>a</i>	4.30	4.35	4.36
	<i>B</i>	2.32	2.22	2.24
2H	<i>a</i>	3.04	3.07	3.08
	<i>c</i>	4.99	5.04	5.05
	<i>B</i>	2.33	2.24	2.23
4H	<i>a</i>	3.04	3.07	3.07
	<i>c</i>	9.95	10.06	10.05
	<i>B</i>	2.34	2.23	
6H	<i>a</i>	3.04	3.07	3.07
	<i>c</i>	14.92	15.07	15.08
	<i>B</i>	2.33	2.24	

Table 3.5: Calculated lattice constants a and c (in Å) and bulk moduli B (in Mbar) of the four investigated SiC polytypes in comparison with experiment [57].

3.5. Structural properties of cubic and hexagonal bulk silicon carbide

Structural parameters of solids such as lattice constants or bulk moduli usually result in good agreement with experiment from LDA calculations. Lattice constants are underestimated in the order of 1% and bulk moduli are overestimated often by a somewhat larger percentage. In general, SIC potentials are attractive causing the electrons to be stronger localized around the atomic nuclei. This gives rise to an increased screening of the atomic nuclei leading to an increase in the lattice constants and a decrease in the bulk moduli. Therefore one can expect these quantities to result from this approach in even better agreement with the data than from usual LDA calculations. For comparison these quantities have also been calculated within standard LDA.

The results for the cubic and hexagonal 3C, 2H, 4H and 6H polytypes are summarized in Table 3.5. The agreement of the structure parameters with the experimental values is excellent. The lattice constants are underestimated by only 0.3% , at most, while the bulk modulus is underestimated by 0.9% for 3C-SiC and overestimated by 0.4% for 2H-SiC. The agreement of the SIC results with experiment is significantly better than that of the standard LDA results which underestimate the lattice constants up to 1.4% and overestimate the bulk moduli up to 4.5%. The lattice constants and bulk moduli thus result from the SIC calculations about one percent larger and about five percent smaller, respectively, than from LDA. This is due to a stronger increase in the localization of the carbon states, as compared to the Si states, by SIC since the former experience a stronger downward shift in energy by self-interaction correction than the latter (cf. the $\Delta\epsilon_\alpha$ values

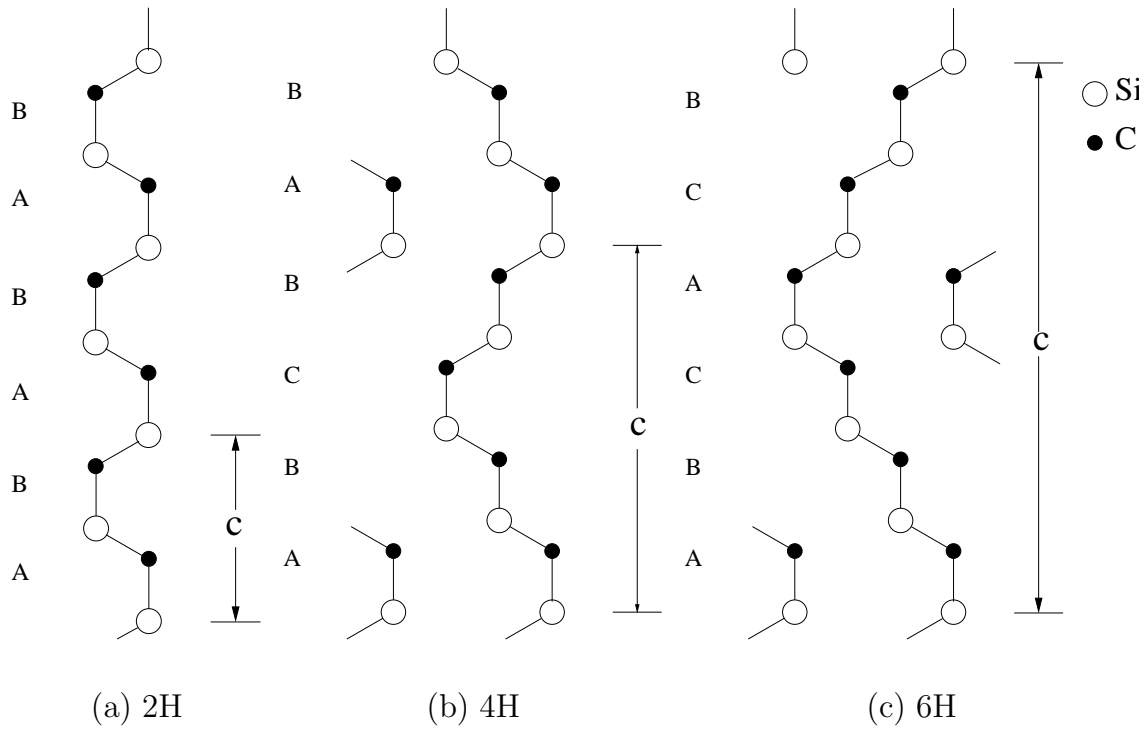


Figure 3.6: Stacking sequences in hexagonal polytypes of SiC in [0001] direction. Side views of six Si-C double layers are shown in each case for better comparison.

in Table 3.2 and the resulting increase in valence-band width within SIC as evidenced in Fig. 3.5 and in the third column of Table 3.3). This stronger localization of the C states, as compared to the Si states, gives rise to a weakening of the Si-C bonds which leads to larger lattice constants, as compared to LDA. By the same token, the lattice becomes 'weaker' so that the bulk moduli show a decrease in the SIC results, as compared to LDA. This behavior was also observed in other approximate SIC results [14] as well as in the results of full SIC calculations [51,53].

3.6. Electronic structure of 2H-, 4H-, and 6H-SiC

As was discussed before, the use of self-interaction-corrected pseudopotentials in a calculation of the band structure for cubic 3C-SiC has turned out gratifying agreement between theoretical and experimental data. Now the question arises whether the very same SIC pseudopotentials work equally well for the band structure of other SiC lattices. To this end, the most common hexagonal 2H, 4H and 6H polytypes are considered in the following.

Fig. 3.6 shows a two-dimensional representation of the stacking sequences of these three hexagonal polytypes along the [0001] direction. To ease the comparison, all plots have

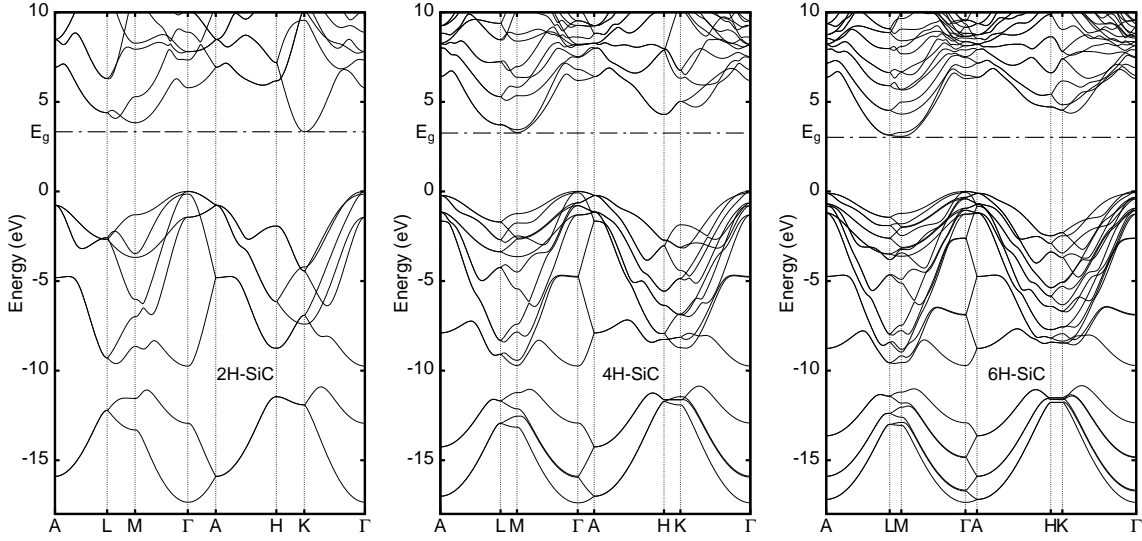


Figure 3.7: Band structures of the hexagonal 2H-, 4H- and 6H-SiC polytypes as resulting from SIC calculations. The respective experimental energy gaps are indicated for reference.

	LDA	SIC	QPR	QPW	Exp
3C	1.29	2.46	2.34	2.59	2.42 ^a
2H	2.12	3.33		3.68	3.33 ^b
4H	2.14	3.30		3.56	3.26 ^b
6H	1.94	3.08		3.25	3.02 ^b

Table 3.6: Calculated band-gap energies (in eV) of the four investigated SiC polytypes in comparison with the results of quasiparticle calculations by Rohlffing *et al.* [7] (QPR) and Wenzien *et al.* [8] (QPW) and with experiment.

^afrom Ref. [46]

^bfrom Ref. [57]

been extended along the [0001] direction to six Si-C double layers, with the actual lengths of the unit cell marked by the hexagonal lattice constants c . The purely hexagonal 2H-SiC exhibits a stacking sequence ABAB, in contrast to ABCB for 4H-SiC and ABCACB for 6H-SiC. Electronic properties are being influenced by the stacking sequence and the related hexagonality of the crystals. The 2H polytype has the largest and the 6H polytype has the smallest hexagonality while the cubic 3C-SiC has no hexagonality at all. Choyke *et al.* [58] have found in experiment that there is a linear dependence between the width of the fundamental gap and the hexagonality of the polytypes. The purely hexagonal 2H-SiC has the largest while cubic 3C-SiC has the smallest energy gap. The position of the conduction-band minimum in \mathbf{k} -space and the band-splitting at the top of the valence bands are affected by hexagonality, as well.

The experimental lattice constants of 2H-SiC are $a = 3.08 \text{ \AA}$ and $c = 5.05 \text{ \AA}$ [57]. The calculated lattice constants (see Table 3.5) are very close to these values. The calculated band gap energies for 2H-SiC, as resulting from LDA and SIC calculations are compared

in Table 3.6 with the results of quasiparticle calculations and with experiment. The electronic band structure of 2H-SiC as resulting from SIC calculations is shown in the left panel of Fig. 3.7. Respective band-structure energies resulting from the same LDA and SIC calculations are summarized in Table 3.7 in comparison with the GWA results from Ref. [8]. Experimental data for 2H-SiC are very scarce, the only known quantity seems to be the width of the fundamental gap of 3.33 eV [57], with the minimum of the conduction bands at the K -point of the hexagonal Brillouin zone. The band gap of 3.33 eV calculated with the SIC pseudopotentials happens to exactly agree with the experimental value showing a very significant improvement as compared to the LDA result of 2.12 eV. Since there are four ions per unit cell in 2H-SiC the band structure features eight valence bands. Contrary to cubic 3C-SiC, for which the upper valence band is triply degenerate at the Γ -point, hexagonal 2H-SiC features a splitting of the top of the valence bands by 0.14 eV. This is attributed to the hexagonal crystal field which gives rise to doubly degenerate states with p_x - and p_y -symmetry and a single p_z -like state. The valence-band width of 17.35 eV, resulting within SIC, is 1.9 eV larger than that resulting in LDA. Note that it is close to the valence band width of 17.18 eV resulting from SIC calculations for 3C-SiC. This is, like in the case of 3C-SiC, mostly caused by a strong lowering of the C $2s$ band which is most noticeably around the Γ -point. Due to the lack of further experimental data the SIC results can only be compared with the GWA results of Ref. [8]. The agreement of the SIC results with the GWA results is quite good, in particular for band-structure energies around the fundamental gap and with respect to the valence-band width. But also in this case the GWA calculations yield higher band-structure energies further up in the conduction bands as was already the case for 3C-SiC (see Table 3.3).

Similarly satisfying results follow for 4H-SiC, which crystallizes with the hexagonal lattice constants [57] $a = 3.07 \text{ \AA}$ and $c = 10.05 \text{ \AA}$. Also in this case the calculated lattice constants in this work are in excellent agreement with these values (see Table 3.5). The gap energies resulting from LDA and SIC calculations are compared to GWA results [8] and experiment in Table 3.6. The SIC band structure is shown in the middle panel of Fig. 3.7 and respective band-structure energies are compared with GWA results from Ref. [8] in Table 3.7. Also for this polytype the band gap of 3.30 eV, calculated with the SIC pseudopotentials, is in very good agreement with the experimental gap of 3.26 eV (see also Table 3.6). The LDA gap of only 2.14 eV strongly underestimates the measured gap, as usual. In 4H-SiC there are eight inequivalent ions per unit cell so that sixteen valence bands result. They are separated from the conduction bands by the fundamental gap which occurs in this case between the Γ - and M -points. The splitting of the upper valence bands at the Γ -point by 0.08 eV is smaller than in 2H-SiC. This is not surprising since 4H-SiC has a smaller hexagonality than 2H-SiC. Hence the crystal field is less pronounced. The total valence-band width of 4H-SiC results from SIC calculations as 17.38 eV and is very close to the respective value for the 2H polytype. As was the case for 2H-SiC,

2H	LDA	SIC	QPW	4H	LDA	SIC	QPW
Γ_{1v}	-15.45	-17.35	-17.39	Γ_{1v}	-15.45	-17.38	-17.30
Γ_{6v}	0.00	0.00	0.00	Γ_{6v}	0.00	0.00	0.00
Γ_{1c}	4.60	5.79	6.66	Γ_{1c}	5.00	6.20	6.92
K_{2v}	-3.79	-4.22	-4.12	K_{2v}	-1.66	-1.86	-1.85
K_{2c}	2.12	3.33	3.68	K_{2c}	3.84	5.02	5.45
H_{3v}	-1.73	-1.93	-1.83	H_{3v}	-2.45	-2.72	-2.68
H_{3c}	4.92	6.17	6.86	H_{3c}	3.10	4.30	4.68
$A_{5,6v}$	-0.71	-0.77	-0.75	$A_{5,6v}$	-0.21	-0.22	-0.20
$A_{1,3c}$	5.70	6.94	7.81	$A_{1,3c}$	5.21	6.41	7.14
M_{4v}	-1.18	-1.30	-1.13	M_{4v}	-1.11	-1.24	-1.23
M_{1c}	2.59	3.84	4.28	M_{1c}	2.14	3.30	3.56
$L_{1,2,3,4v}$	-2.32	-2.59	-2.30	$L_{1,2,3,4v}$	-1.54	-1.71	-1.68
$L_{1,3c}$	3.16	4.39	4.85	$L_{1,3c}$	2.53	3.72	4.06

Table 3.7: Calculated band-structure energies (in eV) at high-symmetry points of the Brillouin zone for 2H-SiC (left table) and 4H-SiC (right table) in comparison with the results of quasiparticle calculations by Wenzien et al. [8] (QPW).

the SIC band-structure energies for 4H-SiC are in very gratifying agreement with most of the GWA results of Ref. [8] near the gap-energy region. In the higher conduction bands similar deviations as noted above for the 3C and 2H polytypes occur in this case, as well. Finally, 6H-SiC is addressed. The measured hexagonal lattice constants are [57] $a = 3.07 \text{ \AA}$ and $c = 15.08 \text{ \AA}$. The calculated lattice constants in this work are basically identical with these values (see Table 3.5). The band structure calculated using the SIC approach is shown in the right panel of Fig. 3.7 and a comparison of the calculated band-structure energies with the GWA results of Ref. [8] is given in Table 3.8. As in the other cases above, the band gap of 3.08 eV, calculated using the SIC approach, closely agrees with the experimental value [57] of 3.02 eV (see also Table 3.6) while the respective LDA gap of 1.94 eV is again much too small. In 6H-SiC there are twelve inequivalent ions per unit cell so that twenty-four valence bands result. Their total width of 17.35 eV is basically identical to those of the other two hexagonal polytypes. Due to the further reduced hexagonality of the crystal field, the Γ -point splitting of the upper valence bands is only 0.06 eV and thus less pronounced than in both 2H- and 4H-SiC. The band structure of 6H-SiC has one particularly intriguing feature. Unlike the cases of the 2H and 4H polytypes, the exact position of the conduction-band minimum has been a matter of dispute [8, 59, 60]. Standard LDA calculations yield the conduction-band minimum at a

Table 3.8: Calculated band-structure energies at high-symmetry points of the Brillouin zone for 6H-SiC (in eV) in comparison with the results of quasiparticle calculations by Wenzien et al. [8] (QPW).

6H	LDA	SIC	QPW
Γ_{1v}	-15.42	-17.35	-17.28
Γ_{6v}	0.00	0.00	0.00
Γ_{1c}	5.10	6.30	6.95
K_{2v}	-2.06	-2.30	-2.31
K_{2c}	3.35	4.54	4.88
H_{3v}	-2.26	-2.48	-2.49
H_{3c}	3.54	4.71	5.06
$A_{5,6v}$	-0.10	-0.10	-0.09
$A_{1,3c}$	5.17	6.37	7.02
M_{4v}	-1.09	-1.22	-1.40
M_{1c}	1.94	3.08	3.25
$L_{1,2,3,4v}$	-1.30	-1.45	-1.63
$L_{1,3c}$	1.98	3.15	3.36

k-point along the L - M line. The present SIC calculations, however, yield the minimum at the M -point as in 4H-SiC, albeit that the lowest conduction band is very flat along the L - M line. This might be viewed as an indication that it actually does not occur along the L - M direction. Comparing the SIC results in Table 3.8 with the GWA results of Ref. [8] very similar conclusions can be drawn as in the case of the 2H and 4H polytypes.

As noted above, there are no experimental data on the valence-band width of the 3C, 2H and 4H polytypes of SiC. For 6H-SiC, however, King *et al.* [61] have performed x-ray photoemission spectroscopy measurements which are especially useful for assessing the lower valence bands. In Fig. 3.8 the calculated density of states after Lorentzian broadening of 0.5 eV is shown compared to the measured spectrum. One finds good agreement for the peaks originating from the lowest C $2s$ band and the following C $2p$ -Si $3s$ bands, in particular. From this agreement it can be inferred that the calculated valence-band widths for all four polytypes seem to be realistic.

In summary, the SIC pseudopotentials turn out to yield very reliable band-structure energies also for all three considered hexagonal SiC polytypes. In particular, the band gaps of all four polytypes considered resulting from the SIC calculations (see Table 3.6) are in excellent agreement with experiment so that the usual LDA shortcomings in describing gap energies seem to be conquerable entirely at least for the SiC polytypes by taking self-interaction corrections into account.

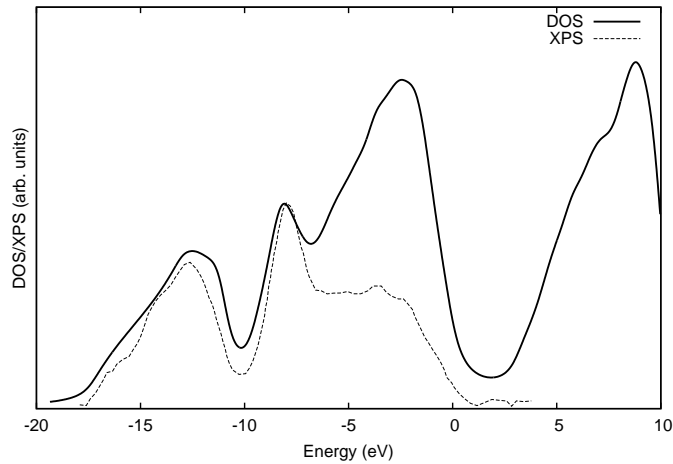


Figure 3.8: Calculated density of states (DOS) of 6H-SiC as resulting from a SIC calculation compared to the XPS spectrum of Ref. [61].

3.7. Summary

In this chapter the origin of the “LDA problem” has been discussed as resulting from self-interaction errors inherent in the local-density approximation. The atomic self-interaction scheme based on the idea of Perdew and Zunger [13] has been presented as well as subsequently developed attempts to apply this correction to the solid. In particular, the method of approximately using the atomic SIC in solid calculations by constructing self-interaction corrected pseudopotentials has been described and its effect exemplarily discussed for four bulk polytypes of silicon carbide. It turns out that this approach yields both structural and electronic properties that are in much better agreement with experimental reference than the results of LDA calculations. The calculated band gaps of 2.46 eV (3C), 3.33 eV (2H), 3.30 eV (4H), and 3.08 eV (6H) are within 2% of the experimental reference.

Chapter 4.

Properties of (110) and (001) surfaces of 3C-SiC

Silicon carbide (SiC) is a compound semiconductor of large fundamental interest and high application potential [57, 62, 63]. Its cubic and hexagonal polytypes have wide band gaps and a very high thermal stability making SiC especially suitable for high-temperature, high-frequency, high-power, high-voltage and high-speed electronic devices and sensors [64]. Additional characteristics of SiC are its chemical inertness and very high hardness qualifying it as an especially attractive material to operate under harsh environmental conditions [65]. Furthermore, SiC is one of the best bio-compatible materials, very promising for biophysics applications [66–68].

Among the key issues for practical microelectronics devices are high quality SiC surfaces with a low defect density. There exist many cubic *or* hexagonal SiC surfaces which exhibit a wealth of reconstructions. Many of these have been studied in great detail both from a fundamental as well as an applications point of view (for reviews, see Refs. [69–74]).

As was shown in Sec. 3.4 the SIC pseudopotentials are constructed based on the fundamental nature of the electronic structure of the bulk solid they are applied to. Surfaces of bulk solids exhibit translational symmetry in only two instead of three dimensions, i.e. only parallel to the surface. Phenomena like surface relaxation and reconstruction, as well as possible adsorption of atoms or molecules can have significant influence on the surface electronic structure leading to strong modifications compared to the bulk electronic structure. It can not *a priori* be expected that the SIC pseudopotentials as defined by Eq. (3.18) yield similar improvements for such surface systems as they do for the bulk polytypes of silicon carbide as shown in Sec. 3.6.

To scrutinize the applicability of the SIC pseudopotentials, the surfaces of silicon carbide offer a wide variety of possible surface structures with unique physical properties. For all polytypes there are polar surfaces with either anionic (C) or cationic (Si) surface terminations and nonpolar ones, in which the outer surface layer equally consists of anions and cations. These different surface types also differ in terms of their tendency to reconstruct and their affinity to adsorption. In this section, some instructive examples of 3C-

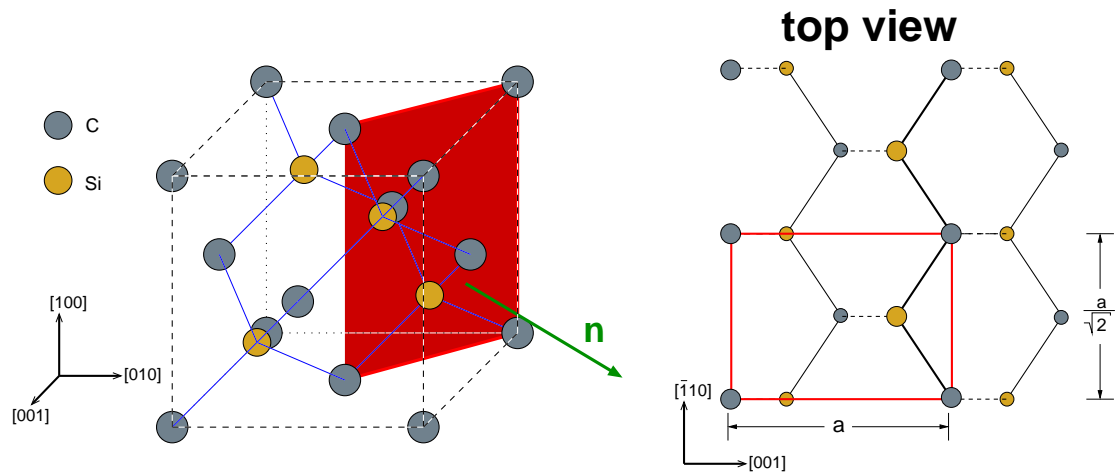


Figure 4.1: Basic geometric properties of the 3C-SiC(110)-(1x1) surface. The left panel shows the position of the surface unit cell (red rectangle) within the bulk crystal. Positions of carbon (silicon) atoms are indicated by black (ocher) filled circles. A schematic top view on the ideal surface is given in the right panel. Large symbols identify atoms within the top layer, small ones those located on the first subsurface layer. Solid and dashed lines indicate intra- and interlayer bonds, respectively.

and 4H-SiC surfaces are chosen to study the effects of the SIC pseudopotentials on the respective surface electronic structures. At first, the 3C-SiC(110) surface will be investigated as it retains many of the bulk features. The complexity of the surface structure will then be increased considering two different reconstructions of the 3C-SiC(001) surface, which feature characteristic formations of double- or triple-bonded carbon dimers. The fact that these surfaces are already intensively discussed in the literature allows for a suitable assessment of the effect of the SIC pseudopotentials.

4.1. The nonpolar 3C-SiC(110)-(1x1) surface

The first surface to which the SIC pseudopotentials are applied is the 3C-SiC(110)-(1×1) surface. The atomic and electronic structure of this surface has already been treated on an *ab initio* level in great detail, for instance in Refs. [75–77]. Especially Chapter 5 of Ref. [76] contains a very detailed description of the various surface properties including an exhaustive discussion of the surface relaxation properties with explicitly given atomic coordinates. As an analysis of the effects of SIC on the calculated electronic structure is the objective of this study, these properties will only be briefly summarized.

Figure 4.1 shows the basic atomic geometry of an (110)-(1×1) surface of a zinc blende crystal. In the left panel the positioning of the surface unit cell within the bulk crystal is indicated by the red rectangle (see caption of Fig. 4.1 for details). The surface is oriented

perpendicular to the [110] direction and consists of Si-C layers with a mutual distance of $a/2\sqrt{2}$. As can be seen in the top view in the right panel of Fig. 4.1, each of these layers contains one silicon and one carbon atom per unit cell giving rise to the *nonpolarity* of the 3C-SiC(110) surface. Each atom is two-fold coordinated within the layer it resides in and exhibits one bond to the layers above and below, respectively. On the top layer, both atoms form a kind of zigzag Si-C chain and lack one binding partner each. The broken bonds give rise to two dangling-bonds per unit cell which feature prominently in the surface electronic structure. Nonpolar (110) surfaces of ionic semiconductors that crystallize in the zinc blende structure, like GaAs, InAs etc., show no reconstructions beyond (1×1) based on the orientation of the broken surface bonds. It can safely be assumed that this is also the case for 3C-SiC(110). Upon relaxation only atomic displacements parallel to the [001] and [110] directions are noticed. The resulting relaxed geometry is usually characterized by a tilting of the Si-C chains with respect to the surface layer of the ideal structure together with a reduction of the Si-C bond length.

The calculations in this work are performed using a slab consisting of eight Si-C layers. The broken bonds at the bottom of the slab are saturated by hydrogen atoms. The positions of the atoms in the topmost three layers of the slab are allowed to relax in the LDA calculation. An extended set of three shells of Gaussian orbitals is used for the atoms in the first two layers (decay constants in atomic units: 0.18, 0.50, and 1.00 for Si; 0.25, 1.00, and 2.86 for C) in order to suitably represent the exponential decay of surface states into vacuum. For the remaining layers two shells per atom (0.20 and 0.60 for Si; 0.35 and 1.70 for C; 0.35 and 2.00 for H) are sufficient. Brillouin zone integrations are performed using 12 special k -points in the irreducible wedge of the surface Brillouin zone, generated by the prescription of Monkhorst and Pack [30].

The respective electronic structure of the relaxed 3C-SiC(110)-(1×1) surface as resulting from LDA and SIC calculations is shown in Fig. 4.2. The projection of the bulk band structure on the surface Brillouin zone is indicated by the grey shaded areas. In both plots bands that can uniquely be assigned to the surface carbon (silicon) atom via a Mulliken analysis are marked by black circles (ocher triangles). Only the energy region around the projected bulk band gap is shown in order to highlight the effects of the SIC on this particular property. The reader is referred to Fig. 5.4(b) in Ref. [76] for a plot of the full surface band structure. The surface electronic structure as resulting from LDA shown in the left panel of Fig. 4.2 most prominently features two dangling-bond derived bands residing within the projected bulk gap. The occupied one, labeled as A_5 , originates from the surface carbon atom, while the unoccupied one (C_3) can be assigned to the respective silicon atom. Both bands are separated by an indirect surface band gap between the M - (VBM) and X -points (CBM) of 0.25 eV. The assignment of the two bands to the dangling-bonds of the surface Si and C atoms is further corroborated by respective plots of the state-resolved charge densities shown in Fig. 4.3. At the M -point of the surface

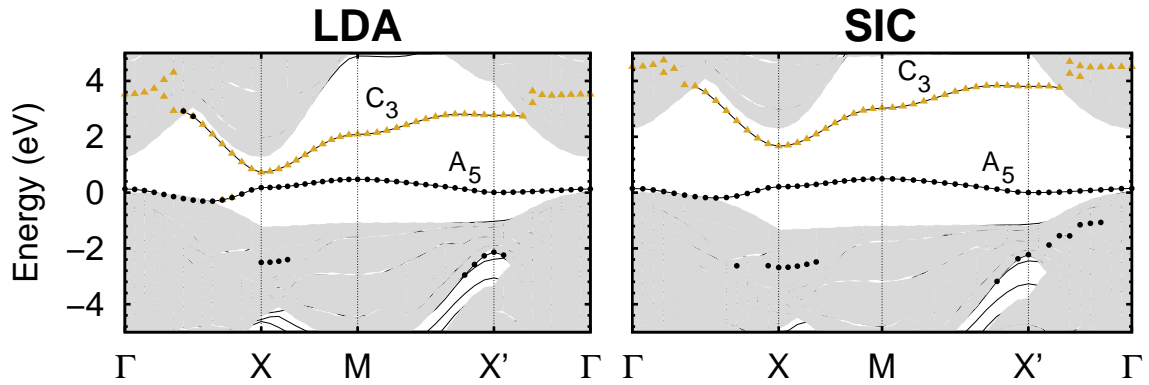


Figure 4.2: Electronic structure of the relaxed 3C-SiC(110)-(1×1) surface as resulting from LDA (left panel) and SIC (right panel) calculations, respectively. Grey shaded regions indicate the projected bulk band structure. Bands that can uniquely be assigned to the top layer silicon (carbon) atom are marked by other triangles (black circles).

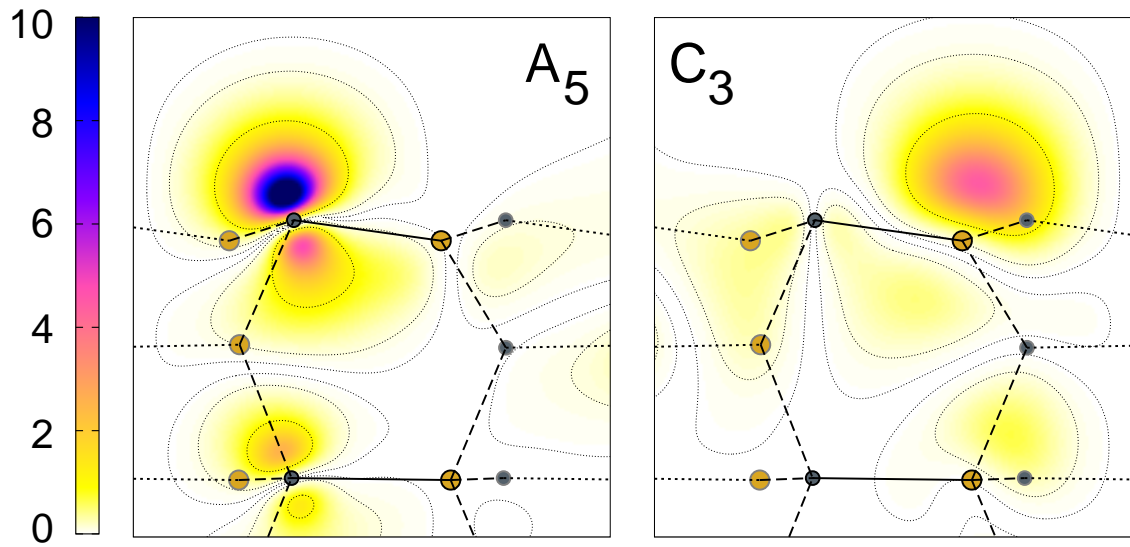


Figure 4.3: State-resolved charge density contours (LDA, in $10^{-2} a_B^{-3}$) of the occupied A_5 and unoccupied C_3 states at the M point of the surface Brillouin zone plotted in a plane containing the Si-C surface bond as indicated in the right panel of Fig. 4.1. For the definition of symbols see caption of Fig. 4.1.

Table 4.1: Fundamental bulk and surface gaps (in eV) of 3C-SiC and its (110)-(1x1) surface as resulting from LDA and SIC calculations, respectively. Δ is the SIC induced opening of the gaps.

3C-SiC	LDA	SIC	Δ
bulk	1.29	2.46	1.17
(110)-(1x1)	0.25	1.17	0.92

Brillouin zone, the charge density of the A_5 state is predominantly localized at the carbon atom of the topmost layer. In particular, the strong maximum of the charge density is pointing into the vacuum which is typical for a dangling-bond state. It should be noted that there are contributions to the charge density from third-layer carbon atoms, as well. For the C_3 state, one in principle finds a largely similar situation. Most of the charge density is localized at the surface silicon atom while additional contributions are registered from subsurface layers. It should be noted at this point that the maximum value of the charge density of the C_3 state is roughly half of the respective value of the A_5 state. However, one should not be misled to think that less total charge is located at the silicon atom. The respective C_3 state is more extended parallel to the surface compared to the A_5 state. This fact also manifests itself in the stronger dispersion of the associated band. A combination of theoretical and experimental data point to the fact that the charge transfer between anion and cation on the (110) surfaces of binary compound semiconductors that crystallize in zinc blende structure is largely similar to the one in the bulk crystal [78]. As a consequence, one can expect the SIC pseudopotentials that work well in the 3C-SiC bulk solid to yield qualitatively and quantitatively similar effects for 3C-SiC(110).

The surface band structure of 3C-SiC(110) as resulting from a SIC calculation is shown in the right panel of Fig. 4.2 for easy comparison to the LDA result discussed above. The basic features of the band structure remain unchanged by the use of the SIC pseudopotentials. Obviously, the projected bulk band gap opens up according to the effects known for the bulk crystal. The fundamental surface band gap opens up in a similar fashion and is increased to 1.17 eV. The indirect nature of this gap is conserved as well as the dispersion of the bands. Some other features are more intricate.

In Table 4.1 the gap energies of bulk 3C-SiC and the 3C-SiC(110)-(1 \times 1) surface are compared. As mentioned before, the surface band gap opens up from 0.25 eV in LDA to 1.17 eV in SIC by $\Delta = 0.92$ eV. The opening of the band gap in the bulk crystal is slightly larger, amounting to 1.17 eV. The fact that the SIC induced band gap increase is slightly smaller at the surface than in the bulk can also be seen in the band structure plot of Fig. 4.2. While in the LDA calculation, the C_3 band runs close to the edge of the projected bulk conduction bands along the Γ - X line, there is an easily visible distance between the two resulting in SIC.

All in all, however, the results have shown that for a surface in which the fundamental nature of the surface band structure is largely equivalent to that of the bulk crystal, the use

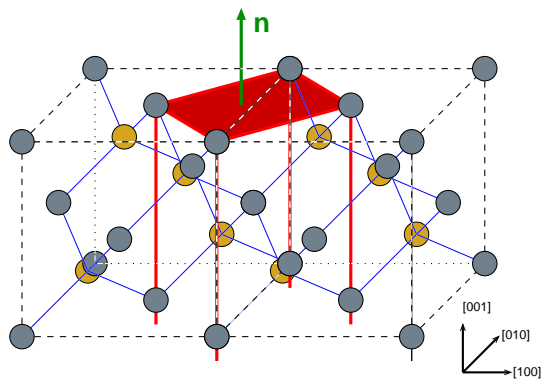


Figure 4.4: Orientation of the (001)-(1×1) surface in the 3C-SiC bulk crystal. Grey (ocher) filled circles symbolize carbon (silicon) atoms, the red plane indicates the surface unit cell.

SIC pseudopotentials yields a qualitatively and quantitatively comparable opening of the band gaps. Experimental data or beyond-LDA calculations for this surface would enable a more detailed comparison and assessment for the quantitative changes. Unfortunately, no such data is available in the literature, to date.

4.2. The polar 3C-SiC(001) surface

In contrast to the previously analyzed nonpolar (110) surface of 3C-SiC for which no higher reconstructions than (1×1) are found, the respective (001) surface holds far more potential for reconstructions.

Figure 4.4 shows the basic orientation of this surface within the zinc blende bulk crystal. Along the [001] direction the surface consists of alternating layers of silicon and carbon. Depending on the nature of the topmost layer of the surface, one has to differentiate between Si-terminated and C-terminated 3C-SiC(001) surfaces. In the following, the latter shall be analyzed in more detail. The resulting polarity of the surface is not the only significant difference between the (001) and (110) surfaces. As can be seen from Fig. 4.4, the (1×1) unit cell (red shaded area) contains one carbon atom in the top layer which is two-fold coordinated to the sublayer. The two broken bonds give rise to two dangling-bonds. Unlike at 3C-SiC(110), the dangling-bonds on neighboring C atoms do not point away from but towards each other, resulting in a comparatively high tendency of the surface to reconstruct.

Possible reconstruction models for the C-terminated 3C-SiC(001) surface have been intensively studied in theory and experiment (cf. Refs. [74, 76] and references therein for a full account). For quite some time, the question of the optimal model for this surface has stirred quite some controversy. Two models have been proposed that have been found to be close in total energy. These models are schematically shown in a top view in Fig. 4.5. The left panel shows the ideal surface with the square unit cell. The orientation of the broken bonds at this surface intuitively leads to the (2×1) reconstruction in the *Dimer*

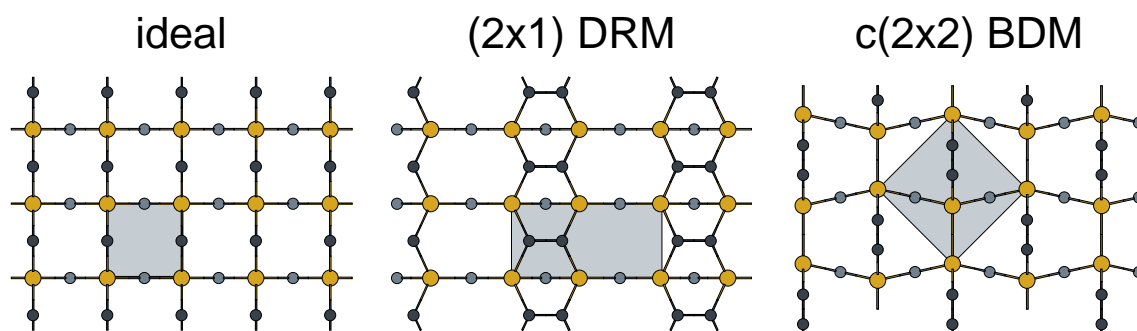


Figure 4.5: Top views of the ideal C-terminated 3C-SiC(001) surface (left panel) and the two competing reconstruction models. The middle panel shows the (2×1) reconstruction in the Dimer Row Model (DRM), the right panel the Bridging Dimer Model (BDM) of the $c(2\times 2)$ surface. Dark and light gray filled circles represent first and third layer carbon atoms, respectively. The second layer silicon atoms are depicted by other filled circles. Respective surface unit cells are indicated by the shaded tetragons.

Row Model (DRM) that is shown in the middle panel. It is characterized by the formation of one double-bonded C=C dimer per unit cell, leading to a dimer row on the top layer of the surface. This is a very intuitive model as the formation of such a dimer occurs by a bending of the C-Si bonds only and does not involve any bond breaking, which costs energy. The $c(2\times 2)$ reconstruction in the right panel of Fig. 4.5, on the contrary, features one triple-bonded C≡C dimer per unit cell that resides in positions bridging second layer silicon atoms. This model is hence referred to as *Bridging Dimer Model* (BDM). In this case, the carbon dimers form a staggered pattern on the surface giving rise to a $c(2\times 2)$ translational symmetry parallel to the surface. On the basis of a whole body of experimental data and recent *ab initio* DFT calculations there is now general agreement on the bridging-dimer model (BDM) of the 3C-SiC(001)- $c(2\times 2)$ surface [74]. The significant amount of research that has been done on this topic has resulted in theoretical and experimental data in the literature to which the results of SIC calculations for the electronic structure of these surface models can be compared to. To explore the usefulness of the SIC pseudopotentials for such reconstructed silicon carbide surfaces, their application to both aforementioned models of the C-terminated 3C-SiC(001) surface is addressed in the following. In particular, there is a quasiparticle surface band structure for the (2×1) DRM, as well as angle-resolved photoelectron spectroscopy (ARPES) and angle-resolved inverse photoelectron spectroscopy (ARIPES) data available for comparison in the case of the $c(2\times 2)$ BDM.

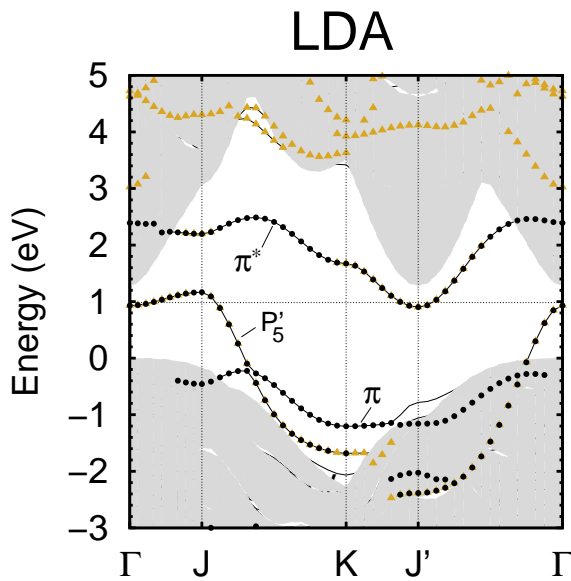


Figure 4.6: Electronic band structure of the DRM of the 3C-SiC(001)-(2 \times 1) surface. Black circles (open triangles) mark bands that can uniquely be assigned to the C=C dimer (silicon layer).

4.2.1. 3C-SiC(001)-(2 \times 1) Dimer Row Model

At first, the most prominent characteristics of the electronic structure of the Dimer Row Model of 3C-SiC(001)-(2 \times 1) surface shall be discussed. The surface is modeled using a slab consisting of nine atomic layers. The broken bonds at the bottom of the slab are saturated by hydrogen atoms. Eight special k-points according to the prescription of Monkhorst and Pack [30] are used for Brillouin zone integrations. The positions of atoms in the upper three layers of the slab are allowed to relax.

Figure 4.6 shows the electronic band structure for the DRM as resulting from a standard LDA calculation. Bands that can be attributed to the atoms of the carbon dimer (silicon sublayer) are marked by black circles (open triangles). As in the case of the 3C-SiC(110) surface discussed before, only the energetic region around the Fermi level is shown. For a detailed discussion of the full band structure, the reader is referred to Chapter 6.2 of Ref. [76].

Within the projected bulk band gap, three unique surface bands can be seen. From the markings it is evident that they dominantly arise from carbon dimer states. The charge density contours in Fig. 4.7 shed some more light on the physical characteristics of the bands labeled as π , π^* , and P'_5 in Fig. 4.6, respectively. It is quite evident that the two former states at the K -point are associated to the bonding of the C=C dimer at the top surface layer. They are formed as binding (π) and antibinding (π^*) linear combinations of the free dangling-bonds at the ideal surface. The P'_5 state, in contrast, is mainly derived from the p_x - and p_y -orbitals of the surface carbon atoms and contributes to the binding of the carbon dimer to the silicon layer on the substrate. It is apparent in Fig. 4.6 that the P'_5 band overlaps energetically with the π^* band leading to a metallic character of the surface

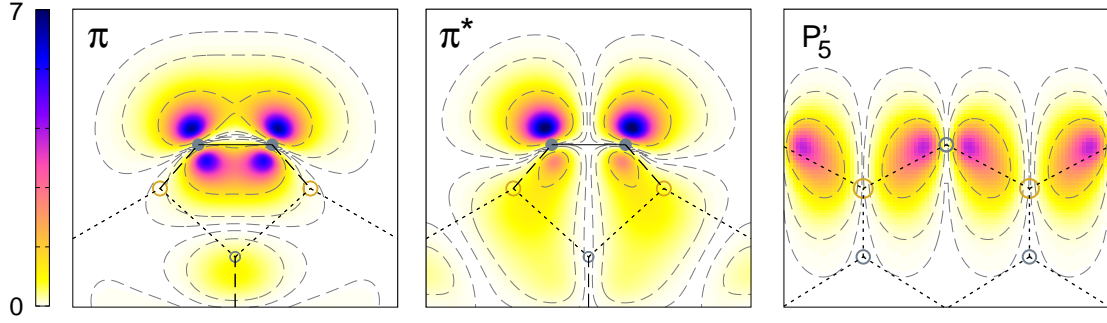


Figure 4.7: Charge density contours (in $10^{-2} a_B^{-3}$) of three selected states within the projected bulk band gap of the 3C-SiC(001)-(2×1) surface. π and π^* states at the K -point are shown in a [100]-[001] plane containing the C=C dimer bond. A [010]-[001] plane is chosen for the contours of the P'_5 state at the Γ -point. Full [open] gray (ocher) circles represent positions of carbon (silicon) atoms within [outside] the drawing plane.

resulting from the LDA calculation.

In Ref. [79], Sabisch and coworkers presented a quasiparticle band structure for this surface as resulting from a GWA calculation. A reproduction of the result is shown in the left panel of Fig. 4.8. Fundamentally, it turns out from this calculation that the surface is semiconducting instead of metallic. There is an indirect surface gap from J to J' of 0.9 eV between the totally occupied P'_5 state and the totally unoccupied π^* state. The energetic positions of the occupied bands relative to the projected bulk valence bands is hardly affected compared to the LDA calculation. The projected bulk gap is enlarged by approximately 1.2 eV due to the quasiparticle corrections. A comparable shift is found for the π^* state, resulting in the opening of the surface band gap.

This quasiparticle band structure is very helpful for the assessment of effects the SIC pseudopotentials have on such surface systems. In the right panel of Fig. 4.8, the respective band structure for the surface at hand is shown as resulting from a SIC calculation. While it is quite apparent that, naturally, the projected bulk band gap opens up in SIC in a comparable fashion as in the GWA calculation, the surface remains metallic. The overlap between the P'_5 band and the π^* band is still present mostly due to the π^* band retaining its position relative to the projected valence band. Obviously, the SIC pseudopotential calculation fails to describe the electronic structure of the 3C-SiC(001)-(2×1) surface accurately.

Now, the presentation of band structures as in Fig. 4.8 is often misleading. Aligning the energy zero to the top of the valence band maximum creates the impression that, upon inclusion of SIC, the conduction bands are shifted upward in energy relative to the valence bands. From the discussion in Section 3.2 it is known, however, that the SIC potentials are exclusively attractive. In atoms, this leads to a consistent lowering of the calculated term values with respect to the energy zero. For a bulk crystal or a surface, this

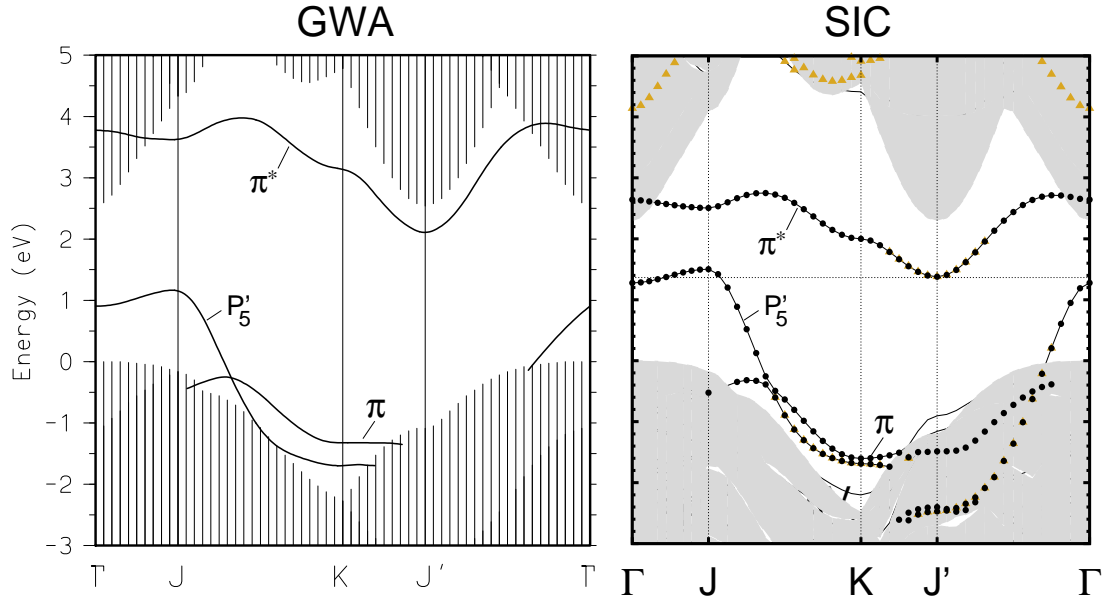


Figure 4.8: Electronic band structure of the DRM of the 3C-SiC(001)-(2 \times 1) surface as resulting from GWA (see Ref. [79]) and SIC calculations. See caption of Fig. 4.6 for the definition of labels.

means that all occupied states are affected by SIC in such a fashion that their respective energies are lowered compared to a standard LDA calculation. The conduction bands are only indirectly affected by changes in the effective potential. It is important to keep in mind that SIC calculations really affect the occupied states and shift them down in energy relative to the unoccupied conduction band states. The unsatisfying result of the SIC calculation for the DRM of the 3C-SiC(001)-(2 \times 1) surface must be interpreted in this respect.

It is evident that the position of the π and P'_5 bands relative to the projected bulk valence bands is hardly changed in the SIC calculation compared to the LDA result. At Γ , the P'_5 band resides only about 0.2 eV higher in energy than in LDA. This indicates that the associated state is slightly less strongly affected by the use of the SIC pseudopotentials than the top of the bulk valence band. Basically, however, the observed effect is in good accord with what could be expected from the nature of the respective occupied states. Both the π and the P'_5 bands originate from states that can be interpreted as linear combinations of the carbon p -orbitals. The self-interaction correction to the C $2p$ states is strongly active by construction of the SIC pseudopotentials. Hence it is not surprising that these two bands experience strong SIC on the surface. The main error in the description of the surface electronic structure obviously originates from an inadequate treatment of the unoccupied π^* band.

The fact that the energetic position of the π^* band remains practically unchanged relative

to the π band and the bulk valence band projection can be explained by a spurious self-interaction correction to its respective states. It has already been indicated that π and π^* states can be interpreted as binding and antibinding linear combinations of the carbon dangling-bonds, which in turn have mainly C p_z character. From the charge densities in Fig. 4.7 this can easily be visualized. It is important to remember that in the process of constructing the SIC pseudopotentials, it was ensured that the respective atomic corrective potentials of Si $3s$, C $2s$, and C $2p$ effectively contribute in the bulk crystal. This is rationalized by the contribution of these atomic states to the occupied bulk states. At this surface, in contrast, the situation is not as straightforward. In the case that occupied (π) and unoccupied (π^*) bands are equally linear combinations of an atomic orbital that is assumed to be occupied in the bulk (C $2p_z$), the unoccupied band will be spuriously affected by the SIC pseudopotentials.

In order to achieve a reasonable description of a surface electronic structure containing such features, it is necessary to account for these spurious effects on unoccupied states. One possibility to quantify the effects for each band n and \mathbf{k} -point is to calculate the expectation value of the non-local SIC operator containing the approximate self-interaction correction as defined by Eq. (3.19), i.e. to calculate

$$\Delta\epsilon_{n,\mathbf{k}}^{\text{SIC}} = \langle \psi_{n,\mathbf{k}} | \hat{V}_{\text{nlloc}}^{\text{SIC}} | \psi_{n,\mathbf{k}} \rangle \leq 0. \quad (4.1)$$

When n_{occ} is the number of occupied bands, $\Delta\epsilon_{n,\mathbf{k}}^{\text{SIC}}$ should vanish for all bands $n > n_{\text{occ}}$. One way to eliminate the spurious self-interaction correction of empty surface states is to subtract the respective corrections as given in Eq. (4.1) from the calculated single-particle energies $\epsilon_{n,\mathbf{k}}^{\text{SIC}}$ for unoccupied bands and plot the band structure according to

$$\tilde{\epsilon}_{n,\mathbf{k}}^{\text{SIC}} = \begin{cases} \epsilon_{n,\mathbf{k}}^{\text{SIC}} & \text{for } n \leq n_{\text{occ}} \\ \epsilon_{n,\mathbf{k}}^{\text{SIC}} - \Delta\epsilon_{n,\mathbf{k}}^{\text{SIC}} & \text{for } n > n_{\text{occ}} \end{cases}. \quad (4.2)$$

A SIC calculation according to Eq. (4.2) is referred to as a SIC- Δ calculation in the following. In Fig. 4.9, the band structure of bulk 3C-SiC is shown as resulting from the application of the SIC- Δ approach. A band gap of 2.48 eV results which represents only a minor deviation in the order of a couple of meV from the standard SIC result. The dots indicating optical data as derived from Refs. [46,55,57,58] show equally good agreement to the calculated band energies at the respective high-symmetry points. Only concerning the lowest unoccupied band along the $L - \Gamma$ symmetry line, slightly bigger changes occur as it is pushed up in energy by roughly 0.2 eV. From a Mulliken analysis of the atomic contributions to this band, it becomes evident that C $2s$ contributes significantly ($\approx 25\%$) to the respective states. Thus they are also slightly affected by the self-interactions, as well. However, the effect is minor overall, which is to be expected from the way the SIC

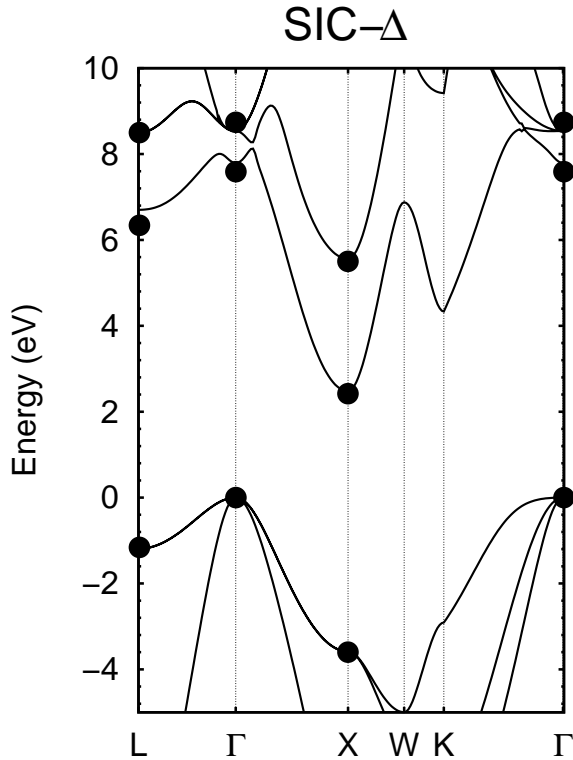


Figure 4.9: Bulk band structure of 3C-SiC as resulting from the SIC- Δ approach defined by Eq. (4.2). The full dots are derived from optical data. For the respective references, see Tab. 3.3.

pseudopotentials are constructed.

Based on this conceptual agreement between a SIC and a SIC- Δ calculation for the underlying bulk solid, an investigation of the band structure of the 3C-SiC(001)-(2 \times 1) surface seems to be worthwhile. Figure 4.10 shows the surface band structure as resulting from a SIC- Δ calculation compared to the GWA band structure from Ref. [79]. The most apparent change compared to the standard SIC calculation shown in the right panel of Fig. 4.8 is that the surface results as semiconducting by the SIC- Δ approach, thus agreeing qualitatively with the quasiparticle result. Moreover, the resulting band gap is indirect with the top of the occupied P'_5 surface band located at the J -point of the surface Brillouin zone. The bottom of the lowest unoccupied surface band is found at J' . The surface band gap that results from the SIC- Δ calculation amounts to 0.99 eV which is also in very good quantitative accord with the quasiparticle gap of 0.94 eV.

Summarizing, the analysis of the surface electronic structure of the dimer row reconstruction of 3C-SiC(001)-(2 \times 1) has shown that the standard SIC approach, which is originally developed with the characteristics of the bulk electronic structure in mind, fails to deliver an accurate description of the fundamental surface electronic properties. This is traced back to spurious self-interaction corrections to unoccupied surface states that can be interpreted as linear combinations of atomic states that contribute significantly to occupied bulk states. For such cases, the SIC- Δ approach which relies on the subtraction of the unphysical self-interaction correction from empty states has been introduced as a pragmatic

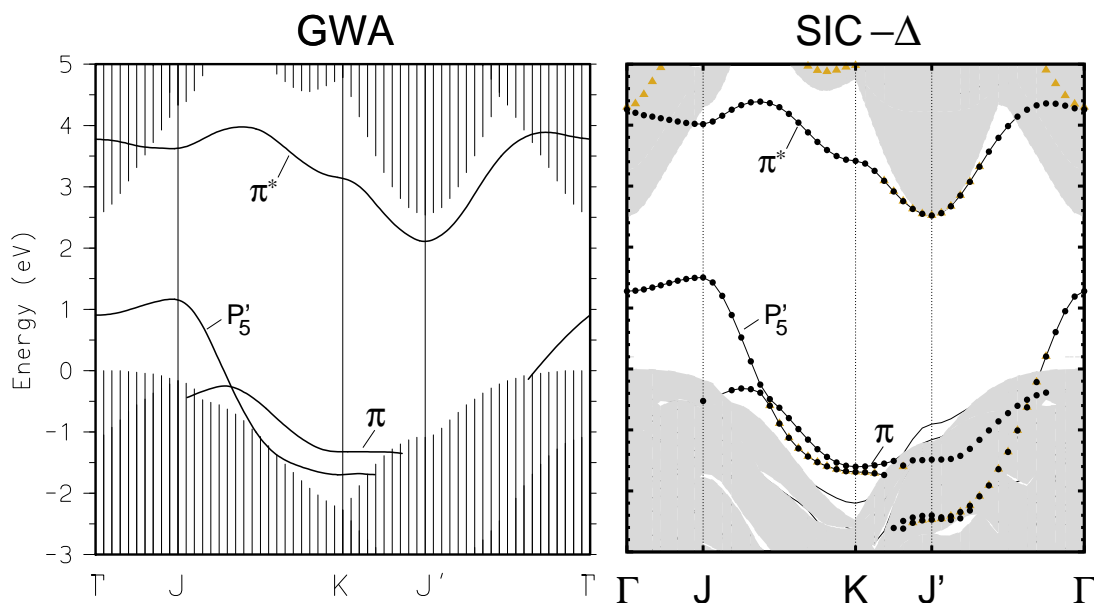


Figure 4.10: Electronic band structure of the DRM of the 3C-SiC(001)-(2×1) surface as resulting from GWA (see Ref. [79]) and SIC- Δ calculations. See caption of Fig. 4.6 for the definition of labels.

tool to improve the calculated electronic structure considerably.

4.2.2. 3C-SiC(001)-c(2x2) Bridging Dimer Model

As has already been mentioned in the beginning of this chapter, there had been some controversy about which is the "true" reconstruction model of the 3C-SiC(001) surface. In particular, the previously discussed Dimer Row Model in a (2×1) reconstruction and the Bridging Dimer reconstruction model with c(2×2) symmetry have been at the focus of attention. On the basis of quite a lot of experimental and theoretical data, this open question was solved in favor of the latter. The main building block for this reconstruction model is, again, a carbon dimer in the top layer of the surface. In contrast to the (2×1) DRM reconstruction, however, this dimer is triple-bonded and each carbon atom is only linked by one single Si-C bond to the surface.

In order to study the effects of the SIC and SIC- Δ approaches, the surface electronic structure of the BDM is calculated employing both standard LDA as well as the SIC pseudopotentials. To describe the surface a supercell approach with ten atomic layers (one H, four Si and five C layers) per supercell is used. The H layer saturates the C bottom layer of the SiC slab in each supercell to avoid spurious surface states from the bottom layer.

The surface band structure resulting from a standard LDA calculation is shown in Fig.

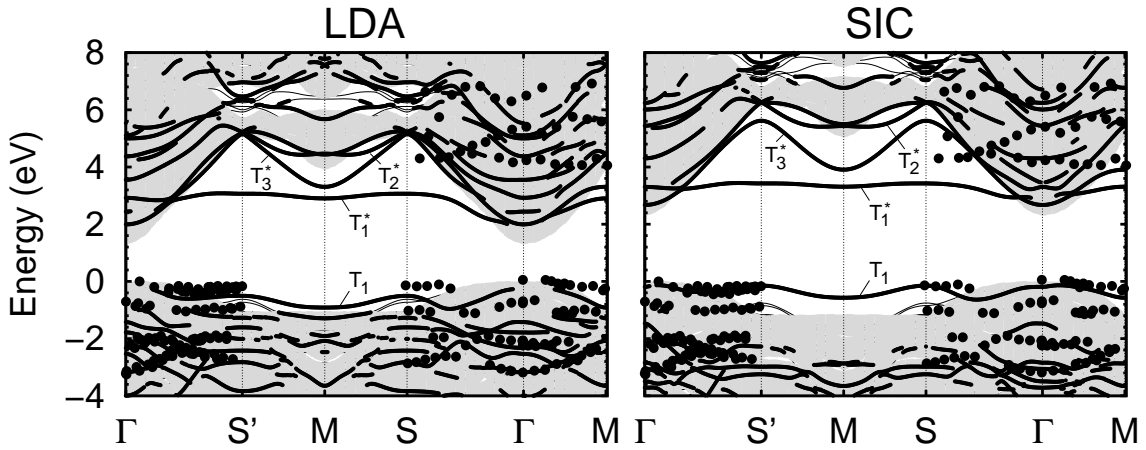


Figure 4.11: Surface band structure of the BDM of the C-terminated SiC(001)-c(2 \times 2) surface as resulting from standard LDA (left panel) and SIC (right panel) calculations. The gray-shaded areas show the projected bulk band structure. Surface states and resonances are indicated by thick and thin lines. The thick lines refer to pronounced surface states or resonances which are predominantly localized on the first two surface layers. ARPES data from Ref. [80] and ARIPES data from Ref. [81] show measured valence and conduction band states, respectively. ARPES data have not been reported along the S'-M-S line, to date, and ARIPES data have only been measured along the S- Γ -M line.

4.11. It basically agrees with the respective surface band structure which was reported in Ref. [82]. The calculations of the surface band structure reported in this work and those in Ref. [82] slightly differ concerning the basis sets, the standard pseudopotentials and the number of SiC layers (9 versus 12) per supercell. The most pronounced surface state bands are labeled in Fig. 4.11 according to Ref. [82]. The T_1 band originates from bonding states of the $C\equiv C$ surface dimers while the T_1^* band originates from the respective antibonding states (cf. respective charge densities in Ref. [82]). The T_2^* and T_3^* bands originate from antibonding surface states, as well. Note that the latter two bands coincide with the projected bulk bands of SiC along the Γ -S' and Γ -S symmetry lines in the LDA surface band structure.

The surface band structure resulting from the standard SIC calculation is shown in the right panel of Fig. 4.11. It shows the same topology of the most salient surface state bands as the respective LDA surface band structure in the left panel. There are significant differences to be noted, however. First and foremost the SIC approach yields an appropriate projected bulk band structure and a realistic projected gap energy region, in particular, at last. The T_1 surface band results slightly higher in energy relative to the projected bulk valence bands than in LDA. The T_1^* band results in the SIC surface band structure throughout most parts of the surface Brillouin zone 0.4 eV higher in energy than in the LDA surface band structure. Note, in particular, that it has moved up in energy by about

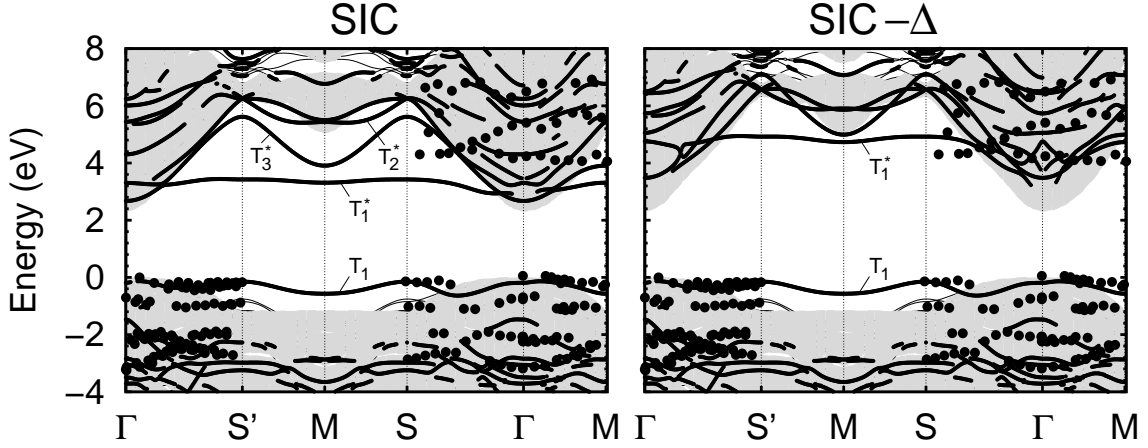


Figure 4.12: Surface band structure of the BDM of the C-terminated SiC(001)-c(2×2) surface as resulting from standard SIC (left panel) and SIC- Δ (right panel) calculations. See caption of Fig. 4.11 for details.

1 eV close to the Γ -point along the Γ - S' line where it becomes resonant with the projected Si-derived conduction bands. The T_3^* band, which is Si-derived to a considerable extent, is about 0.7 eV higher in energy in the SIC results than in the LDA results. Yet, it remains to be a band of localized surface states within the projected gap also along most of the Γ - S' and Γ - S symmetry lines. This is due to the fact that the projected bulk conduction bands have shifted up in energy by more than 1 eV as compared to the projected LDA bulk band structure in consequence of the realistic description of the bulk conduction bands within the SIC approach. Experimental ARPES and ARIPES data are included in Figs. 4.11 and 4.12 for comparison.

In the ARPES experiments, the measured occupied valence-band states have been referred to the extrinsic Fermi level of the samples used, but the doping has not been explicitly given in Ref. [80]. Therefore, the top of the measured bands is aligned to the top of the projected bulk valence bands in Figs. 4.11 and 4.12. A number of valence-band surface states from the SIC calculations, most noticeably the T_1 dangling-bond band, result in very satisfying agreement with the ARPES data [80]. By construction the same holds for the SIC- Δ surface band structure shown in the right panel of Fig. 4.12. The standard SIC result is repeated in the left panel for easier comparison. It might well be that some of the valence-band features observed in experiment are bulk-derived since there is no counterpart at all for these features in the calculated surface band structure. The same good overall agreement in the valence bands could also be achieved with the LDA results if the experimental ARPES data were aligned, in view of the lack of knowledge of their absolute energy position, with the T_1 band of the LDA surface band structure at the S' -point, as was done in Ref. [82].

Also the ARIPES data have been referred to the extrinsic Fermi level of the samples

used in Ref. [81]. In this case the Fermi level position with respect to the valence band maximum has been inferred from other literature data on equally doped samples to be located 1.5 eV above the top of the valence bands. If this assignment is correct one can refer the ARPES data to the top of the valence bands, as is done in Figs. 4.11 and 4.12 without the need of any rigid relative shift. Comparing the two figures it becomes obvious that the lowest empty surface-state band resulting from LDA deviates more strongly from the lowest band determined in ARPES, actually by 1.3 eV, while this deviation is reduced to 0.9 eV in the SIC surface band structure. Upon application of SIC- Δ the T_1^* band is shifted strongly upwards in energy, residing at about 0.5 eV above the measured data. If one compares the position of the calculated T_1^* band at the Γ point of the surface Brillouin zone to the measured data in Fig. 7 in Ref. [81], it is interesting to note that in the SIC calculation, the respective energy is found to be only 0.6 eV higher than the projected conduction band minimum. In experiment, however, it is found to reside 1.8 eV above this value. In the SIC- Δ band structure, it is quite intricate to isolate the respective band signal. From the lack of dispersion of the band an energetic position of about 2.4 eV above the CBM can be estimated, which is generally in better accord with the experimental findings. In general one should note from the comparison that some of the dispersions of the ARPES data (even if the lowest measured empty band was aligned with the calculated T_1^* band) can not be reconciled with the theoretical results, neither with the LDA nor the SIC (or SIC- Δ) surface band structure. The fact that the Fermi level of the sample in the ARPES was not directly determined adds an additional uncertainty to the relative positioning of calculated and measured band signals.

From this comparison one can conclude that the surface band structure of 3C-SiC(001)-c(2 \times 2), calculated within the SIC approach, shows general improvements over the standard LDA surface band structure concerning the projected bulk band structure and the projected gap, in particular, the absolute energy positions of empty surface-state bands, the character of localized surface states (most noticeably the band T_3^*) and the antibonding T_1^* band which is in somewhat better agreement with experiment. Obviously, these improvements are less impressive than those for the bulk band structures of the SiC polytypes discussed above. The fact that the upward shift of the T_1^* band resulting within SIC, as compared to LDA, is relatively small (only 0.4 eV) is largely due to the fact that the occupied T_1 and the empty T_1^* bands both originate from the triple-bonded C \equiv C surface dimers and thus are mainly derived from bulk states in the upper valence bands. Such bands are equally influenced in the standard SIC calculation, as was shown in detail for the related case at the 3C-SiC(001)-(2 \times 1) surface. The SIC- Δ approach yields a very significant upward shift of the respective empty bands as could be expected from the nature of the associated states. This results in a further improved agreement with experimental data from angle-resolved inverse photoemission spectroscopy. As there is no GWA calculation for this surface in the literature, it is uncertain whether the remaining differences

are due to the simplicity of the presented theoretical approach or originate from intricacies in the determination of the experimental energies.

4.3. Summary

In this chapter it has been analyzed how atomic self-interaction corrections that are incorporated in the nonlocal part of ionic Si and C pseudopotentials can be used in surface electronic structure calculations. While within DFT calculations for the most commonly considered cubic and hexagonal polytypes of silicon carbide the application of the SIC pseudopotentials are suitable to overcome the typical LDA shortcomings in the description of the electronic band structure, respective calculations for surfaces are more intricate. In the case of the nonpolar 3C-SiC(110)-(1×1) surface, the standard application of the SIC pseudopotentials yields changes in the surface band structure that are qualitatively and quantitatively comparable to the one known from the bulk crystal. At this surface, the fundamental characteristics of the electronic structure do not deviate significantly from the situation in the bulk.

For the 3C-SiC(001) surfaces, in contrast, the occurrence of empty surface bands that are linear combinations of states that are occupied in the bulk, i.e. the antibinding C=C and C≡C dimer states at the (2×1) and c(2×2) reconstructions, respectively, results in a spurious self-interaction correction for these bands. The SIC- Δ approach in which the expectation value of the nonlocal SIC pseudopotential operator is subtracted from the energies of the empty states, pragmatically accounts for this error. The application of this approach to the two reconstruction models of the 3C-SiC(001) surface and the comparison of the results to GWA quasiparticle calculations and experimental data validate this method.

It must be emphasized that these results have been achieved without any extra computational effort compared to standard LDA calculations, much in contrast to GWA calculations. In particular in view of this fact, the reached agreement with literature data from experiment and GWA calculations is highly satisfactory and emphasizes that the approach to account for self-interaction corrections is a powerful tool for a more accurate description of the electronic properties of 3C-, 2H-, 4H- and 6H-SiC crystals. The SIC and SIC- Δ approaches have hence shown itself to be useful tools with small computational costs for investigations of silicon carbide surfaces with similar characteristics as the examples chosen in this chapter.

Chapter 5.

Properties of $(10\bar{1}0)$ and $(1\bar{1}02)$ - $c(2\times 2)$ surfaces of 4H-SiC

In the previous chapter, the application of SIC pseudopotentials to the well-studied surfaces of 3C-SiC has offered detailed insight into their effectiveness in surface electronic structure calculations.

More recently, surfaces of the hexagonal 4H-SiC polytype have moved into the focus of research interest. Experimental preparations and investigations of several surfaces of this crystal have been reported. Due to the complexity of these surfaces, theoretical calculations are important to shed light on the atomic geometry of the surfaces as well as their respective electronic properties. In this regard it is imperative to obtain both qualitatively and quantitatively reliable results. As the unit cell of bulk 4H-SiC is already comparatively large containing eight atoms, any surface modeling within the supercell approach will involve respectively large unit cells and a considerably high number of atoms per unit cell. Combining reliability and light additional numerical demands, SIC calculations as shown in Chapter 4 can be expected to be a powerful tool to elucidate the surface electronic properties.

5.1. The 4H-SiC($10\bar{1}0$) Surface

The $(10\bar{1}0)$ surface of 4H-SiC is a nominally nonpolar surface very much like the previously discussed 3C-SiC(110) surface.

The basic geometry of the surface is shown in Fig. 5.1. The left panel shows a top view on the basal plane of a wurtzite structure. As usual, the bulk unit cell is described by the

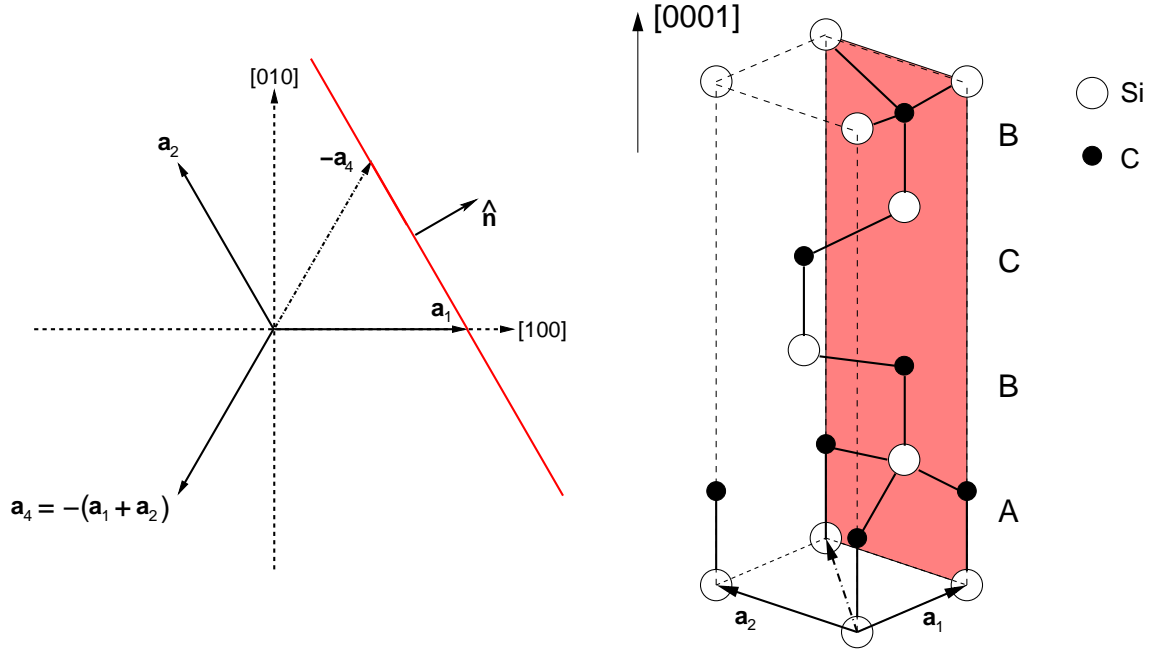


Figure 5.1: Schematic representation of the orientation of the 4H-SiC($10\bar{1}0$) surface relative to the bulk crystal. The left panel indicates the surface cut within a $[001]$ - $[100]$ plane. The bulk stacking sequence (ABCB) is shown in the right panel. Open (closed) circles represent positions of silicon (carbon) atoms. The red shaded face marks the positioning of the surface unit cell.

Bravais vectors

$$\begin{aligned}
 \mathbf{a}_1 &= a \cdot (1, 0, 0) \\
 \mathbf{a}_2 &= a \cdot \left(-\frac{1}{2}, \frac{\sqrt{3}}{2}, 0 \right) \\
 \mathbf{a}_3 &= c \cdot (0, 0, 1)
 \end{aligned} \tag{5.1}$$

and the positions of the eight non-primitive base atoms

silicon atoms	carbon atoms	
$\tau_1 = a \cdot (0, 0, 0)$	$\tau_2 = a \cdot \left(0, 0, \frac{3c}{16a} \right)$	(5.2)
$\tau_3 = a \cdot \left(0, \frac{1}{\sqrt{3}}, \frac{1c}{4a} \right)$	$\tau_4 = a \cdot \left(0, \frac{1}{\sqrt{3}}, \frac{7c}{16a} \right)$	
$\tau_5 = a \cdot \left(\frac{1}{2}, \frac{1}{2\sqrt{3}}, \frac{1c}{2a} \right)$	$\tau_6 = a \cdot \left(\frac{1}{2}, \frac{1}{2\sqrt{3}}, \frac{11c}{16a} \right)$	
$\tau_7 = a \cdot \left(0, \frac{1}{\sqrt{3}}, \frac{3c}{4a} \right)$	$\tau_8 = a \cdot \left(0, \frac{1}{\sqrt{3}}, \frac{15c}{16a} \right)$	

Aiming at an unambiguous identification of surfaces of hexagonal crystals, a four index notation is commonly used. An additional vector within the basal plane

$$\mathbf{a}_4 =: -(\mathbf{a}_1 + \mathbf{a}_2) \quad (5.3)$$

is introduced (cf. Fig. 5.1). The surface index then consists of the indices assigned to the vectors within the basal plane (\mathbf{a}_1 , \mathbf{a}_2 , \mathbf{a}_4) followed by the one assigned to the vector $\mathbf{a}_3 \parallel \mathbf{e}_z$. For a (10 $\bar{1}$ 0) surface, this yields a surface cut as indicated by the red line in the left panel of Fig. 5.1. In the right panel, the position of the resulting surface unit cell within the bulk crystal is given by the red shaded rectangle. As can be seen from the also supplied stacking sequence of bulk 4H-SiC, the surface exhibits a quite intricate atomic structure in the perpendicular direction. In fact, the surface is only periodic after six unique surface layers.

The rectangular unit cell of the 4H-SiC(10 $\bar{1}$ 0) surface is described by the two Bravais vectors

$$\begin{aligned} \mathbf{a}_1^S &= c \cdot (1, 0, 0) \\ \mathbf{a}_2^S &= a \cdot (0, 1, 0) \end{aligned} \quad (5.4)$$

where the bulk unit Bravais vectors \mathbf{a}_3 ([0001] direction) and \mathbf{a}_2 are oriented parallel to x and y , respectively.

Each of the six surface layers (sequence ABCDEF¹) contains an equal number of silicon and carbon atoms, respectively, which nominally makes this surface nonpolar. The atomic positions of the ideal surface can explicitly be written as

$$\begin{aligned} \tau_{\text{Si}}^{\text{A}} &= a \cdot (0, 0, 0) & \tau_{\text{C}}^{\text{A}} &= a \cdot \left(\frac{3}{16} \frac{c}{a}, 0, 0 \right) \\ \tau_{\text{Si}}^{\text{B},1} &= a \cdot \left(\frac{1}{4} \frac{c}{a}, \frac{1}{2}, \frac{-1}{2\sqrt{3}} \right) & \tau_{\text{C}}^{\text{B},1} &= a \cdot \left(\frac{7}{16} \frac{c}{a}, \frac{1}{2}, \frac{-1}{2\sqrt{3}} \right) \\ \tau_{\text{Si}}^{\text{B},2} &= a \cdot \left(\frac{3}{4} \frac{c}{a}, \frac{1}{2}, \frac{-1}{2\sqrt{3}} \right) & \tau_{\text{C}}^{\text{B},2} &= a \cdot \left(\frac{15}{16} \frac{c}{a}, \frac{1}{2}, \frac{-1}{2\sqrt{3}} \right) \\ \tau_{\text{Si}}^{\text{C}} &= a \cdot \left(\frac{1}{2} \frac{c}{a}, 0, \frac{-1}{\sqrt{3}} \right) & \tau_{\text{C}}^{\text{C}} &= a \cdot \left(\frac{11}{16} \frac{c}{a}, 0, \frac{-1}{\sqrt{3}} \right) \\ \tau_{\text{Si}}^{\text{D}} &= a \cdot \left(0, \frac{1}{2}, \frac{-3}{2\sqrt{3}} \right) & \tau_{\text{C}}^{\text{D}} &= a \cdot \left(\frac{3}{16} \frac{c}{a}, \frac{1}{2}, \frac{-3}{2\sqrt{3}} \right) \end{aligned} \quad (5.5)$$

¹Note that these labels are not identical with those in the bulk stacking sequence.

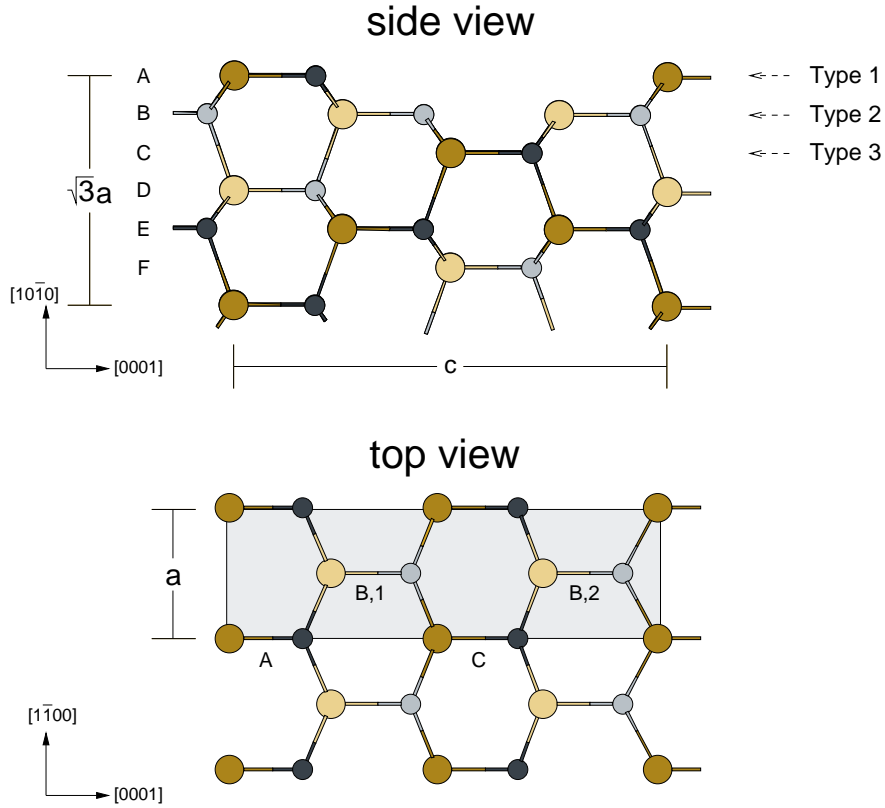


Figure 5.2: Side and top views on the 4H-SiC($10\bar{1}0$) surface. The layer sequence (ABCDEF) within the surface is given on the left hand side. Dark ocher (grey) circles represent positions of silicon (carbon) atoms within the side view drawing pane ($y = 0$). Light symbols specify atoms in a plane parallel to it ($y = \frac{a}{2}$). The three distinct types of surface terminations are indicated by the arrows on the right hand side. The shaded area in the top view indicates the surface unit cell.

$$\begin{aligned}
 \tau_{\text{Si}}^{\text{E},1} &= a \cdot \left(\frac{1}{4} \frac{a}{c}, 0, \frac{-2}{\sqrt{3}} \right) & \tau_{\text{C}}^{\text{E},1} &= a \cdot \left(\frac{7}{16} \frac{c}{a}, 0, \frac{-2}{\sqrt{3}} \right) \\
 \tau_{\text{Si}}^{\text{E},2} &= a \cdot \left(\frac{3}{4} \frac{c}{a}, 0, \frac{-2}{\sqrt{3}} \right) & \tau_{\text{C}}^{\text{E},2} &= a \cdot \left(\frac{15}{16} \frac{c}{a}, 0, \frac{-2}{\sqrt{3}} \right) \\
 \tau_{\text{Si}}^{\text{F}} &= a \cdot \left(\frac{1}{2} \frac{c}{a}, \frac{1}{2}, \frac{-5}{2\sqrt{3}} \right) & \tau_{\text{C}}^{\text{F}} &= a \cdot \left(\frac{11}{16} \frac{c}{a}, \frac{1}{2}, \frac{-5}{2\sqrt{3}} \right) .
 \end{aligned}$$

Figure 5.2 shows side and top views on the 4H-SiC($10\bar{1}0$) surface as defined by these vectors. Much in contrast to the nonpolar 3C-SiC(110) surface discussed in Ch. 4.1, not all surface cuts are equivalent. In fact, there are three distinctly different surface types, labeled Type 1 to 3 in Fig. 5.2, that can possibly form the 4H-SiC($10\bar{1}0$) surface. The variant shown is called a type 1 surface and consists of a layer A surface termination,

Table 5.1: Calculated displacements of atoms from their ideal positions (in Å) upon relaxation of the 4H-SiC(10 $\bar{1}$ 0) surface.

4H-SiC			
(10$\bar{1}$0)-(1x1)	Δx	Δy	Δz
$\tau_{\text{Si}}^{\text{A}}$	+0.10	+0.00	-0.19
$\tau_{\text{C}}^{\text{A}}$	-0.06	+0.00	-0.11
$\tau_{\text{Si}}^{\text{B},1}$	+0.07	+0.00	+0.12
$\tau_{\text{C}}^{\text{B},1}$	+0.04	+0.00	-0.04
$\tau_{\text{Si}}^{\text{B},2}$	-0.10	+0.00	-0.13
$\tau_{\text{C}}^{\text{B},2}$	-0.14	+0.00	+0.13
$\tau_{\text{Si}}^{\text{C}}$	-0.05	+0.00	+0.04
$\tau_{\text{C}}^{\text{C}}$	-0.04	+0.00	-0.03
$\tau_{\text{Si}}^{\text{D}}$	+0.04	+0.00	+0.01
$\tau_{\text{C}}^{\text{D}}$	+0.03	+0.00	+0.03
$\tau_{\text{Si}}^{\text{E},1}$	+0.01	+0.00	+0.02
$\tau_{\text{C}}^{\text{E},1}$	+0.01	+0.00	-0.01
$\tau_{\text{Si}}^{\text{E},2}$	+0.00	+0.00	-0.03
$\tau_{\text{C}}^{\text{E},2}$	-0.00	+0.00	+0.03

including one carbon and one silicon atom within the outer surface layer. In total there are four broken bonds per unit cell on such a surface of which two belong to layer A atoms and two to the inner atoms $\tau_{\text{C}}^{\text{B},1}$ and $\tau_{\text{Si}}^{\text{B},2}$ residing on layer B. In contrast, surfaces of Types 2 and 3 exhibit six broken bonds each. This indicates that the Type 1 surface will be energetically more favorable than these two surface terminations. In the following, any reference to the 4H-SiC(10 $\bar{1}$ 0) surface implies the Type 1 structure, if not explicitly stated otherwise.

In the calculations, the surface is modeled by a slab consisting of twelve layers in total, i.e. the double of the non-primitive base given in Eq. (5.5). The broken bonds at the bottom of the slab are saturated by hydrogen atoms. Gaussian orbitals with the decay constants as in Sec. 4.1 are used to expand the wave functions. For the atoms within the first three surface layers, extended sets consisting of three shells of Gaussian orbitals are employed. A vacuum layer of 10 Å electronically decouples neighboring slabs. As the structure of the surface is relatively open, additional slowly-decaying Gaussian orbitals are placed in the virtual positions of additional three ideal surface layers in order to allow for a more suitable representation of extended surface states. Brillouin zone integrations are performed using ten special \mathbf{k} -points in the irreducible wedge of the surface Brillouin zone, generated by the prescription of Monkhorst and Pack [30]. The positions of the atoms in the upper five layers of the slab are allowed to relax.

In Table 5.1 the resulting displacements of the surface atoms with respect to their ideal bulk position upon relaxation are listed. Note that $\mathbf{e}_x \parallel [0001]$, $\mathbf{e}_y \parallel [1\bar{1}00]$ and $\mathbf{e}_z \parallel$

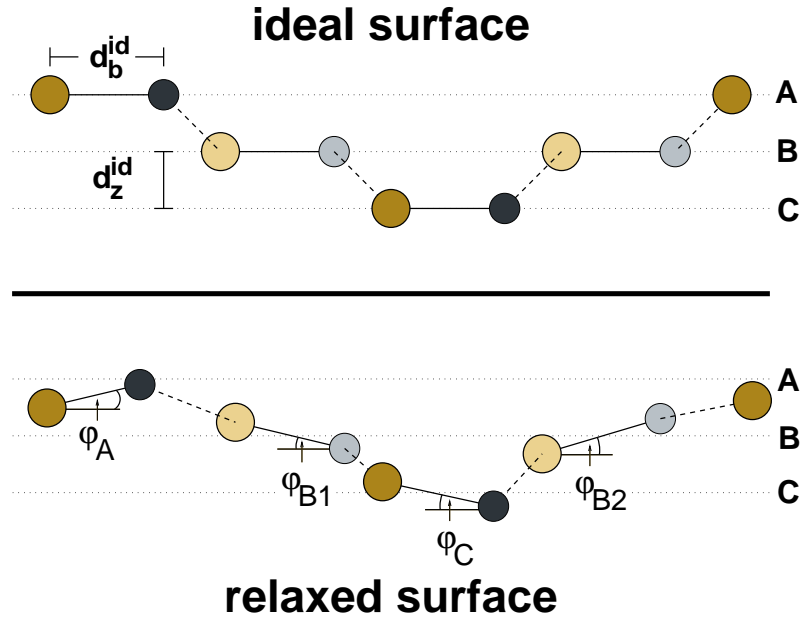
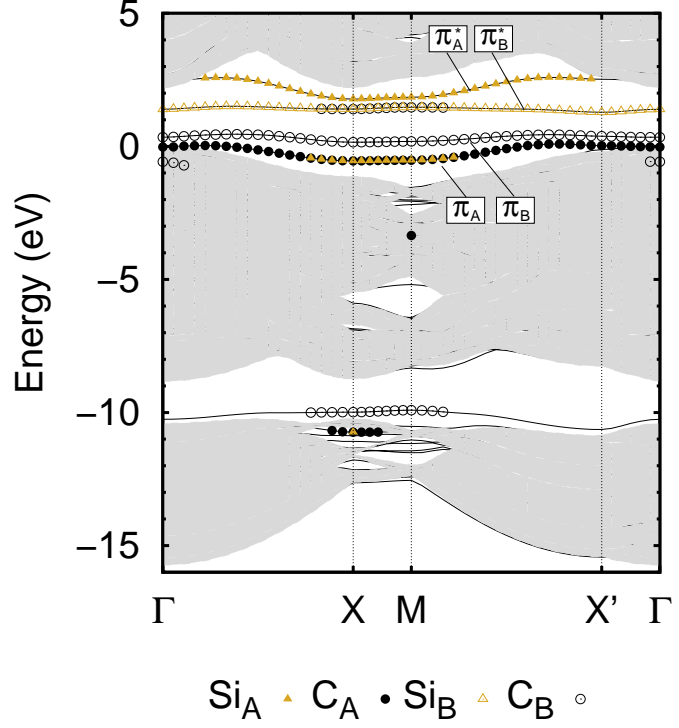


Figure 5.3: Schematic relaxation pattern of the 4H-SiC($10\bar{1}0$) surface within the x - z -plane. Color code as in Fig. 5.2. Tilt angles φ are defined for the four Si-C pairs within the first three layers. Note that the pattern is not drawn to scale.

$[10\bar{1}0]$. It is most obvious that the atoms only change their positions in x - and z -directions. Figure 5.3 schematically shows the resulting relaxation pattern. It is somewhat similar to the bond length contracting rotation relaxation known for GaAs(110), 3C-SiC(110) and 2H-SiC($10\bar{1}0$) [70, 75]. In layer A, both atoms move closer to the substrate, the silicon atom more strongly than the carbon atom leading to a tilted Si-C bond within the top surface layer. The tilt angle φ_A amounts to 2.7° only, which is small compared to the value of 30° at GaAs(110) and of similar magnitude as the 3.8° on 2H-SiC($10\bar{1}0$). The rotation is accompanied by a contraction of the Si-C bond length d_A . While in the bulk the bond length amounts to 1.87 \AA , it is reduced to 1.71 \AA at the surface. The bond length contraction thus amounts to 8.6%, which is very similar to the contraction at the respective 2H-SiC($10\bar{1}0$) surface. On the second layer (B), there are two Si-C structures. The first one consisting of base atoms $\tau_{\text{Si}}^{\text{B},1}$ with fully saturated bonds and $\tau_{\text{C}}^{\text{B},1}$ with one broken bond shows an inverted tilt. Here, the silicon atom resides above the carbon atom and its tilt angle amounts to $\varphi_{\text{B},1} = 5.0^\circ$. The second Si-C pair is formed by the unsaturated silicon atom $\tau_{\text{Si}}^{\text{B},2}$ and the saturated carbon atom $\tau_{\text{C}}^{\text{B},2}$. In this case, the tilt pattern is identical to the one in layer A, although the tilt angle is much larger amounting to $\varphi_{\text{C}} = 8.1^\circ$. In both cases, the contraction of the Si-C bond is only very small with $d_{\text{B},1} = 1.84 \text{ \AA}$ and $d_{\text{B},2} = 1.85 \text{ \AA}$ being only fractionally smaller than the ideal bond length. As far as layer C is concerned, the silicon atom is found above the carbon atom. The tilt angle $\varphi_{\text{C}} = 2.1^\circ$ is characteristically small and the bond length of 1.88 \AA is almost bulk-like.

Figure 5.4: Electronic band structure of the relaxed 4H-SiC(10 $\bar{1}$ 0)-(1x1) surface as resulting from LDA calculations. The projected bulk band structure is indicated by the grey shaded area. Triangles and circles mark bands that can be uniquely assigned to silicon and carbon atoms, respectively. Filled (open) symbols stand for atoms with broken bonds residing on layer A (B). See text for the definition of bands.



The energy gain per unit cell compared to the ideal surface amounts to 1.15 eV.

Figure 5.4 shows the electronic band structure of the relaxed 4H-SiC(10 $\bar{1}$ 0) surface as resulting from LDA calculations. In accord with the four broken Si-C bonds at the Type 1 surface, four salient surface bands are visible within the projected bulk band gap. The surface is semiconducting with an indirect surface gap of 0.82 eV. Additionally, there is one unique surface derived band visible within the projection of the heteropolar gap. In order to understand the nature of these surface derived bands, a Mulliken analysis is used to resolve the atomic contributions to the respective states. The bands in Fig. 5.4 are marked accordingly (see caption of figure for details). In addition Fig. 5.5 contains charge density contours for states of the four different bands at the M -point of the surface Brillouin zone shown in suitable [0001]-[10 $\bar{1}$ 0] planes. The state associated to the energetically lowest band is shown in panel (a). Two aspects become immediately apparent. First of all, the charge density is predominantly located at the layer A atoms. This is also evident from the band markings in the band structure. The contour lines in the figure clearly indicate a significant overlap between the two atomic contributions. In fact, it bears resemblance to a π -bond, i.e. a binding linear combination of the silicon and carbon dangling-bond orbitals. In the following, this band is therefore labeled as π_A . Accordingly, the charge density in Fig. 5.5(b) associated to the energetically highest band has got a much higher contribution located at the surface silicon atom. There is a clear nodal plane visible, indicating the antibonding character of this state, which is hence further referred to as π_A^* .

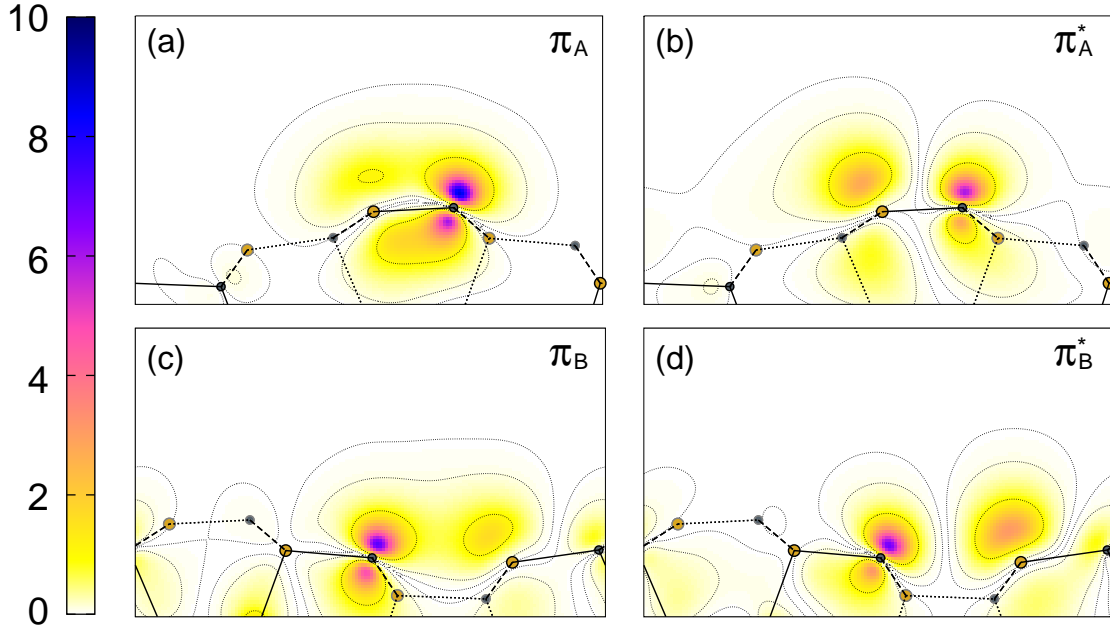


Figure 5.5: Charge density contours (in $10^{-1} a_B$) for four states within the projected bulk band gap at the M -point of the surface Brillouin zone. The contours in (a) and (b) are plotted in a x - z -plane containing the Si-C bond of layer A ($y = 0$), (c) and (d) in the parallel plane at $y = a/2$. Note that the plot window is also changed along x to center the relevant charge densities. Other (black) symbols represent positions of surface silicon (carbon) atoms.

A very similar situation is observed for the highest occupied state at the M -point, whose charge density contours are shown in Fig. 5.5(c). Again there is a substantial π -like overlap between the dangling-bond contributions from the silicon and carbon atoms residing in layer B. An antibinding linear combinations of the same orbitals as visible in Fig. 5.5(d) leads to the lowest unoccupied surface band. Accordingly, these two bands are labeled as π_B and π_B^* in Fig. 5.4.

The notion of an additional π -like Si-C bond in surface layer A is corroborated further by an analysis of the bonding characteristics based on maximally-localized Wannier functions [83] which is shown in Fig. 5.6. In panel (a), the surface geometry is shown in a stick model viewed within the x - z -plane. The color code of the sticks is identical to the one used for the atomic symbols in Fig. 5.2. Centers and spreads of the respective Wannier functions are represented by the filled red circles. Most of the Wannier functions in the lower layers are located on the Si-C bonds at bulk-like positions. Due to the ionic component of the bond, they do not reside at the bond center but closer to the carbon atom. In the upper layers slight distortions of this pattern are visible. Most noticeable in this regard are three centers labeled $\text{Si}=\text{C}_t$ (top), $\text{Si}=\text{C}_b$ (bottom), and C_B . The first two of these are most unique at this surface. As can easily be seen, the respective centers

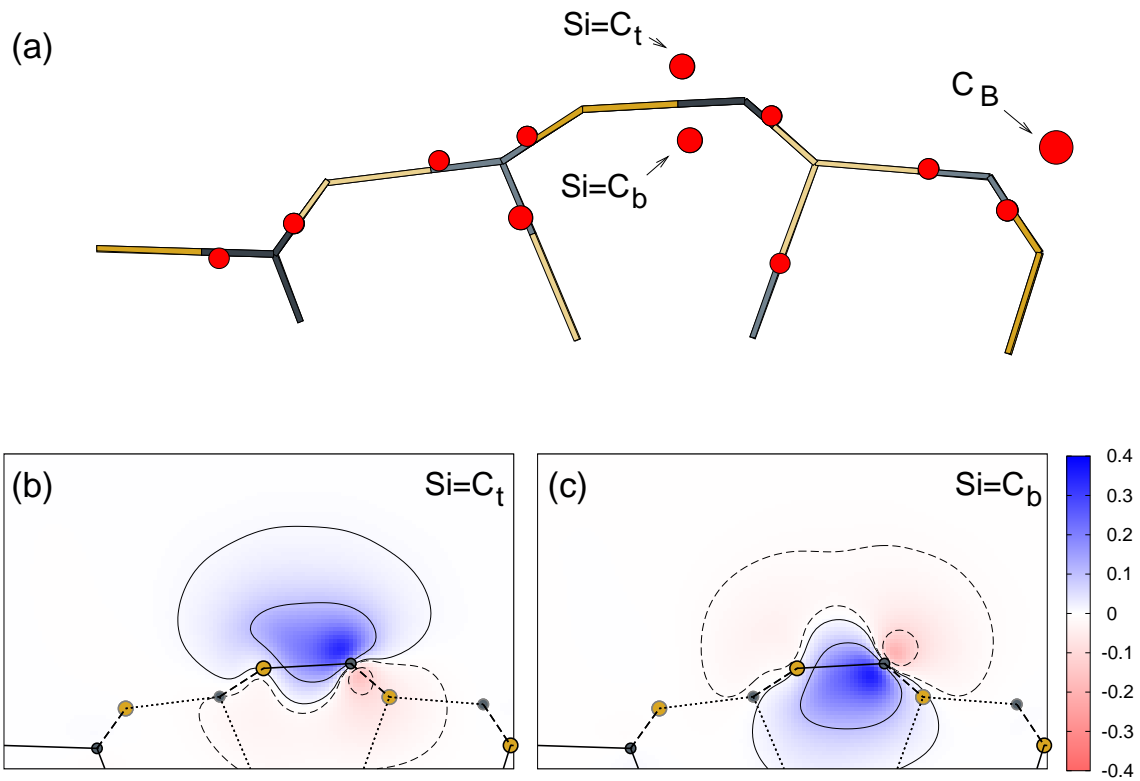


Figure 5.6: Analysis of the bonding characteristics at the relaxed 4H-SiC(10 $\bar{1}$ 0) surface in terms of Wannier functions. The side view in (a) contains the centers and spreads of the Wannier functions indicated by the position and radius of the red circles. Panels (b) and (c) show the contours of the two Wannier functions labeled as Si=C_t and Si=C_b in panel (a), which are associated to the Si-C bond in layer A.

reside above and below the Si-C bond. Parallel to the surface, they are found to be slightly closer to the carbon atom than in lower layers. The spread of both functions amounts to 1.3 Å. Such a distribution of Wannier centers is indeed characteristic for a double-bond as was already assumed based on Fig. 5.5. If one inspects the Wannier functions for Si=C_t and Si=C_b more closely, as in Figs. 5.6(b) and (c), this characteristic becomes even more apparent. In the former case, the function is positive mostly in the space above the Si-C bond, and negative below it. For function Si=C_b the situation is inverted. All in all, both the inspection of single state charge densities and the analysis of accordingly constructed localized Wannier functions point to the fact, that in the surface layer A of 4H-SiC(10 $\bar{1}$ 0) a Si=C double bond is formed. In contrast, on layer B the Wannier center C_B is located in the empty region above the layer and close to the carbon atom in that particular layer. Due to the mutual distance of 2.97 Å between silicon and carbon atoms, no real bond can be formed, although there is substantial attractive π -interaction inherent. The electron therefore retains most of the original dangling-bond characteristics.

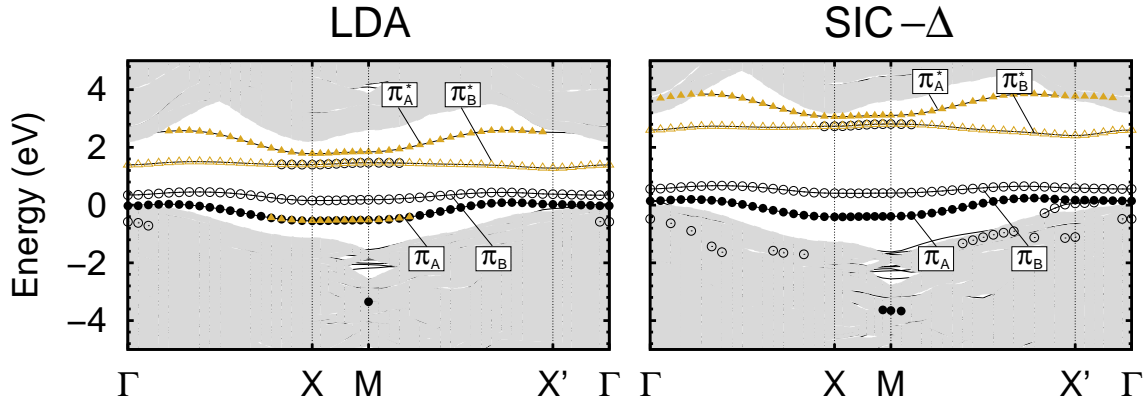


Figure 5.7: Electronic band structure of the relaxed 4H-SiC($10\bar{1}0$)-(1x1) surface around the projected bulk band gap as resulting from LDA (left panel) and SIC- Δ calculations (right panel). The projected bulk band structure is indicated by the grey shaded area. Band markings are the same as in Fig. 5.4.

It should be noted at this point that due to the purely Wurtzite bulk crystal structure, the related 2H-SiC($10\bar{1}0$) surface contains only one Si-C pair that can contribute to surface bands. In Ref. [84] it has been argued on the basis of charge density contour plots that the occupied band is almost exclusively derived from carbon dangling-bond states, while the unoccupied band is mostly located at the surface silicon atom although a substantial contribution from the carbon atom is noted, as well. However, these bands have the same physical origin as the π_A and π_A^* bands at the 4H-SiC($10\bar{1}0$) surface. As a matter of fact, respective Wannier functions at 2H-SiC($10\bar{1}0$) show the same characteristics as Si=C_t and Si=C_b. Together with the equally shortened bond length, this indicates that a Si=C double bond is formed at the 2H-SiC surface, as well.

These realizations do shed some light on the forces that drive the atomic relaxation of the surface. In general, there are three distinct mechanism: Firstly, a reduction of Coulomb repulsion between electrons leads the more electronegative ion to reside high above the rest of the surface. Secondly, there is a quantum mechanically driven configuration change due to new hybridization of orbitals. For very strongly ionic systems, classical electrostatic interaction must be taken into consideration as a third possibility. Given the highly quantum mechanical nature of the π -interaction leading to the Si=C bond within layer A, it can be assumed that hybridization effects play a vital role in this particular relaxation. In layer B, the situation is conceptually different because the respective silicon and carbon atoms hosting the two dangling bonds are not directly connected to begin with. Instead they are equally bound to another atom that is fully saturated. Consequently, the atom hosting the broken bond moves downward relative to the bonding partner.

Based on this broad knowledge about the fundamental character of the electronic structure of 4H-SiC($10\bar{1}0$), and in particular of its salient surface bands, it is apparent that

the SIC- Δ approach should be the method of choice to study the effect of the SIC pseudopotentials on the present electronic structure. The band structure of the relaxed 4H-SiC(10 $\bar{1}$ 0) surface around the projected bulk band gap as resulting from a respective calculation is shown in the right panel of Fig. 5.7. The LDA result is repeated for easier comparison in the left panel. It is apparent that the fundamental character of the bands remains unchanged. There are two occupied and unoccupied surface bands, respectively. The band gap is opened due to the influence of SIC and amounts to 1.74 eV as compared to 0.82 eV resulting from LDA. The position of the occupied π_A and π_B bands relative to the projected bulk valence bands is hardly changed. On the contrary, the π_B^* band resides on average roughly 0.8 eV higher relative to the VBM than in the LDA reference. As the position of the occupied surface bands relative to the bulk is only slightly affected, this change accounts for the change in the surface band gap.

Some influence of SIC on the band markings is discernible, as well. The occupied π_A band, for instance, contains visible amounts of the silicon atom in layer A in the LDA result. In contrast, these markings vanish in SIC, which is an indication of the usual slightly increased localization of the charge densities at the surface carbon atom. This does not influence the fundamental characteristics of the bonding at the surface, however. Generally, the dispersion of the bands is unaffected, as well. The interaction along the x -direction is small leading to only very faintly dispersive bands along the X - M and X' - Γ symmetry lines. In the longer directions of the surface Brillouin zone, there is a slightly stronger dispersion as indication of more electronic interactions along the y -direction of the surface (see top view in Fig. 5.2).

Comparison to experimental reference data

For the 4H-SiC(10 $\bar{1}$ 0) surface, there is some preliminary experimental reference data by Emtsev and coworkers [85] available to compare the calculated electronic structure to. The authors performed a combined study of low energy electron diffraction (LEED), ARPES and core-level spectroscopy (CLS) for two different surface preparations. In the first approach, silicon has been pre-deposited on the sample. Subsequent annealing at 1050°C has resulted in a surface exhibiting a 1 \times 1 LEED pattern. A strong surface state close to the projected valence band maximum is visible in ARPES as shown in Fig. 5.8. The second preparation of the surface starts with an *ex-situ* treatment with hydrogen. This leads to a hydrogen passivated surface. Annealing at a temperature of 650°C results in a desorption of hydrogen. LEED and ARPES experiments yield the same results as for the first surface preparation. The dispersion and energetic position of the observed surface band is compatible with the π_A band in Figs. 5.4 and 5.7. This notion is further corroborated by the measured surface core level shifts as one surface derived component in the C 1s line points to a Si-C dimer in layer A. This is basically inferred by a comparison to the

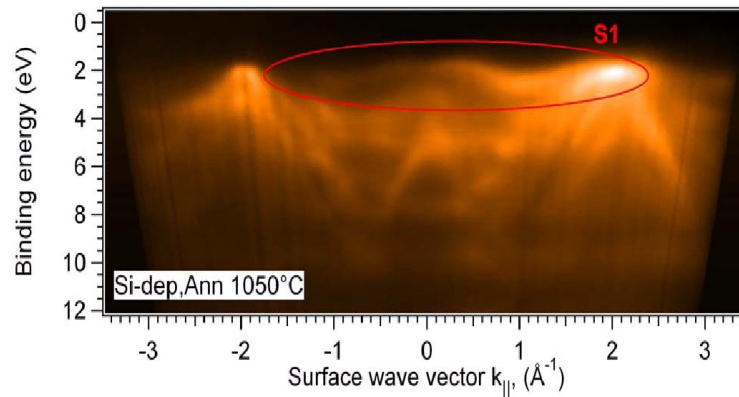


Figure 5.8: Experimental ARPES spectrum of the 4H-SiC($10\bar{1}0$) surface taken from Ref. [85]. Shown are the results for the surface preparation based on Si pre-deposition and subsequent annealing at 1050°C . The single salient surface band S_1 along the Γ - X symmetry line is highlighted.

2H-SiC($10\bar{1}0$) surface.

It is important to note that for both surface preparations only one single surface band is found close to the projected bulk valence bands. This is obviously in disagreement with the results of the electronic structure calculation. Due to the four broken bonds at the surface, a total of four salient surface bands are expected of which two are occupied and two are empty, respectively. The ARPES experiment should hence yield two occupied bands in the projected bulk band gap region. Apparently, either one of the occupied bands should be resonant with bulk states indicating a saturation of the broken bonds at the surface or the surface structure is more complex than what is assumed so far. Several possible variants have been considered. First of all, it can be excluded that the resolution of the ARPES experiment is not sufficient to separate the bands π_A and π_B , which is assumed to be missing. Also, Emtsev and coworkers strongly argue against residual hydrogen coverage of the surface since in the surface preparation with silicon pre-deposition, there is no hydrogen present at all.

Influence of hydrogen adsorption

It is assumed that the Fermi level of the sample is pinned by the lowest empty surface band in the ARPES experiments. From the spectra as in Fig. 5.8, a lower limit for the surface band gap of 1.8 eV can be deduced. This is in very close agreement to the calculated gap of 1.74 eV. However as it is, this would indicate that the band gap is formed between the π_B and π_B^* bands. Although there is no evidence that partial hydrogen coverage of the surface is responsible for the noted absence of a second occupied surface band, a calculation for the 4H-SiC($10\bar{1}0$) surface covered by 0.5 monolayers (ML) of hydrogen

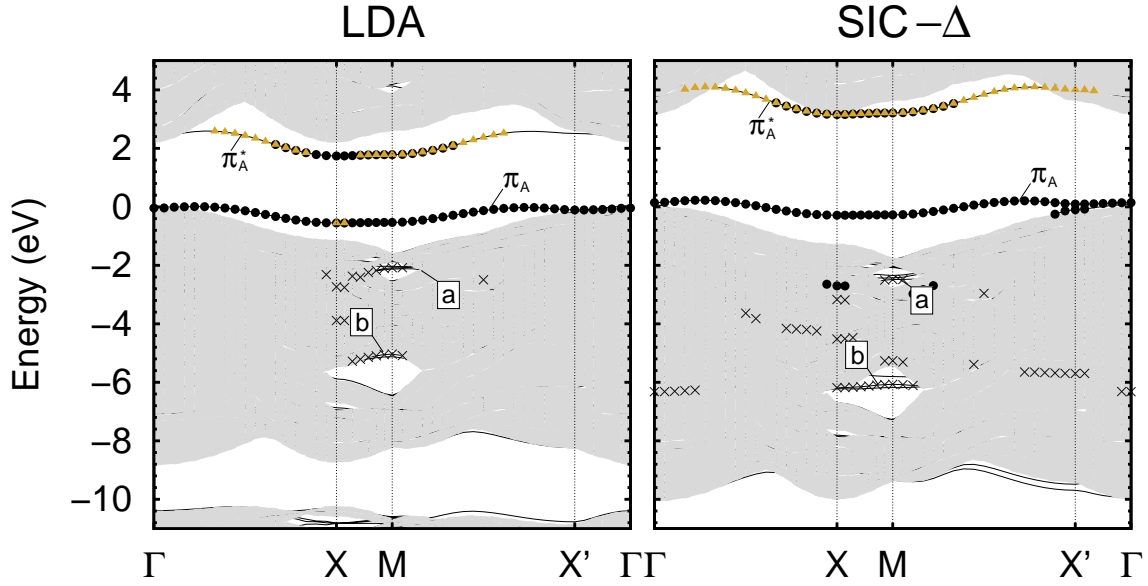


Figure 5.9: Electronic band structure of the 4H-SiC(10 $\bar{1}0$) surface covered by 0.5ML of hydrogen as resulting from LDA and SIC- Δ calculations. Specifically, the hydrogen atoms saturate the broken bonds of layer B. Band markings are the same as in Fig. 5.4. Additionally, crosses indicate bands that are derived from the adsorbed hydrogen.

saturation of the broken bonds of layer B is helpful in determining whether the π_A - π_A^* gap is compatible with such a lower limit of the band gap.

The resulting electronic band structure for the optimized geometry [see Fig. 5.11(a)] is shown in Fig. 5.9 as resulting from both LDA and SIC- Δ calculations. The bands π_B and π_B^* disappear, as expected. In LDA the surface band gap between the π_A and π_A^* band amounts to 1.71 eV. SIC opens this gap to 2.32 eV, which is in general accord with the experimentally derived lower limit of about 1.8 eV. Aside from the opening of the surface band gap, another more intricate notion of the use of SIC pseudopotentials becomes apparent. In Fig. 5.9 states within the band structure that can uniquely be assigned to the adsorbed hydrogen atoms are marked by crosses. Comparing the LDA and SIC- Δ band structures, slight changes become discernible around the M -point of the surface Brillouin zone. The hydrogen derived bands a and b experience slight downward energy shifts of 0.5 and 1.0 eV. These shifts yield to lower absolute energetic positions relative to the pockets in the projected bulk band structure and the bands reside visibly within them. It must be emphasized that these changes are not an artificial effect of SIC but are physically sound.

To support this notion, Fig. 5.10 shows the calculated band structure of the H:Si(111) surface, for which experimental photoemission [86] and theoretical quasiparticle data [87, 88] are available. At the K -point in the LDA band structure, the hydrogen derived band a is located within the top pocket while a' runs just at the bottom of the projection. An

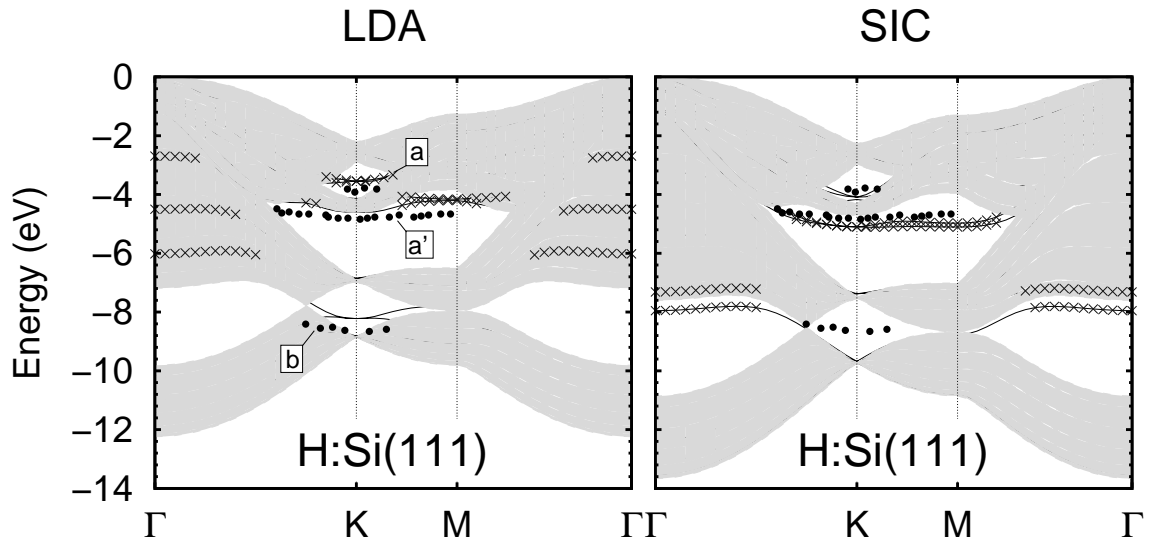


Figure 5.10: Electronic band structure of H:Si(111) as resulting from LDA and SIC calculations. Crosses indicate bands that are derived from the adsorbed hydrogen. Data from ARPES [86] is plotted by filled circles.

additional band b , which is strongly derived from Si atoms (cf. Fig. 9.12 in Ref. [88]) is found at about -8 eV again clearly within a pocket. Comparing these bands to the ARPES data symbolized by the black dots, it is apparent that the calculated band positions are slightly too high by a couple of tenths of an eV. The application of SIC improves the general agreement between the calculated and measured band positions for bands a and a' . As in the quasiparticle calculation (cf. Fig. 9.11 in [88]) the a band is located closer to the bottom of the pocket, while the a' band is found clearly within the empty region of the bulk projection with significantly reduced dispersion. For the b band, the SIC calculation can not reproduce the ARPES or GW results. However, this can be traced back to the inherent inadequacies of the SIC pseudopotential approach for purely covalently bonded systems. In particular, one notes for bulk silicon that the band gap is almost unaffected by SIC but the total valence band width increases more than is compatible with GWA and experimental data (cf. the projected bulk band structure in Fig. 5.10). For silicon carbide, in contrast, there is no such problem and thus the results in Fig. 5.9 can be regarded as reliable. This nicely illustrates, again, that SIC affects calculated band structures more intricately than a simple scissors operation on the conduction bands.

Discussion of alternative structures for 4H-SiC($10\bar{1}0$)

All in all, everything considered so far points to the fact that the signal observed in ARPES indeed originates from the π_A bonding linear combination of the layer A Si=C dimer. However, it is not yet clear which surface configuration can produce such an electronic

structure. The C $1s$ core level spectra contain additional shifts that could be interpreted in terms of additional carbon atoms present at the surface. This casts doubt on the stoichiometry of the surface. There is no experimental evidence for impurity atoms, like oxygen, either.

Therefore, several additional structures based on alternative arrangements of carbon and silicon atoms have been investigated. The surface core level spectrum for C $1s$ supplied by Emtsev *et al.* suggests that carbon based adstructures might be present on the surface. As was discussed above, the band structure for the true surface model should qualitatively be similar to the one of the 4H-SiC(10 $\bar{1}$ 0) surface with 0.5ML coverage of hydrogen adsorbed on layer B. Figure 5.11(a) shows the top and side view projections of the atoms within the first three layers of the surface unit cell additionally to the SiC- Δ band structure for the sake of reference. Three different surface models are given in Figs. 5.11(b)-(d). All are found to be stable. Due to the different stoichiometry of the models, however, it is not easily possible to compare their total energies. The first model in Fig. 5.11(b) is characterized by a substitution of the silicon atom in layer A by another carbon atom. A carbon dimer with a bond length of 1.34 Å is formed, which is the typical distance for a C=C dimer. The dimer is slightly buckled due to the different sublayer atoms it binds to. As a consequence of the substitution, the binding π_A and anti-binding π_A^* bands (filled black circles) move largely into the projected bulk regions. Only the two respective bands associated with the layer B structure (open symbols) remain within the projected gap and form a surface gap of 1.58 eV, which is somewhat smaller than indicated by ARPES. While there is as desired only one occupied surface band, its position relative to the projected valence band as well as its dispersion do not fit the experimental data. For instance, in ARPES, the occupied band is found clearly below the VBM at the X' point, while it remains definitely above it in the calculation. This model can hence be rejected.

The idea of using a carbon dimer to saturate the bonds of the layer B atoms leads to the optimized structure visible in Fig. 5.11(c). Two additional carbon atoms are deposited on the surface. A dimer with a bond length of only 1.24 Å is formed, indicating a triple-bonded carbon C \equiv C structure. Again a strong buckling of the dimer results from the different kind of sublayer atoms its constituting atoms are bound to. The down atom binds to another carbon atom in layer B with a mutual distance of 1.41 Å, which is some 10% smaller than in bulk diamond. In contrast, the up atom is found at a distance of 1.81 Å from the silicon atom, which is close to the ideal bulk Si-C bond length of 1.87 Å. In the band structure, the occupied π_A and empty π_A^* bands from the first layer Si=C dimer are clearly visible by the markings with full symbols. The open circles mark states that are derived from the additional C \equiv C dimer. Clearly, the occupied band associated with the bonding dimer states moves closer to the bulk projection than the π_B band in Fig. 5.7. It might be possible that such a band cannot be separated from bulk bands in ARPES. However, especially at the Γ -point and the Γ - X' symmetry line of the surface

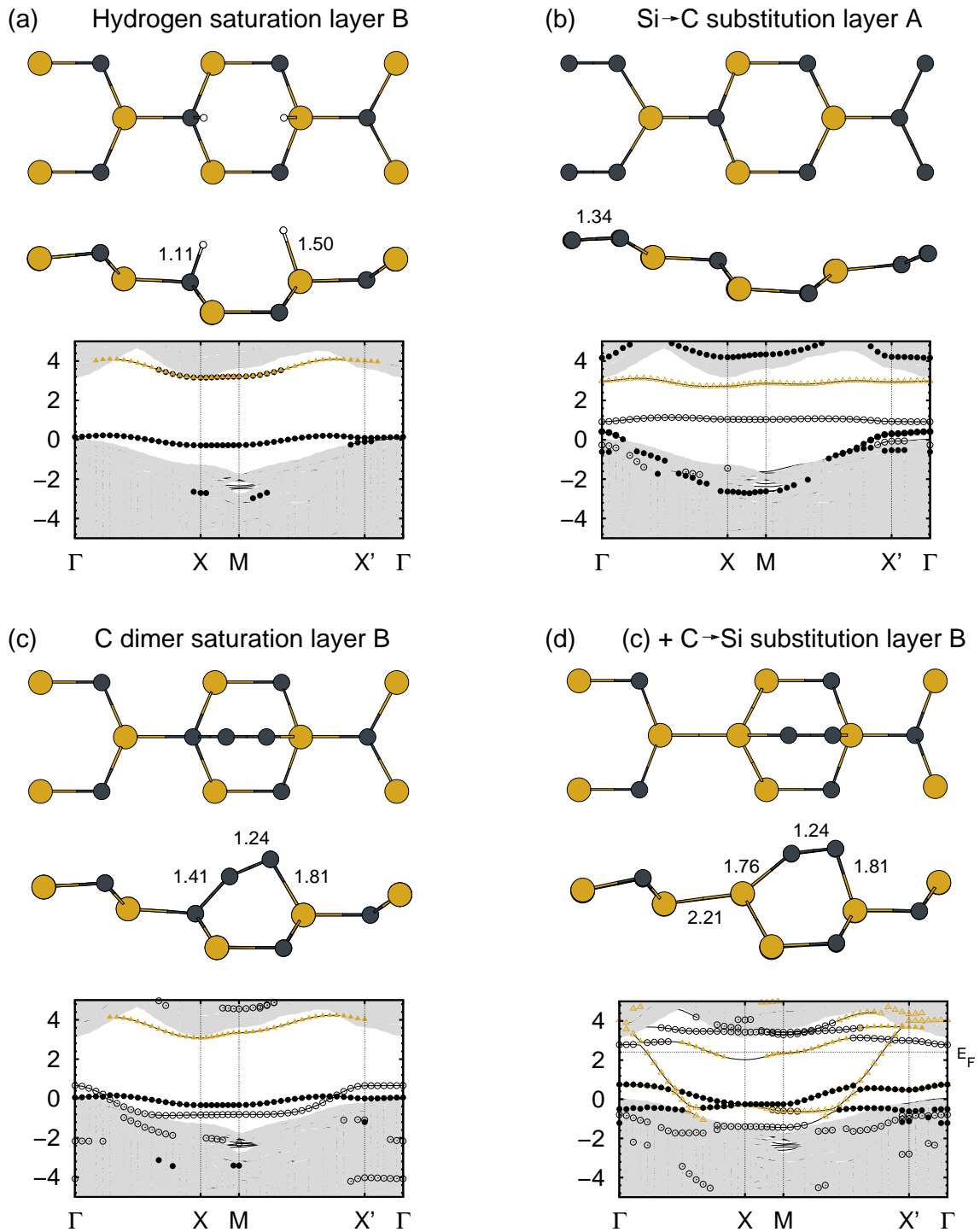


Figure 5.11: Alternative structure models for the 4H-SiC($10\bar{1}0$) surface. Each panel contains top and side view projections of the atoms within the first three surface layers, as well as the respective SIC band structures. Filled circles mark bands associated to atoms within layer A. For the respective definitions of open symbols, see text.

Brillouin zone, this particular band resides 0.8 eV above the π_A band and should thus be experimentally resolvable. It is therefore considered fairly unlikely that the model as depicted in Fig. 5.11(c) is observed in experiment. It should be noted that the addition of a Si-C structure instead of a C-C structure on layer B is effectively equivalent to a Type 3 surface cut (cf. Fig. 5.2). However, it cannot be expected that a similar triple-bonded Si \equiv C structure will be formed as in the case of the carbon dimer. Consequently, there will be additional dangling-bonds on both atoms giving rise to additional bands in the surface band structure.

Finally, the model in Fig. 5.11(d) is based on the previous model with an additional substitution of a second layer carbon by a silicon atom. A less strongly buckled C \equiv C dimer results. However, due to the second layer Si-Si bond, this does not yield a band structure in which the respective bonding band of the carbon dimer moves even closer to the projected valence bands. Instead, the Si-Si interaction on layer B (open triangles) leads to a metallic surface that contains a lot of different bands within the projected bulk band gap. Obviously, such a structure is way off from all experimental reference.

Obviously, none of these models is suitable to resolve the apparent incompatibility of the calculated electronic structure of the 4H-SiC(10 $\bar{1}$ 0) surface and the available experimental data. In light of the uncertain stoichiometry of the surface, further experimental evidence, e.g. a tensor LEED study or scanning tunneling microscopy, is needed to pursue different possible surface structures. With the limited amount of data currently available, the number of feasible geometries exceeds what can sensibly be calculated without too much guesswork.

5.2. The 4H-SiC($1\bar{1}02$)- $c(2\times 2)$ surface

Very recently, Virojanadara *et al.* [89, 90] have added a particularly intriguing facet to the broad spectrum of SiC surface studies. They have shown that a C-terminated 4H-SiC($1\bar{1}02$)- $c(2\times 2)$ surface can be prepared by a diagonal cut through the SiC bulk unit cell and have investigated this surface by photoemission spectroscopy, scanning tunneling microscopy (STM) and low-energy electron diffraction. This type of SiC surfaces had first been observed by Shiskin *et al.* [91] in an investigation of triangular channels in porous 4H-SiC which have been studied later by Starke *et al.* [92]. The 4H-SiC($1\bar{1}02$)- $c(2\times 2)$ surface resulting from the diagonal cut is largely free from defects exhibiting basically an ideal stoichiometry and consists of a periodic arrangement of alternating cubic *and* hexagonal stripes with an atomic structure very close to the C-terminated cubic 3C-SiC(001) and hexagonal 6H-SiC(0001) surfaces, respectively. The very narrow (about 0.6 nm) alternating stripes constitute well-defined nanostructures which occur side by side on 4H-SiC($1\bar{1}02$)- $c(2\times 2)$. Based on their LEED, core level spectroscopy, angle-resolved ultraviolet photoelectron spectroscopy (ARUPS) and STM data the authors have suggested a model for the surface structure consisting of a specific distribution of Si adatoms on the hexagonal stripes in H3 sites with a particular arrangement of triple-bonded bridging carbon dimers on the cubic stripes. The authors emphasized that their tentative model should be viewed as a plausible starting point for a quantitative structure determination by crystallography or total energy calculations. Total energy calculations are employed, therefore, in the following to unravel the structure of the 4H-SiC($1\bar{1}02$)- $c(2\times 2)$ surface. Contrary to the practice up to this point, the calculations are carried out within the framework of the generalized-gradient approximation (GGA) of density-functional theory. This approximation takes the gradient of the charge density $|\nabla n|$ into account when the XC-energy and XC-potential are evaluated (cf. Ref. [10]) and has been established as the method of choice for an appropriate description of the energetics involved in carbon dimerization, most prominently the difference between double- and triple-bonded carbon dimers. The exchange-correlation functional of Perdew and Wang [93] and nonlocal, norm-conserving pseudopotentials [94] in separable form [31] are used. The surface is treated within the supercell approach. Each slab consists of four Si-C double layers and is saturated by a layer of hydrogen atoms at the bottom. A vacuum layer of 10 Å separates neighboring slabs in order to avoid unphysical interactions between them. Brillouin-zone integrations are performed using a total set of 16 k-points generated by the prescription of Monkhorst and Pack [30]. The positions of the atoms within the topmost five layers of each slab and the Si adatoms are allowed to relax until all components of the calculated Hellmann-Feynman and Pulay forces are smaller than 0.6 mRy/a_B.

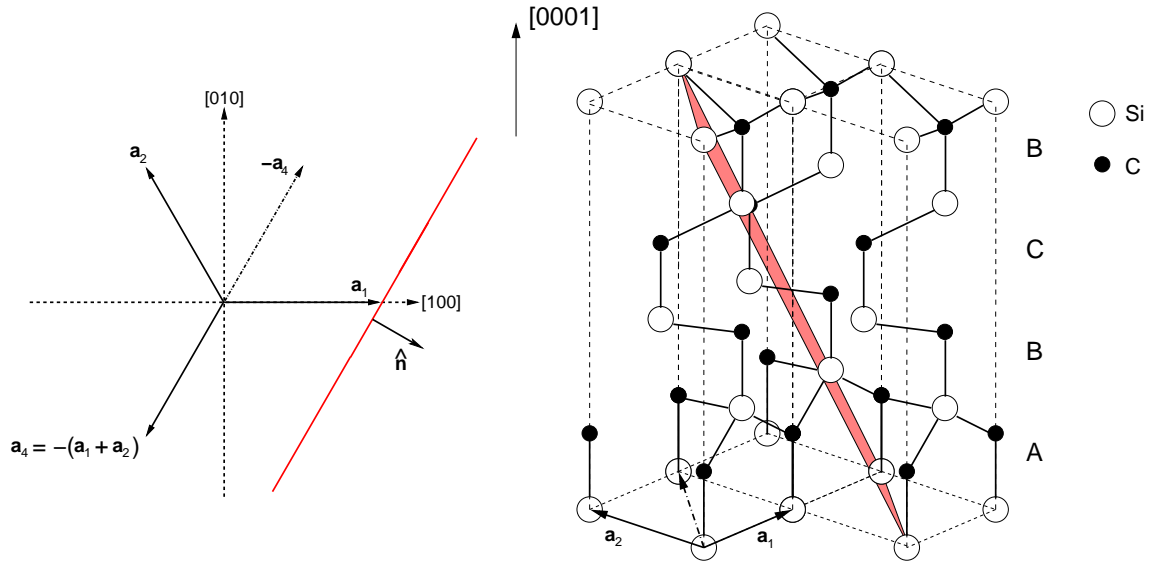


Figure 5.12: Schematic representation of the orientation of the 4H-SiC($1\bar{1}02$)- $c(2\times 2)$ surface relative to the bulk crystal. The left panel indicates the basal surface cut within a $[001]$ - $[010]$ plane. The bulk stacking sequence (ABCB) is shown in the right panel. Open (closed) circles represent positions of silicon (carbon) atoms. The red shaded region marks the positioning of the rectangular surface unit cell. Note that not all bonds are shown for the sake of clarity.

5.2.1. Atomic structure

Experimentally a $c(2\times 2)$ structure, among others, was observed. A large variety of conceivable $c(2\times 2)$ reconstructions of the 4H-SiC($1\bar{1}02$) surface are fathomable and need to be investigated. For reference, the features of the ideal surface are presented which allows us to introduce some useful nomenclature easing the discussion of the rather complex surface reconstructions to follow.

Ideal surface and building blocks for reconstructions

The 4H-SiC($1\bar{1}02$) surface represents a diagonal cut through the unit cell of bulk 4H-SiC (cf. Fig. 5.12), which is usually defined by the three bulk vectors given in Eq. (5.1). In order to generate the surface unit cell, one has to define its unit vectors. In the bulk coordinate system, the two vectors

$$\begin{aligned} \mathbf{a}_1^S &= \left(\frac{a}{2}, \frac{\sqrt{3}a}{2}, 0 \right) \\ \mathbf{a}_2^S &= \left(\frac{3a}{2}, -\frac{\sqrt{3}a}{2}, -c \right) \end{aligned} \quad (5.6)$$

span the plane of this diagonal cut. The associated normal vector on this plane is

$$\hat{\mathbf{n}} = \frac{1}{2\sqrt{3a^2 + c^2}} \left(\sqrt{3}c, -c, 2\sqrt{3}a \right). \quad (5.7)$$

For a full representation of the bulk system, one has to choose a (virtual) third base vector, in this case

$$\mathbf{a}_3^S = (-a, 0, 0). \quad (5.8)$$

As one can see, the \mathbf{a}_i^S are linear combinations of the \mathbf{a}_i :

$$\begin{aligned} \mathbf{a}_1^S &= \mathbf{a}_1 + \mathbf{a}_2 \\ \mathbf{a}_2^S &= \mathbf{a}_1 - \mathbf{a}_2 - \mathbf{a}_3 \\ \mathbf{a}_3^S &= -\mathbf{a}_1. \end{aligned} \quad (5.9)$$

It is convenient to rotate the coordinate system so that $\mathbf{a}_1^S \parallel \mathbf{e}_x$, $\mathbf{a}_2^S \parallel \mathbf{e}_y$ and $\hat{\mathbf{n}} \parallel \mathbf{e}_z$. This can be achieved using the rotation matrix

$$\underline{\underline{\mathbf{D}}} = (\mathbf{e}'_x, \mathbf{e}'_y, \mathbf{e}'_z) \quad (5.10)$$

containing the corresponding unit vectors

$$\begin{aligned} \mathbf{e}'_x &= \frac{\mathbf{a}_1^S}{|\mathbf{a}_1^S|} = \left(\frac{1}{2}, \frac{\sqrt{3}}{2}, 0 \right) \\ \mathbf{e}'_y &= \frac{\mathbf{a}_2^S}{|\mathbf{a}_2^S|} = \frac{1}{2\sqrt{3a^2 + c^2}} \left(3a, -\sqrt{3}a, -2c \right) \\ \mathbf{e}'_z &= \hat{\mathbf{n}} = \frac{1}{2\sqrt{3a^2 + c^2}} \left(\sqrt{3}c, -c, 2\sqrt{3}a \right). \end{aligned} \quad (5.11)$$

Application of this rotation matrix to the bulk base vectors and the nonprimitive basis $\boldsymbol{\tau}_\nu$ of the bulk cell as given in Eq. (5.5) transforms the unit cell and atomic positions of the bulk crystal into the surface orientation.

It is notable that the third vector \mathbf{a}_3^S is not parallel to the surface normal. The unit cell is not rhombic but monoclinic. The length of the reciprocal vector $\mathbf{G} = \mathbf{b}_1 - \mathbf{b}_2 + 2\mathbf{b}_3$ (with \mathbf{b}_i the basis of the bulk reciprocal lattice) defines the \mathbf{k}_\perp -space periodicity of the surface unit cell. In real space, equivalent surface cuts are separated by $\frac{2\pi}{|\mathbf{G}|} = 2.35 \text{ \AA}$. Due to the monoclinic cell, these equivalent planes are shifted parallel to the surface, however.

In principle, two distinct surface terminations are feasible. On the carbon terminated (1×1) surface, a total of six dangling bonds exist in the ideal configuration. In particular, one finds that four of these dangling bonds are associated with two two-fold coordinated carbon atoms. The remaining two carbon atoms are three-fold coordinated and

consequently show one dangling bond each, which is oriented almost perpendicular to the surface. In contrast to the carbon terminated surface, a silicon terminated surface cut contains two one-fold instead of three-fold coordinated silicon atoms. This leads to a significant increase of the number of free dangling bonds on this surface to ten. It can be assumed that the ground-state configuration of the 4H-SiC($1\bar{1}02$)- $c(2\times 2)$ surface is the carbon terminated structure.

Top and side views of the ideal carbon-terminated 4H-SiC($1\bar{1}02$) surface are shown in Fig. 5.13(a). Only the outermost Si-C double-layer is indicated. Carbon and Si atoms reside on the top and second layer, respectively. The calculated lattice constants $a = 3.11$ and $c = 10.17$ Å overestimate the experimental values [57] of 3.07 and 10.05 Å by about 1%, as is usual within GGA. Accordingly, an overestimate of this order occurs in the surface structure parameters, as well. Viewed along the $[\bar{1}101]$ direction, the surface consists of alternating stripes characteristic for the cubic 3C-SiC(001) and the hexagonal 6H-SiC(0001) surfaces. The respective stripes are separated by dashed lines in the top and side views and indicated by the labels c (for cubic) and h (for hexagonal) in the side view. The top view of the Si-C double-layer shows hexagons within the hexagonal stripes. They are formed by three C and three Si atoms on the top and second layer, respectively. The top-layer C atoms are three-fold coordinated to Si sublayer atoms. Consequently, they have only one dangling-bond which is almost perpendicular to the surface. In the cubic stripes, the top-layer C atoms are two-fold coordinated to Si sublayer atoms. They have two dangling bonds which lie in the $[\bar{1}\bar{1}20]$ - $[1\bar{1}02]$ plane. The red dashed diamond indicated in Fig. 5.13(a) shows a $c(2\times 2)$ unit cell which applies to the reconstructed surfaces to be discussed below. The ideal surface has twelve dangling bonds in the $c(2\times 2)$ mesh (eight in the two cubic sections and four on the two hexagons). This is energetically very unfavorable so that the ideal surface reduces the number of its dangling bonds by an appropriate reconstruction. Both Si adatom adsorption and carbon dimerization are conceivable to this end because they can lead to a significant dangling-bond reduction.

As to the hexagonal stripes, it is well-known from related reconstructions of the SiC(000 $\bar{1}$) surface, that adsorption of Si adatoms can lead to an efficient saturation of carbon dangling bonds [70, 95, 96]. A Si atom may adsorb in a *hollow* site above the center of a hexagon establishing three bonds to its carbon neighbors on the top layer (H3 site) or *on top* of a second layer Si atom where it has four neighbors (T4 site), the three C atoms on the top layer and the Si atom underneath on the second layer. Obviously, the ideal surface has two equivalent H3 and two equivalent T4 sites in the $c(2\times 2)$ unit cell which are marked by the positions H_1 and H_2 or T_1 and T_2 , respectively, in Fig. 5.13(a).

Concerning the cubic stripes, it is likewise well-known from related reconstructions of the C-terminated cubic SiC(001) surface that carbon dimerization reduces the number of dangling bonds significantly [79, 80, 82, 97–101]. The most favorable atomic structure of this surface [80, 82, 98, 101] turned out to be a staggered configuration of triple-bonded

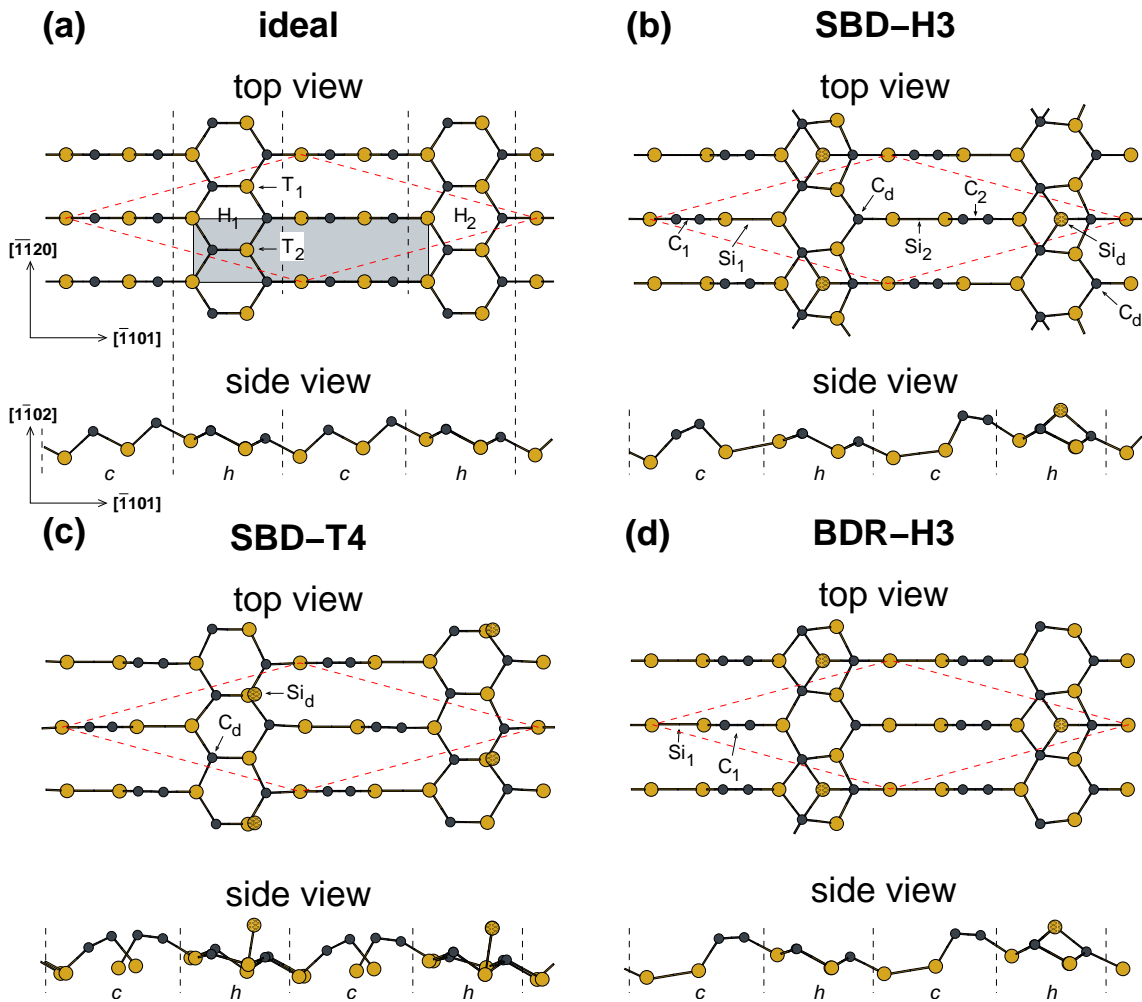


Figure 5.13: Top and side views of different reconstruction models of the 4H-SiC($1\bar{1}02$)- $c(2\times 2)$ surface: (a) ideal surface, (b) and (c) staggered bridging-dimer (SBD) model with the Si adatom in H3 or T4 position, respectively, as well as (d) bridging-dimer row (BDR) model with Si adatom in H3 position. Si and C surface atoms are represented by ochre (light gray) and black circles, respectively. The Si adatom is additionally marked by a crosshatching. The side views in (b) to (d) contain almost exclusively only the projected atoms from the unit cell. For the definition of the labels, see text. The grey shaded area equals the (1×1) surface unit indicated in Fig. 5.12.

carbon dimers each of which bridges two Si atoms on the second layer forming the so-called bridging dimer (BD) model. This structure was found to be very close in total energy [79, 82, 99–101] to the so-called dimer row (DR) model which features rows of double-bonded carbon dimers in its top layer. These structures have been discussed in detail in Chapter 4.2. From the top view of Fig. 5.13(a) it is apparent that on 4H-SiC($1\bar{1}02$) triple-bonded carbon dimers can form along the $[\bar{1}101]$ direction bridging two second-layer Si atoms. On the other hand, dimers can also form along the perpendicular $[\bar{1}\bar{1}20]$ direction. In this case, they become double-bonded since each carbon dimer atom is bound to two Si atoms on the second layer.

Consequently, the different possibilities for separate reconstructions in the hexagonal and cubic stripes of the fairly large c(2×2) unit cell give rise to a large variety of conceivable structural models of the 4H-SiC($1\bar{1}02$)-c(2×2) surface which will be addressed separately in the following.

Reconstructions with triple-bonded carbon dimers

First, bridging dimer reconstruction models one of which has been proposed by Virojandara *et al.* [90] on the basis of their experimental data will be analyzed. From an analysis of LEED intensities and STM images of 4H-SiC($1\bar{1}02$)-c(2×2) in comparison with those of a nearly stoichiometric 6H-SiC($000\bar{1}$)-(2 \times 2) surface, the authors have inferred that a single Si adatom adsorbs in an H3 site above the center of one of the two hexagons in the unit cell. Concerning the cubic facets, they have assumed that a staggered pattern of bridging dimers closely related to the energetically favorable BD model of the cubic SiC(001)-c(2×2) surface exists on the 4H-SiC($1\bar{1}02$)-c(2×2) surface, as well. The structure of this model has been optimized by total energy minimization. To this end, the Si adatom is placed in an H3 site above the right hexagon (position H₂) in the unit cell. The resulting reconstruction model is shown by a top and a side view in Fig. 5.13(b). The Si adatom in the H3 site binds to the three subjacent C atoms in a tripod-like configuration fully saturating their dangling bonds. As a consequence, only one unsaturated dangling bond, which is basically perpendicular to the surface, remains on the Si adatom. Correspondingly, the Si adatom is labeled as Si_d in Fig. 5.13(b). On the other hexagon in the unit cell only the dangling bond of the C atom that is not directly affected by Si adsorption [see Fig. 5.13(b)] remains unsaturated. It is also largely perpendicular to the surface. This C atom is labeled as C_d in Fig. 5.13(b), therefore. In the following the hexagon with an adsorbed Si atom will be addressed as an *occupied* and that without a Si adatom as an *empty* hexagon. Note that by translational symmetry the Si_d and C_d atoms reside on neighboring hexagons of the structure [see Fig. 5.13(b)]. By this specific Si adsorption, the positions H₁ and H₂ at the ideal surface become inequivalent so that the reconstruction has c(2×2) symmetry.

On the cubic stripes there are two carbon dimers per unit cell [labeled C_1 and C_2 in Fig. 5.13(b)] bridging second-layer Si atoms. They are inequivalent due to their different positions in the unit cell. By symmetry, these dimers form a staggered bridging dimer structure (SBD). The respective full reconstruction with the Si adatom in an H3 site is referred to from now on as SBD-H3 model. The first carbon dimer C_1 is formed in the left half of the left while the second carbon dimer C_2 is formed in the right half of the right cubic stripe. This arrangement is called a l/r dimer configuration if necessary for clarity. Obviously, not only the l/r dimer configuration but also a r/l configuration (not shown in Fig. 5.13), as well as a r/r [see Fig. 5.13(d)] and a l/l configuration (not shown in Fig. 5.13) are compatible with the $c(2\times 2)$ symmetry constituting conceivable reconstructions of 4H-SiC($1\bar{1}02$)- $c(2\times 2)$, as well. The latter two structures feature bridging dimer rows (BDR) along the $[\bar{1}\bar{1}20]$ direction and are labeled BDR-H3 reconstructions, therefore. The appearance of two bridging carbon dimers per unit cell on the top layer of these four models is accompanied by the formation of two Si dimers on the second layer which are indicated as Si_1 and Si_2 in Fig. 5.13(b). They have different distances to the filled and empty hexagons in the different models and their bonds are fully saturated. The triple-bonded bridging carbon dimers have no dangling bonds because three of the valence electrons of each involved C atom fill the $C\equiv C$ dimer bonds while the remaining valence electron establishes a bond to a Si atom on the second layer. As a consequence, there remain only two dangling bonds per $c(2\times 2)$ unit cell, one on the surface carbon atom C_d and the other on the adatom Si_d . Thus, by these reconstructions the total number of dangling bonds is drastically reduced from twelve at the ideal to only two at the reconstructed surfaces giving rise to a correspondingly large energy gain.

Respective reconstruction models with Si adatoms adsorbed in T4 sites need to be considered, as well. Figure 5.13(c) shows one such model resulting when the Si adatom is placed in position T_1 [cf. Fig. 5.13(a)] and the carbon dimers are distributed as in the SBD-H3 model in Fig. 5.13(b). Correspondingly, this model is labeled SBD-T4. The two possible positions T_1 and T_2 in Fig. 5.13(a) for T4 adsorption remain equivalent after forming bridging dimers in the cubic stripes since the mirror symmetry with respect to the central atomic line of the unit cell along the $[\bar{1}101]$ direction is preserved. Therefore, it is irrelevant whether the Si adatom is placed in the T_1 or T_2 position. Note that the Si_d and C_d atoms now reside on the same hexagon. Actually, Fig. 5.13(c) shows the l/r SBD-T4 model. Apparently, also for T4 adsorption of Si, the three complementary models with r/l , r/r and l/l distributions of the carbon dimers are compatible with the $c(2\times 2)$ symmetry. The latter two models again feature bridging dimer rows and are labeled BDR-T4 models, accordingly. In total, eight unique reconstruction models have been specified so far, which involve four different configurations of triple-bonded bridging carbon dimers on the cubic stripes and Si adatoms in either H3 or T4 sites on the hexagonal stripes of the surface.

model	BD conf.	d_{Si_1}	d_{Si_2}	d_{C_1}	d_{C_2}	ΔE	$E_{\text{g}}^{\text{SIC}}$	$E_{\text{g}}^{\text{GGA}}$
Triple-bonded staggered bridging dimers (SBD)								
or bridging dimer rows (BDR)								
SBD-H3	l/r	2.61	2.57	1.23	1.24	0.00	1.34	0.14
SBD-H3	r/l	2.55	2.51	1.23	1.24	-0.64	1.29	0.46
BDR-H3	l/l	2.47	2.37	1.22	1.23	-0.61	1.65	0.36
BDR-H3	r/r	2.48	2.46	1.22	1.22	-0.81	1.37	0.20
SBD-T4	l/r	2.60	2.56	1.23	1.23	0.25	1.49	0.06
SBD-T4	r/l	2.60	2.56	1.23	1.23	0.25	1.49	0.06
BDR-T4	l/l	2.44	2.44	1.22	1.22	-0.01	1.52	0.09
BDR-T4	r/r	2.48	2.48	1.22	1.22	-0.30	1.19	0.02
Double-bonded staggered dimers (SD) or dimer pairs (DP)								
SD-H3				1.38	1.38	-1.73	1.53	0.28
DP-H3				1.38	1.38	-2.08	1.49	0.26
SD-T4 ₁				1.38	1.39	-0.75	1.42	metallic
DP-T4 ₁				1.38	1.37	-1.74	1.29	metallic
SD-T4 ₂				1.38	1.38	-1.50	1.37	0.04
DP-T4 ₂				1.38	1.38	-1.23	1.42	0.02
Bridging dimer (BD) or dimer row (DR) reconstructions of 3C-SiC(001)								
BD c(2×2)		2.42		1.23		-0.11	2.46	1.24
DR p(2×1)				1.39		0.00	0.99	metallic

Table 5.2: Dimer bond-lengths (in Å) and total energy differences per unit cell ΔE (in eV) of different reconstruction models of 4H-SiC($1\bar{1}02$)-c(2×2) referred to the energy of the l/r SBD-H3 model as resulting from GGA calculations. Respective data for the bridging dimer and dimer row models of the cubic SiC(001) surface from Wang *et al.* (Ref. [82]) are given for reference. In this case, ΔE is referred to the DR model. In addition, surface band gaps (in eV) as calculated using self-interaction-corrected (SIC) pseudopotentials are listed together with respective GGA band gaps. For further details, see text.

In Table 5.2, calculated bond lengths of carbon and Si dimers, as well as total energies of the different bridging dimer models are summarized. The latter are referred to the total energy of the l/r SBD-H3 model. The carbon dimer bond lengths in all four H3 models are near 1.23 Å, which is very close to respective bond lengths of triple-bonded carbon dimers in acetylene (C_2H_2) or in the BD model of $\text{SiC}(001)\text{-c}(2\times 2)$ (see Table 5.2). The Si dimers on the second layer adjust their bond lengths accordingly. Due to the existence of cubic and hexagonal sections in the large unit cell of $4\text{H-SiC}(1\bar{1}02)\text{-c}(2\times 2)$ the Si dimer bond lengths are larger at this surface than at the $\text{SiC}(001)\text{-c}(2\times 2)$ surface (cf. Table 5.2). Among the bridging dimer H3 models the l/r SBD-H3 reconstruction, suggested previously [90], turns out to be the least favorable. The other three dimer configurations lead to considerably lower total energies. The different distances of the top-layer carbon and second-layer Si dimers to the empty and occupied hexagons, on the one hand, as well as the different bond lengths of the second-layer Si dimers in the four models, on the other hand, account for the differences in total energy. For example, the l/r SBD-H3 structure exhibits the largest bond lengths of the Si dimers Si_1 and Si_2 rationalizing why this structure has the highest total energy. Respective results for the T4 models are given in Table 5.2, as well. In this case, the l/r and r/l configurations of the SBD model are equivalent by symmetry. Again, the staggered model (SBD-T4) has the highest total energy because it features the largest bond lengths of the Si dimers on the second layer, as well. All T4 models have total energies that are considerably higher than those of the corresponding H3 models. The former are thus less favorable than the latter with the only exception of the r/r BDR-T4 model which is lower in total energy by 0.3 eV than the l/r SBD-H3 model. Thus, it appears fairly unlikely that a bridging carbon dimer configuration combined with Si adatoms in T4 sites occurs at the $4\text{H-SiC}(1\bar{1}02)\text{-c}(2\times 2)$ surface. This conclusion is consistent with the experimental evidence [90].

Reconstructions with double-bonded carbon dimers

In the previous section, triple-bonded bridging carbon dimers have been considered as building blocks for the reconstructions. However, double-bonded carbon dimers are comparably conceivable at $4\text{H-SiC}(1\bar{1}02)\text{-c}(2\times 2)$. The related BD and DR row reconstructions of $\text{SiC}(001)\text{-c}(2\times 2)$ differ only slightly in total energy by some 0.1 eV [82, 101] which does not necessarily mean that triple-bonded carbon dimers are also more favorable at the much more complex $4\text{H-SiC}(1\bar{1}02)\text{-c}(2\times 2)$ surface. Therefore, one should also consider reconstruction models featuring double-bonded carbon dimers. From Fig. 5.13(a) it is obvious that neighboring two-fold coordinated surface C atoms can easily tilt along the $[\bar{1}\bar{1}20]$ direction towards each other until their free dangling bonds establish a dimer bond. Neither bond breaking nor bond-length changes are involved. The resulting $\text{C}=\text{C}$ dimers can again arrange in staggered or row configurations.

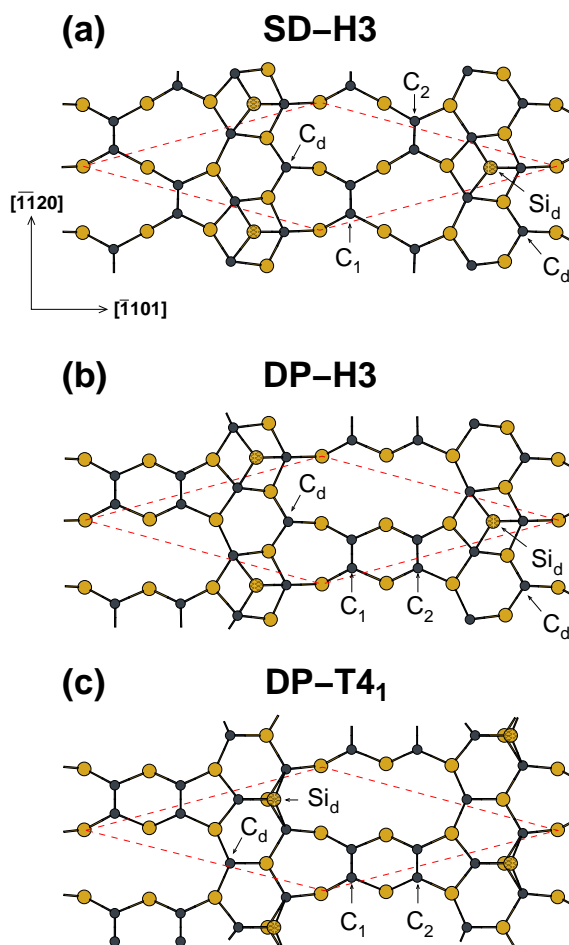


Figure 5.14: Top views of different reconstruction models of the 4H-SiC($1\bar{1}02$)-c(2×2) surface: (a) staggered-dimer (SD) and (b) dimer-pair (DP) models with the Si adatom in H3 position, (c) dimer-pair (DP) model with the Si adatom in T4₁ position. For further details, see text and caption of Fig. 5.13.

Fig. 5.14 shows top views of three exemplary reconstructions involving double-bonded carbon dimers. In Fig. 5.14(a) the carbon dimers form staggered dimer (SD) patterns and the Si adatoms occupy H3 sites (SD-H3). The reconstruction shown in Fig. 5.14(b) features dimer pairs (DP) with the Si adatom in the same H3 site, as before (DP-H3). In both of these models there are two possible configurations of the dimers in the two halves of the unit cell but they are equivalent by symmetry. So there are only two unique H3 structures. The double-bonded carbon dimers are symmetric and there are no Si dimers on the second layer of these structures. The formation of double-bonded dimers does not conserve the mirror symmetry of the ideal surface mentioned above. Consequently, the positions T₁ and T₂ [see Fig. 5.13(a)] for Si adatom adsorption in a T4 site are no longer equivalent. Thus, one has to differentiate between models with Si adatoms adsorbed in a T₁ or a T₂ position, respectively, which are labeled T4₁ [as shown in Fig. 5.14(c)] or T4₂ models, accordingly. Also in both of these cases, there are only two unique structures (SD and DP) by symmetry.

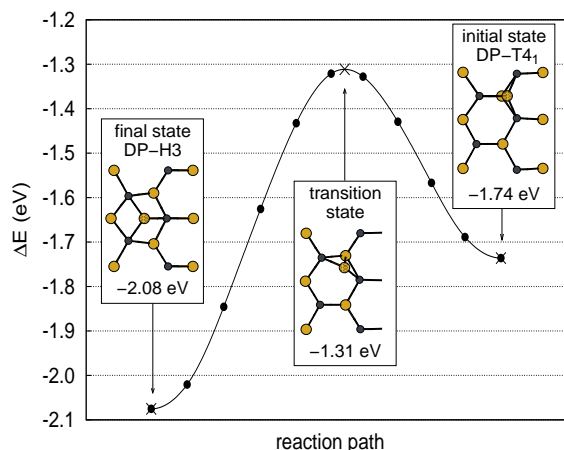
The carbon dimer bond lengths and total energies of the respective six reconstruction

models are also listed in Table 5.2. The bond lengths of the carbon dimers in all models result basically as 1.38 Å as is typical for C=C double-bonds well known from ethane (C_2H_4) or the related DR model of the SiC(001)- $p(2\times 1)$ surface (cf. Table 5.2). Energetically, both the SD-H3 and DP-H3 models turn out to be substantially more favorable than any of the bridging-dimer models discussed above. Their energy differences with respect to the l/r SBD-H3 model amount to about 1.73 (SD-H3) and 2.08 eV (DP-H3), respectively. The difference in total energy of 0.35 eV between these two models originates from different relaxations in the subsurface layers. The respective T4 models are again all higher in total energy than their H3 counterparts. Nevertheless, most of them have total energies that are more than 1 eV lower than those of the respective SBD-T4 and BDR-T4 models, discussed in the previous section.

Thus, most of the reconstruction models with double-bonded carbon dimers turn out to be more favorable than those involving triple-bonded bridging carbon dimers in the cubic stripes of the surface. Double-bonded carbon dimers can easily form without bond breaking or bond-length changes, as described above. The formation of triple-bonded bridging carbon dimers, on the contrary, necessitates breaking three Si–C bonds and forming three new bonds (one carbon dimer bond at the surface, one Si dimer bond on the second layer and one Si–C bond between the top and second layer). As a consequence, a very delicate balance between the energy loss and gain involved in breaking three original and forming three new bonds, respectively, determines which reconstruction mechanism is more favorable. At the SiC(001) surface, the balance is slightly in favor of the triple-bonded bridging dimers because of the highly symmetric environment both perpendicular and parallel to the surface. In contrast, the 4H-SiC($1\bar{1}02$)- $c(2\times 2)$ surface is not only different because it exhibits alternating cubic and hexagonal stripes parallel to the surface but also because it has a considerably more complex structure perpendicular to the surface. This much more complex environment and the intricate interactions between the atoms on the respective stripes and in the surface layers result in a different energetic order of configurations with triple-bonded bridging versus double-bonded carbon dimers on 4H-SiC($1\bar{1}02$)- $c(2\times 2)$ than on the purely cubic SiC(001) surface.

On the basis of the structure optimization results for the fourteen considered reconstruction models one must conclude that the DP-H3 model constitutes the most favorable reconstruction of the 4H-SiC($1\bar{1}02$)- $c(2\times 2)$ surface. Virojanadara *et al.* [90] have reported C1s and Si2p core level spectra of the surface. They observed one shifted component in the C1s and two shifted components in the Si2p spectra, respectively. These surface-induced shifts were interpreted in terms of the configuration of surface features in the SBD-H3 model. The same reasoning would apply to the DP-H3 model, so that one can not identify any model-discerning features from a comparison with the core level spectra. Finally, a more subtle point concerning the surface reconstruction shall be addressed. From a purely thermodynamics point of view the DP-H3 model is the most favorable

Figure 5.15: Minimum energy pathway (in eV) for the conversion from the initial DP-T4₁ to the final DP-H3 structure of the 4H-SiC($1\bar{1}02$)-c(2×2) surface. The insets show top views of the surface atomic structure around the occupied hexagon. For details, see text.



reconstruction. Yet, it is conceivable that under experimental surface preparation conditions [90], the Si adatoms might adsorb in metastable T4 sites. The question then arises whether the T4 reconstructions are thermodynamically stable or whether they convert from a metastable T4 to the more stable H3 structure. To additionally investigate the possibility of such structural conversions between different conceivable reconstructions respective minimum-energy pathways (MEPs) are determined using the quadratic string (QS) method as presented by Burger and Yang in Ref. [102]. The QS method is based on the same idea as the nudged elastic band method [103] but it differs from the latter by integrating the perpendicular forces on the tangents of the reaction pathway numerically using a quadratic expansion of the potential energy surface [104].

As an example, Fig. 5.15 shows the MEP from the DP-T4₁ to the DP-H3 reconstruction. The local atomic structure around the occupied hexagon is shown in the insets for the initial, transition and final states. Initially, the adatom moves from the T4₁ towards the H3 position stretching its bond to the upper C atom (cf. Fig. 5.15) and compressing its bonds to the other two C atoms. This process obviously involves a steady energy loss. When the Si atom has arrived in the transition state, its bond to the upper C atom has become broken. Moving further to the final state, the adatom continuously gains energy until it eventually occupies the H3 site. In the final state it forms three covalent bonds with the three subjacent C atoms. Obviously, there is an energy barrier of about 0.4 eV that needs to be overcome by the Si adatom on its MEP from the T4₁ to the H3 site. One finds similar barrier energies for respective T4 ↔ H3 conversions of other reconstruction models addressed in this work. In view of the fact, that Si adatoms that may adsorb initially in local minimum T4 sites have sufficient time and energy at high surface preparation temperature to surmount a barrier of 0.4 eV, one can consider it unlikely that Si adatoms are observed in T4 sites when the surface is eventually investigated at room temperature. Structural conversions from models with double-bonded dimers to models with triple-bonded bridging dimers have been analyzed, as well. For example, for the conversion

from the SD-H3 to the l/r SBD-H3 model a barrier of some 1.9 eV is found corroborating that a large energy is involved in creating bridging dimers in the cubic stripes of the 4H-SiC($1\bar{1}02$)- $c(2\times 2)$ surface.

5.2.2. Electronic structure

The electronic properties of all reconstruction models optimized in Sec. 5.2.1 has been investigated employing self-interaction-corrected pseudopotentials. For shortness sake, only the surface band structures of the energetically most favorable DP-H3 and DP-T4₁ models, as well as the l/r SBD-H3 model proposed by Virojanadara *et al.* [90] are presented and discussed. Figure 5.16(a) shows the surface Brillouin zone (SBZ) and the respective surface band structures resulting from the SIC- Δ calculations are plotted in (b) to (d) within an energy range near the fundamental gap from -3 to 5 eV. The grey shaded areas in the band structure plots indicate the projected bulk band structure of 4H-SiC($1\bar{1}02$). Based on a Mulliken analysis, bands originating from Si or C surface dangling bonds are marked by ochre (light gray) and black triangles, respectively. Bands originating from the Si dimers Si₁ and Si₂ on the second layer of the SBD-H3 model are denoted by open and full ochre (light gray) circles in (d) while bands originating from the top layer carbon dimers C₁ and C₂ are indicated by open and full black circles in (b) to (d), respectively. Since the available photoemission data is limited to the gap energy region [90], the band structure is only shown in the energy range from -3 to +5 eV. It can be noted in passing that all three band structures exhibit weakly dispersing C 2s surface bands near the lower edge of the projected carbon bulk bands around -15 eV and weakly dispersing *p*-type surface bands within the ionic gap around -10 eV. The fundamental band gaps of all reconstructions investigated are given in Table 5.2.

The carbon dimers of the DP-H3 model give rise to bonding (C_{1,2}) and antibonding (C_{1,2}^{*}) bands close to the upper and lower edges of the projected valence and conduction bands, respectively [see Fig. 5.16(b)]. The dangling bonds on the C_d and Si_d surface atoms yield dangling-bond bands which are also labeled C_d and Si_d, for simplicity. These bands show only weak dispersions due to the weak interaction of the respective dangling bonds. The C_d band is occupied while the Si_d band is empty. Charge density contours of respective surface states at the *Y'* point of the SBZ, shown in Figs. 5.17(a) to (d), confirm the above assignments. The main contribution to the Si_d state originates from the empty dangling bond at the Si adatom in H3 position [see Fig. 5.17(a)] but there are also contributions at the three subjacent C atoms (only one lies in the drawing plane). The dominant contribution to the C_d state apparently comes from the occupied dangling bond at the C_d surface atom [see Fig. 5.17(b)]. The charge density in Fig. 5.17(c) clearly exhibits the bonding character of the C₁ state while the charge density in Fig. 5.17(d) shows a nodal plane between the two C atoms of the C₁ dimer confirming the antibonding character of the C₁^{*}

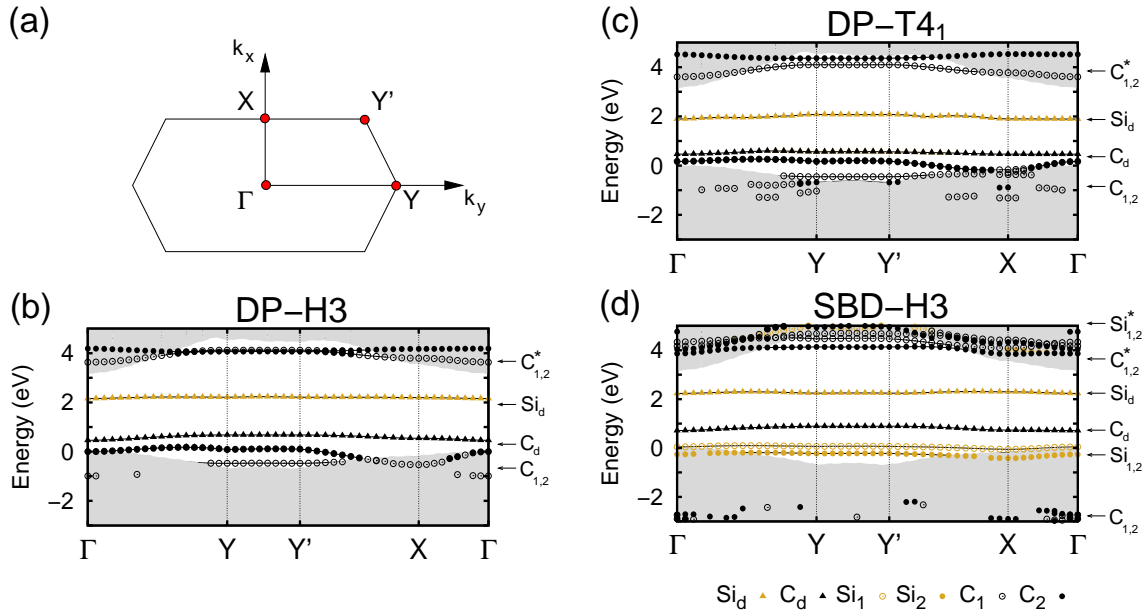


Figure 5.16: Surface Brillouin zone (a) and sections of the band structures of the DP-H3 (b), DP-T4₁ (c) and the l/r SBD-H3 (d) models, as resulting from SIC- Δ calculations. Bands that can uniquely be assigned to Si or C atoms are marked by ochre (light gray) and black symbols. Triangles represent bands originating from surface atoms featuring dangling bonds while open and filled circles represent bands originating from Si and carbon dimers.

state.

The DP-T4₁ model exhibits largely similar surface bands [see Fig. 5.16(c)]. Those originating from the bonding and antibonding states of the carbon dimers are only slightly affected by the change of the Si adsorption site from H3 to T4₁. Only the splitting of the $C_{1,2}^*$ dimer bands is somewhat larger than in the DP-H3 band structure which appears to be due to the structural differences in the hexagonal stripes of the DP-T4₁, as compared to the DP-H3 model [cf. Fig. 5.14(b) and (c)]. The charge densities of respective states are very similar to those of the DP-H3 model and not shown, therefore.

The band structure of the SBD-H3 model in Fig. 5.16(d) shows two characteristic differences to the former band structures. On the one hand, the bonding and antibonding bands originating from the triple-bonded $C\equiv C$ dimers occur lower and higher in energy, respectively, than in the DP models whose $C=C$ bonds are comparatively weaker. In addition, the SBD-H3 model features Si dimers on the second layer (not occurring in the DP models) which give rise to two bonding dimer bands indicated as $Si_{1,2}$ residing slightly above the projected bulk valence bands and two antibonding dimer bands indicated as $Si_{1,2}^*$ which are close in energy to the antibonding bands of the carbon dimers. The charge density in Fig. 5.17(e) confirms this assignment showing that a large contribution to the Si_1 state originates from the Si_1 dimer. In addition, admixtures from the neighboring C

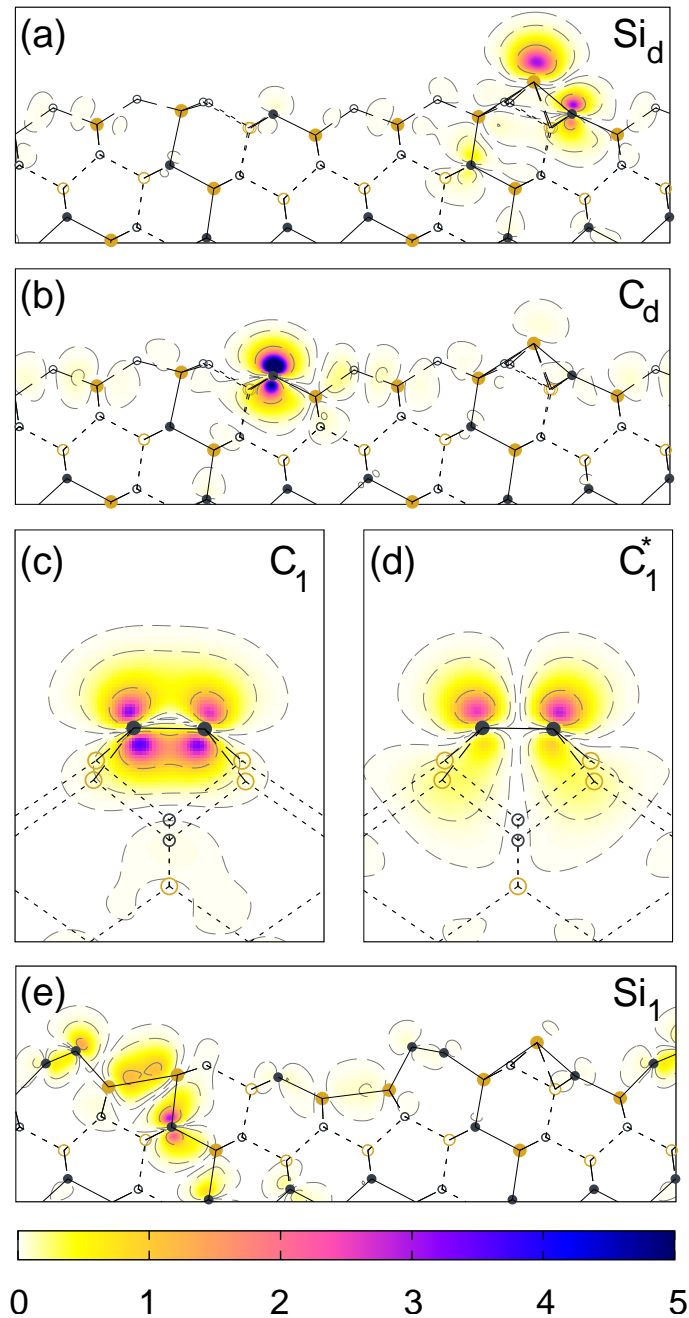


Figure 5.17: Charge density contours (in $10^{-2} a_B^{-3}$) of the Si_d , C_d , C_1 , C_1^* and Si_1 states at the Y' point of the SBZ. Si and C atoms are depicted by ochre (light gray) and black dots, respectively. Filled (open) symbols represent atoms within (outside) the drawing pane. Panels (a) to (d) show charge densities of the DP-H3 model of 4H-SiC($1\bar{1}02$)- $c(2\times 2)$ surface while (e) shows one charge density of the SBD-H3 model. Panels (a), (b) and (e) are plotted in the $[\bar{1}101]$ - $[1\bar{1}02]$ plane while panels (c) and (d) are plotted in the $[\bar{1}\bar{1}20]$ - $[1\bar{1}02]$ plane containing the carbon dimer C_1 .

atom on the next subsurface layer, as well as from the C_1 dimer at the top layer contribute to this state.

The ARUPS data presented in Ref. [90] exhibit a band gap of at least 1 eV and four occupied bands (labeled S1-S4) which were tentatively interpreted as resulting from surface states or surface resonances since they were found to be more sensitive to surface contamination than other measured valence band features. Only the band S1, which occurs highest in energy, could clearly be identified as a surface state band since it appears in the projected bulk band gap. It has a very weak dispersion of 0.1 ± 0.05 eV, only. The other three bands show more pronounced dispersions in sections of the SBZ. For example, the band S2, observed 0.7 eV below the S1 band at Γ , exhibits a dispersion of 0.55 eV from the Y to the X point. It was assigned to the Si adatoms on the hexagonal stripes. Since the valence band maximum (E_{VBM}) could not be identified in experiment, the bands S2-S4 could not definitely be attributed to particular surface states or resonances. The surface band structures are referred to E_{VBM} . Therefore, one can not directly compare them with the ARUPS data on an absolute energy scale. Nevertheless, it appears fairly clear that the band S1 observed in experiment originates from the weakly dispersing occupied carbon dangling bond band C_d resulting in all three band structures [see Figs. 5.16(b) to (d)]. Likewise, all three calculated band structures show surface band gaps larger than 1 eV (cf. Table 5.2) which is consistent with the experimentally determined gap, as well. The interpretation of the S2 band suggested in Ref. [90] as resulting from the Si adatoms on the hexagonal stripes, contradicts the results of the present calculations in that the dangling bonds on the Si adatoms are empty, as noted above. There are, however, groups of occupied bands ($C_{1,2}$ or $\text{Si}_{1,2}$, respectively) below the C_d band in the band structures of the DP-H3 and SBD-H3 models [see Figs. 5.16(b) and (d)] which could be related to the measured S2 band. The $C_{1,2}$ bands in the band structure of the DP-H3 model in fact occur only about 0.5 eV below the C_d band at Γ , but their dispersion of 0.55 eV is in excellent agreement with experiment. The $\text{Si}_{1,2}$ bands of the SBD-H3 model indeed occur 0.7 eV below the respective C_d band, which would be in agreement with experiment, but they actually show only a very weak dispersion in contradiction to experiment. As to the measured bands S3 and S4, there are no direct counterparts in the calculated band structures [see Figs 5.16(b) to (d)]. The energy range from 0 to -3 eV has been scrutinized looking for pronounced surface resonances but none could be identified. This discrepancy could be related to bulk states with a small k_{\perp} dispersion giving rise to uncertainties in the band-mapping carried out in experiment [90]. To this end the bulk band structure of 4H-SiC for k_{\perp} along the surface normal has been calculated as shown in Fig. 5.18. As a matter of fact, two groups of rather flat bulk bands are found in the energy region in question.

In general, the calculations in this work yield band gaps for all fourteen presented models of the 4H-SiC($1\bar{1}02$)-c(2×2) surface in the range of 1.19 to 1.65 eV (cf. Table 5.2). They are fairly similar due to the similar nature of the states forming the gap and all of them

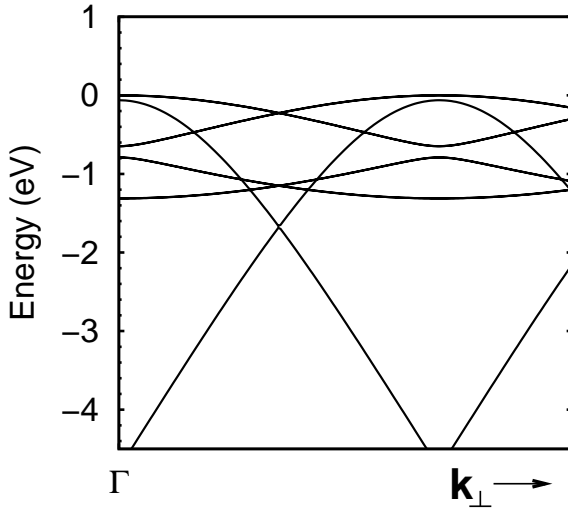


Figure 5.18: Band structure of bulk 4H-SiC for k_{\perp} along the surface normal of 4H-SiC($1\bar{1}02$)- $c(2\times 2)$. On this energy scale, two only weakly dispersing groups of bands can be identified.

are consistent with the gap estimated from photoemission [90]. This corroborates that band gaps alone are not suitable to discern between different reconstruction models by comparison with experiment for the surface at hand.

5.2.3. Scanning tunneling microscopy

Scanning Tunneling Microscopy (STM) makes use of the physical phenomenon of electrons tunneling through a barrier. In the particular situation as depicted in Fig. 5.19, a thin metallic tip is positioned at a distance d in the order of a couple of Å from a sample surface. The electronic wave functions of the probe and the sample overlap. If one applies a bias voltage V to this system, a tunneling current I flows. The magnitude of the current depends on the overlap of the wave functions and thus is a function of the distance d . A simple estimate for the current is based on the assumption of a one-dimensional tunneling effect between two planar electrodes. In the case of a small voltage, i.e. much smaller than the work function W , it holds that

$$I \sim V \exp(-2\kappa d), \quad (5.12)$$

with $\kappa = \hbar^{-1}\sqrt{2mW}$. It is apparent that the tunneling current decreases by roughly an order of magnitude if the distance is increased by 1 Å. This leads to a possible vertical resolution of about 0.01 Å, while the lateral resolution is determined by the dimension of the tip.

A three-dimensional sampling of the surface can be achieved by moving the tip parallel to the surface. Two basic operational modes can be used:

1. *Constant Current Mode*

In the Constant Current Mode, the vertical position of the tip is adjusted at each

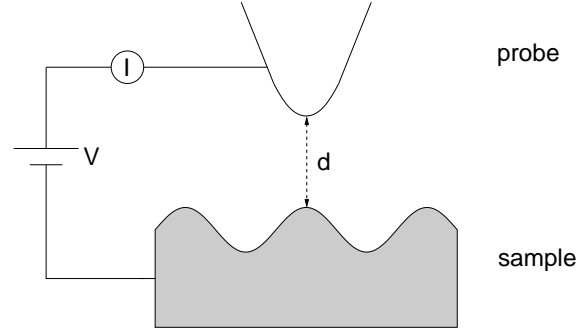


Figure 5.19: Schematic setup of a scanning tunneling microscope.

sampled position parallel to the surface such that the tunneling current remains constant. The image of the surface is determined by the respective tip position $z(x, y)$.

2. Constant Height Mode

If the STM is operated in the Constant Height Mode, the vertical position z is kept constant and the tunneling current $I(x, y)$ is measured as a function of the lateral position. Typically this is only suitable for comparatively smooth surfaces.

For any detailed interpretation of such images the simple model used above based on two planar electrodes is not realistic enough. A more sophisticated approach is that of Tersoff and Hamann [105]. Here the tip is assumed to be a small sphere located at the position \mathbf{r}_0 . The tunneling current follows as

$$I \sim \sum_{\nu} |\psi_{\nu}(\mathbf{r}_0)|^2 \delta(E_{\nu} - E_F - eU) \approx n(\mathbf{r}_0, E_F - eU) , \quad (5.13)$$

where $\psi_{\nu}(\mathbf{r}_0)$ is the wave function of the sample at the position of the tip. Consequently, the current is proportional to the local charge density $n(\mathbf{r}_0, E_F - eU)$ at the surface. Note that depending on the applied voltage U , both occupied and empty states can contribute to this density. The resulting image is a constant local density contour plot. As ψ_{ν} decays exponentially from the surface, the same holds for I . In metals, for which Eq. (5.13) holds, the local density is closely related to the atomic structure of the surface so that a realistic representation of the atomic configuration is achieved. However, for semiconductors, this notion does not directly apply.

When STM images are calculated in the framework of the Tersoff-Hamann approach [105], the constant-current operational mode is simulated by calculating topograms of constant charge density above the surface. To this end, at first the three-dimensional charge density $n(\mathbf{r}, E \pm \Delta E)$ formed by all bands residing in the energy window $E - \Delta E \leq E \leq E + \Delta E$ is calculated. A fixed n_0 is chosen and the topogram, i.e. $z(\mathbf{r}_{\parallel}; n_0, E)$, is determined by solving $n(\mathbf{r}_{\parallel}, z; E) = n_0 = \text{const.}$ by linear interpolation with respect to z for every \mathbf{r}_{\parallel} . As the resulting topogram is very ragged, it is smoothed by

folding it with a Gaussian according to

$$\tilde{z}(\mathbf{r}_{\parallel}; n_0, E) = \frac{\pi}{\alpha} \int e^{-\alpha(\mathbf{r}_{\parallel} - \mathbf{r}'_{\parallel})^2} z(\mathbf{r}'_{\parallel}; n_0, E) d^2 r'_{\parallel} , \quad (5.14)$$

where α is a suitably chosen decay constant. In the following $\alpha = 2$ (in atomic units) has been chosen. $\tilde{z}(\mathbf{r}_{\parallel}; n_0, E)$ is finally plotted and can be compared to experimentally determined STM images.

From the discussion of the band structures of different reconstruction models in Sec. 5.2.2 it has become quite evident that a comparison of the calculated surface band structures with the ARUPS data [90] is not sufficiently instructive to unequivocally conclude which model has actually been observed in experiment. However, the band structures of the DP-H3 and SBD-H3 models in Figs. 5.16(b) and (d) reveal that it is possible to identify other features that might be useful to resolve this question. The carbon dimers giving rise to the antibonding bands $C_{1,2}^*$, residing within the projected bulk band gap region as true surface state bands, are oriented orthogonally in the DP and SBD models, respectively. In addition, antibonding Si dimer bands $Si_{1,2}^*$ occur in the same energy region as the $C_{1,2}^*$ bands of the SBD model, only. It is to be expected, therefore, that empty state STM images at bias voltages corresponding to that particular energy region show characteristic differences for the two models.

In Fig. 5.20 calculated constant-current STM images for specifically chosen empty states of the SBD-H3 and DP-H3 models are shown. The images in the upper (lower) panels were calculated for a bias voltage of 1.5 V (3.7 V, respectively) above the highest occupied surface state with an energy window of $\Delta E=0.25$ eV. At a bias voltage of 1.5 V, only states of the empty Si_d band, which is present in both surface models at the same energy, can contribute to the images. As a consequence, the STM images in the top panels of Fig. 5.20 which only sample the hexagonal stripes are largely similar. The bright protrusions originate from the empty dangling bonds on the Si adatoms in H3 sites and their almost triangular shape arises from the charge-density contributions of the antibonding states of the Si–C bonds to the three subjacent C atoms, as discussed above [cf. Fig. 5.17(a)]. Obviously, the spatial arrangement of the protrusions exhibits the c(2 \times 2) symmetry of the surface. An arrangement of similar protrusions is seen in experiment, as well [90]. This finding corroborates that the dangling bonds at the Si adatoms are empty, indeed, rather than occupied, as conjectured in the interpretation of the ARUPS data [90] (cf. Sec. 5.2.2). Likewise, the vertical and horizontal distances of the bright protrusions results as 6.22 and 11.51 Å from the calculations in good accord with the experimentally determined distances of 6.16 and 11.42 Å, respectively, given the fact that GGA overestimates lattice constants by about 1%. The above results yield only information on the distribution of the Si adatoms on the hexagonal stripes since only states of the empty Si_d band are sampled.

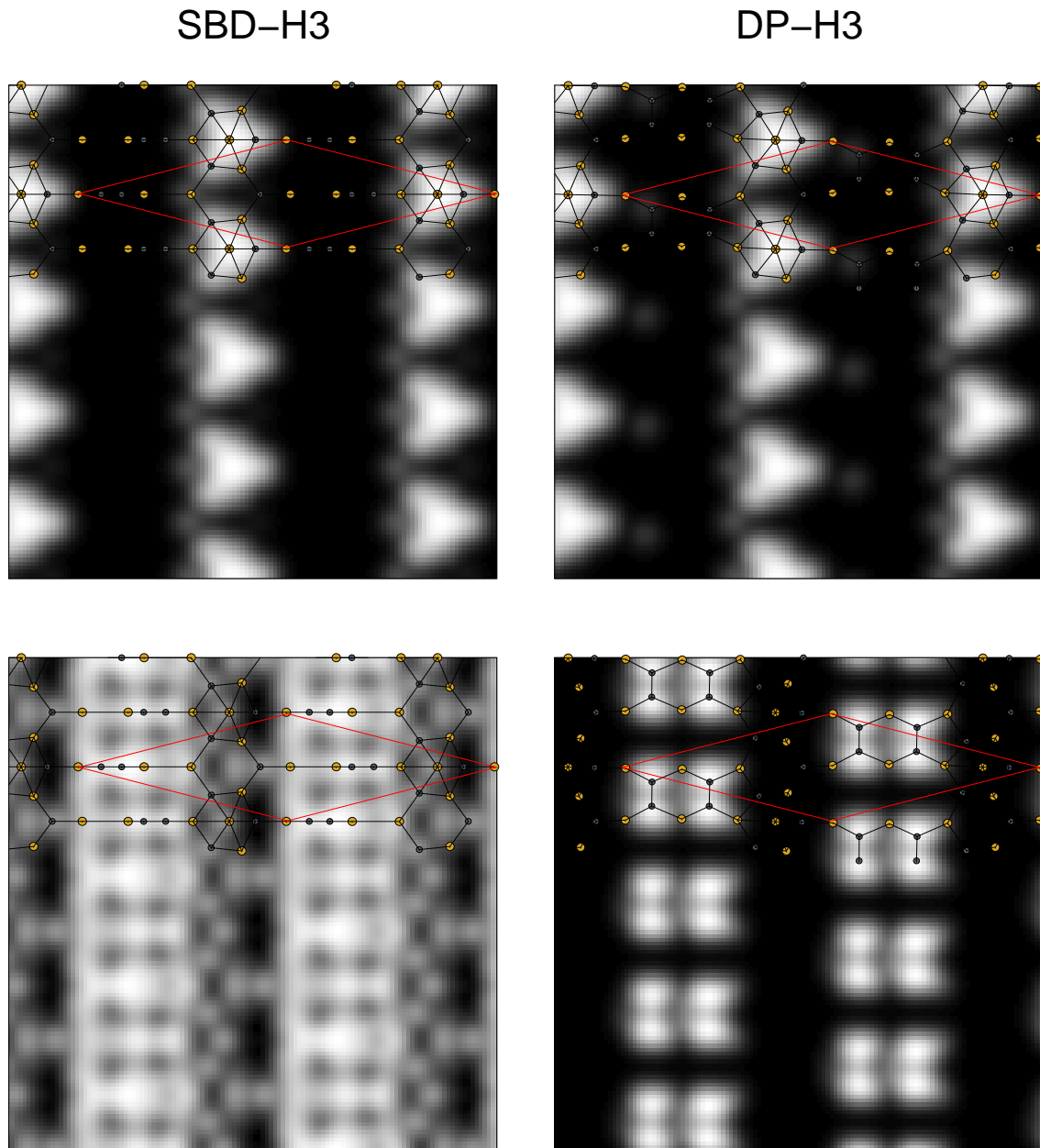


Figure 5.20: Calculated constant-current STM images for empty states of the SBD-H3 (left panel) and DP-H3 (right panel) models of the 4H-SiC($1\bar{1}02$)-c(2×2) surface. The upper and lower panels show images calculated at bias voltages of 1.5 and 3.7 V, respectively, with an energy window of ± 0.25 eV in both cases. One exemplary surface unit cell with the respective atoms is superimposed on both images.

To become more sensitive to the different dimers and their different arrangement on the cubic stripes of the SBD and DP models, STM images for more appropriate ranges of the bias voltage have been calculated. Respective STM images simulated again with an energy window of ± 0.25 eV at a bias voltage of 3.7 V are shown in the lower panels of Fig. 5.20. In these energy ranges the previously mentioned antibonding carbon dimer states $C_{1,2}^*$ are accessible for both reconstructions. Their nature and origin is very different in the two models, as discussed before. As a consequence, entirely different STM images result now sampling the cubic stripes of the surface. Very amazingly, at a first glance, the STM image for the SBD model shows straight rows of somewhat intricate protrusions along the $[\bar{1}\bar{1}20]$ direction, pretending a 2×2 reconstruction, although the carbon dimers are arranged in a staggered pattern. This is due to the fact that not only the antibonding carbon dimer states $C_{1,2}^*$ but also the antibonding Si dimer states $Si_{1,2}^*$ on the second layer [see Fig. 5.16(d)] contribute to this image. Thus, if 4H-SiC($1\bar{1}02$)- $c(2\times 2)$ reconstructs in the SBD-H3 model, an experimental confirmation of the full structure by STM from the subtle intensity variations originating from the antibonding carbon and Si dimer states, respectively, could be very difficult.

In contrast, the respective STM image of the DP-H3 model calculated at 3.7 V turns out to be much more clear-cut. From the lack of Si dimers in this model it follows that the image only contains contributions from the antibonding $C_{1,2}^*$ states of the C=C dimers. As a consequence, the simulated image in the lower right panel of Fig. 5.20 clearly reveals the pair configuration of the double-bonded carbon dimers at the 4H-SiC($1\bar{1}02$)- $c(2\times 2)$ surface. The dimer pairs occur at different heights in the left and right cubic stripes. The nodal plane in the middle of the individual dimer bonds is clearly revealed as was the case in the side view of the charge density in Fig. 5.17(d). Note that the STM image is plotted in a plane orthogonal to the plotting plane of the charge density. The dimer pair arrangement in the DP-H3 model thus gives rise to very localized signals in the calculated STM image.

Given these substantial differences of empty-state STM images in the SBD-H3 and DP-H3 models, experimental images taken at respectively large bias voltages should yield a clear indication of the type of carbon dimers forming on the 4H-SiC($1\bar{1}02$)- $c(2\times 2)$ surface and their spatial arrangement thus allowing for an identification of the surface structure not only in the hexagonal but also in the cubic stripes.

5.3. Summary

The surface atomic and electronic structure of fourteen distinctly different reconstruction models of the 4H-SiC($1\bar{1}02$)- $c(2\times 2)$ surface has been investigated by *ab initio* GGA and SIC calculations, respectively. Si adatom adsorption on the hexagonal stripes of the sur-

face in H3 and T4 positions, as well as a number of configurations of triple-bonded bridging $C\equiv C$ dimers or double-bonded $C=C$ dimers on the cubic stripes have been considered. All reconstruction models investigated exhibit only two surface dangling bonds while the ideal surface has twelve dangling bonds per unit cell. The DP-H3 reconstruction model featuring Si adatoms in H3 sites on the hexagonal stripes and pairs of double-bonded carbon dimers on the cubic stripes is found to be energetically most favorable. The results suggest that Si adatoms which might conceivably adsorb initially in metastable T4 sites convert to the most stable H3 sites during experimental preparation of the surface at high temperature. Therefore, it is not to be expected that Si adatoms are found in T4 sites when the surface is eventually investigated at room temperature. The surface electronic structure of the two energetically most favorable reconstructions (DP-H3 and DP-T4₁) and that of the previously suggested staggered bridging dimer model with Si adatoms in H3 sites (SBD-H3) as calculated using the SIC- Δ approach has been discussed in comparison with ARUPS data. So far, this comparison showing several good agreements but also some disagreements between theory and experiment is not yet sufficiently revealing to allow for an identification of the true reconstruction of 4H-SiC(1 $\bar{1}$ 02)-c(2 \times 2). Finally STM images have been reported which reveal that particular empty-state STM topograms could resolve the question when the bias voltage is chosen appropriately. Nevertheless, a decisive structure identification by comparing theory with the available experimental data is not yet possible, at present. This situation calls for a joint experimental (LEED, STM, CLS, ARUPS) and theoretical (total energy, band structure, charge densities, STM images) investigation which would try to narrow down the number of possible structures to a very few and then investigate these candidates in great detail by as broad a spectrum of methods as possible.

Chapter 6.

Bulk and surface properties of alkaline-earth metal oxides

After having studied the electronic structure of bulk silicon carbide polytypes and some selected surfaces using the SIC approach with considerable success, it is to be expected that the description of properties of materials with related chemical characteristics will also be positively influenced by this method.

The alkaline-earth metal oxides constitute a technologically relevant class of materials. With the exception of beryllium oxide (BeO) the remaining group-II-oxygen compounds (MgO, CaO, SrO, and BaO) crystallize in the sodium chloride structure and thus share many physical properties. Due to the highly ionic character of all five compounds, any study of their properties relying on the SIC pseudopotential approach should yield not only qualitatively but also quantitatively convincing results.

The first section of this chapter will deal with the structural and electronic properties of BeO and its $(10\bar{1}0)$ surface. The hexagonal crystal structure of this oxide discerns it from the remaining alkaline-earth metal oxides and is separately treated in this work, therefore. In the second section, the properties of bulk MgO, CaO, SrO, and BaO will be analyzed collectively. For their (001) surfaces, the nature of the unoccupied electronic structure will be scrutinized with respect to the occurrence of image-potential states.

6.1. Atomic and electronic structure of BeO and the BeO($10\bar{1}0$) surface

The alkaline-earth metal oxides play a vital role as supports in catalysis [106–108]. BeO is special in this class of materials in that it crystallizes in the hexagonal wurtzite structure while the other alkaline-earth metal oxides crystallize in the cubic sodium chloride structure. This indicates that the Be–O chemical bond is not exclusively ionic but has also some covalent character. BeO is of technological importance, e.g., as catalyst, for semiconductor devices and as moderator in nuclear reactors. For semiconductor device

applications an understanding of the geometric and electronic properties of bulk BeO and its surfaces is highly desirable. As to more complex structures, very recently graphitic BeO nanofilms have been shown to be useful as precursors in the growth of wurtzite films [109] and BeO nanotubes have been investigated [110], as well.

The electronic structure of bulk BeO has been studied previously in experiment and by first-principles calculations employing standard LDA [111, 112], generalized gradient approximation [112] and Hartree-Fock [112] (HF) calculations. While LDA and GGA calculations yield a band gap that is significantly too small, HF calculations often yield too large band gaps and valence-band widths. The atomic structure of BeO has been studied by Chang and Cohen [111], as well as by Van Camp *et al.* [113] employing LDA total energy minimization. Both studies show that the ground state configuration of BeO is the wurtzite structure. According to Ref. [113] it is slightly more stable than the zincblende structure, the total energy difference per unit cell being as small as 5.6 meV. The atomic structure of the BeO(10 $\bar{1}$ 0) surface has been calculated by Jaffe and Zapol employing HF total energy minimization [114]. The electronic structure of the BeO(10 $\bar{1}$ 0) surface has not been previously investigated.

According to the previous results, it appears that standard LDA calculations fail to describe the band gap of bulk BeO appropriately. As a consequence, the electronic structure of BeO surfaces can not result very accurately from such calculations. Therefore, SIC pseudopotentials are employed to evaluate the atomic and electronic structure of BeO.

In the standard LDA reference calculations nonlocal, norm-conserving *ab initio* pseudopotentials in separable Kleinmann-Bylander form [31] are employed, as usual. The pseudopotentials are constructed according to the prescription of Hamann [94]. To expand the wave functions, three shells of Gaussian orbitals of *s*, *p*, *d*, and *s** symmetry per atom are used. The decay constants (in atomic units) 0.18, 0.40, 0.90 for Be and 0.30, 0.90 and 3.50 for O, respectively, yield results with good convergence.

In a first step, O 2*s*, O 2*p* and Be 2*s* atomic term values are calculated within SIC according to the prescription of Perdew and Zunger [13] and respective atomic SIC pseudopotentials are constructed. By construction, the overlap of the atomic SIC pseudopotentials in the solid is largely eliminated by the transfer procedure and the self-interaction correction of the extended Be 2*s* conduction band states is mostly suppressed while it is fully operational in the localized O 2*p* and O 2*s* valence bands.

6.1.1. Properties of the BeO bulk crystal

Structural properties of BeO as calculated using the formalism developed in Sec. 3.4 are summarized in Tab. 6.1 together with respective LDA results for comparison. Lattice constants are usually slightly underestimated in LDA, amounting in the current case to 1.3% for *a* and 0.8% for *c*, respectively. The agreement of the structure parameters resulting in

Table 6.1: Calculated lattice constants a , c and internal parameter u (in Å), a/c ratio and bulk modulus B (in Mbar) of wurtzite BeO in comparison with experiment.

	LDA	SIC	Exp
a	2.664	2.689	2.699 ^a , ^b
c	4.337	4.380	4.373 ^a , 4.38 ^b
u	0.377	0.377	0.378 ^a
c/a	1.628	1.629	1.620 ^a , 1.623 ^b
B	2.24	2.21	2.10 ^a , 2.24 ^c , 2.49 ^d

^afrom Ref. [115]^bfrom Ref. [116]^cfrom Ref. [117]^dfrom Ref. [118]

SIC with the experimental values is very good, indeed. The lattice constant a is underestimated by 0.4 % and the calculated c value overestimates one of the two experimental values by 0.2 %, only, while it agrees with the other. Comparing LDA and SIC lattice constants it can be recognized that the latter show an increase of about 1 %. The c/a ratio and the internal structure parameter u result very close in both LDA and SIC. The calculated c/a ratios are slightly larger while the experimental ratios are slightly smaller than the ideal ratio of 1.625 and they agree with experiment to better than 0.6 %. The SIC bulk modulus is smaller than the one resulting in LDA due to the increased lattice constants. Both agree reasonably well with the more recent experimental value of 2.10 Mbar [115] with the SIC value being slightly closer. The same general improvements have been observed in bulk lattice constants and bulk moduli in SIC as compared to LDA previously. For the cohesive energy of bulk BeO values of 14.72 eV in LDA and 13.63 eV in SIC per BeO pair are obtained. Lambrecht and Segall [119] have previously reported a theoretical value of 13.5 eV. All values are somewhat larger than the estimated experimental value [119] of 12.2 eV.

Figures 6.1 and 6.2 show the bulk band structure and the density of states of wurtzite BeO as resulting in standard LDA and SIC, respectively. For a meaningful comparison, in both cases the theoretical bulk BeO structure is used, as optimized in SIC (see Table 6.1), which agrees most closely with experiment. In Table 6.2 some band-structure energies at high-symmetry points of the bulk Brillouin zone are compiled. The general topology of the LDA and SIC band structures in Fig. 6.1 is largely similar. Both exhibit two O $2s$ bands in the lower and six O $2p$ bands in the upper valence-band energy region, separated by a large ionic gap (E_g^{ion}). The former give rise to one pronounced peak while the latter yield a double peak structure in the DOS (see Fig. 6.2). The conduction bands originate predominantly from Be $2s$ states. They are separated by a large fundamental band gap (E_g) from the top of the valence bands. The large size of the ionic and the fundamental

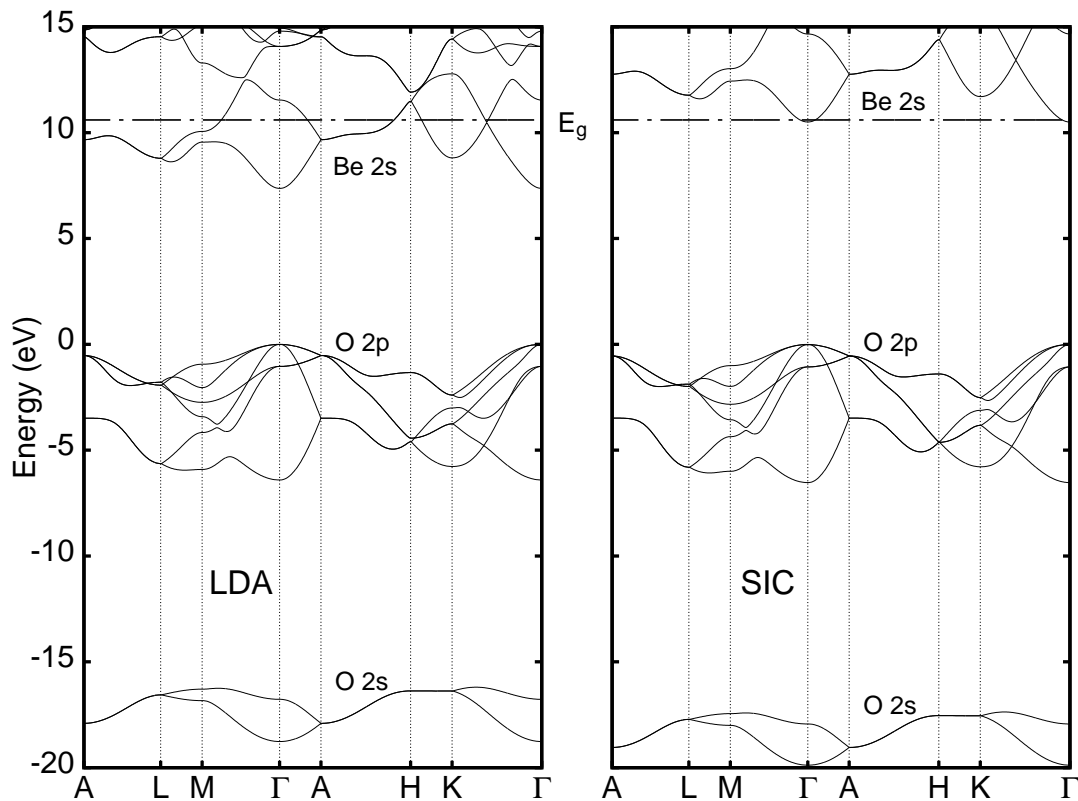


Figure 6.1: Bulk band structure of BeO along high-symmetry lines of the bulk Brillouin zone calculated in standard LDA (left panel) and SIC (right panel). The experimental gap energy is indicated by the horizontal dashed line.

gap is typical for a highly ionic insulator.

Comparing the LDA and SIC band structures, similarities and very significant quantitative differences are to be noted. The lower O $2s$ valence bands have very similar dispersion (see Fig. 6.1) and bandwidths W_s (see Tab. 6.3) but in LDA they occur about 1 eV higher in energy than in SIC. As a consequence, their spectral distribution in the DOS is similar but the O $2s$ peak results in LDA about 1 eV higher in energy than in SIC. The upper O $2p$ valence bands resulting in LDA and SIC are very similar in dispersion and bandwidth W_p (see Table 6.3) and so are their spectral distributions in the DOS (see Fig. 6.2). The total valence-band width W_{tot} is 18.77 eV in LDA while it is 19.88 eV in SIC (see Table 6.3). This increase in W_{tot} mainly originates from a stronger SIC-induced lowering of the O $2s$ as compared to the O $2p$ valence bands. The Be $2s$ conduction bands result much lower in LDA than in SIC. The LDA band gap energy is 7.36 eV strongly underestimating the measured gap energy of 10.6 eV [120, 121], as usual. The underestimate is 3.24 eV or about 30% in the case at hand. The SIC gap energy of 10.5 eV, on the contrary, is in excellent agreement with the measured values (see Table 6.3). The DOS in Fig. 6.2 clearly reveals the main SIC effects. Basically the same O $2p$ bands result in LDA and SIC, while

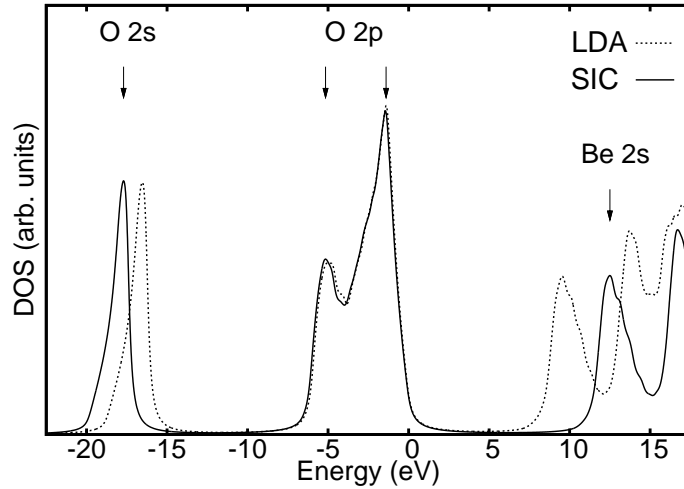


Figure 6.2: LDA and SIC density of states of bulk BeO (Lorentzian broadened by 0.2 eV).

	Γ_{1v}	Γ_{3v}	Γ_{6v}	Γ_{1c}	K_{2v}	K_{2c}	H_{3v}	H_{3c}
LDA	-18.77	-6.41	0.00	7.36	-2.40	8.80	-1.36	11.48
SIC	-19.88	-6.53	0.00	10.50	-2.52	11.70	-1.40	14.39

	$A_{5,6v}$	$A_{1,3c}$	M_{4v}	M_{1c}	$L_{1,2,3,4v}$	$L_{1,3c}$
LDA	-0.53	9.67	-0.94	9.55	-1.79	8.79
SIC	-0.61	12.76	-1.01	12.44	-1.88	11.77

Table 6.2: Band-structure energies of BeO at high-symmetry points of the bulk Brillouin zone, as resulting in LDA and SIC.

LDA yields a smaller ionic (about 1 eV) and a much smaller fundamental (about 3 eV) gap. Comparing the LDA and SIC band structure energies of the lowest conduction band in Table 6.2 it must be noted that the SIC-induced upward shift is largest for the Γ_{1c} state amounting to 3.14 eV and smallest for the M_{1c} state amounting to 2.89 eV. Thus the conduction bands are not shifted rigidly by SIC. Instead, their dispersion changes, e.g., by an increase of 0.25 eV for the lowest conduction band. Certainly, this value is small on the scale of the global band-gap improvement of 3.14 eV or the full width of the lowest conduction band. Yet, it is not negligible showing that a rigid shift of the conduction bands simply does not apply.

Naturally, the theoretical results should be compared with the experimental data compiled in Table 6.3. It has been noted already that SIC yields the band gap almost quantitatively while LDA underestimates its value by some 30%. The measured band width W_s of the O 2s bands [112] is smaller than the calculated values and previous theoretical results [111, 112]. Experimental literature data for the width W_p of the O 2p valence

	LDA	SIC	Exp
E_g	7.36	10.50	$10.6^a, 10.63 \pm 0.1^b$
E_g^{ion}	9.79	10.84	
W_s	2.57	2.51	1.7 ± 0.2^c
W_p	6.41	6.53	$4.7 \pm 0.2^c, 6.8^d, 8.8^e, 10.8^f$
W_{tot}	18.77	19.88	$19.4 \pm 0.3^c, 19.5^e, 20.0^g, 21.3^f$

^afrom Ref. [120]

^bfrom Ref. [121]

^cfrom Ref. [112]

^dfrom Ref. [122]

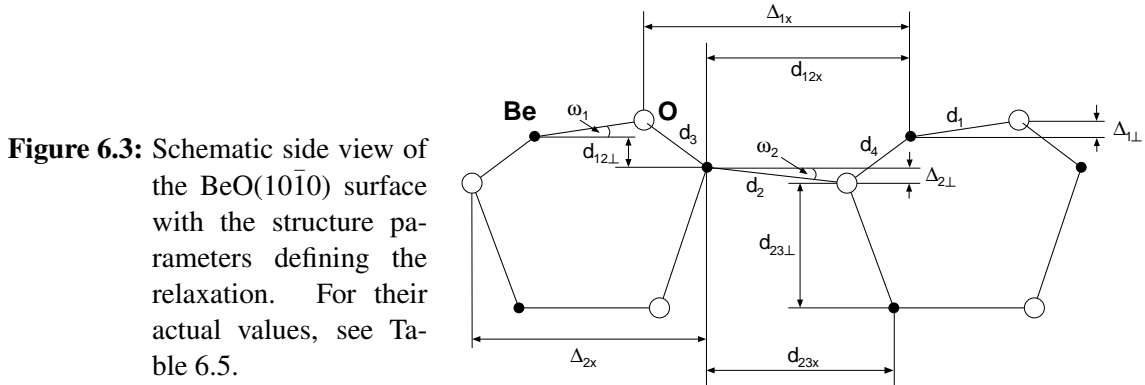
^efrom Ref. [123]

^ffrom Refs. [124] and [125]

^gfrom Ref. [126]

Table 6.3: Calculated LDA and SIC gap energies of the fundamental and ionic gap (E_g , E_g^{ion}), as well as O 2*p*, O 2*s* and total valence-band widths (W_p , W_s , W_{tot}), in comparison with experimental data (in eV).

bands, many of which have been measured already quite some time ago, span a considerable range in energy (see Table 6.3). In view of the results of this work, as well as of several earlier theoretical results [111, 112], the value of 6.8 eV determined in x-ray photoemission spectroscopy [122] appears to be the most realistic. In particular, the energy separation of the two peaks of the O 2*p* double peak structure in the DOS results as 3.7 eV from SIC calculations in close agreement with the experimental XPS value [122] of 3.9 eV. It should be noted that the relatively small bandwidths of $W_s = 1.7 \pm 0.2$ eV and $W_p = 4.7 \pm 0.2$ eV, as measured by transmission electron spectroscopy [112], can neither be reconciled with the theoretical values nor with previous *ab initio* results [111] including the LDA and GGA results of the authors of Ref. [112] themselves. The published data for the total valence-band width W_{tot} show considerable scatter, as well (see Table 6.3). While the valence-band width is clearly defined in one-particle theory as the energy difference between the Γ_{6v} and the Γ_{1v} band-structure energies, its determination from XPS or ultraviolet photoemission spectroscopy (UPS) data may be somewhat uncertain due to manybody effects as well as instrumental broadening, thermal broadening or surface charging effects making it difficult to directly compare photoemission DOS measurements with calculations, as has been pointed out already previously [127]. The contribution of the lower part of the O 2*s* valence bands around Γ to the DOS is very small due to the correspondingly restricted phase space. Therefore, the determination of the experimental valence-band width from a wave-vector integrated XPS or UPS spectral feature related to the O 2*s* bands might be complicated as is obvious already in the DOS shown in Fig. 6.2. While the theoretical valence-band width in SIC results as 19.88 eV, the respective DOS in Fig. 6.2 shows already an increase of the width to more than 20 eV due to the 0.2 eV Lorentzian broadening. This increase in the width would even be larger if instrumental



broadening of the spectra would be larger than 0.2 eV, as is often the case. Taking these complicating facts into consideration, the theoretical valence-band width W_{tot} resulting in SIC appears to be in better agreement with experiment than the LDA bandwidth which is about 1 eV smaller (see Fig. 6.2 and Table 6.3).

In summary, the SIC approach appears to yield a very reliable band structure together with the associated wave functions for the BeO bulk crystal. It can therefore be considered as a trustworthy effective one-particle band theory for BeO. In particular, the SIC band gap is in excellent agreement with experiment so that the usual LDA shortcomings in describing gap energies seem to be conquerable for the highly ionic insulator BeO by taking self-interaction corrections into account. The SIC results are in good agreement with the majority of the experimental data. Therefore, the bulk band structure resulting from SIC calculations can serve as a reliable basis for electronic structure calculations of more complex BeO structures.

6.1.2. Structural and electronic properties of the BeO(10 $\bar{1}$ 0) surface

In this section, the structural and electronic properties of the nonpolar BeO(10 $\bar{1}$ 0) surface are addressed. There is one Be and one O atom per (10 $\bar{1}$ 0) layer unit cell so that the surface is nonpolar. The supercell approach is employed with a slab of ten BeO layers per supercell and a 16 Å thick vacuum layer between BeO slabs. Six special \mathbf{k}_{\parallel} -points are used to carry out sums over the surface Brillouin zone. As it turns out, ten BeO layers per slab are sufficient to *electronically* decouple its two equivalent surfaces.

The surface atomic structure of BeO(10 $\bar{1}$ 0) has been investigated previously by Jaffe and Zapol [114] using an *ab initio* Hartree-Fock supercell approach considering slabs of six BeO layers per supercell. To find out whether thicker slabs are needed for the determination of the surface *atomic* structure, the relaxation geometry has been optimized using six, eight and ten BeO layers per slab at the theoretical LDA bulk lattice constants.

The relaxation geometry is schematically shown in Fig. 6.3. The actual displacements of the Be and O atoms on the first and second layer in surface-parallel (Δx) and surface-perpendicular (Δz) direction are compiled in Table 6.4.

Obviously, the atomic displacements converge very fast to their final values when the slab thickness is increased from six to ten layers. For eight layers, the displacements are already very close to those for the ten layer slab while some of them show small deviations for the six layer slab. The latter are insignificant, however, since the respective absolute displacements are very small. Nevertheless, a ten layer slab is employed in the electronic structure calculations addressed in the next section since specific states on the top and bottom layer of the slabs show interaction effects of longer range than the total valence charge density entering the structure optimization.

The displacements of the Be and O atoms on the first and second surface layer compiled in Table 6.4 highlight already the basic structural changes occurring upon relaxation. These are most pronounced for Be on the surface layer. The Be cations move significantly downward perpendicular to the surface by 0.24 Å and parallel to the surface by 0.13 Å. The O anions move only slightly downward perpendicular to the surface by 0.03 Å and parallel to the surface by 0.04 Å. They thus basically remain in their ideal surface positions. This is typical for a highly ionic surface. The more electronegative O anions stay on top of the surface to reduce the Coulomb repulsion of the surface electrons with the backbonds. The more electropositive Be cations move strongly downward forming planar arrays with their three neighboring O anions to increase the electrostatic ion-ion attraction as much as possible. The Be and O atoms, forming BeO dimers in the top layer, move closer to each other by 0.17 Å. This corresponds to a contraction of the dimer-bond length by about 10%. The Be and O atoms in the second layer move slightly upward with respect to their positions at the ideal surface. As a consequence, of the downward movement of the first and the upward movement of the second layer atoms, the backbond lengths are contracted by 3%. This relaxation is another example of the *bond-lengths contracting*

atom	6 layers		8 layers		10 layers	
	Δx	Δz	Δx	Δz	Δx	Δz
Be ₁	+ 0.135	- 0.238	+ 0.130	- 0.235	+ 0.130	- 0.235
O ₁	- 0.036	- 0.035	- 0.041	- 0.029	- 0.041	- 0.027
Be ₂	- 0.027	+ 0.097	- 0.037	+ 0.095	- 0.037	+ 0.095
O ₂	- 0.012	+ 0.053	- 0.017	+ 0.050	- 0.017	+ 0.048

Table 6.4: Relaxation-induced displacements of first and second layer Be and O atoms (indices 1 and 2, respectively) relative to their positions at the ideal surface (in Å) calculated using slabs of six, eight and ten BeO layers per supercell.

Table 6.5: Structure parameters of the BeO(10 $\bar{1}$ 0) surface, calculated at the respective theoretical bulk lattice constants, as resulting from this work and previous HF structure optimization [114] (Lengths in Å and bond angle rotations in °).

	this work		ab initio HF	
	ideal	relaxed	ideal	relaxed
$\Delta_{1\perp}$	0.00	0.21	0.00	0.11
Δ_{1x}	2.70	2.87	2.69	2.86
$\Delta_{2\perp}$	0.00	-0.05	0.00	-0.05
Δ_{2x}	2.70	2.68	2.69	2.70
$d_{12\perp}$	0.77	0.44	0.77	0.43
d_{12x}	2.17	2.34	2.17	2.27
$d_{23\perp}$	1.54	1.63	1.55	1.69
d_{23x}	2.17	2.21	2.17	2.15
ω_1	0.0	8.1	0.0	4.1
ω_2	0.0	-1.6	0.0	-1.7
d_1	1.64	1.48	1.65	1.48
d_2	1.64	1.66	1.65	1.63
d_3	1.63	1.58	1.63	1.56
d_4	1.63	1.57	1.63	1.56

rotation relaxation characteristic for heteropolar ionic surfaces, as observed previously, e.g., for SiC(110) [75] or ZnO(10 $\bar{1}$ 0) [128, 129]. The physical origins of this type of relaxation as opposed to the *bond-lengths conserving rotation relaxation*, typically encountered at (110) surfaces of III-V compound semiconductors, have been discussed at length before [75, 114, 128–130].

Most often structure parameters, as defined in Fig. 6.3, are used to characterize the relaxation of a (10 $\bar{1}$ 0) surface instead of considering atomic displacements. For convenience, respective results are shown in comparison with those of Jaffe and Zapol [114] in Table 6.5. Taking into account that HF yields bulk lattice constants slightly different from the DFT values, it can be recognized that both calculations yield many similar relaxation-induced changes of the structure parameters and a grossly similar relaxation geometry. There is one very distinct difference to be noted, however. HF yields a $\Delta_{1\perp}$ value of 0.105 Å which is only half as large as our calculated value of 0.209 Å. As a consequence, the tilt angle ω_1 of the BeO surface dimer is only 4.1° in HF while it results as 8.1° from our DFT-LDA calculations. A considerably smaller HF value of ω_1 has also been observed for ZnO(10 $\bar{1}$ 0) where HF [130] yields 2.3° while LDA [129] yields 10.7°. There are some minor differences between the HF and the results of this work, in addition. To mention only one, for example a small increase of the bond length d_2 of the BeO dimer

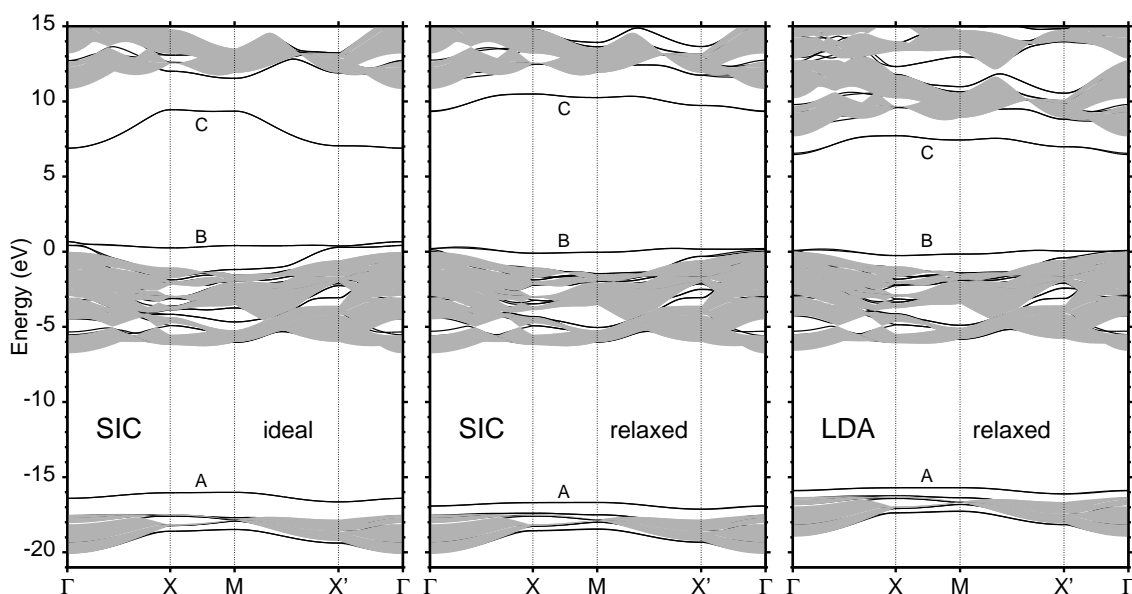


Figure 6.4: Surface band structure of the ideal (left panel) and relaxed (middle panel) BeO($10\bar{1}0$) surface as resulting from SIC calculations. The band structure of the relaxed surface, as resulting from LDA, is shown in the right panel for comparison. The gray-shaded areas show the projected bulk band structure. Surface state bands are indicated by full lines.

on the second layer by 1.2 % is found while the HF result shows a decrease of the same size (see Table 6.5). The counter-rotation angle ω_2 of the Be–O bond on the second layer is in close agreement with that resulting in HF. In summary, the surface atomic structure as optimized using ten layer slabs can serve as a reliable basis for the electronic structure calculations in the next section.

Finally, the surface energy per unit cell of the ideal surface results as 2.05 eV in LDA and 1.92 eV in SIC from the present calculations corresponding to 2.84 and 2.66 Jm^{-2} , respectively. Significantly lower values of 1.44 eV (LDA) and 1.37 eV (SIC) per unit cell are obtained for the relaxed surface corresponding to 1.99 and 1.90 Jm^{-2} , respectively, as was to be expected.

Based on the optimized geometry the surface band structure of the BeO($10\bar{1}0$) surface as resulting from SIC calculations will be discussed in the following¹. It is shown in Fig. 6.4 along the high-symmetry lines of the rectangular surface Brillouin zone for both the ideal surface (left panel) and the relaxed surface (middle panel). The most salient bands related to localized surface states are labeled by *A–C*. Bands *A* and *B* originate from O $2s$ and O $2p$ bulk valence band states, respectively, while band *C* originates from Be $2s$ bulk con-

¹It should be noted at this point that the SIC- Δ approach is not needed for the calculation of the surface electronic structure of the ionic oxides in this chapter since no linear-combined states like on the polar SiC surfaces are expected to occur.

6.1. Atomic and electronic structure of BeO and the BeO(10 $\bar{1}$ 0) surface

	A_Γ	B_Γ	C_Γ	A_X	B_X	C_X	A_M	B_M	C_M	$A_{X'}$	$B_{X'}$	$C_{X'}$
SIC												
id.	-16.4	0.7	6.9	-16.0	0.3	9.5	-16.0	0.4	9.4	-16.6	0.4	7.0
rel.	-16.9	0.2	9.3	-16.7	-0.1	10.5	-16.7	0.0	10.3	-17.1	0.2	9.7
LDA												
rel.	-15.9	0.1	6.5	-15.7	-0.2	7.7	-15.7	-0.1	7.5	-16.1	0.1	7.0
id.	-15.4	0.6	4.6	-15.0	0.1	7.1	-15.0	0.3	6.9	-15.6	0.3	4.8

Table 6.6: Energies of the surface states A , B and C at the high-symmetry points Γ , X , M and X' of the surface Brillouin zone for the ideal and the relaxed BeO(10 $\bar{1}$ 0) surface, as resulting from standard LDA and SIC calculations.

duction band states. To ease the discussion, band-structure energies of the surface states at several high-symmetry points of the surface Brillouin zone are summarized in Table 6.6. The LDA results in the table, as well as in Fig. 6.4 will be addressed at a later point. Both SIC band structures for the ideal and the relaxed surface (left and middle panel of Fig. 6.4) show the same global topology of the most salient surface state bands. However, upon relaxation the bands of the ideal surface partially show very significant shifts in energy and changes in their dispersion. Band A shifts down in energy at the relaxed surface on average by 0.5 eV reducing its dispersion from 0.6 to 0.4 eV. Band B shifts down in energy upon relaxation by roughly 0.4 eV reducing its dispersion from 0.4 to 0.3 eV. Thus both occupied surface bands shift down in energy explaining the relaxation-induced total energy gain. On the contrary, the empty C band strongly shifts up in energy upon relaxation. In particular, its shift strongly depends on \mathbf{k}_\parallel and thus on the symmetry point considered and ranges from 0.9 to 2.7 eV reducing the C band dispersion drastically from 2.6 to 1.2 eV. In general, one can conclude from these findings that the relaxation shifts the surface bands much closer to their parent bulk projected bands from which they are derived and reduces their dispersion. The SIC band gap of the ideal surface is 6.2 eV while that of the relaxed surface is significantly larger amounting to 9.1 eV. The electronic structure of the BeO(10 $\bar{1}$ 0) surface obviously shows very pronounced relaxation-induced changes although the atomic structure of the ideal and the relaxed surface is not entirely different.

Concluding the discussion of relaxation-induced effects, the absolute dispersion of the surface state bands A - C should be briefly addressed. An orthogonal x, y coordinate system in the surface layer is chosen such that the x -direction is parallel to the BeO surface dimer bonds while the y -direction is perpendicular to them. So the unit cell is long in x -direction (4.38 Å) and short in y -direction (2.69 Å). As a consequence, the short high-symmetry lines from X to M and X' to Γ correspond to the x - while the long high-symmetry lines from Γ to X and M to X' correspond to the y -direction in real space.

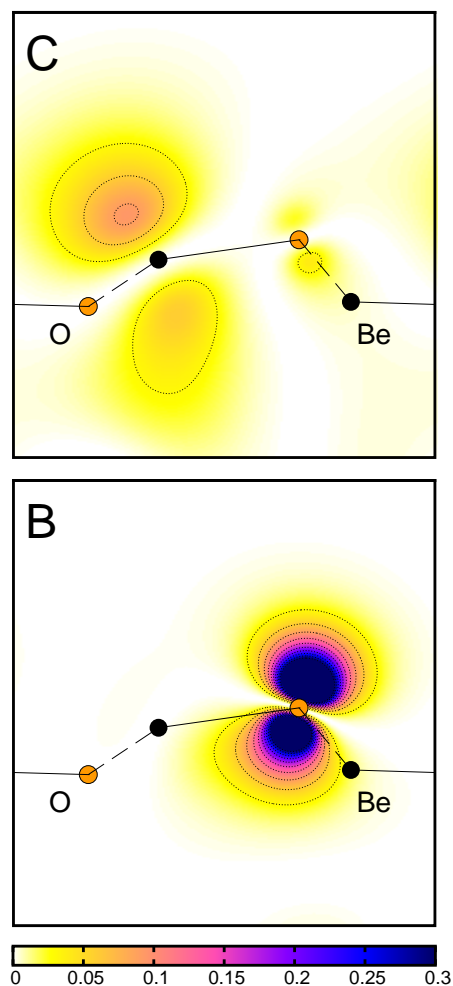


Figure 6.5: Charge density contours of the *B* and *C* states at the *M* point of the surface Brillouin zone of the relaxed BeO($10\bar{1}0$) surface, as resulting from SIC calculations. The size of the densities is defined by the color code (gray scale) below the plots. Be and O atoms are shown by black and orange (gray) circles, respectively.

The distance of nearest-neighbor surface atoms in x -direction is 4.38 \AA so that their interaction is small. Therefore all surface bands at the ideal and the relaxed surface show a very small dispersion from X to M and X' to Γ , as can easily be seen in Fig. 6.4. On the contrary, the nearest-neighbor distance of the atoms in the y -direction is only 2.69 \AA , so that they can more strongly interact if their orbitals are sufficiently extended. Since bands *A* and *B* originate from highly localized O $2s$ and O $2p$ states they show also little dispersion at both the ideal and the relaxed surface from Γ to X and M to X' . Band *C*, on the contrary, shows much stronger dispersion for both surface configurations along the latter high-symmetry lines since it originates from the spatially more extended Be $2s$ states which strongly interact. As a consequence, the dispersion of the *C* band amounts to 2.6 eV at the ideal surface. At the relaxed surface, its dispersion is reduced to 1.2 eV , only. This is due to a very significant change of the electrostatic potential in the surface layer upon structural relaxation.

Discussing Fig. 6.4 it has already been shown that there occur salient localized surface states

in the gaps of the projected bulk band structure. To identify their nature more precisely, charge density contours of the states B and C at the M point of the surface Brillouin zone are considered. The contours for the corresponding states at the ideal and the relaxed surface are largely similar just with slight differences in absolute values. Therefore, only charge densities for the experimentally more relevant relaxed surface are shown in Fig 6.5. Obviously, the O $2p$ -derived dangling-bond state B is mostly localized at the surface oxygen atom while the Be $2s$ -derived empty dangling-bond state C is mainly localized at the surface Be atom. Both have a typical dangling-bond character. The absolute charge density is considerably larger for the occupied O than for the empty Be dangling-bond state since O $2p$ orbitals, from which the former is derived, are much more localized than Be $2s$ orbitals, from which the latter is derived.

Having discussed the SIC surface band structure of the ideal and relaxed BeO(10 $\bar{1}$ 0) surface scrutinizing the relaxation-induced effects, one can finally turn to the LDA surface band structure for comparison sake and identify the SIC-induced effects. The LDA surface band structure of the relaxed surface is shown in the right panel of Fig. 6.4. For shortness sake, the ideal surface band structure resulting in LDA is not shown but respective band structure energies at high-symmetry points are included in Table 6.6, as well. The global topology of the LDA surface band structures is similar to those of the SIC surface band structures (see Fig. 6.4 for the relaxed surface). Qualitatively, the same surface bands A - C occur. But there are very significant quantitative differences to be noted. First and foremost the SIC approach yields an appropriate projected bulk band structure and a realistic projected gap, in particular. In LDA the projected gap is 3.14 eV smaller than in SIC so that the surface band C resulting from LDA is much too low in energy at both the ideal and the relaxed surface (cf. Table 6.6). Comparing the LDA and SIC surface band structures (see Fig. 6.4 and Table 6.6) one can easily identify the SIC-induced shifts of the bands A - C . Band A is rigidly shifted down in energy by 1 eV at all symmetry points of both the ideal and the relaxed surface due to SIC, very much like the O $2s$ bulk bands from which it is derived (see Fig. 6.1). Band B is essentially shifted up in energy rigidly by 0.1 eV, only, for both surface geometries. Band C is strongly shifted up in energy due to SIC very much like the projected Be $2s$ bulk bands. This shift amounts to 2.8 eV at the relaxed surface. The LDA surface band gap is 6.4 eV while the SIC surface band gap is 9.1 eV at the relaxed surface. Thus the surface band gap opens up by 2.7 eV due to SIC, as compared to the LDA surface band gap (cf. Table 6.6). This value is somewhat smaller than the SIC-induced opening of the bulk band gap by 3.14 eV, as discussed above. Similar behaviour has been observed earlier, e.g., in the results of GW quasiparticle calculations for bulk Si and the Si(001) surface where the quasiparticle corrections of the energy positions of dangling-bond states in the gap are found to be somewhat smaller than respective quasiparticle corrections of the bulk valence- and conduction-band edges [131].

From this comparison one can conclude that the LDA shortcomings in the BeO bulk band structure description fully translate into respective shortcomings in the surface band structure of BeO(10 $\bar{1}$ 0). The surface band structure, calculated within the SIC approach, shows very significant improvements over the standard LDA surface band structure concerning the projected bulk band structure, the projected gap and the absolute energy positions of surface-state bands. The SIC-induced effects are quantitatively very similar to those obtained for the bulk band structure of BeO. It would be highly desirable to check these notions against experimental data or, e.g., quasiparticle band-structure results.

6.1.3. Summary

SIC pseudopotentials are applied in DFT calculations of bulk BeO to calculate the electronic structure of the nonpolar BeO(10 $\bar{1}$ 0) surface for the first time. It is found that typical LDA shortcomings in the description of the electronic structure of BeO and the BeO(10 $\bar{1}$ 0) surface can almost entirely be overcome by SIC. The results for the bulk crystal are highly satisfactory and emphasize that the SIC approach to account for self-interaction corrections is a powerful tool for an accurate description of the electronic properties of the BeO bulk crystal. In addition, structural parameters, such as bulk lattice constants and the bulk modulus, derived from total energies calculated employing the SIC approach, result in very good agreement with experiment. On the basis of these results it can be concluded that the approximate SIC approach should also be most suitable for electronic structure calculations on more complex BeO structures. To this end, it could be shown that the SIC approach yields very significant improvements in the surface electronic structure of the BeO(10 $\bar{1}$ 0) surface which exhibits three salient bands of surface states.

6.2. Bound surface and image potential states of alkaline-earth metal oxides

Alkaline-earth metal oxides play an important role in many technological applications, most notably as supports in catalysis. Usually, surface properties of the oxides are exploited in such applications, putting them in the focus of scientific interest. The role which metal-supported ultrathin oxide films can play as designable catalysts or catalyst supports has been discussed most recently by Freund [132]. Due to their importance, alkaline-earth metal oxides have attracted significant attention and have been studied both experimentally and theoretically on different levels of sophistication.

In experiment, elastic and electronic properties of the bulk oxides have been derived using ultrasonic pulse-echo techniques [133], as well as soft x-ray emission spectroscopy [134], x-ray photoelectron spectroscopy [135, 136] and electron momentum spectroscopy [137]. The geometric structure of the MgO(001) surface has been the subject of a number of low-energy electron diffraction [138–142], reflection high-energy electron diffraction [143, 144], impact collision ion scattering spectroscopy [145] and surface extended energy-loss fine-structure [146] measurements leading to a geometry model characterized by a decreased distance between the first and second surface layer with respect to their bulk distance and a positive rumpling of the surface layer. In contrast, a LEED study for CaO(001) indicates a negatively rumpled surface [147].

Experimental data on the surface electronic structure of alkaline earth metal oxides is comparatively sparse. The valence band structure of MgO(001) has been analyzed by Tjeng *et al.* using ARUPS [148], while Ochs and coworkers [149] conducted a study on MgO thin films, combining metastable impact electron spectroscopy, XPS and UPS. From electron energy loss spectroscopy (EELS), a lowest transition energy of 6.2 eV [150, 151] was established. Using scanning tunneling spectroscopy (STS) and EELS, Schintke *et al.* [152] have shown that the same transition energy is constituted already for three atomic MgO layers on Ag(001).

In theory, quite a number DFT calculations have been performed both on bulk and surface systems, employing the local-density or generalized gradient approximations [153–160]. In these theoretical studies, the authors arrive at structural parameters, e.g. lattice constants, bulk moduli and surface relaxation geometries that are in good agreement with experimental findings. However, the description of the electronic structure within these approximations turns out to be unsatisfactory, as usual, as far as the fundamental gap and the conduction bands are concerned. Several methods conceived to overcome the well known DFT gap problem in semiconductors and insulators have been applied to bulk alkaline-earth metal oxides, most prominently the *GW* approximation for the quasiparticle band structure [21, 161–165]. Also, results from *ab initio* Hartree-Fock [166, 167],

screened exchange and weighted density approximation [168] as well as exact exchange calculations [169] have been reported.

With the notable exception of the MgO(001) surface [21, 164], all investigations going beyond LDA or GGA, respectively, have been limited to bulk systems so far.

From a calculational point of view, special care has to be taken in constructing the pseudopotentials for the heavier cations. Nonlinear core effects necessitate the inclusion of respective s and p states of the highest closed atomic shell. Otherwise, rather unphysical structural properties of the systems result. Also, the energetic position of the associated cationic semicore p states is of significance for the electronic structure of the valence bands since intricate interactions with occupied oxygen states occur. See App. B for details.

As decay constants (in atomic units) for the basis of Gaussian orbitals employed for the expansion of the wave functions 0.20, 0.55 and 0.95 are used for Mg, 0.16, 0.38, 0.85 and 1.30 for Ca, 0.18, 0.40, 0.90 and 1.70 for Sr, 0.10, 0.25, 0.42, 0.88 and 1.75 for Ba and 0.25, 1.00 and 3.70 for O. The properties of the (001) surfaces are calculated within the supercell approach. The slabs consist of eight anion-cation layers, separated by 8 layers of vacuum so that unphysical interactions between neighboring slabs are avoided. The vacuum region is filled with slowly decaying s -type orbitals (decay constants 0.14 a.u.) located at virtual atomic positions to appropriately represent the vacuum states. Brillouin-zone integrations are performed using special k point sets in the irreducible wedge generated according to the prescription of Monkhorst and Pack [30]. The number of special points needed to obtain convergent results in bulk and surface systems amount to 28 and 15 (MgO), 28 and 10 (CaO), 19 and 10 (SrO, BaO), respectively. Lattice constants of the bulk crystals are optimized by total energy minimization. In the surface systems, the atomic positions of the two outer layers of the slabs are allowed to relax until all components of the calculated Hellmann-Feynman and Pulay forces are smaller than 0.6 mRy/a_B. Based on the fully optimized geometry, the electronic structure is determined.

6.2.1. Bulk structural and electronic properties

First, the structural parameters of the alkaline-earth metal oxide bulk crystals will be discussed. They all crystallize under normal conditions in the sodium-chloride structure, which is typical for ionic compounds such as MgO, CaO, SrO and BaO. In order to determine the equilibrium structural parameters, the total energy is calculated around its minimum for different values of the lattice constant a employing the formalism described in Sec. 3.4. From the resulting $E_{\text{tot}}(a)$ curve, the optimized structure parameters are derived.

In Table 6.7, the resulting lattice constants a and bulk moduli B are summarized together with reference data from LDA calculations and experiment, for comparison. The LDA

Table 6.7: Lattice constants a in Å and bulk moduli B in Mbar, as resulting from LDA and SIC calculations. Other LDA reference data is taken from Refs. [157] and [158], experimental data from Refs. [170] and [171].

		LDA	SIC	other LDA	Exp.
MgO	a	4.16	4.17	4.16, 4.21	4.21
	B	1.58	1.57	1.52	1.55
CaO	a	4.75	4.78	4.69, 4.72	4.81
	B	1.24	1.23	1.25	1.15
SrO	a	5.09	5.10	5.07, 5.09	5.11
	B	1.09	1.05	1.03	0.89
BaO	a	5.44	5.47	5.45, 5.48	5.52
	B	0.89	0.88	0.81	0.74

values typically underestimate the lattice constants by $\sim 1\%$. The SIC results slightly improve the values for a , as compared to the LDA results. As far as the bulk moduli are concerned, the increased lattice constants resulting in SIC, as compared to the LDA values, give rise to somewhat lower B values which are in marginally better agreement with experiment. In general, the values given in Table 6.7 show that the LDA and SIC results compare well with other LDA results from the literature [157, 158]. This illustrates that SIC pseudopotentials yield bulk structural properties of the investigated alkaline-earth metal oxides of the same quality as those resulting from standard LDA pseudopotentials. In Fig. 6.6 the bulk band structures of MgO, CaO, SrO and BaO as resulting from SIC calculations, carried out at the experimental lattice constant, are shown. The dashed lines indicate the respective experimental values for the fundamental energy gap. Basically, the bands can be classified by the atomic levels they originate from. In the valence bands, two band groups originating from oxygen occur. There is a low-lying O $2s$ band at the bottom separated by a large inter-anionic valence gap from the group of three O $2p$ bands at the top of the valence bands. Additionally, for the heavier cations (Ca, Sr, Ba), three semicore p bands occur close in energy to the O $2s$ band. The Ca $3p$ bands reside below the valence band region shown in Fig. 6.6. They push the O $2s$ band slightly up in energy so that the latter is somewhat higher in CaO than in the other three oxides. The O $2s$ band has an almost inverted dispersion in SrO and BaO, as compared to MgO and CaO, due to its interaction with the cationic p bands occurring above the O $2s$ band in the former two crystals. The lowest unoccupied band originates in all four oxides from cationic s states. Note that the conduction band minimum occurs at Γ in MgO while it occurs at X in the other three oxides and the valence band maximum occurs at Γ in MgO, CaO and SrO while it occurs at X in BaO. As a consequence, the gap is direct at Γ in MgO and at X in BaO while it is indirect from Γ to X in CaO and SrO.

Table 6.8 summarizes relevant electronic structure data resulting from SIC calculations consisting of the fundamental energy gap (E_g), the width of the O $2p$ band group (W_p),

		LDA	SIC	GWA	Exp.
MgO	E_g	4.54	7.86	7.79 ^a , 8.2 ^b , 8.2 ^c	7.8 ^d
	W_p	4.76	4.55	5.5 ^a , 5.0 ^b	3.33 ^e
	E_s	-16.41	-17.22	-18.6 ^a , -17 ^b , -20.1 ^c	-17.6 ^f
	E_p	—	—	—	—
CaO	E_g	3.71	7.16	6.64 ^b	7.1 ^e
	W_p	2.74	2.29	2.9 ^b	0.9 ^f
	E_s	-14.80	-15.59	-16 ^b	-16.5 ^f
	E_p	-19.10	-21.02	—	—
SrO	E_g	3.04	6.35	6.39 ^c	5.9 ^e
	W_p	2.13	1.64	2.1 ^c	—
	E_s	-15.73	-17.39	-17.4 ^c	—
	E_p	-13.85	-14.72	-14.2 ^c	—
BaO	E_g	1.76	4.77	3.91 ^f	4.3 ^e
	W_p	2.46	2.06	3.68 ^d	—
	E_s	-15.53	-16.38	—	—
	E_p	-11.19	-11.05	-11 ^d	—

^afrom Ref. [164]

^bfrom Ref. [163]

^cfrom Ref. [162]

^dfrom Ref. [172], reported values are direct gaps at Γ

^efrom Ref. [137]

^ffrom Ref. [165]

Table 6.8: Calculated LDA and SIC gap energies (E_g), O 2p band widths (W_p), as well as average energy positions of O 2s and cationic semicore p bands (E_s , E_p) of MgO, CaO, SrO and BaO bulk crystals in comparison with results from the GW approximation (GWA) for the quasiparticle band structure and experiments (in eV).

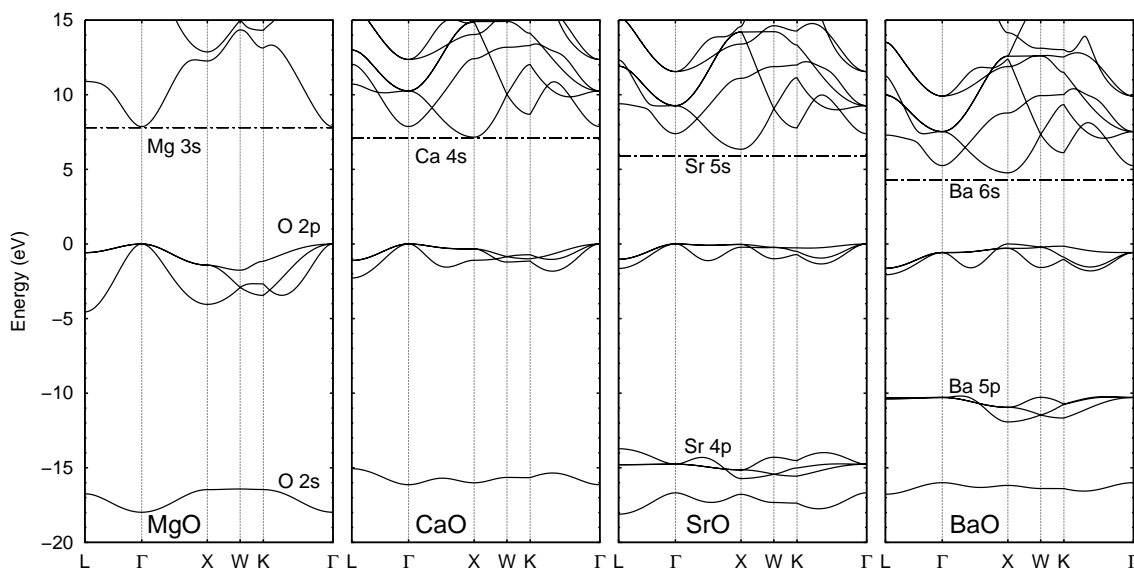


Figure 6.6: Bulk band structures of MgO, CaO, SrO and BaO along high-symmetry lines of the bulk Brillouin zone as resulting from SIC calculations. Respective experimental energy gaps are indicated by the horizontal dashed lines.

the average energetic position of the O $2s$ band (E_s) and the cationic semicore p band group (E_p), respectively. For further comparison, respective values resulting from standard LDA calculations as well as GW results and experimental data from the literature are given. Obviously, the results of the SIC calculations agree favorably with the reference data. Very good agreement is achieved concerning the fundamental gaps, in particular, as compared to the GWA results and experiment. Also, trends with the decreasing ionicity of the compounds along the series from MgO to BaO, namely a reduction of the gap energy, a narrowing of the O $2p$ bands and rising energetic positions of the cationic semicore p bands are well accounted for. As a matter of fact, the narrowing of the O $2p$ bands from MgO to CaO by 2.26 eV, as calculated within SIC, is in close agreement with the experimentally determined value of 2.46 eV. Yet, it is interesting to note that both the SIC and GWA calculations yield considerably larger widths of the O $2p$ valence bands for MgO and CaO, as compared to experiment. This is astonishing in view of the fact that valence band widths of wide-band-gap semiconductors such as SiC or BeO result in good agreement with experiment from SIC or GWA calculations (cf. Sections 3.6 and 6.1.1). There is a very distinct effect in the SIC results for the valence band structure of SrO. In LDA, the O $2s$ band results in resonance with the lower part of the Sr $4p$ bands at the bottom of the valence bands. Cappellini *et al.* [162] have pointed out in their GWA study of SrO that a splitting of this group of bands into isolated, less dispersive bands fits XPS data [135] much better than the LDA results. SIC calculations show similar changes with respect to the LDA. Due to the stronger localization of the O $2s$ state, its self-interaction-

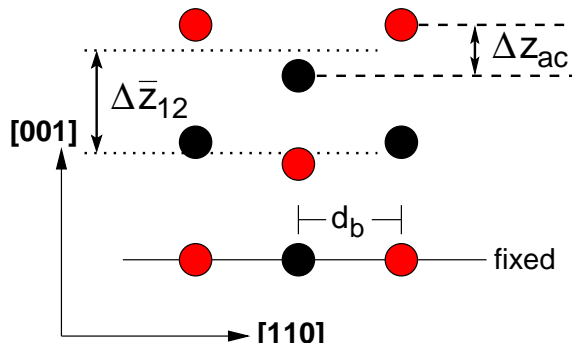


Figure 6.7: Schematic relaxation pattern (side view) of relaxed alkaline-earth metal oxide (001) surface, shown in the [001]-[110] plane. Red (grey) and black dots represent positions of O atoms and cations, respectively.

correction is stronger than that of the Sr 4p states. As a consequence, the associated O 2s band clearly separates from the Sr 4p band group.

In view of this rather accurate description of the bulk electronic structure of the investigated alkaline-earth metal oxides, one can expect that the use of SIC pseudopotentials in a study of the respective (001) surfaces yields results of comparably good quality.

6.2.2. Structural and electronic properties of the relaxed (001) surfaces

Based on intensive experimental and theoretical studies, a relaxation model for (001) alkaline-earth metal oxide surfaces is commonly accepted. A side view of this model is schematically depicted in Fig. 6.7. It is characterized by small atomic displacements of the ions which move slightly perpendicular to the surface only. The resulting relaxation pattern can be described in terms of only two structure parameters, a *surface rumpling*

$$d_{\text{rum}} = \frac{\Delta z_{ac}}{d_b}, \quad (6.1)$$

defined as the difference of the z positions of surface layer anions and cations Δz_{ac} related to the ideal bulk distance d_b and an *interlayer relaxation*

$$d_{\text{rel}} = \frac{\Delta \bar{z}_{12}}{d_b}, \quad (6.2)$$

which describes the changed spacing between the average surface and first subsurface layer in relation to the ideal bulk distance d_b of these two layers.

The geometric structure of the (001) surfaces has been discussed in the literature already in quite some detail. Therefore, the results for the surface rumplings, interlayer relaxations and surface energies are only briefly summarized together with reference data from the literature in Table 6.9. First, note that MgO(001) shows an opposite surface rumpling, as compared to the other three oxides, as observed in experiment. In particular, MgO(001)

		$d_{\text{rum}}(\%)$	$d_{\text{rel}}(\%)$	$\sigma_{\text{sur}}(\text{J/m}^2)$
MgO	this work	+2.0	+0.1	1.29
	LDA ^a	+1.8	-0.2	1.14
	LDA ^b	+2.2	~ 0	1.39
	LDA ^c	+1.9	+0.2	1.18
	GGA ^d	+2.3	~ 0	0.90
	Exp	0 to +5 ^e	0 to -2 ^e	1.04 ^f to 1.12 ^g
CaO	this work	-1.1	-2.0	0.95
	LDA ^a	-0.6	-2.3	0.81
	LDA ^b	-0.6	~ 0	1.05
	LDA ^c	-1.3	-2.3	0.87
	GGA ^d	-0.7	-1.1	0.63
SrO	this work	-2.5	-2.6	0.84
	LDA ^a	-1.5	-3.2	0.69
	GGA ^d	-2.3	-1.7	0.53
BaO	this work	-5.8	-6.3	0.57
	LDA ^a	-1.8	-4.6	0.56
	GGA ^d	-4.9	-2.5	0.33

^afrom Ref. [157], four layer slab

^bfrom Ref. [156], three layer slab

^cfrom Ref. [156], four layer slab

^dfrom Ref. [158], seven, nine and eleven layer slabs

^efrom Ref. [139]

^ffrom Ref. [138]

^gfrom Ref. [173]

Table 6.9: Calculated surface rumpling, interlayer relaxation and surface energy of the relaxed MgO, CaO, SrO and BaO (001) surfaces in comparison with other theoretical and with experimental results.

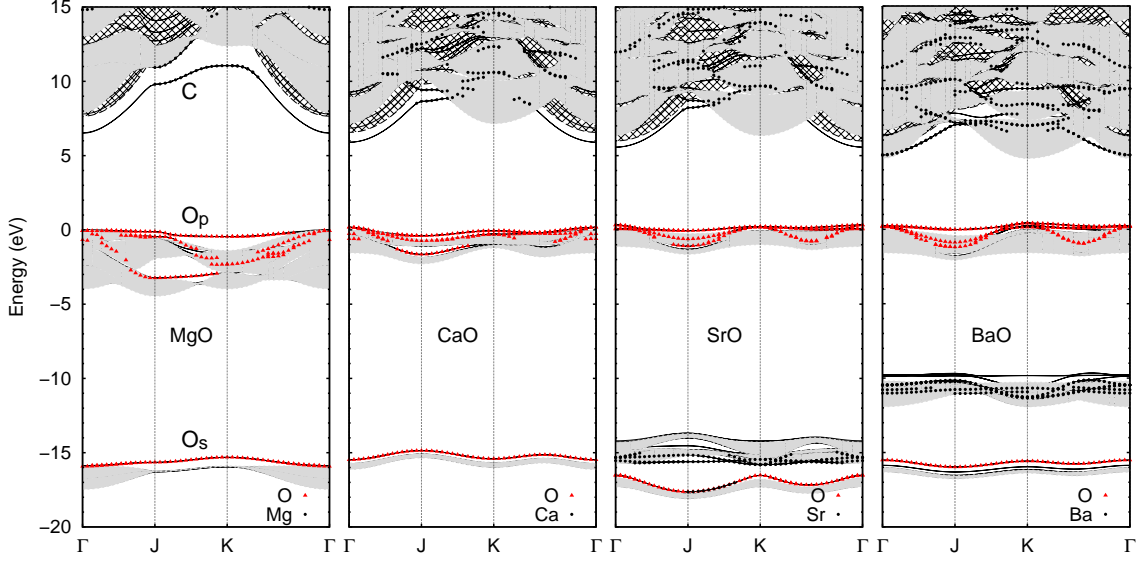


Figure 6.8: Calculated SIC surface band structures of the relaxed (001) surfaces of MgO, CaO, SrO and BaO along the high symmetry lines of the surface Brillouin zone. Red triangles and black circles mark bound surface states that are strongly localized *at* the surface oxygen atoms or *at* the cations, respectively. The parabolas (full lines) exhibit the dispersion of image states residing in vacuum *in front of* the surface. The gray-shaded regions represent the projected bulk band structure and the cross-hatched areas indicate the projected bands of free-electron vacuum states.

exhibits a positive rumpling, meaning that the surface O atoms are located further above the surface than the Mg atoms, while the latter surfaces show a negative rumpling. A very small interlayer relaxation is usually found for MgO(001) while it is larger and negative for the other oxide surfaces. The surface energy is found to decrease from the most to the least ionic surface, i.e., from MgO(001) to BaO(001). The results, which are well in accord with the literature data, corroborate these general notions.

The electronic structure of the relaxed (001) surfaces of the four oxides, as resulting from SIC calculations is shown in Fig. 6.8 along the high symmetry lines of the surface Brillouin zone. The grey shaded areas represent the projection of the bulk band structure. Red triangles and black dots mark bound surface states that are strongly localized at the surface O atoms and cations, respectively. The cross-hatched areas in the conduction band energy regions indicate the ranges of projected free-electron vacuum states, starting at

$$E = E_{\text{vac}} + \hbar^2 \mathbf{k}_{\parallel}^2 / 2m \quad (6.3)$$

with \mathbf{k}_{\parallel} being the two-dimensional wave vector parallel to the surface.

There are two distinctive differences to be noted in the projected conduction bands of the four surfaces. The projected bulk CBM lies at Γ in the case of MgO(001) while it occurs

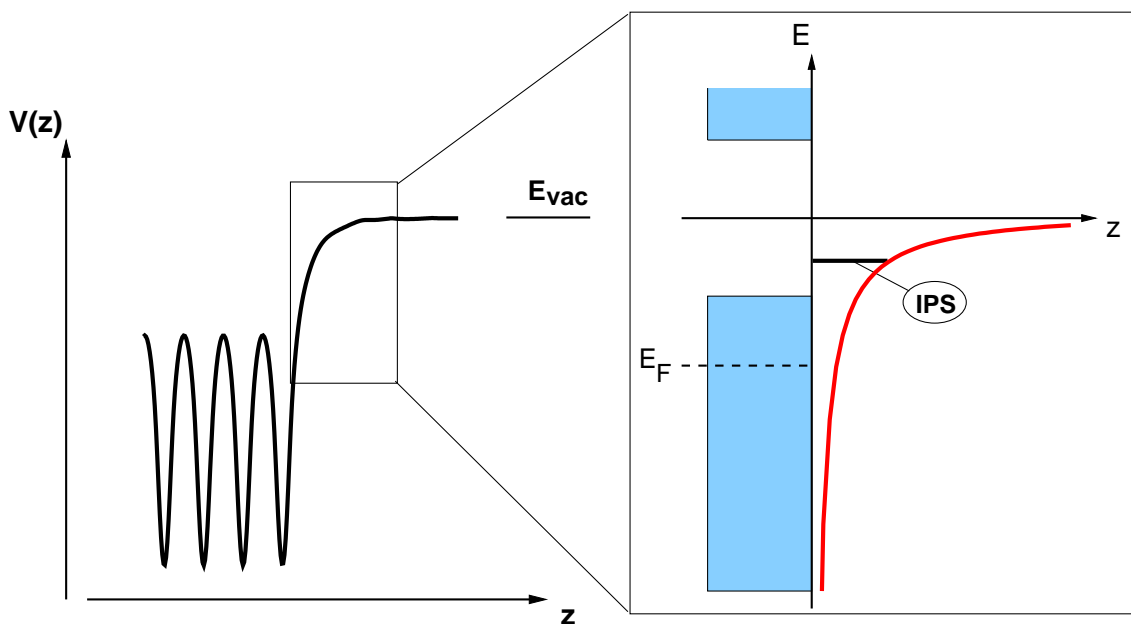


Figure 6.9: Schematic representation of the occurrence of image potential states. The left panel shows the x - y -averaged effective potential of the surface. In the right panel the energy range close to the vacuum level is enlarged and the position of an image potential state (IPS) is indicated.

at the K point of the surface Brillouin zone for the other three oxide surfaces. This is due to the fact that the bulk CBM is located at the Γ point of the bulk Brillouin zone in MgO as opposed to the X point for CaO, SrO and BaO.

Much more importantly, in the case of the MgO(001), CaO(001) and SrO(001) surfaces the projected free-electron vacuum states lie below the projected bulk conduction bands in sections of the surface Brillouin zone while they occur higher in energy than the latter in the case of the BaO(001) surface throughout the whole surface Brillouin zone. Thus the former three surfaces are negative electron affinity systems while the latter is not. This has significant influence on the surface electronic structure near the bottom of the projected conduction bands. Negative electron affinity surfaces allow for the formation of loosely bound image potential states. An electron can be trapped in the image potential if its energy lies below the vacuum level and it is reflected from the surface due to the lack of allowed projected bulk states in the range of its energy (cf. Fig. 6.9). Since the two-dimensional wave vector k_{\parallel} is a good quantum number this holds for all k_{\parallel} values at which the projected free-electron vacuum states are lower in energy than the projected bulk conduction bands.

Addressing the surface band structures in Fig. 6.8, one can note that all surfaces have some general features in common. They are all insulating, as could be expected. Most of the surface states occur close to the projected bulk bands which is typical for ionic

compounds. Separating a bulk insulator in two halves does not involve cutting covalent bonds. Thus no dangling bonds are generated at the surface, as is the case for typical semiconductors, and no salient dangling bond states occur. Instead, the ions are merely separated from each other giving rise to relatively small changes of the charge densities of occupied states so that localized surface states or ionic resonances occur very close to or within the projected bulk band energy regions, respectively.

To be more specific, the MgO(001) surface band structure is addressed in the left panel of Fig. 6.8 which shows the most salient bands of surface states. Some of these surface states have been labeled explicitly to ease the following discussion. In the valence band energy region, the band labeled O_s clearly has O $2s$ character and can be attributed to ionic O $2s$ states. Likewise, the almost dispersionless band close to VBM, labeled O_p , is solely derived from O $2p_z$ states. Furthermore, a salient band of unoccupied surface states occurs below the projected conduction bands which is labeled C , therefore. The character of the surface states in the C band is more intricate since it changes dramatically as a function of the surface parallel wave vector k_{\parallel} . Analyzing the wave functions of the respective states in detail, one finds that the C band consists from about J to $K\Gamma/3$ of surface states which are truly localized at the surface cations. From Γ to about J and from about $K\Gamma/3$ to Γ , on the contrary, it consists of image potential states which reside in vacuum in front of the surface. Electrons in these states can move freely parallel to the surface so that the k_{\parallel} dispersion of the band of image potential states is basically parabolic. Perpendicular to the surface they are localized in the image potential. It turns out that the image potential states exist in the k_{\parallel} space regions where the projection of the free-electron vacuum states is lower in energy than the projected bulk conduction bands, i.e., in the k space regions where the surface has negative electron affinity. The existence of image potential states at the MgO(001) surface has been pointed out previously [21, 151, 160].

To highlight the different character of the bound surface states and the image states in band C , Fig. 6.10 shows charge density contours of the unoccupied C band states at the K and Γ points of the surface Brillouin zone. They are drastically different. The C state at K has its charge density maximum above the surface cation, at which it is mostly localized, and extends into vacuum to some extent as is obvious in the left panel of Fig. 6.10. There are also small contributions on subsurface layers. Since the interaction of such localized surface states is weak parallel to the surface the dispersion of the C band from J to $K\Gamma/3$ is fairly weak. The C state at Γ , on the contrary, is mostly delocalized and neither directly related to the surface cations nor to the anions, as can be seen in the right panel of Fig. 6.10. Its charge density extends considerably into vacuum showing a very small surface corrugation, only. As a consequence, the dispersion of the C band around Γ is parabolic and thus free-electron like.

The band structures of the other three relaxed (001) surfaces in Fig. 6.8 show a number of similar features. As for MgO(001), also for the (001) surfaces of CaO, SrO and BaO one

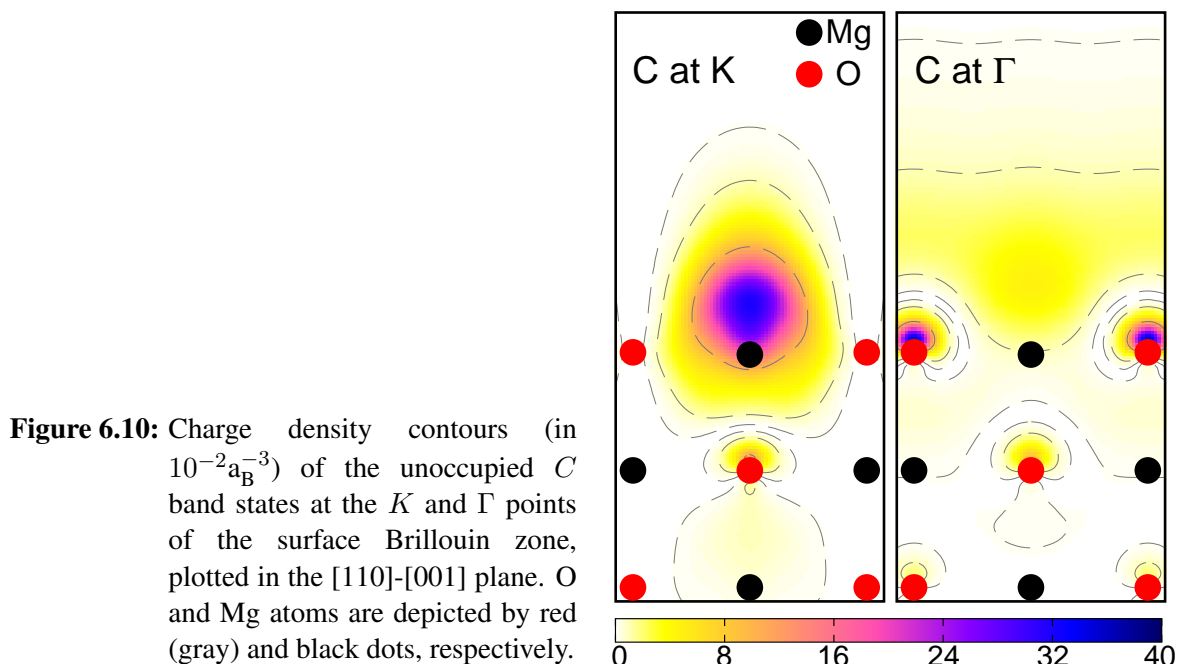


Figure 6.10: Charge density contours (in $10^{-2}a_B^{-3}$) of the unoccupied C band states at the K and Γ points of the surface Brillouin zone, plotted in the $[110]$ - $[001]$ plane. O and Mg atoms are depicted by red (gray) and black dots, respectively.

observes $O 2s$ - and $O 2p$ -derived bands of localized surface states or ionic resonances very close to or within the projected bulk valence bands, respectively. In addition, surface bands originating from cationic semicore p states occur within the valence bands, as can be seen in Fig. 6.8 for $SrO(001)$ and $BaO(001)$. Some of these bands originate from strongly localized surface states (shown by dotted lines) while others are derived from less localized surface states (shown by full lines). Interestingly, these bands are energetically lower than the projected bulk bands when they are associated with surface layer cations while the opposite is true for those associated to the subsurface layer cations. This is related to the reduced interlayer distance in the relaxed geometry and the opposite rumpling of the surface and subsurface layers. Like in the case of $MgO(001)$, the C band at the $CaO(001)$ and $SrO(001)$ surfaces consists of image potential states in similar sections of the surface Brillouin zone while in the complementary sections it consists of localized cationic surface states. Since the $BaO(001)$ surface has no negative electron affinity, the C band at the latter surface consists of truly bound surface states derived from Ba orbitals throughout the surface Brillouin zone.

As a more quantitative reference concerning characteristic energies of the four surfaces, the calculated bulk and surface band gap energies, ionization energies, electron affinities as well as the energies of the C band at Γ for all four oxide surfaces are summarized in Table 6.10. As mentioned already, all surfaces are insulating having a band gap decreasing with decreasing ionicity of the compounds from 6.5 eV for MgO to 4.4 eV for BaO . The energy difference $E_g - E_g^s$ between the bulk and surface gaps reduces from 1.4 eV over 1.3 eV and 0.8 eV to 0.4 eV with decreasing ionicity. This is due to intricate effects on

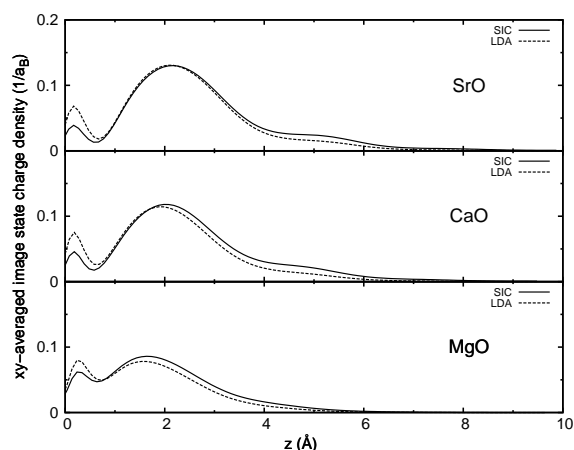
	MgO	CaO	SrO	BaO
E_g	7.9 (7.8)	7.2	6.4	4.8
E_g^s	6.5 (6.9)	5.9	5.6	4.4
E_I	7.7 (7.4)	6.5	6.0	5.6
E_A	-0.2 (-0.4)	-0.7	-0.4	0.8
E_C at Γ	6.5 (6.9)	5.9	5.6	4.9

Table 6.10: Bulk (E_g) and surface (E_g^s) band gaps, ionization energy (E_I), electron affinity (E_A) and energy of the lowest unoccupied state at the Γ point (E_C at Γ) of the (001) alkaline-earth metal oxides surfaces (in eV), as calculated within SIC. The results of the GW calculation for MgO(001) from Ref. [21] are given in parentheses.

both the energetic positions of the surface VBM and CBM in the compounds. As can be seen in Fig. 6.8, the surface VBM shows a slight increase in energy with respect to the bulk VBM, fixed at 0 eV, when proceeding from MgO to BaO. This is related to the missing cations above the surface O atoms, raising the energy of the surface O p_z band. At the same time, the energy of the C band at Γ moves closer to, or for BaO(001) even higher than the projected bulk CBM. The ionization energy E_I constitutes the onset (at Γ) of the continuum of projected vacuum states indicated by the cross-hatched areas in Fig. 6.8. It decreases with decreasing ionicity from MgO to BaO following a well known general trend. The difference of the vacuum energy and the energy of the bulk gap, given by $E_I - E_g$, finally yields the value of the negative electron affinity at the Γ point of the surface Brillouin zone. As pointed out before, BaO(001) does not exhibit negative electron affinity.

In order to assess the accuracy of the SIC results for the relaxed (001) surfaces, one can compare the calculated electronic properties with quasiparticle results from GW calculations [21] and with experimental data which are available for MgO(001)-(1 \times 1), only. The respective quasiparticle results are given in parentheses in Table 6.10. The overall agreement between the SIC and the GWA results is very satisfying, the deviations being 0.4 eV at most. Both calculations agreeingly arrive at the result that MgO(001) is a negative electron affinity surface and obtain the absolute energy position of the image state E_C at Γ in reasonably close agreement (6.5 eV in SIC and 6.9 eV in GWA). Nevertheless, it should be noted, that the energy position of the image state E_C at Γ relative to the vacuum level, i.e, relative to the ionization energy E_I , results as $E_{\text{vac}} - 1.2$ eV in SIC and at $E_{\text{vac}} - 0.5$ eV in GWA. Formally, the difference is due to the fact that the deviations between E_I and E_C at Γ of the two approaches are opposite. Physically, it is due to the fact, that the one-particle DFT-SIC calculations do not properly describe the $-1/4z$ dependence of the image potential while the many-body GW approximation does. Therefore,

Figure 6.11: Comparison of x - y -averaged image state charge densities on MgO, CaO, and SrO(001) as resulting from LDA and SIC calculations, respectively.



the image state results more strongly bound with respect to the vacuum level in SIC than in GWA. Nevertheless, the absolute energy position of the image state resulting in SIC (6.5 eV) and GWA (6.9 eV) is satisfyingly close.

In this context, a comparison of the x - y -averaged IPS charge density as resulting from LDA and SIC calculations as in Fig. 6.11 is instructive. While the previous remark that the calculations do not properly describe the $-1/4z$ dependence of the image potential holds for both approaches, slight differences are noticeable, nevertheless. In all three cases, the image states calculated within the SIC approach reside marginally further in front of the surface. Especially the local charge density maximum close to $z = 0$ is reduced compared to LDA. This is due to more intricate changes to the effective potential. While SIC does not yield the true long-range characteristic due to the cutoff of the respective components in the construction of the pseudopotentials, the localized short-range contributions from the surface anions give rise to the observed changes.

The surface band gap of MgO(001)-(1×1) has been determined by EELS experiments [150–152] to be 6.2 eV. In view of the fact that EELS measures the onset of transitions to the lowest exciton state, the result for the one-particle surface band gap of 6.5 eV compares favorably with experiment. It appears that the exciton binding energy at the MgO(001) surface is fairly small in the order of 0.3 eV. This notion is further corroborated by the experimental results of Schintke *et al.* [152] who find basically the same gap value in their STS and EELS experiments although STS probes transitions between one-particle states while EELS resolves the onset of transitions to the lowest exciton state. The above comparison of the results with data from far more elaborate GWA calculations and experiment for MgO(001)-(1×1) reveal that the description of the surface electronic structure of MgO(001) within the SIC approach is satisfyingly reliable. On this basis it is expected that the electronic structure of the other three (001) alkaline-earth metal oxide surfaces investigated in this work is appropriate, as well.

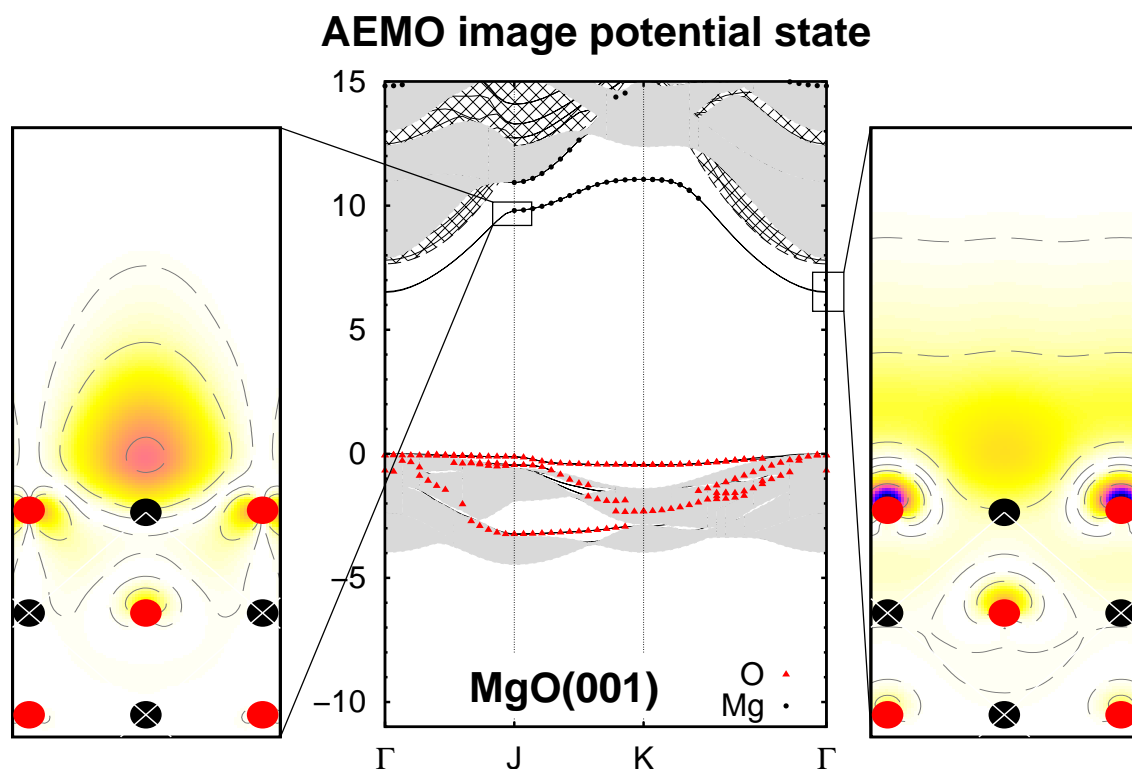


Figure 6.12: SIC band structure and charge densities at the Γ - and J -point for the image potential state at the MgO(001) surface.

6.2.3. On the nature of alkaline-earth metal oxide image potential states

Image potential states are classically known to appear on metal surfaces due to the easy polarizability of the free charge density (cf. Ref. [174]). The surfaces of the alkaline-earth metal oxides (AEMO) investigated in this work are obviously insulating and thus do not contain free electrons. It can be assumed that the characteristics of the image potential states hosted at such surfaces differ from the traditional IPS, for instance at Cu(001).

Figure 6.12 again shows the surface band structure of MgO(001) and the charge density contours of the IPS at Γ and J for easier comparison. The basic features of the IPS have been discussed above, most notably its tendency to strongly localize depending on the actual \mathbf{k} -point in the surface Brillouin zone. At Γ the charge density is delocalized and predominantly homogenous in front of the surface plane. Moving to the J -point, a symmetry-induced formation of a nodal plane through the position of the top layer anions (oxygen) is found. Concomitantly the charge density localizes, though it still remains visibly above the surface.

To compare these characteristics to those of a traditional image potential state, the band

structure of Cu(001) has been analyzed, as well. Figure 6.13 shows the resulting surface band structure as well as the respective charge density contours of the IPS at the Γ and J points of the Brillouin zone. Overall, the band structure of Cu is vastly different compared to that of ionic insulators. Copper features one highly dispersive s -band crossing the Fermi level giving rise to its metallicity. Closely below E_F reside five flat d -bands. Consequently, there is no fundamental surface band gap at Cu(001). However, there are characteristic pockets in selected regions of the surface Brillouin zone, most notably the one at Γ .

Principally, there are some analogies between the IPS at Cu(001) and MgO(001). At the Γ -point the traditional IPS at Cu(001) is almost entirely detached from the surface. It reaches much further into the vacuum region than the related state at MgO(001). Also, there is an additional nodal plane parallel to the surface between the top layer copper atoms and the reflected charge density. Moving to the J -point, one realizes again that there is a symmetry-induced localization of the density due to the formation of a nodal plane perpendicular to the surface. Still, the charge density lobes extend considerably into the vacuum region. Of course, the atomic structure of Cu(001) is conceptually different to the one of MgO(001) as the positions of the respective Mg atoms in MgO are empty in the former case. This significantly affects the resulting electronic structure.

In order to highlight the differences between these two image potential states and a traditional bound surface state, the band structure of MgS(001) is shown in Fig. 6.14. The atomic structure of the surface has first been determined using the optimized lattice constant. Afterwards, the geometry has been scaled to a smaller lattice parameter to ensure that the empty surface band resides close to the bulk projection. The band structure itself hence should only be regarded as a qualitative model system. No quantitative information should be extracted.

In principle, the surface band structure of MgS(001) exhibits many similarities to that of MgO(001). In the bulk crystal, anionic p -bands ($S\ 3p$) define the upper valence bands and determine the surface band gap to the Mg $3s$ conduction bands. Due to the change of the anionic atom from oxygen to sulfur, the bonding character of MgS is less ionic compared to MgO. The fact that the empty band resides close to the projected bulk conduction bands clearly influences the character of the state visible by the charge density plots in Fig. 6.14. At Γ the charge density is definitely localized at the top surface layer, with contributions coming both from Mg and S atoms. Also, a significant amount is found at subsurface layers. No coupling to the vacuum is registered. At the J -point only slight changes are to be noted. The formation of the symmetry-induced nodal plane again leads to an increased localization of the respective charge density at the surface cation. Qualitatively, however, the state is very similar at Γ and J .

In Fig. 6.15 an energy level diagram schematically sketches the different types of surface states at the Γ point of the surface Brillouin zone. Group A summarizes the energetic

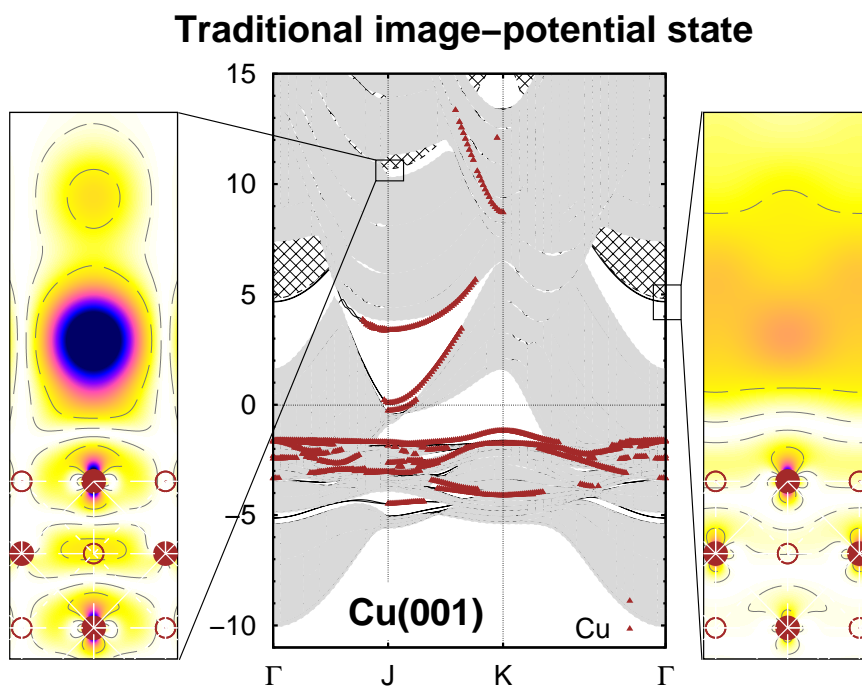


Figure 6.13: SIC band structure and charge densities at the Γ - and J -point for the image potential state at the Cu(001) surface.

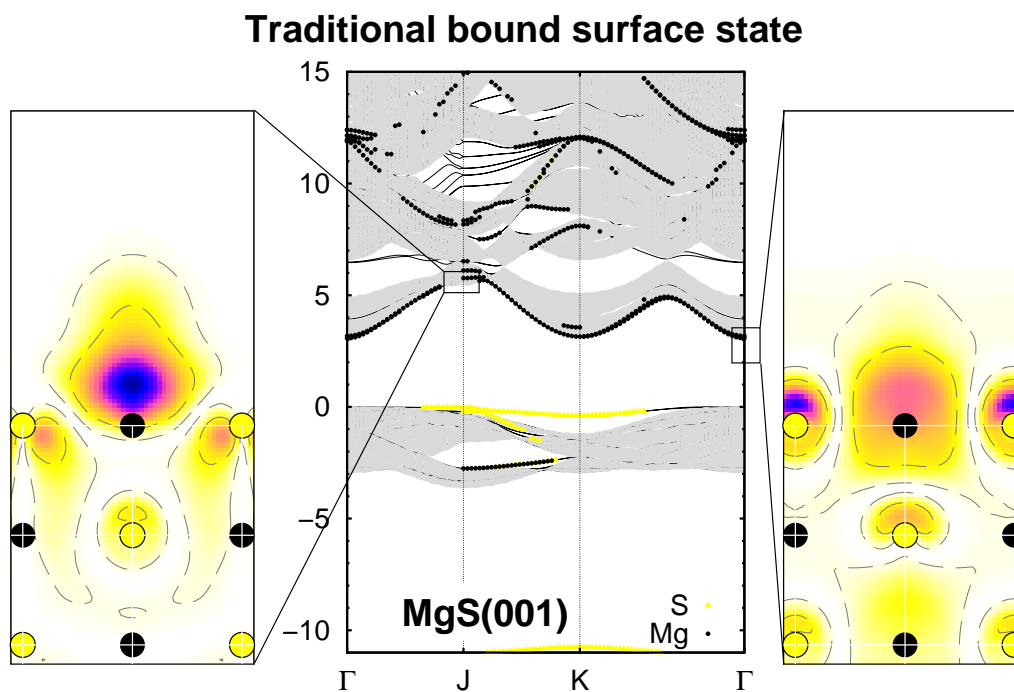


Figure 6.14: SIC band structure and charge densities at the Γ - and J -point for the localized surface state at the MgS(001) surface.

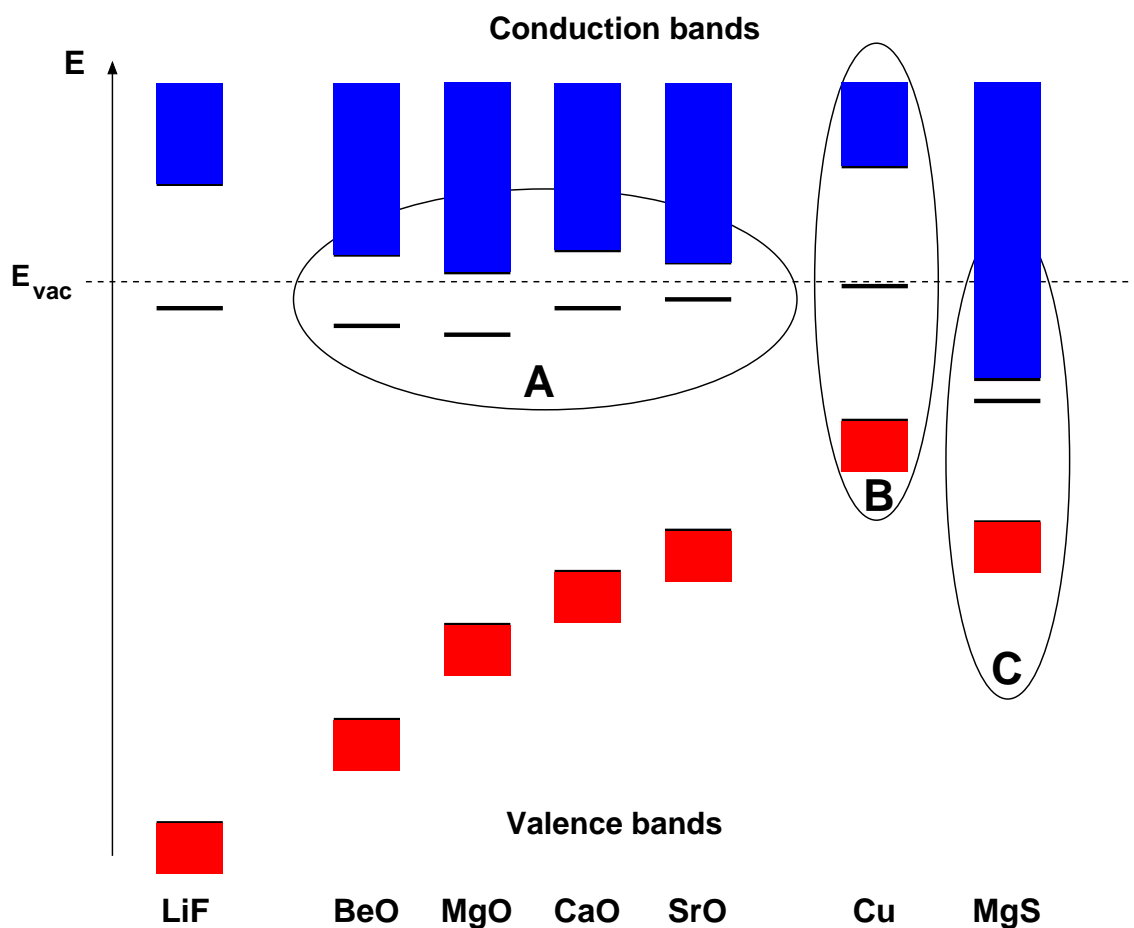


Figure 6.15: Γ -point energy level schematics for different types of surfaces. The onsets of the projected valence and conduction bands are indicated by the red and blue bars, respectively. The isolated lines give the energies of the empty surface state. All energies are referred to the respective vacuum level, for a meaningful comparison. See text for definition of groups.

characteristics of the image potential states at the alkaline-earth metal oxide surfaces. As was discussed above, the respective states reside in closer proximity to the surface than the traditional IPS at Cu(001). Inspecting Fig. 6.15, two factors become apparent that contribute to these features. Firstly, the IPS at Γ at Cu(001) is energetically very close to the vacuum level. Here the effective potential (cf. Fig. 6.9) is very weak and the IPS can consequently extend very far into vacuum. Secondly, there is a considerable distance to projected bulk conduction and valence band states. Any coupling to such bulk states is thus unlikely and the IPS is repelled from the surface. In contrast, the respective states at the alkaline-earth metal oxide surfaces reside somewhat lower with respect to E_{vac} and are consequently bound stronger to the surface, in general. More importantly, they are also rather close to the projected bulk conduction bands. Compared to Cu(001) there is a much higher possibility for the IPS to couple to these bulk states. It can be argued that the energetic proximity of the conduction bands inhibits the coupling to the vacuum and the concomitant detachment from the surface. This notion is further corroborated by the GWA results known for LiF(001) and MgO(001). In Ref. [21] it has been pointed out that in the former case the quasiparticle corrections allow for the IPS to extend considerably farther into vacuum as compared to the LDA result. For MgO(001) in contrast, no such effect is observed and the IPS remains relatively close to the surface. As the conduction bands are similarly far away from the IPS for LiF(001) as for Cu(001), this can be considered as an indication that the stronger possibility for the IPS at alkaline-earth metal oxides to couple to these states is the driving factor for the stronger localization of their IPS.

To finalize this discussion, the situation for the bound surface state at MgS(001) is straightforward. The surface is not negatively electron affine in the first place. The energy of the surface state is far below the vacuum energy and actually much closer to the projected bulk states. Coupling to the vacuum is energetically impossible for such a surface.

6.2.4. Summary

In this chapter, the structural and electronic properties of group-II oxides have been studied using density-functional theory with self-interaction-corrected pseudopotentials. The properties of bulk BeO, MgO, CaO, SrO and BaO and their relaxed non-polar (10 $\bar{1}$ 0) and (001) surfaces, respectively, have been analyzed in detail. For the bulk crystals, the SIC approach yields reliable structural properties and band structures which are much superior to standard LDA results and in good agreement with the results of more elaborate quasiparticle calculations and experiment. Based on optimized relaxation geometries of the surfaces, the electronic structure of the respective (001) surfaces has been scrutinized with special attention to the salient bands of unoccupied surface states. In particular, it was found that the results for MgO(001) on the valence and conduction band structure, as well as the ionization potential and negative electron affinity agree very well with the results

of GWA calculations. They are also in satisfying accord with EELS data. The parabolic sections of its lowest unoccupied surface band are interpreted as originating from image potential states. The surface band structures of CaO(001) and SrO(001) reveal very similar characteristics with image potential states, as well, also exhibiting an appreciable separation of the unoccupied C band from the projected bulk conduction bands. In contrast, it turns out that BaO(001) is not a negative electron affinity surface and as such can not give rise to an image state band. In this case the C band constitutes a band of true surface states throughout the surface Brillouin zone which are mostly localized at the Ba cations from which they are derived.

Chapter 7.

Structural, elastic and electronic properties of SiC, BN and BeO nanotubes

The initial discovery of carbon nanotubes (CNTs) by Iijima [22] in 1991 has sparked considerable interest in this kind of nanosized one-dimensional structures due to their unique physical properties and the associated potential for applications.

While experimental observations indicate that CNTs preferentially exist in multi-walled configurations with an inter-wall distance comparable to the spacing of planes in graphite, the generation of single-walled structures consisting of a single rolled-up graphene strip is technically feasible, as well. The chirality and diameter of such NTs are uniquely specified [175] by the pair of helical indices (n, m) defining the vector $\mathbf{c}_h = n\mathbf{a}_1 + m\mathbf{a}_2$, where $\mathbf{a}_1, \mathbf{a}_2$ are the unit vectors of a graphitic sheet.

In addition to CNTs, a considerable number of different composite nanoscale tubular structures has either already been fabricated, based on crystals like BN, SiC, MoS₂, WS₂ [176–179], or suggested, as in the case of BeB₂ and B₂O [180] or BeO [110] NTs. Carbon, SiC, BN and BeO NTs differ in their increasing ionicity. As a consequence, the properties of SiC, BN and BeO NTs are different from those of the covalently bonded, homopolar CNTs. Most notably, the electronic characteristics are strongly dependent on the type of chemical binding in these solids. While CNTs have been found to be either metallic or semiconducting depending on their helicity [175, 181, 182], previous studies have shown that both BN and SiC NTs are semiconducting, their structural as well as electronic properties depending in characteristic ways on the chirality and the diameter of the NTs [23, 183–196].

Theoretically, BNNTs have been studied quite intensively during the last decade on different levels of sophistication [183], e.g., by tight-binding calculations [183–185], density-functional theory within local-density approximation [183, 186–189] and hybrid functional calculations [193]. Studying excitons in NTs, Park *et al.* [197] as well as Wirtz *et al.* [198] have more recently carried out *GW* quasiparticle energy calculations on a

(8, 0) or several selected BNNTs, respectively. SiCNTs and defects in SiCNTs have been addressed only in the last couple of years. Cluster or DFT supercell calculations have been reported [23, 190–192, 194, 195] and very recently H and its interaction with B acceptors and N donors in (8, 0) zigzag and (5, 5) armchair SiCNTs have been studied employing a hybrid density-functional approach, as well [196]. The computations within hybrid density-functional theory are considerably more demanding than usual DFT-LDA calculations. Concerning BeONTs, only one recent DFT-LDA study [110] is available.

The application potential of carbon and non-carbon nanotubes is enormous. It ranges from nano-electronic and nano-mechanic devices, such as nanotube field-effect transistors, nano gears, or gas sensing devices, to macroscopic uses, e.g. in lightweight composite materials. Their curvature leads to a large surface area that can be used, for instance, for hydrogen storage and also holds many opportunities for functionalization of nanotubes by adsorption of atoms or molecules. Among the non-carbon nanotubes those based on silicon carbide are expected to open roads to the design of nanocables or improved nanotips for use in atomic force microscopy or STM [199].

For applications of NTs in electronic devices and from a more fundamental point of view the accurate determination of the band gap energy of NTs is crucial. Within standard DFT-LDA band gaps are significantly underestimated, while structural properties follow with a good level of confidence. Many of the studies reported so far suffer from the LDA shortcomings as far as the electronic properties of NTs are concerned.

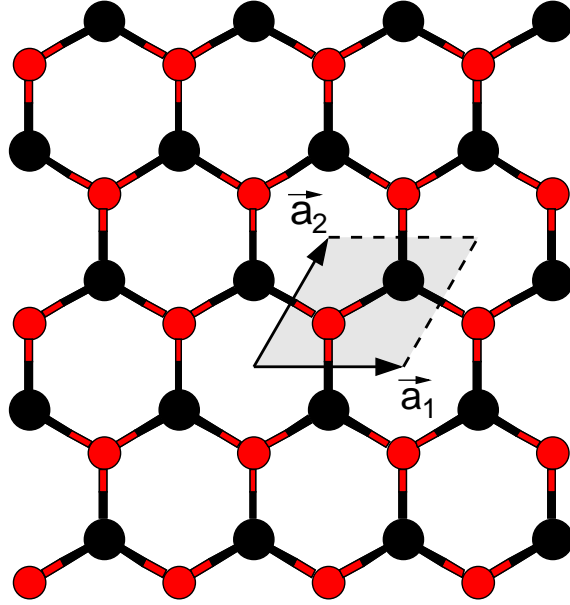
In this chapter a fairly comprehensive comparative study of structural, elastic and electronic properties of a large variety of SiC, BN and BeO NTs in $(n, 0)$ zigzag and (n, n) armchair configurations with n values ranging from 4 to 15 and diameters up to 25 Å, respectively, is performed. Applying the SIC approach to SiC, BN and BeO NTs on equal footing, yields a host of quantitatively and qualitatively comparable results. In particular, a most quantitative analysis of the effects which the increasing ionicity of the chemical bond in these tubular nanostructures has on their physical properties is given.

7.1. Graphitic monolayers

Materials which can under certain conditions occur in a layered graphite-like structure are of scientific interest in many respects. It is often possible to design very thin films of such substances, i.e. by chemical vapor deposition. If such a thin film consists of only a single layer of the graphitic structure, the constituting atoms arrange a planar hexagonal honeycomb structure.

Figure 7.1 shows the top view of such a single graphitic monolayer. Its hexagonal unit

Figure 7.1: Top view of a graphitic monolayer. The grey shaded area indicates the two-dimensional unit cell containing one cation (black) and one anion (red), respectively.



cell (grey shaded) is spanned by the two vectors

$$\begin{aligned} \mathbf{a}_1 &= a(1, 0, 0) \\ \mathbf{a}_2 &= a\left(\frac{1}{2}, \frac{\sqrt{3}}{2}, 0\right) . \end{aligned} \quad (7.1)$$

The non-primitive cell contains one cation and one anion, respectively, at the positions

$$\begin{aligned} \boldsymbol{\tau}_C &= a\left(1, \frac{1}{\sqrt{3}}, 0\right) \\ \boldsymbol{\tau}_A &= a\left(\frac{1}{2}, \frac{1}{2\sqrt{3}}, 0\right) . \end{aligned} \quad (7.2)$$

The lattice constant is related to the anion-cation bond length b according to $a = \sqrt{3}b$. The particular geometric structure evidently influences the electronic structure of such a system. A planar hexagonal structure as shown in Fig. 7.1 is based on a sp^2 hybridization of the base atoms, most importantly of the anions. Assuming that the layer is oriented within the x - y -plane, planar hybrids are formed from the atomic s -, p_x -, and p_y -states, while the p_z orbitals are oriented perpendicular to the layer. The latter in particular are of great importance with regard to the electronic structure of the layers. They define the existence and potential characteristics of a gap between occupied and empty monolayer bands. Therefore, a most reliable description of such bands is required from a theoretical point of view. In this respect, published results in the literature for bulk graphite or hexagonal boron nitride [200,201] point to the importance of so called extended interlayer

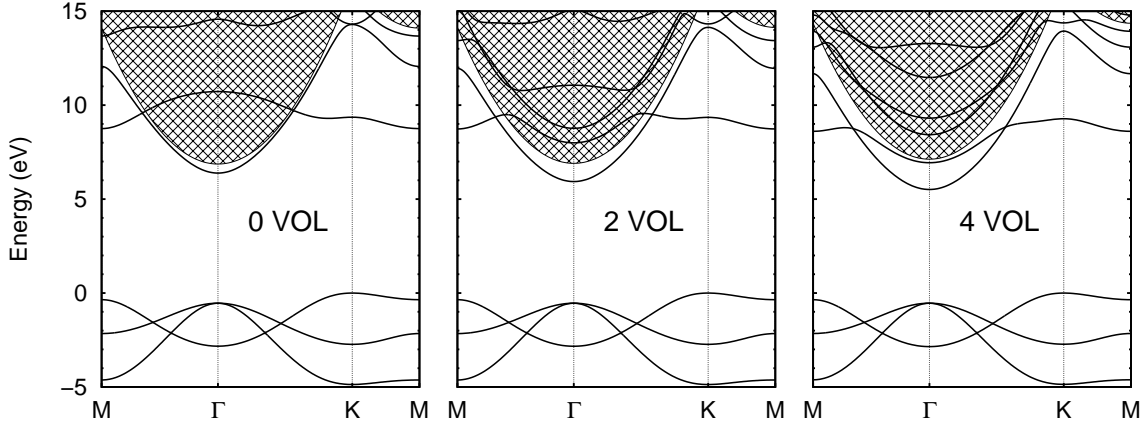


Figure 7.2: Influence of additional vacuum orbital layers (VOL) on the electronic band structure of a graphitic monolayer of BeO as resulting from LDA calculations. The cross-hatched area indicates the projection of free electron vacuum states.

states that couple the individual planar layers. These extended states need to be suitably represented in electronic structure calculations. In the present case, such extended states are the free-electron states of the vacuum. A basis set of plane waves would be an intuitive choice as a basis for the expansion of the wave function in such a situation. In terms of the basis of localized Gaussian orbitals used in this work, this means that not only the atomic positions can be used as localization points of these orbitals. Instead additional Gaussian orbitals τ_i^{VO} must be placed into the vacuum, i.e. at a distance κ above and below the atomic positions τ_i as in Eq. (7.2) of the monolayer:

$$\tau_i^{\text{VO}} = \tau_i \pm \kappa \hat{z}. \quad (7.3)$$

Any pair of such vacuum orbital layers (VOL) is then uniquely defined by the value of κ . Later, the physical properties of SiC, BN, and BeO graphitic monolayers and nanotubes shall be studied. For these three substances, the effect of additional VOL is expected to be largest in BeO. Therefore, a study of the influence of different configurations of VOL is most instructive for this highly ionic compound. In Figure 7.2 the electronic band structure along the high-symmetry lines of the two-dimensional Brillouin zone of such a BeO monolayer is shown as resulting from different configurations of vacuum orbital layers. The low-lying O $2s$ band is omitted in the figures. The band structure in the left panel of Fig. 7.2 is the result of a calculation without an additional orbital layer (0VOL). Three O $2p$ derived bands are occupied and their energetic maximum is found at the K point. In contrast the lowest unoccupied band has its minimum at Γ , forming an indirect band gap. The same characteristics are visible in the other two band structures. The band structure in middle panel (2VOL) of Fig. 7.2 results from a calculations with two (one above, one below the monolayer) VOL with a decay constant of 0.24 a.u.^{-2} and $\kappa = 1.5a$. A calcu-

Table 7.1: Anion-cation bond lengths (in Å) in graphitic monolayers and bulk crystals, as resulting from LDA and SIC calculations. Experimental bulk-bond lengths are given for comparison.

	graphitic layer		bulk crystal		
	LDA	SIC	LDA	SIC	Exp
SiC	1.76	1.77	1.87	1.89	1.89 ^a
BN	1.41	1.43	1.54	1.56	1.56 ^b
BeO	1.52	1.53	1.63	1.65	1.65 ^c

^afrom Ref. [57]

^bfrom Ref. [202]

^cfrom Ref. [116]

lation with four vacuum orbital layer ($\kappa_1 = a$, $\kappa_2 = 2a$) yields the electronic structure in the right panel. While the valence bands are hardly affected, significant changes in the conduction bands are notable. On the one hand, the width of the band gap reduces with increasing number of vacuum orbitals (0VOL: 6.38 eV; 2VOL: 5.93 eV; 4VOL: 5.51 eV). On the other hand, the dispersion of the second unoccupied band is dramatically changed. Without any additional orbitals, this band is rather flat and has a maximum at the Γ -point. When additional orbitals are introduced into the system, the dispersion of the band changes since the respective states can now delocalize more. This also affects higher bands that clearly move down in energy in the conduction band region. With 4VOL the dispersion of these bands has become more and more parabolic, hinting at the nearly-free electron character of these states. As expected it is very important to place virtual Gaussian orbitals into the vacuum regions in order to appropriately describe the properties of unoccupied electronic states at graphitic monolayers.

Keeping in mind that the studies in this work primarily concern the structural and electronic properties of nanotubes, graphitic monolayers and nanotubes must be calculated using comparable basis sets. Due to the unique tubular structure of the latter it is not possible to add two additional vacuum orbital layers above and below the atomic plane or ring, respectively, as has turned out to be most suitable above. As a compromise, the subsequent calculations for the monolayers are performed with additional s -like orbitals with a decay constant of 0.14 a.u.^{-2} placed at $\kappa = 1.5 a$, respectively.

Now, structural and electronic properties of the SiC, BN and BeO graphitic monolayers constitute the large diameter limit of the NTs and thus the respective results serve as an important reference for the NTs to be discussed subsequently.

The respective bond lengths for the three graphitic layers, as resulting from standard LDA and SIC calculations, are summarized in Table 7.1. Respective bulk-bond lengths of wurtzite SiC and BeO as well as zinblende BN, as calculated previously (cf. Ref. [18] as well as Sec. 3.6 and 6.1.1) using LDA and SIC, are given for reference in Table 7.1 in comparison with experimental values. The bulk-bond lengths calculated within SIC are in very good accord with experiment. Therefore, it is to be expected that the bond lengths

	graphitic layer		bulk crystal		Exp
	LDA	SIC	LDA	SIC	
SiC	2.85	3.94	2.12	3.33	3.33 ^a
BN	4.51	6.19	4.45	6.13	6.10 ^b
BeO	5.73	8.72	7.41	10.50	10.6 ^c

^afrom Ref. [57]

^bfrom Ref. [203]

^cfrom Ref. [120]

Table 7.2: Fundamental band gap energies (in eV) of SiC, BN and BeO graphitic monolayers and wurtzite SiC and BeO as well as zincblende BN bulk crystals, resulting from LDA and SIC calculations. Experimental bulk gaps are given for comparison.

for the graphitic layers calculated within SIC are very accurate, as well. The LDA values slightly underestimate the experimental values by about 1% but these deviations are not really significant. It is interesting to note that all bond lengths in the graphitic layers are systematically smaller by about 0.12 Å than in the tetrahedrally bonded bulk crystals. As a matter of fact, the same obtains for graphene (1.42 Å), as compared to bulk diamond (1.54 Å).

The energy gaps of SiC, BN and BeO graphitic layers are summarized in Table 7.2. Respective calculated bulk band gaps are given for reference in comparison with measured bulk band gaps, as well. The LDA bulk gaps underestimate the experimental gaps very significantly, as usual. On the contrary, the bulk gaps calculated within SIC are in very good agreement with experiment. In addition, the SIC band gap for the BN graphitic sheet of 6.2 eV is in good accord with the reported results from quasiparticle [201] (6.0 eV) and hybrid-functional [193] (6.3 eV) calculations. Hence, one can expect the SIC band gaps for the three graphitic layers to be also very accurate.

The electronic band structures of graphene and SiC, BN and BeO graphitic sheets are shown in Fig. 7.3. In contrast to graphene, which exhibits a characteristic degeneracy of the π and π^* states at the Fermi level occurring at the K point of the hexagonal Brillouin zone, all three types of graphitic sheets investigated in this work are wide-band-gap semiconductors or insulators. The band gaps of the SiC and BN sheets are direct at K . The band gap of BeO is indirect with the valence band maximum at K and the conduction band minimum at Γ . Since the two atoms in the unit cell are not identical for SiC, BN and BeO graphitic layers, the aforementioned degeneracy of the π and π^* states is removed. As a consequence, the electronic properties of respective NTs can be expected to be qualitatively different from those of carbon NTs.

In all three cases the valence bands consist of a low-lying anionic s band and three upper mostly anionic s, p bands. The latter originate in all three compounds from mixtures of anionic p and cationic s states. The uppermost of these s, p bands has mainly s, p_z character. Since the p_z orbitals are perpendicular to the graphitic layers their interaction is a fairly small π - π interaction giving rise to the weaker dispersion of these bands, as

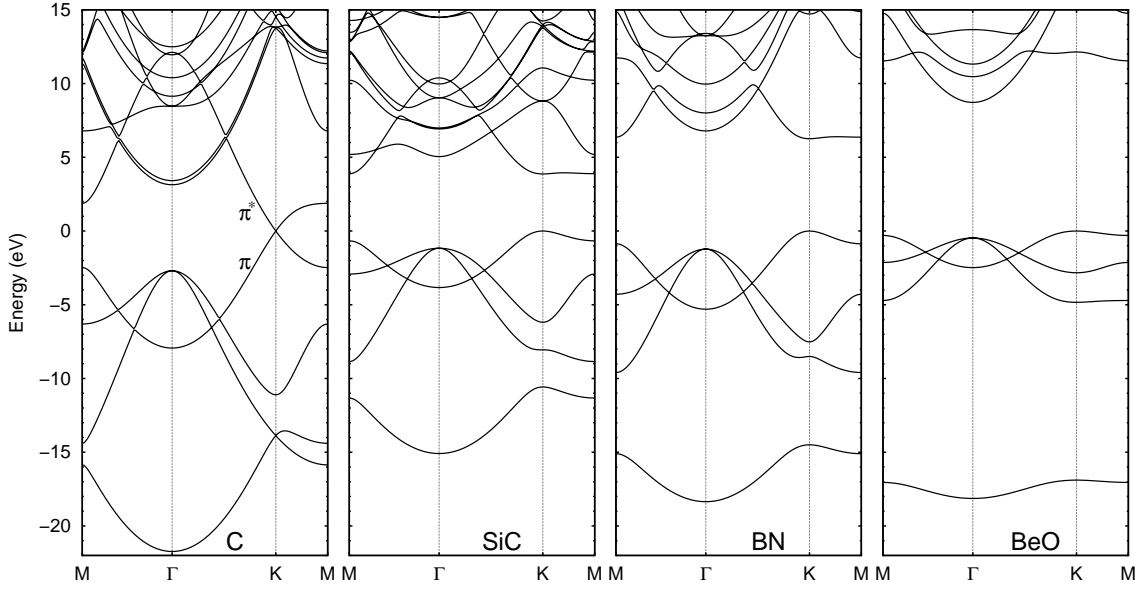


Figure 7.3: Band structure of graphitic SiC, BN and BeO monolayers along the high-symmetry lines of the two-dimensional hexagonal Brillouin zone, referred to the top of the valence bands, as calculated within the SIC approach.

compared to the other two upper valence bands. The spatial dependence of the interaction of the p_z orbitals is the same as that of valence s orbitals. As a consequence, the low-lying s and the upper s, p_z valence bands have very similar dispersions, as is most obvious in Fig. 7.3. The anion p_x, p_y orbitals, on the contrary, lie in the graphitic sheets giving rise to a significantly different and larger dispersion, therefore. The lowest conduction band in the SiC and BN sheets occurs at the K point of the hexagonal Brillouin zone and has cationic p character. The lowest conduction band of the highly ionic BeO compound occurring at the Γ point, on the contrary, mainly originates from cation s orbitals. The bandstructure of the BN graphitic sheet in Fig. 7.3, in particular in the energy range from -10 to +10 eV, is in very good accord with the respective GW quasiparticle band structure as reported by Blase *et al.* [201].

The dispersion of the lowest conduction band of BeO is basically parabolic and thus nearly free-electron (NFE) like. The physical origin and the NFE character of the respective lowest conduction band at Γ in BN has been discussed in detail previously [184,201]. The VBM states of the SiC and BN graphitic sheets are largely similar. The CBM state of the BeO graphitic sheet, on the contrary, shows very significant differences to the CBM states of the SiC and BN graphitic sheets. To highlight this difference, only the charge density contours of the VBM and CBM states of SiC and BeO graphitic sheets are compared in Fig. 7.4. The figure clearly reveals that the VBM state has anionic p_z character in both compounds. The CBM state of the SiC graphitic sheet is of Si p_z character while that of the BeO sheet has O s character. It is largely different from the former state

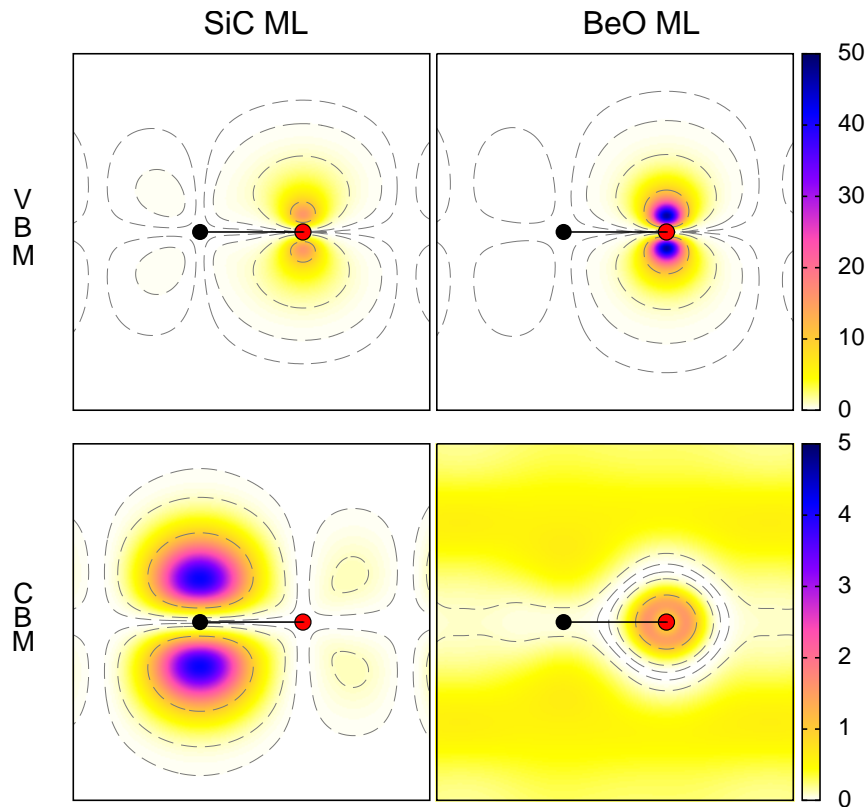


Figure 7.4: Charge density contours of the VBM and CBM states of graphitic SiC (left panels) and BeO (right panels) monolayers (in $10^{-2} a_B^{-3}$) plotted in the $[110]$ - $[001]$ plane containing the anion-cation bond, as calculated within the SIC approach. Anions and cations are depicted by red and black dots, respectively. The VBM and CBM states for SiC and the VBM state for BeO occur at the K point. The CBM state for BeO occurs at the Γ point.

exhibiting its NFE-character. This has important consequences for the electronic properties of BeO, as compared to SiC and BN NTs.

7.2. Nanotubes

Based on the results obtained for the graphitic monolayers of SiC, BN, and BeO in the previous section, the attention now turns to the calculation of the respective properties of the nanotubes that are derived from them.

7.2.1. Geometry of nanotubes

At first, the geometric properties of nanotubes must be defined. For simplicity, this will be done for the original carbon nanotubes, in which the anionic and cationic positions as

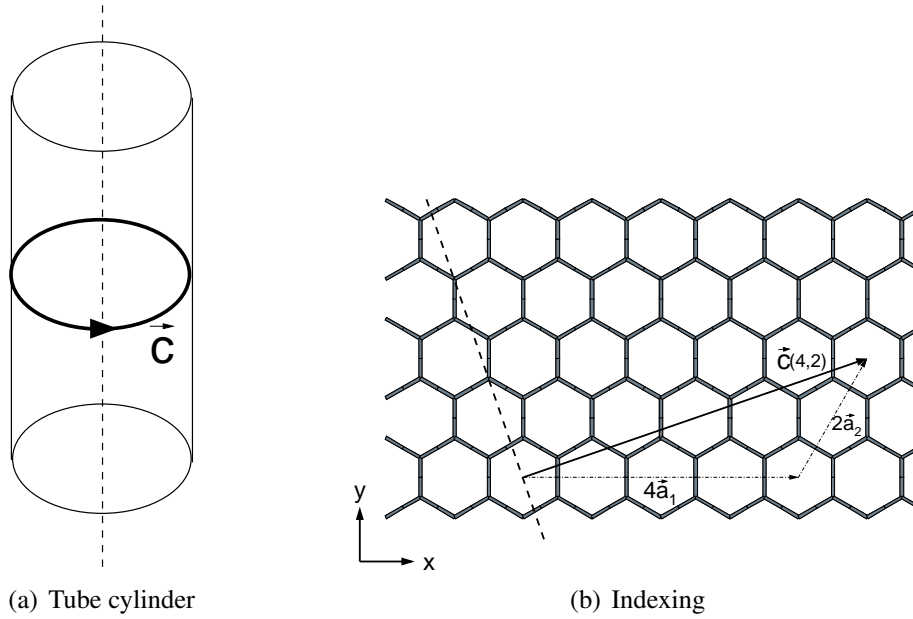


Figure 7.5: Schematic depiction of (a) the cylinder defining the nanotube and (b) the definition of the vector $\mathbf{c}_\perp(n, m)$ for $n = 4$ and $m = 2$.

in Eq. (7.2) are both occupied by carbon atoms. As has already been mentioned before, the starting point for the construction of the nanotubes is a two-dimensional graphitic monolayer, which is in this case also known as graphene. This layer, or better a certain stripe of it, shall now be rolled on the surface of a cylinder. Depending on the orientation of the stripe relative to the graphene layer, a huge variety of configurations is possible in this regard.

The cylinder as in Fig. 7.5(a) is uniquely characterized by its longitudinal axis and a circumferential vector $\mathbf{c}_\perp(n, m)$, which is identical to one of the translational vectors within the hexagonal graphene layer. With the vectors \mathbf{a}_1 and \mathbf{a}_2 as in Eq. (7.1) it is hence defined as

$$\mathbf{c}_\perp(n, m) = n\mathbf{a}_1 + m\mathbf{a}_2 . \quad (7.4)$$

The longitudinal axis is to be chosen perpendicular to this vector and consequently can be considered to be parallel to another vector $\mathbf{c}_\parallel(n, m)$, which defines the stripe within the graphene layer. Finally the nanotube is uniquely identified by the index pair (n, m) .

The vector $\mathbf{c}_\parallel(n, m)$ parallel to the longitudinal axis of the tube can be generated by rotating $\mathbf{c}_\perp(n, m)$ by $\pi/2$ around the z -axis and is expressed in Cartesian components as

$$\mathbf{c}_\parallel^\lambda(n, m) = a\lambda \left[\frac{\sqrt{3}}{2}m\hat{\mathbf{x}} - \left(n + \frac{m}{2}\right)\hat{\mathbf{y}} \right] . \quad (7.5)$$

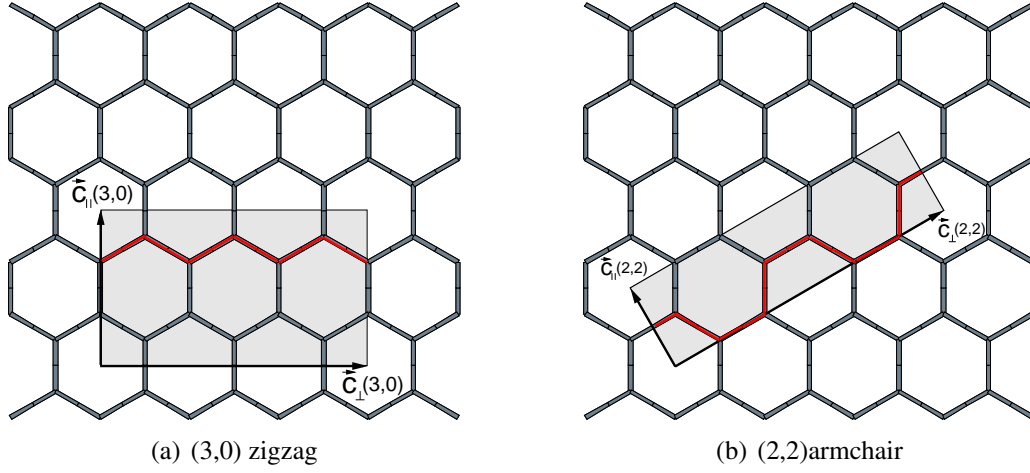


Figure 7.6: Planar stripes of a (3,0) zigzag and a (2,2) armchair nanotube within the graphitic layer. Also shown are the vectors \mathbf{c}_\perp and \mathbf{c}_\parallel for both structures as well as the resulting edge profile of the tubes (red).

The factor λ is introduced to ensure that the vector truly ends at a point of the 2D graphene lattice, such as

$$\mathbf{R}(n', m') = a \left[\left(n' + \frac{m'}{2} \right) \hat{\mathbf{x}} + \frac{\sqrt{3}}{2} m' \hat{\mathbf{y}} \right]. \quad (7.6)$$

The sought vector $\mathbf{c}_\parallel(n, m)$ is now identical to the shortest lattice vector $\mathbf{R}(n', m')$ pointing in the same direction as $\mathbf{c}_\parallel^\lambda(n, m)$. The condition

$$\hat{\mathbf{c}}_\parallel^\lambda(n, m) = \hat{\mathbf{R}}(n', m') \quad (7.7)$$

yields a set of compatible $\{(n', m')\}$ fulfilling the set of conditional equations

$$\begin{aligned} \frac{\sqrt{3}m}{\sqrt{n^2 + nm + m^2}} &= \frac{2n' + m'}{\sqrt{n'^2 + n'm' + m'^2}} \\ \frac{-2n - m}{\sqrt{n^2 + nm + m^2}} &= \frac{\sqrt{3}m'}{\sqrt{n'^2 + n'm' + m'^2}}. \end{aligned} \quad (7.8)$$

Out of this set, the combination for which $\Omega = |n' + m'|$ is smallest, i.e. the shortest compatible lattice vector, finally defines $\mathbf{c}_\parallel(n, m)$.

Typically one distinguishes between nanotubes of different geometry, most notably between the two special cases of zigzag ($m = 0$) and armchair ($m = n$) nanotubes. In Fig. 7.6 the stripes of the graphene layer that form a zigzag (3,0) and an armchair (2,2) nanotube, respectively, are shown. The red line indicates the respective edge profile of the nanotube, which is the basis for the nomenclature. For these special tubes, the deter-

mination of the translational vectors $\mathbf{c}_{\parallel}(n, m)$ and $\mathbf{c}_{\perp}(n, m)$ simplifies.

1. Zigzag nanotubes ($\mathbf{m} = \mathbf{0}$)

In this case, the relation $m' = -2n'$ solves Eq. (7.8). It follows that

$$\mathbf{R}(n', -2n') = -a\sqrt{3}n'\hat{\mathbf{y}} \stackrel{!}{=} \mathbf{c}_{\parallel}(n, 0) \quad (7.9)$$

The shortest vector is found for $n' = -1$. Then it finally holds that

$$\mathbf{c}_{\parallel}(n, 0) = a\sqrt{3}\hat{\mathbf{y}} \quad (7.10)$$

The length of this vector now equates to the periodicity length of the nanotube and defines the nanotube unit cell lattice constant $a^{\text{NT}} = \sqrt{3}a$. All in all, the stripe of the graphene layer that belongs to a zigzag nanotube is given by

$$\begin{aligned} \mathbf{c}_{\perp}(n, 0) &= a^{\text{NT}} \frac{n}{\sqrt{3}} \hat{\mathbf{x}} \\ \mathbf{c}_{\parallel}(n, 0) &= a^{\text{NT}} \hat{\mathbf{y}} \neq \text{fnc.}(n) \end{aligned} \quad (7.11)$$

Note that the vector $\mathbf{c}_{\parallel}(n, 0)$ of a zigzag nanotube is independent of the tube index n . The circumference of the tube cylinder U is equal to the length of $\mathbf{c}_{\perp}(n, 0)$, and the ideal tube diameter $d(n, 0)$ results as

$$d(n, 0) = \frac{a^{\text{NT}}n}{\sqrt{3}\pi} = \frac{an}{\pi} \quad (7.12)$$

2. Armchair nanotubes ($\mathbf{m} = \mathbf{n}$)

Here, one obtains solutions of Eq. (7.8) for $n' = -m'$. Consequently it follows that

$$\mathbf{R}(n', -n') = a \left[\frac{n'}{2} \hat{\mathbf{x}} - \frac{\sqrt{3}n'}{2} \hat{\mathbf{y}} \right] \stackrel{!}{=} \mathbf{c}_{\parallel}(n, n) \quad (7.13)$$

Again, the shortest vector is found for $n' = \pm 1$. Choosing $n' = -1$ yields

$$\mathbf{c}_{\parallel}(n, n) = \mathbf{R}(-1, 1) = a \left[-\frac{1}{2} \hat{\mathbf{x}} + \frac{\sqrt{3}}{2} \hat{\mathbf{y}} \right] \quad (7.14)$$

For an armchair nanotube, the one-dimensional lattice constant amounting to $a^{\text{NT}} = a$ is shorter than for its zigzag counterpart. The graphene stripe that is rolled into

cylindrical form is then defined by

$$\begin{aligned} \mathbf{c}_{\perp}(n, n) &= a^{\text{NT}} \left[\frac{3n}{2} \hat{\mathbf{x}} + \frac{\sqrt{3}n}{2} \hat{\mathbf{y}} \right] \\ \mathbf{c}_{\parallel}(n, n) &= a^{\text{NT}} \left[-\frac{1}{2} \hat{\mathbf{x}} + \frac{\sqrt{3}}{2} \hat{\mathbf{y}} \right] \neq \text{Fnc.}(n) . \end{aligned} \quad (7.15)$$

The armchair nanotube has a diameter of

$$d(n, n) = \frac{\sqrt{3}a^{\text{NT}}n}{\pi} = \frac{\sqrt{3}an}{\pi} = \sqrt{3}d(n, 0) . \quad (7.16)$$

It is apparently by a factor of $\sqrt{3}$ larger than the diameter of a zigzag nanotube.

With this knowledge of the graphene stripe defined by the vectors $\mathbf{c}_{\perp}(n, m)$ and $\mathbf{c}_{\parallel}(n, m)$ within the layer and the non primitive basis

$$\boldsymbol{\tau} = \tau_x \hat{\mathbf{x}} + \tau_y \hat{\mathbf{y}} + \tau_z \hat{\mathbf{z}} \quad (7.17)$$

the stripe can be rolled onto the surface of a cylinder with the respective orientation and diameter. The cylinder is described within a related Cartesian coordinate system $(\hat{\mathbf{x}}', \hat{\mathbf{y}}', \hat{\mathbf{z}}')$. It is suitable to orient the vector \mathbf{c}_{\parallel} parallel to the z' -axis in such a fashion that the origin of the stripe is located at the point $(R, 0, 0)$, where R is the radius of the tube. The original vector \mathbf{c}_{\perp} points into x' -direction. Now this vector can be rolled onto the surface of the cylinder by uniquely assigning an angle φ to the atomic positions along \mathbf{c}_{\perp} . If one explicitly labels these positions as $\tau_x = \bar{x} \cdot |\mathbf{c}_{\perp}| = \bar{x} \cdot U$, the angle is calculated as

$$\varphi = \pi \left(2\bar{x} + \frac{1}{2} \right) \quad (7.18)$$

and the atomic position on the tube cylinder are given by

$$\boldsymbol{\tau}' = R [\sin(\varphi) \hat{\mathbf{x}}' + \cos(\varphi) \hat{\mathbf{y}}'] + \tau_y \hat{\mathbf{z}}' . \quad (7.19)$$

This procedure shall be exemplified for the armchair (2,2) nanotube from Fig. 7.6(b) in the following. If the shown coordinate system is rotated clockwise by $\frac{\pi}{6}$, \mathbf{c}_{\perp} points into x - and \mathbf{c}_{\parallel} to the y -direction. The positions of the atoms within the stripe are

Table 7.3: Determination of the atomic positions within a unit cell of armchair (2,2) nanotube.

\bar{x}	φ	$\tau'_x = R \sin$	$\tau'_y = R \cos$	$\tau'_z = \tau_y$
$\frac{1}{12}$	$\frac{2\pi}{3}$	$\frac{3a}{2\pi}$	$-\frac{\sqrt{3}a}{2\pi}$	$\frac{a}{2}$
$\frac{1}{6}$	$\frac{5\pi}{6}$	$\frac{\sqrt{3}a}{2\pi}$	$-\frac{3a}{2\pi}$	0
$\frac{1}{3}$	$\frac{7\pi}{6}$	$-\frac{\sqrt{3}a}{2\pi}$	$-\frac{3a}{2\pi}$	0
$\frac{5}{12}$	$\frac{4\pi}{3}$	$-\frac{3a}{2\pi}$	$-\frac{\sqrt{3}a}{2\pi}$	$\frac{a}{2}$
$\frac{7}{12}$	$\frac{5\pi}{3}$	$-\frac{3a}{2\pi}$	$\frac{\sqrt{3}a}{2\pi}$	$\frac{a}{2}$
$\frac{2}{3}$	$\frac{11\pi}{3}$	$-\frac{\sqrt{3}a}{2\pi}$	$\frac{3a}{2\pi}$	0
$\frac{5}{6}$	$\frac{1\pi}{6}$	$\frac{\sqrt{3}a}{2\pi}$	$\frac{3a}{2\pi}$	0
$\frac{11}{12}$	$\frac{1\pi}{3}$	$\frac{3a}{2\pi}$	$\frac{\sqrt{3}a}{2\pi}$	$\frac{a}{2}$

$$\begin{aligned}
\tau_1 &= \frac{b}{2}\hat{x} + \frac{a}{2}\hat{y} & \tau_2 &= b\hat{x} \\
\tau_3 &= 2b\hat{x} & \tau_4 &= \frac{5b}{2}\hat{x} + \frac{a}{2}\hat{y} \\
\tau_5 &= \frac{7b}{2}\hat{x} + \frac{a}{2}\hat{y} & \tau_6 &= 4b\hat{x} \\
\tau_7 &= 5b\hat{x} & \tau_8 &= \frac{11b}{2}\hat{x} + \frac{a}{2}\hat{y} .
\end{aligned} \tag{7.20}$$

Rolling this stripe onto the surface of the cylinder according to Eq. (7.19) results in the atomic positions that are summarized in Table 7.3.

Calculating the properties of one-dimensional periodic structures, like nanotubes in this case, requires an extension of the slab concept used for the calculations of surface properties. In order to retain the formal three-dimensional periodicity that is necessary for the Fourier expansion of the local potential, one has to substitute the originally one-dimensional configuration with a three-dimensional ersatz geometry. Assuming that the longitudinal axis of the nanotube lies in x -direction and is located in the center of a box of the edge length L , i.e. at $y = z = 0$, periodic images of this tube must be placed at neighboring edges parallel to \mathbf{e}_x . The size L must be chosen large enough so that the resulting vacuum region is large enough to electronically decouple periodic images of the nanotube. So all in all, the nanotube is simulated using a simple orthorhombic unit cell with the unit vectors

$$\begin{aligned}
\mathbf{a}_1 &= a^{\text{NT}}(1, 0, 0) \\
\mathbf{a}_2 &= a^{\text{NT}}(0, L, 0) \\
\mathbf{a}_3 &= a^{\text{NT}}(0, 0, L) .
\end{aligned} \tag{7.21}$$

The associated reciprocal lattice is spanned by the vectors

$$\begin{aligned}
 \mathbf{b}_1 &= \frac{2\pi}{a^{\text{NT}}} (1, 0, 0) \\
 \mathbf{b}_2 &= \frac{2\pi}{a^{\text{NT}}} (0, 1/\zeta, 0) \\
 \mathbf{b}_3 &= \frac{2\pi}{a^{\text{NT}}} (0, 0, 1/\zeta) .
 \end{aligned} \tag{7.22}$$

It is clear that for large values of L , a one-dimensional Brillouin zone results, effectively. Its irreducible wedge is limited by the two high-symmetry points Γ and $X = \frac{2\pi}{a^{\text{NT}}} (1/2, 0, 0)$. Along this line, the electronic band structure of the nanotubes must be determined. For Brillouin zone integrations, an equidistant set of special \mathbf{k} -points along the k_x -direction according to

$$k_x = \frac{2\pi}{a^{\text{NT}}} \frac{1}{2} \frac{2i + 1}{2N} \tag{7.23}$$

must be employed. N is the total number of special points and $i = 0, \dots, N - 1$.

Calculating elastic and structural properties

For the reliable study of its electronic properties, the exact knowledge of the underlying atomic structure of the nanotubes is vital. Concerning possible technological applications of these NTs their elastic and structural properties are of particular interest. The procedure of the generation of atomic positions for nanotubes as described above only yields an ideal geometry. Due to significantly distorted bonds in this configuration compared to the graphitic monolayer, it can be expected that the atoms gain energy upon relaxation.

Still, the optimized structure of the monolayer constitutes the starting point for any further optimization. As the nanotube structure is a very different structure compared to the planar graphitic sheet, it does not necessarily hold that the ideal lattice constant a^{NT} as defined in the previous paragraph actually yields the minimum energy structure. Therefore the following procedure has proven to be suitable in terms of an LDA optimization.

1. Determination of the total energy curve $E_{\text{tot}}^{\text{rel,LDA}}(a^{\text{NT}})$
 For a set of values around the ideal nanotube lattice constant derived from the graphitic sheet, the atomic structure is optimized. From the minimum and the curvature of the resulting total energy curve the ground state properties are calculated.
2. At $a_{\text{opt}}^{\text{NT}}$ the final atomic structure is optimized. When N is the number of atoms in one nanotube unit cell, the energy difference

$$E_s = \frac{1}{N_{\text{NT}}} E_{\text{NT}}^{\text{tot}} - \frac{1}{2} E_{\text{sheet}}^{\text{tot}} \tag{7.24}$$

is the energy necessary to form the nanotube from the graphitic sheet, which is called the strain energy.

3. Finally, for the totally optimized structure, the electronic properties can be determined.

Due to the lack of an explicit method to calculate SIC forces, there are some intricacies in the determination of the self-interaction corrected elastic and structural parameters. First of all, for all LDA optimized structures, the SIC total energy is calculated and evaluated as before. Then, for the obtained $a_{\text{opt}}^{\text{NT,SIC}}$ an LDA calculation is employed to obtain the relaxed atomic positions at this lattice constant. Based on this optimized geometry, a SIC calculation yields the respective band structure of the NTs.

As for the calculational details, the wave functions are expanded using three shells of atom-centered Gaussian orbitals of s , p , d , and s^* symmetry per atom with the decay constants (in atomic units) 0.18, 0.50 and 1.00 for Si, 0.25, 1.00 and 2.86 for C, 0.20, 0.42 and 1.90 for B, 0.31, 1.36 and 6.00 for N, 0.18, 0.40 and 0.90 for Be and 0.30, 0.90 and 3.50 for O. The inclusion of both fairly localized and extended orbitals is necessary to achieve an appropriate representation of the localised ionic bond states on the NT cylinder as well as the exponential decay of the wavefunctions into vacuum. To appropriately describe also the nearly free electron state in the lower conduction bands characteristic for the hexagonal sheets, as previously discussed, additional localized Gaussian orbitals are placed on planes in vacuum above and below the hexagonal sheets. Rolling up the sheets into nanotubes, one point of concern becomes immediately obvious. The additional orbital localization points outside the tubes constitute a separate tube which causes no problems. Inside the tubes, however, localization points originating from opposite inner sides of the NT can come very close to one another so that numerical instabilities could arise. To avoid such instabilities, the additional Gaussian orbitals inside the tubes are placed only along the tube axis. Vacuum layers of approximately 12 Å thickness in the lateral directions of the respective systems are used so that unphysical interactions between neighboring sheets or NTs are avoided. Six and ten uniformly distributed special k points along the NT axis are used for the treatment of zigzag and armchair NTs, respectively.

7.2.2. Structural and elastic properties

First, the structure of the NTs is addressed. When stripes of graphitic SiC, BN or BeO sheets are rolled up into single cylindrical tubes the anions and cations relax from their ideal atomic positions. The cations move slightly inward towards the tube axis, while the anions move outward with respect to their ideal positions. This reduces the total energy of the system since the electron-electron repulsion is lowered. As a result, the NT

surface becomes buckled. After relaxation, the radial geometry of the tubular structures is characterized by two concentric cylindrical tubes, with an outer anionic and an inner cationic cylinder. The strength of the buckling is defined by the radial buckling parameter

$$\beta = \bar{r}_a - \bar{r}_c, \quad (7.25)$$

where \bar{r}_c and \bar{r}_a are the mean radii of the cation and anion cylinders, respectively. The values for the radial buckling of SiC, BN and BeO NTs, as resulting from SIC calculations are shown in Fig. 7.7. For more quantitative comparisons, the respective values are also summarized in Tables 7.4, 7.5, and 7.6. Judging from the data, there is no dependence of β on NT helicity. The independence of the radial buckling on helicity has previously been observed for BNNTs by Hernández *et al.* [185], as well. For all three compounds, the radial buckling decreases with increasing NT diameter and is expected to vanish in the limit of very large NT diameters. The absolute values for β are larger for SiC than those for BeO and BN NTs, which can be explained by the larger Si–C bond length (see Table 7.1) in combination with the physical mechanism giving rise to the relaxed minimum-energy structure. The observed relaxation pattern is a consequence of the curvature strain in the ideal NT structure. By rolling a graphitic stripe up into cylindrical form, the previous planar sp^2 environment is distorted. When the ions arrange in two concentric cylinders as in the equilibrium structure, the cations locally restore that particular coordination with their three neighboring anions. The bond angles do not deviate significantly from 120° after relaxation. Additionally, one observes a small contraction of the bond lengths in the order of $\sim 1\%$. Since this restoration of the sp^2 coordination is a common tendency in ionic systems – as has also been pointed out for a number of surface relaxation patterns of such materials in earlier chapters – it is apparent that the larger absolute values for the radial buckling of SiC compared to BeO and BN NTs is mainly due to its larger bond length.

Next the strain energy necessary to form a NT is addressed. It is defined as the difference in total energy per atom between a NT and the respective graphitic sheet

$$E_s = \frac{1}{N_{\text{NT}}} E_{\text{NT}}^{\text{tot}} - \frac{1}{2} E_{\text{sheet}}^{\text{tot}}, \quad (7.26)$$

where N_{NT} is the number of atoms in the NT unit cell. In simple terms, E_s is the energy per atom necessary to roll up the graphitic stripe into tubular form.

In Fig. 7.8 the strain energy E_s of the NTs resulting from SIC calculations is plotted as a function of their average diameter. Respective values are also summarized in Tables 7.4–7.6. From Fig. 7.8 it becomes apparent that also the strain energy progression with diameter d is independent of the NT helicity and resembles a classical $\sim d^{-2}$ law. As has been pointed out in Ref. [184], the strain energy of BNNTs is somewhat lower

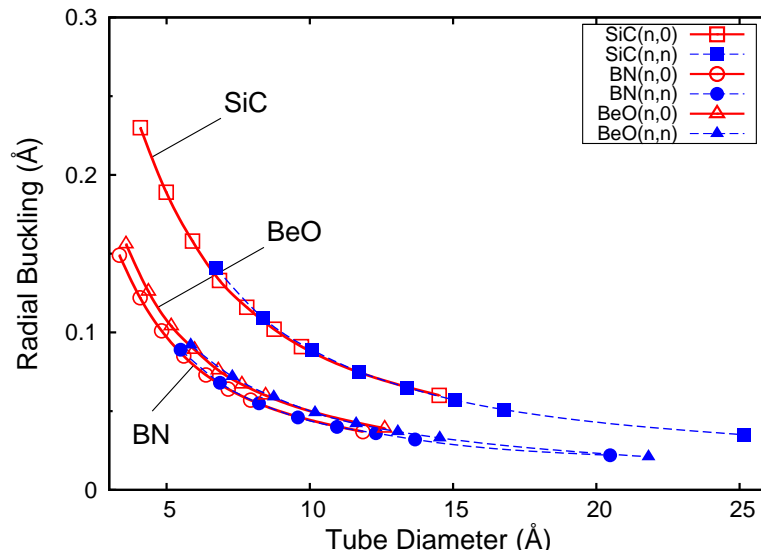


Figure 7.7: Radial buckling β (in Å) of $(n,0)$ zigzag (open symbols) and (n,n) armchair (filled symbols) SiC, BeO and BN NTs as functions of the tube diameter d . Squares, triangles and circles represent results for SiC, BeO and BN, respectively. The solid and dashed lines are drawn to guide the eye.

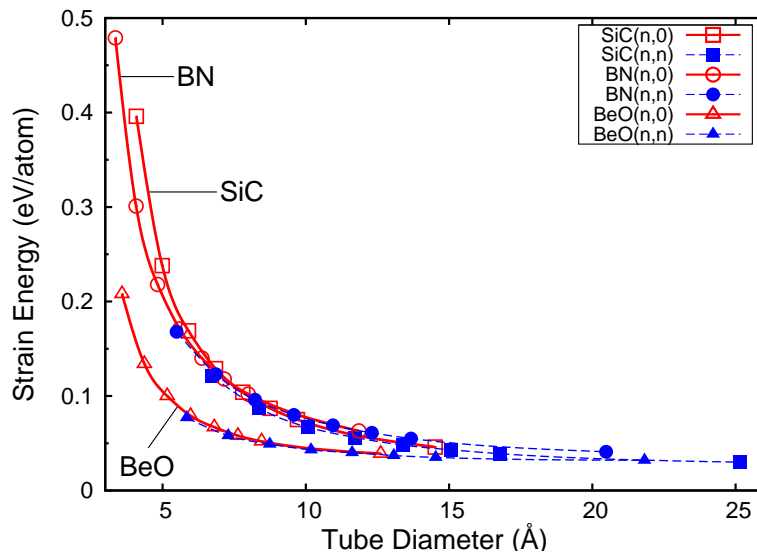


Figure 7.8: Strain energy of SiC, BN and BeO $(n,0)$ zigzag (open symbols) and (n,n) armchair (filled symbols) NTs as functions of the tube diameter d . See caption of Fig. 7.7 for further details.

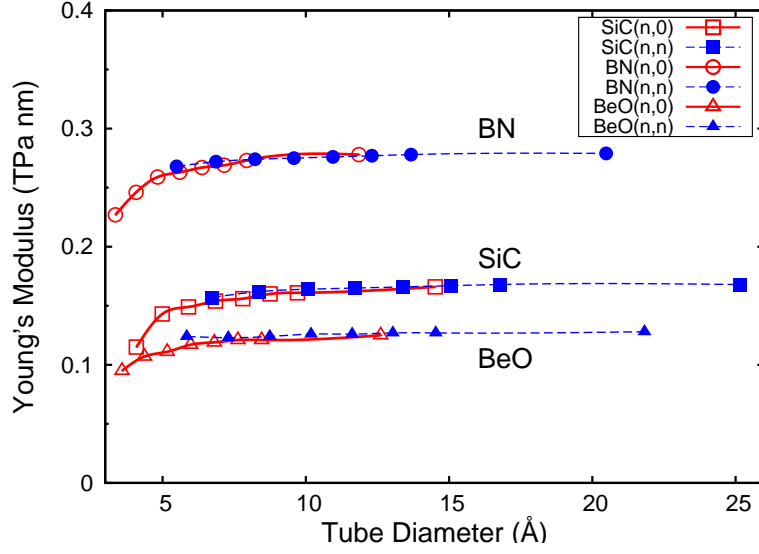


Figure 7.9: Modified Young's moduli Y_s (in TPa nm) of $(n, 0)$ zigzag and (n, n) armchair BN, SiC and BeO NTs as a function of the tube diameter d . See caption of Fig. 7.7 for further details.

than that of carbon NTs. The *ab initio* results for BNNTs calculated within the SIC framework are in good agreement with the respective values calculated previously within tight-binding [184] or standard LDA [186, 191, 192]. They are also in general accord with the strain energies obtained by Hernández *et al.* [185] for BNNTs from a nonorthogonal tight-binding approach in which the tight-binding parameters have been obtained by fitting DFT-LDA results. The calculated progression of the strain energy for SiCNTs is in good agreement with the progression calculated by Zhao *et al.* [23] within DFT-LDA. The strain energies for SiC and BN NTs in Fig. 7.8 are fairly similar. For BeO NTs, the strain energy results significantly lower (up to about $d \sim 12$ Å) which is due to the much higher ionicity of this compound as compared to SiC and BN. Rolling respective sections of graphitic BeO layers up into NTs needs less energy. The O $2p_z$ band is very narrow and the charge density of the CBM state is localized at the O atoms and fairly smooth and small around the Be atoms. In all three cases, the strain energy approaches zero for large NT diameters only very slowly since the NTs become equivalent to graphitic layers only for very large diameters.

Another interesting structural feature of NTs is their behaviour under uniaxial strain along the NT axis. It is described by Young's modulus, which is conventionally defined as the second derivative of the total energy with respect to the strain $\epsilon = \frac{a - a_{\text{opt}}}{a_{\text{opt}}}$

$$Y = \frac{1}{V_0} \left. \frac{\partial^2 E}{\partial \epsilon^2} \right|_{\epsilon=0}, \quad (7.27)$$

Table 7.4: Structural, elastic and electronic properties of SiC NTs. Tube diameters d and radial buckling parameters β are given in Å, strain energies E_s in eV per atom, modified Young's moduli Y_s in TPa nm, and band gap energies E_g in eV.

(n,m)	d	β	E_s	Y_s	E_g
SiC					
(4,0)	4.09	0.230	0.396	0.115	0.62
(5,0)	4.99	0.189	0.238	0.143	1.16
(6,0)	5.90	0.158	0.169	0.149	1.81
(7,0)	6.85	0.133	0.129	0.154	2.38
(8,0)	7.80	0.116	0.104	0.156	2.56
(9,0)	8.75	0.102	0.087	0.160	2.81
(10,0)	9.71	0.091	0.075	0.161	3.04
(15,0)	14.52	0.060	0.046	0.166	3.42
(4,4)	6.73	0.141	0.121	0.157	3.14
(5,5)	8.38	0.109	0.087	0.162	3.47
(6,6)	10.07	0.089	0.067	0.164	3.49
(7,7)	11.73	0.075	0.056	0.165	3.63
(8,8)	13.40	0.065	0.048	0.166	3.65
(9,9)	15.07	0.057	0.043	0.167	3.72
(10,10)	16.77	0.051	0.039	0.168	3.74
(15,15)	25.16	0.035	0.030	0.168	3.78

where V_0 is the equilibrium volume. As the volume for a hollow cylinder is $V_0 = 2\pi LR\delta R =: S_0\delta R$ it is necessary to adopt a certain convention for the shell thickness δR in the case of single-walled NTs. In Ref. [185] the authors suggested to describe the NT stiffness independent of δR by a modified Young's modulus

$$Y_s = \frac{1}{S_0} \left. \frac{\partial^2 E}{\partial \epsilon^2} \right|_{\epsilon=0}, \quad (7.28)$$

which is related to the standard Young's modulus by $Y_s = Y\delta R$. In Fig. 7.9 the progression of the calculated values for Y_s with NT diameter is shown. Respective values are summarized in Tables 7.4–7.6. It is clearly visible that for BN, SiC and BeO NTs the modified Young's moduli reach saturation already at fairly small diameters $d \sim 10$ Å. Significant differences between armchair and zigzag configurations are not to be noted. The saturation values of Y_s are 0.28, 0.17 and 0.13 TPa nm for BN, SiC and BeO, respectively. Obviously, the Young's moduli are different for the BN, SiC and BeO NTs. Those for BeONTs are smallest which correlates nicely with the low strain energies (see Fig. 7.8). The ratio of the Young's moduli for BN and SiC NTs is in good agreement with that of the bulk moduli of BN and SiC. The results corroborate the respective tight-binding results of Hernández *et al.* [185]. They are in quantitative agreement with the few DFT-LDA values

(n,m)	d	β	E_s	Y_s	E_g
BN					
(4,0)	3.35	0.149	0.479	0.227	3.04
(5,0)	4.08	0.122	0.301	0.246	3.45
(6,0)	4.83	0.101	0.218	0.259	3.95
(7,0)	5.60	0.085	0.171	0.263	4.78
(8,0)	6.37	0.073	0.140	0.267	4.89
(9,0)	7.15	0.064	0.118	0.269	5.25
(10,0)	7.99	0.057	0.102	0.273	5.51
(15,0)	11.85	0.037	0.063	0.278	5.83
(4,4)	5.49	0.089	0.168	0.268	5.75
(5,5)	6.87	0.068	0.123	0.272	5.72
(6,6)	8.23	0.055	0.096	0.274	6.06
(7,7)	9.59	0.046	0.080	0.275	6.08
(8,8)	10.95	0.040	0.069	0.276	6.11
(9,9)	12.31	0.036	0.061	0.277	6.22
(10,10)	13.67	0.032	0.055	0.278	6.24
(15,15)	20.48	0.022	0.041	0.279	6.27

Table 7.5: Structural, elastic and electronic properties of BN NTs. See caption of Table 7.4 for details.

given in the latter reference. The deviations between the *ab initio* results in this work and the tight-binding results [185] are in the order of 2% for the NT diameters and about 10% for the Young's moduli.

It should be noted in passing that all structural and elastic properties of the NTs presented above have also been calculated within standard LDA. As expected, only small deviations up to 1 % occur.

7.2.3. Electronic properties

Most fundamentally, it turns out that all SiC, BN and BeO NTs investigated are semiconducting, as was to be expected on the basis of the electronic properties of the respective graphitic sheets, spanning a huge range of band gap energies from 0.5 to about 9 eV. Thus many nanoelectronic applications employing band gap energies of such a large range are conceivable. The band gaps are direct at Γ for $(n, 0)$ zigzag NTs – with the notable exception of the $(4, 0)$ NTs – and indirect for (n, n) armchair NTs. In a simple picture one might consider the band structure of the NTs as resulting from backfolding respective graphitic sheet bands onto the Γ - X line of the one-dimensional NT Brillouin zone. This backfolding increases the number of bands drastically for large n and the new interactions induced by the symmetry breaking of the graphitic sheets give rise to more or less

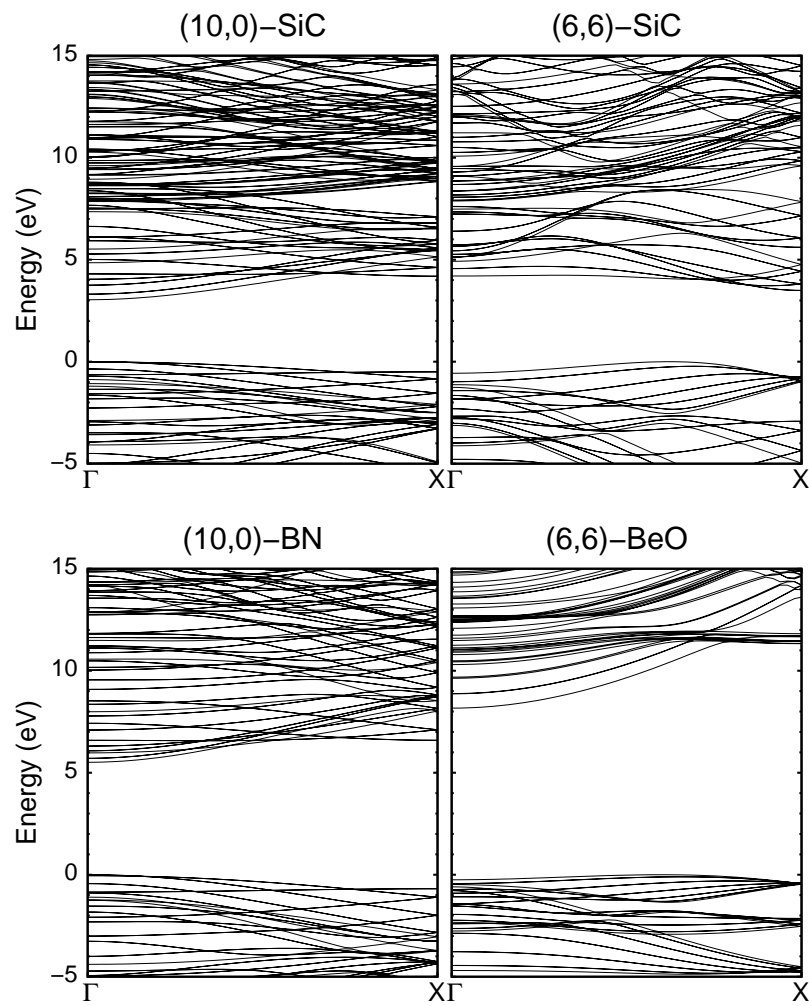


Figure 7.10: Sections of the band structure of SiC and BN (10,0) zigzag as well as SiC and BeO (6,6) armchair NTs along the high-symmetry line Γ -X of the one-dimensional NT Brillouin zone. All energies are referred to the VBM which is defined as the zero of the energy scale.

(n,m)	d	β	E_s	Y_s	E_g
BeO					
(4,0)	3.59	0.156	0.208	0.095	8.69
(5,0)	4.37	0.126	0.134	0.107	8.16
(6,0)	5.17	0.104	0.100	0.111	7.86
(7,0)	5.98	0.089	0.079	0.117	7.71
(8,0)	6.81	0.076	0.067	0.119	7.67
(9,0)	7.63	0.067	0.058	0.121	7.78
(10,0)	8.46	0.060	0.052	0.122	8.03
(13,0)	9.95	0.052	0.044	0.123	8.65
(15,0)	12.61	0.039	0.038	0.125	8.70
(4,4)	5.85	0.092	0.077	0.124	7.27
(5,5)	7.30	0.072	0.058	0.123	7.75
(6,6)	8.74	0.059	0.049	0.124	8.17
(7,7)	10.18	0.049	0.043	0.126	8.65
(8,8)	11.62	0.042	0.040	0.126	8.73
(9,9)	13.07	0.037	0.037	0.127	8.75
(10,10)	14.54	0.033	0.035	0.127	8.77
(15,15)	21.82	0.021	0.032	0.128	8.78

Table 7.6: Structural, elastic and electronic properties of BeO NTs. See caption of Table 7.4 for details.

pronounced splittings of the backfolded bands due to scattering of the sheet electrons at the NT lattice. While this simple picture applies for some regions of the valence and conduction bands in the case of armchair NTs, in particular, it is not fully appropriate for the lower conduction bands of SiC and BN zigzag NTs, in general, as will be discussed below. Fig. 7.10 shows a few exemplary results. The SiC and BN (10, 0) zigzag NTs exhibit a direct gap at Γ while the SiC and BeO (6, 6) armchair NTs show indirect gaps from a k point on the Γ - X line to the X point or the Γ point of the one-dimensional Brillouin zone in the former or latter case, respectively. The bandstructure for the BeO (6, 6) armchair NT is in good agreement with the respective DFT-LDA result reported in Ref. [110] with the notable exception that the calculated band gap is approximately 3 eV larger than the one reported in the latter reference.

Fig. 7.11 shows the progression of the band gaps with NT diameter for SiC, BN and BeO NTs. The respective values are summarized for further comparison in Tables 7.4–7.6, as well. Several interesting features are to be noted. First, there is a qualitative similarity regarding the evolution of the band gaps in SiC and BN NTs. Both show significant differences between zigzag and armchair configurations, i.e., very pronounced helicity effects although their structural and elastic properties are virtually independent of helicity.

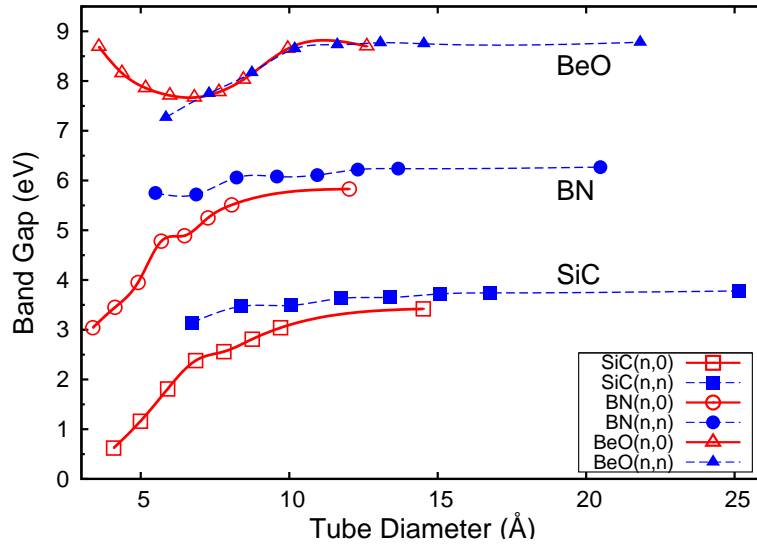


Figure 7.11: Fundamental gap of SiC, BN and BeO $(n, 0)$ zigzag and (n, n) armchair NTs as functions of the tube diameter d . See caption of Fig. 7.7 for further details.

The same general behavior was found by Zhao *et al.* [23] for SiCNTs and by Okada *et al.* [188], Xiang *et al.* [191] and Guo *et al.* [192] for BNNTs in their DFT-LDA results. The absolute band gap values reported previously [23, 188, 191, 192], however, are significantly smaller than the values in this work due to the well known underestimate of band gaps in LDA. Most interestingly, the deviations, e.g., between the SIC band gap values and those of Okada *et al.* [188] and Guo *et al.* [192] for a number of zigzag and armchair BNNTs are not constant but span a range from about 1 to 1.7 eV showing that it is not fully appropriate to just apply the same constant shift to the LDA band gaps of all NTs as is often conjectured. Only the band gaps calculated within hybrid density-functional theory for SiCNTs [196] and BNNTs [193] are in good accord with present results. For that matter, Gali [196] finds gap energies of 2.28 and 3.30 eV for $(8, 0)$ and $(6, 6)$ SiCNTs, respectively, to be compared to the SIC values of 2.56 and 3.49 eV and Xiang *et al.* [193] report gap energies of about 6.2 eV for armchair BNNTs with diameters larger than 12 Å which compare favorably with the respective SIC values for the $(9, 9)$, $(10, 10)$ and $(15, 15)$ BNNTs, respectively (see Tables 7.4–7.6). For large NT diameters the calculated band gaps converge towards the limiting values of the band gaps of the respective graphitic sheets. For small diameters, the differences of their gap energy from that of the respective graphitic monolayers E_g^{ML} is very pronounced, indeed. In particular, the gap of the SiC zigzag NTs reduces dramatically with decreasing diameter almost approaching a band gap collapse. The gaps of the SiC and BN $(15, 0)$ zigzag NTs still deviate from E_g^{ML} by about 13 and 6 %, respectively, while the gaps for the SiC and BN $(9, 9)$ armchair NTs, having comparable respective diameters, deviate only by approximately 6 and

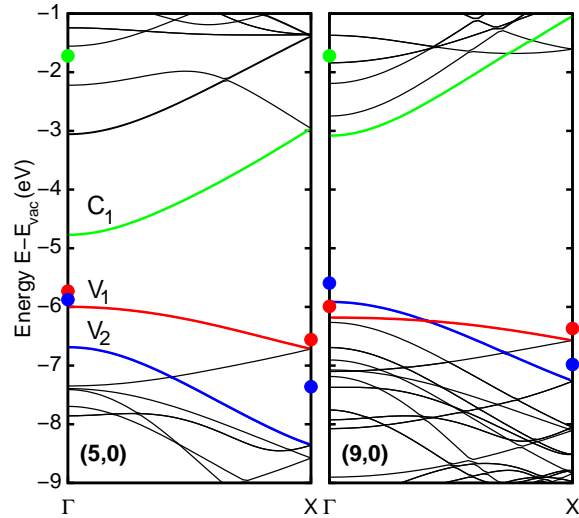
0.5 %, respectively (see Table 7.2 and Tables 7.4–7.6).

In contrast, the progression of the band gap energy of BeONTs is remarkably different (see Fig. 7.11). First of all, there is no discernible difference between zigzag and armchair tubes, except for the (7, 0) zigzag and (4, 4) armchair NTs. Second, one finds that for zigzag NTs of very small diameter, the gap is not strongly reduced, as in the case of SiC and BN, but goes through a minimum and opens up again, instead. In Ref. [110] the authors conclude on the basis of their DFT-LDA results that the band gap of BeONTs is independent of chirality. The present results confirm this notion for zigzag and armchair NTs. At the same time, the authors conclude that the band gap is independent of the NT diameter amounting to about 5 eV for all BeONTs considered [110]. Here, it is clearly revealed that this latter conclusion does not apply. Instead, the gap energies depend on nanotube diameter for $d \leq 10 \text{ \AA}$ and their values range from 7.3 to 8.8 eV (see Fig. 7.11 and Tables 7.4–7.6).

The question whether the band gap narrowing in small diameter SiC and BN NTs originates from a shift of the VBM or the CBM or from both can not be resolved from band-structure plots such as those shown in Fig. 7.10 since the top of the valence bands is defined in each of these plots as the zero of energy, as usual. To shed more light on the above question, Fig. 7.12 shows sections of the band structure of (5, 0) and (9, 0) zigzag SiCNTs but now referred to a common reference level which is chosen to be the vacuum level $E_{\text{vac}} \equiv E_{\text{vac}}^{\text{ML}}$ of the respective graphitic monolayer, as determined from the self-consistent sheet potential. The energy zero is thus put at E_{vac} . Some prominent bands (V_1 , V_2 and C_1) have been labeled explicitly. The figure clearly reveals intricate changes of the order of bands near the top of the valence bands with NT diameter, nevertheless, placing the VBM at nearly the same absolute energy. The CBM, on the contrary, strongly shifts up in energy with increasing n or NT diameter, respectively. Comparing the band structures in Fig. 7.12 – and especially the characteristics of the bands V_1 , V_2 and C_1 – two pronounced effects are to noted. First, one can see that the order of the V_1 and V_2 bands changes from the (5, 0) to the (9, 0) NT, most prominently at the Γ point defining the VBM. Second, the C_1 band strongly separates from the rest of the conduction bands in the (5, 0) NT while it is located rather close to them in the (9, 0) NT. To put it more quantitatively, the transition energy between the two lowest conduction bands at Γ amounts to 1.77 eV for the (5, 0) and 0.35 eV for the (9, 0) NT. For a (15, 0) NT, finally, the transition energy is only 0.09 eV.

For further comparison, energy-band positions (marked by full dots) at the Γ and X points as resulting from backfolding the SiC graphitic-layer bands onto the NT Brillouin zone are included in Fig. 7.12. One can see that for the larger diameter (9, 0) NT the backfolded valence-band energies are close to the calculated NT energies, due to the respectively low NT curvature. The same agreement obtains for valence band V_1 of the (5, 0) NT. However, the backfolded energy values corresponding to the valence band V_2 of the (5, 0) NT

Figure 7.12: Sections of the band structure of (5, 0) and (9, 0) zigzag SiCNTs (left and right panel, respectively) along the high-symmetry line of the one-dimensional NT Brillouin zone. The dots result from backfolding the bands of the SiC graphitic sheet onto the Γ and X points of the respective NT Brillouin zones. See text for the definition of the energy scale.



deviate very significantly from the energies of the NT band. Nevertheless, the backfolded sheet valence bands also yield the VBM of the (5, 0) NT reasonably well. On the contrary, backfolding the conduction bands of the graphitic sheet does not at all yield appropriate values for the NT CBM. The deviation is significant for the (9, 0) and very large for the (5, 0) NT. Compare the green dots with the C_1 bands at Γ , for that matter. The results in Fig. 7.12 can already be viewed as an indication that the band gap narrowing in SiC and BN zigzag NTs originates mainly from a NT-induced shift of the CBM.

Fig. 7.13 shows the calculated VBM and CBM energies (full symbols) of all investigated zigzag SiCNTs, referred to the common reference level $E_{\text{vac}}^{\text{ML}}$ of the graphitic monolayer. In addition, the open symbols represent the respective energetic positions resulting from a simple backfolding scheme for the monolayer bands. This figure clearly reveals that the band gap narrowing with decreasing tube diameter is mainly a result of NT-curvature.

Second, it is most apparent that the dominant contribution to the band gap narrowing originates from a change of the energy position of the lowest conduction band. In particular, the energy decrease of the CBM turns out to be entirely monotonous. The variation of the energy position of the VBM, on the contrary, is not monotonous for small diameters $d < 10 \text{ \AA}$. The differences between the monotonous CBM and the non-monotonous VBM curves directly translates into the non-monotonous band gap progression for zigzag SiCNTs, as shown in Fig. 7.11, explaining the occurrence of two almost linear regimes with different slopes for small NT diameters. This holds for both SiC and BN NTs, albeit on different absolute scales.

This behavior is thus related to the more intricate dependence of the VBM on NT diameter for small diameters and the respective discontinuous change of the neighbor configurations and interactions between occupied atomic orbitals across the inner NT cylinder.

To elucidate the physical origin of the particular band gap progressions in SiC, BN and

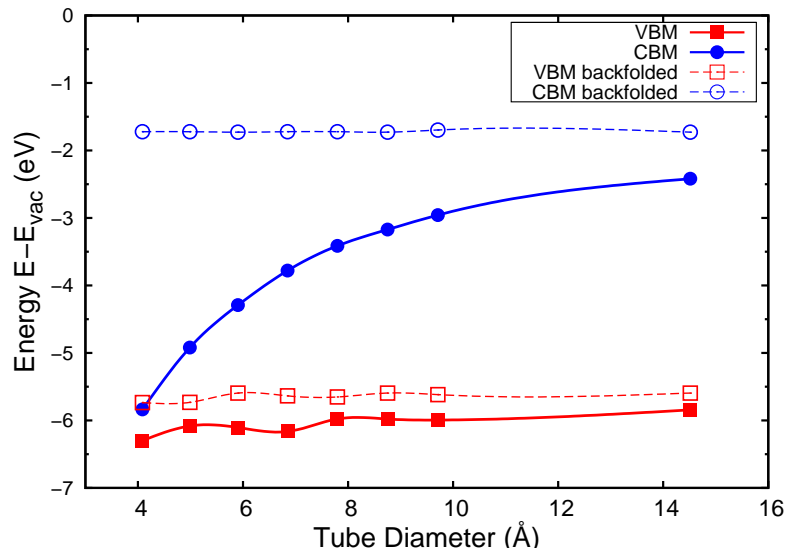


Figure 7.13: Progression of the VBM and CBM energies in zigzag SiCNTs as a function of tube diameter d . Full symbols result from NT calculations while the open symbols follow from backfolding the bands of the graphitic SiC sheet. The solid and dashed lines are drawn to guide the eye.

BeO NTs, one should first address the qualitatively similar progressions for SiC and BN NTs (see Fig. 7.11) focussing on SiCNTs, for that matter. Thereafter, the band gap progression for BeONTs is discussed.

While most of the previous literature on BNNTs discusses the origin of the band gap progression with tube diameter in \mathbf{k} -space in terms of backfolding of the related graphene sheet bands [183–189], a complementary line of approach shall be followed here by addressing its origin in real space using SiC and BeO NTs as examples. When a stripe of graphitic SiC is rolled up into a NT, changes in the charge density occur. These are different for zigzag and armchair NTs because of their fundamentally different geometry. The charge densities of the VBM and CBM states of the graphitic SiC sheet, shown in the left panels of Fig. 7.4, reveal their anionic and cationic p_z character, respectively. When rolling the stripe up into tubular form its curvature generally decreases the distance between neighboring sites. Much more importantly, the respective charge densities start to overlap inside the cylinder. Especially for zigzag NTs, this is a very pronounced effect while it is much smaller for armchair NTs. This is illustrated in Fig. 7.14 by charge density contours of the CBM state at the K point for the (5, 5) armchair and at the Γ point for the (9, 0) zigzag SiCNT. Because the CBM states are mainly responsible for the band gap narrowing, as shown above, they are concentrated upon in the following. In both cases, the contours are drawn in a plane perpendicular to the NT axis containing an anion-cation ring for the armchair and a cation ring of the double-ring structure for the zigzag NT be-

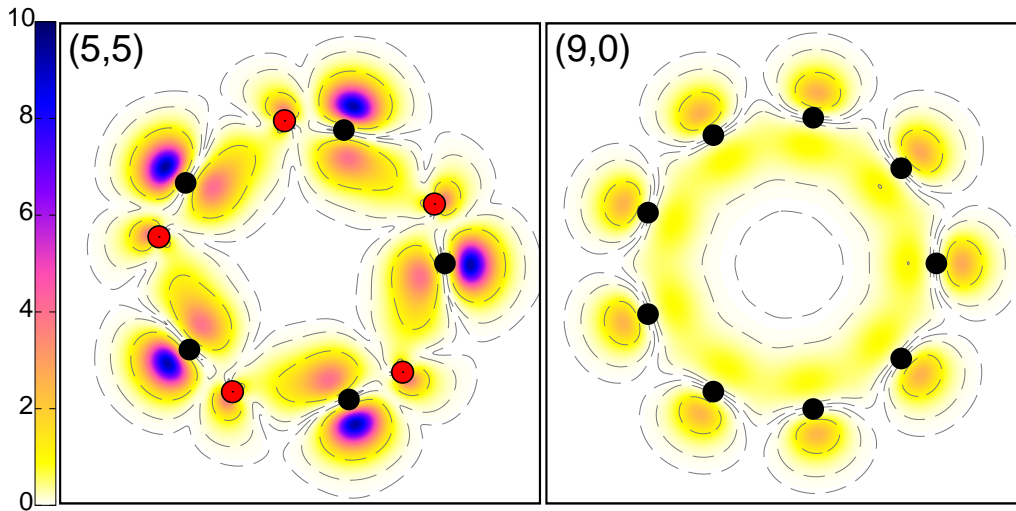


Figure 7.14: Charge density contours of the CBM states (in $10^{-3} a_B^{-3}$) of the one-dimensional Brillouin zone at the K point of a (5, 5) armchair (left panel) and the Γ point of a (9, 0) zigzag (right panel) SiCNT. The contours are drawn in planes perpendicular to the NT axis containing an anion-cation ring for the armchair and a cation ring for the zigzag NT. Anions and cations are again depicted by red and black dots, respectively.

cause the latter gives rise to the CBM. One can see that in the armchair NT (left panel), the charge density remains localized at the cations and is distorted on the inner side of the ring only slightly in the bond direction towards the anions due to the curvature of the NT. In contrast, the charge density contour of the (9, 0) zigzag SiCNT (right panel) very clearly demonstrates that a major redistribution of the charge density has taken place inside the tube building up a ring-like distribution. The former p_z components of the charge density on the SiC graphitic sheet are pushed towards each other and a significant rehybridization leads to a ring-like charge density on the inner side of the tube. The former atomic character of the states on the inner side of the NT is entirely lost. The CBM energy is lowered, therefore, and the fundamental energy gap is reduced with respect to the graphitic sheet. The p_z components of the cation orbitals on the outside of the NT are only slightly affected showing even less coupling between neighboring cations on the ring than in the graphitic sheet. The effects described above are even more pronounced for NTs with smaller diameters giving rise to an even stronger band gap reduction. Respective charge-density contours of the CBM state of (4, 0), (8, 0) and (10, 0) zigzag SiCNTs at the Γ point are compared in the left panels of Fig. 7.15. Note the dramatic increase of the charge density within the nanotube when n is decreased from 10 to 4.

In contrast, the insensitivity of the gap of BeONTs to helicity seems to be related to the particular charge density topology of the CBM state in the graphitic BeO sheet (see the right panels of Fig. 7.4). The bottom of the conduction bands in BeONTs originates from

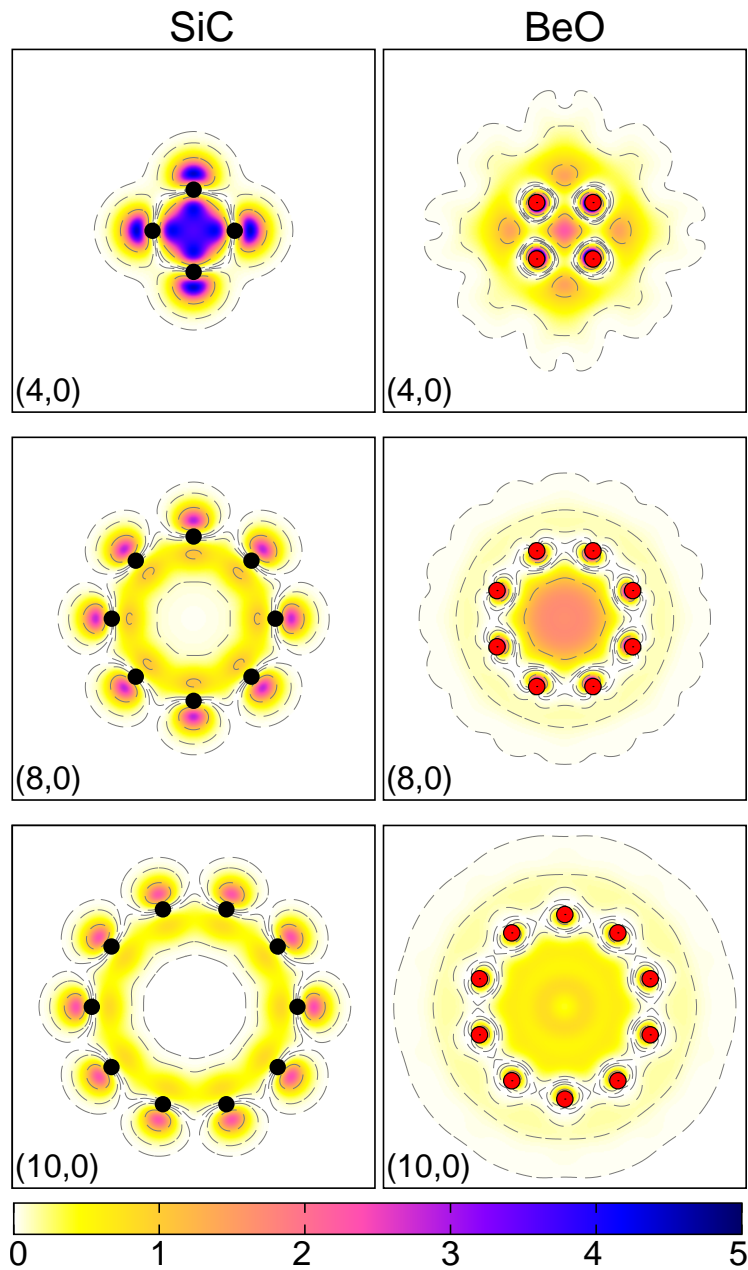


Figure 7.15: Charge density contours of the CBM states (in $10^{-3} a_B^{-3}$) at the Γ point of the one-dimensional Brillouin zone of (4,0), (6,0) and (9,0) SiC (left panels) and BeO (right panels) zigzag NTs. The charge densities for SiC and BeO NTs are plotted in a plane perpendicular to the NT axis containing a Si or an O ring, respectively, since the CBM of zigzag SiCNTs is made up of Si p orbitals, while that of zigzag BeONTs is made up of O s orbitals. For further details, see caption of Fig. 7.14. Note that all charge densities are plotted on the same absolute scale so that they can be compared quantitatively.

localized O s and very extended Be $2s$ states (of NFE-character) which are not strongly influenced by rolling up the graphitic BeO stripe into zigzag or armchair NTs. Thus, there is no helicity-induced difference in the gaps of both types of NTs. The peculiar dependence of the gap on NT diameter showing a minimum is more intricate. Coming from the graphitic sheet limit, the gap first decreases with decreasing d for both zigzag and armchair NTs until d approaches a value of about 7 Å for the (8, 0) NT. The charge density of the CBM state in $(n, 0)$ zigzag BeONTs is shown for $n= 4, 8$ and 10 in the right panels of Fig. 7.15. The figure clearly reveals the different character of the CBM states of the BNNTs (right panels), as compared to the respective CBM states of the corresponding SiCNTs (left panels). The charge densities of the (10, 0) NTs of both compounds approach the respective sheet limit on the outside of the tubes. For the (8, 0) NTs, already more pronounced changes occur inside the tubes. For the (4, 0) NTs the charge densities are largely different from those of the graphitic sheets explaining the specific behavior for $n \leq 8$. For BeO zigzag NTs with $n \leq 8$ the gap increases again (see Fig. 7.11) because the very small NT diameters start to allow for an increased interaction between the anions and the cations across their respective rings. Generally speaking, an increasing interaction between second-nearest neighbors, i.e., between anions or cations, respectively, broadens respective anion- and cation-derived bands. As a result, the energy gaps between the related bands become smaller. For armchair SiCNTs, e.g., there is no interaction across the inner NT cylinder (see the left panel in Fig. 7.14) so that the gap energy remains close to its sheet value. For zigzag SiCNTs (see the left panels in Fig. 7.15) the interaction is minimal for the (10, 0) NT and increases down to the (4, 0) NT. Thus the gap decreases with decreasing n or tube diameter d , respectively. For BeO zigzag NTs, on the contrary, (see the right panels of Fig. 7.15) the interaction across the inner tube cylinder is small for the (10, 0) NT, becomes largest for the (8, 0) NT and becomes smaller again for the (4, 0) NT. Thus the (8, 0) zigzag BeONT has the smallest gap while it is larger for both the (4, 0) and (10, 0) BeONTs. From Fig. 7.15 it becomes obvious that the CBM states of highest charge density and largest interactions across the inner ring are the (4, 0) SiCNT and the (8, 0) BeONT. So among the $(n, 0)$ zigzag NTs, those with the largest interaction across the tube are those with the smallest gap, i.e., the (4, 0) SiCNT and the (8, 0) BeONT (see Figs. 7.11 and 7.15).

7.3. Summary

In this chapter a comprehensive comparison of structural, elastic and electronic properties of compound semiconductor nanotubes with increasing ionicity, as studied by *ab initio* density-functional theory employing self-interaction-corrected pseudopotentials which yield accurate band gaps, in particular, has been performed. The progression of the ra-

dial buckling, strain energy, Young's modulus and energy gap with NT diameter has been investigated and related to the increasing ionicity of the SiC, BN and BeO NTs considered. For all zigzag and armchair NTs investigated, the structural and elastic properties are largely independent of NT helicity while the electronic structure of SiC and BN NTs very sensitively depends on it. This is not the case for BeONTs. The origin of the peculiar helicity dependence of the gap energy in SiC and BN zigzag NTs and its helicity independence in BeONTs has been analyzed in detail. In particular, it was elucidated why no large band gap narrowing occurs for small diameter zigzag BeONTs, as opposed to zigzag SiC and BN NTs. To this end, the nature and origin of the band gap progressions and the peculiar differences of it between SiC and BN NTs, as compared to BeONTs, has been analyzed by considering most relevant charge density contours which highlight the critical differences between the respective NTs and allows to explain the different progressions of E_g in SiC and BN NTs, as compared to BeONTs. The structural and elastic properties of SiC and BN NTs, as resulting from the present calculations, are in good agreement with previous DFT-LDA results and they corroborate respective earlier tight-binding results on BNNTs. For BeONTs, the results appear to be the first comprehensive account of their structural and elastic properties. Concerning electronic properties of SiC, BN and BeO NTs, the SIC results confirm the qualitative outcome of previous tight-binding and DFT-LDA calculations and they are in quantitative accord with the selected hybrid density functional results on the few SiC and BN NTs available in the literature. This should be valued in view of the fact that the SIC calculations, treating all NTs studied on equal footing, are numerically not more demanding than any standard DFT-LDA calculation on NTs.

Chapter 8.

Electronic structure of alkali-metal fluorides, oxides and nitrides

Several years ago, Fischer and Jansen [24] reported the anti-ReO₃ structure for films of metastable sodium nitride (Na₃N) deposited at low temperatures. Recently single crystalline and polycrystalline Na₃N has been synthesized successfully on a laboratory scale by reaction of metallic sodium or a liquid Na-K alloy with plasma-activated nitrogen [25], thus allowing for an intensive experimental investigation of its structural and optical properties employing powder and single-crystal X-ray diffraction and optical absorption [204]. Based on the respective preliminary experimental data, Na₃N appears to be semiconducting with a band gap of 1.6 eV. On the contrary, concomitant band structure calculations [25] based on density-functional theory within local-density approximation have yielded a *negative* gap of 0.6 eV. This theoretically predicted metallicity of Na₃N is in obvious contrast to the experimental data and the expected formulation as (Na⁺)₃N³⁻. Now the description of electronic properties of insulators and semiconductors within the framework of DFT-LDA suffers from the systematic underestimation of the fundamental band gap, as has been exemplified above for several classes of semiconductors and insulators. Based on the achievements of the SIC approach as presented in the previous chapters, one can expect it to be also useful for shedding some light on the question whether Na₃N is a semiconducting or metallic compound.

In this chapter, a comparative study of the k-dependent electronic structure of Na₃N and related compounds ranging from wide-band-gap insulators possibly to metals is performed in order to scrutinize the use of SIC pseudopotentials for the broader class of lithium, sodium, and potassium fluorides, oxides and nitrides. For the fluorides, in particular, and less so for the oxides, there is data in the literature to which the SIC results can be compared.

Computational Details

As usual, standard LDA calculations constitute the reference point for the investigations. The standard pseudopotentials are constructed according to the prescription of Hamann [94]. A notable difference to the previous calculations concerns the alkali metal atoms, for which partial non-linear core corrections, as introduced by Louie *et al.* [205], are included into the pseudopotentials. The wave functions are expanded employing a basis set of atom-centered Gaussian orbitals with several shells of s , p , d , and s^* symmetry per atom with appropriately determined decay constants of (in atomic units) 0.30, 1.34 and 6.00 for Li, 0.16, 0.30, and 0.60 for Na, 0.16, 0.37, and 0.88 for K, 0.20, 0.95, and 4.50 for F, 0.25, 1.00 and 3.70 for O, and 0.31, 1.36, and 6.00 for N. As one has to deal with some relatively low-density substances for the oxides and especially the nitrides, additional slowly-decaying s -like Gaussian orbitals with a decay constant of 0.18 are placed in the empty regions in order to allow for a satisfying description of extended bulk states. Brillouin-zone integrations are performed using special k -point sets in the irreducible wedge generated according to the prescription of Monkhorst and Pack [30]. The number of k -points was tested to yield convergent results. The actual numbers of special k -points in the respective irreducible wedges of the bulk Brillouin zones are 44 (LiF), 28 (NaF), and 19 (KF), 28 (Li₂O), 19 (Na₂O), and 10 (K₂O), as well as 32 (Li₃N), 10 (Na₃N), and 8 (K₃N).

8.1. Atomic term values

Before turning to the properties of the various bulk crystals studied in this chapter, the term values of the different atomic levels, as resulting from SIC and LDA calculations with one another and are compared with experimental ionization energies in Table 8.1. The results show that the cationic s levels experience significantly lower self-interaction corrections $\Delta\epsilon$ than the anionic s and p levels, respectively. This difference gives rise to a significant shift of the related bands in the fluorides, oxides and nitrides and consequently, the gap is opened up in these materials due to self-interaction corrections, as compared to the LDA results. It should be noted that the term values of the highest occupied cationic (Li, Na, K) s levels as resulting from the SIC calculations agree with the experimental ionization energies within better than 0.3 eV. In contrast, the LDA results deviate from the experimental data by 2.49, 2.32, and 1.92 eV, respectively. In the case of the $2p$ levels of N, O and F the SIC calculations appear to yield larger deviations from experiment. A direct comparison of the measured $2p$ ionization energies with the values in Table 8.1 is misleading, however, since the latter are obtained from non-spin-polarized calculations while the former include spin-polarization. As has been discussed in chapter 3, for the bulk crystals investigated in this work, spin-polarization is irrelevant since the respective

Element	Level	$E_{\text{ion}}^{\text{exp}}$	ϵ^{SIC}	ϵ^{LDA}	$\Delta\epsilon$
Li	2s	-5.39	-5.10	-2.90	-2.20
Na	3s	-5.14	-4.92	-2.82	-2.10
K	4s	-4.34	-4.06	-2.42	-1.64
N	2s	—	-25.06	-18.41	-6.65
	2p	-14.53	-13.47	-7.24	-6.23
O	2s	—	-31.38	-23.74	-7.64
	2p	-13.62	-16.48	-9.20	-7.28
F	2s	—	-39.45	-29.61	-9.84
	2p	-17.42	-20.82	-11.33	-9.49

Table 8.1: Atomic term values (in eV) for Li, Na, K, F, O, and N atoms as resulting from non-spin-polarized SIC and LDA calculations. Additionally, the energy shifts $\Delta\epsilon = \epsilon^{\text{SIC}} - \epsilon^{\text{LDA}}$ of the term values due to self-interaction correction are given. Experimental ionization energies for the highest occupied levels from Ref. [37] are listed for comparison.

levels are non-spin-polarized in the solids. Yet, to allow for a more meaningful direct comparison of the results for the atoms with experimental $2p$ ionization energies the $2p$ level energies have also calculated by spin-polarized DFT-SIC calculations. As a result, the energies amount to -14.91 eV for N_{2p} , -13.89 eV for O_{2p} and -18.05 eV for F_{2p} . These values agree with experiment (see Table 8.1) within 0.6 eV lending further support to the appropriateness of the results for the non-spin-polarized case which obtains in the solids. Starting out from this significantly improved description of the underlying atomic term values self-interaction-corrected pseudopotentials are constructed and the SIC effects on the bulk electronic structure of the above mentioned alkali-metal fluorides, oxides and nitrides can be studied.

8.2. Bulk electronic properties

The results of the SIC calculations for the nine bulk crystals are summarized in Figures 8.1 to 8.3 and Table 8.2, which are repeatedly referred to in the course of the following discussion.

8.2.1. Fluorides

All three fluorides crystallize in the sodium-chloride structure (space group $\text{Fm}\bar{3}\text{m}$) with lattice constants of 3.99 Å (LiF), 4.57 Å (NaF), and 5.29 Å (KF), respectively [216]. The calculated SIC band structures for the three fluorides are shown in Fig. 8.1. In these highly

	Band gap			anion <i>s</i> -band	
	LDA	SIC	Exp.	LDA	SIC
LiF	8.5	14.7	13.6 ^a , 14.2 ^b , 14.5 ^c	-21.3	-21.5
NaF	5.7	11.6	11.5 ^a , 11.7 ^d	-20.2	-20.5
KF	5.2	10.6	10.8 ^e , 10.9 ^f , 11.0 ^g	-20.1	-20.4
Li₂O	4.8	8.3	8.0 ^h	-15.2	-16.0
Na₂O	1.8	4.9	(4.4 - 5.8) ⁱ	-14.3	-14.6
K₂O	1.1	3.8	(4.0 - 5.4) ^g	-14.1	-15.0
Li₃N	1.1	2.6	2.2 ^j	-11.2	-11.8
Na₃N	0.0	0.5	1.6 ^k	-10.8	-10.8
K₃N	0.0	0.0	—	-11.6	-11.3

^afrom Ref. [206]

^bfrom Ref. [207]

^cfrom Ref. [208]

^dfrom Ref. [209]

^efrom Ref. [210]

^ffrom Ref. [211]

^gfrom Ref. [212]

^hfrom Ref. [213]

ⁱ(lower - upper) limits (from Ref. [214] - estimated), see text.

^jfrom Ref. [215]

^kfrom Ref. [204]

Table 8.2: Calculated gap energies and average energetic position of the anion *s*-band (in eV) as resulting from SIC, compared to experimental results.

ionic compounds the valence bands are basically anion-derived consisting of one low-lying F 2*s* band (not shown in Fig. 8.1) and three F 2*p* bands defining the top of the valence bands (see Fig. 8.1). These groups of bands are separated in energy by a large ionic gap. The lowest conduction bands are mostly cationic *s* bands. All three compounds are ionic insulators having direct band gaps at Γ of 14.7 eV (LiF), 11.6 eV (NaF), and 10.6 eV (KF), respectively, according to the DFT-SIC results. The band gaps and average F 2*s* band positions, as resulting from the LDA and SIC calculations are summarized in Tab. 8.2. Experimental gap energies from optical reflection and absorption measurements [204, 206–215] are given in the table for comparison. Those for the fluorides are significantly underestimated by some 6 eV within DFT-LDA, while the SIC results are in very good accord with experiment constituting a significant improvement over LDA. In addition, the SIC band gaps are in reasonable agreement with other theoretical results from correlation-corrected Hartree-Fock calculations [217–219] ranging from 14.0 to 16.5 eV for LiF, 12.0 to 14.7 eV for NaF, and 10.9 to 13.3 eV for KF. To the best of our knowledge, results of quasiparticle calculations have only been reported for LiF [207, 220, 221], to date. The

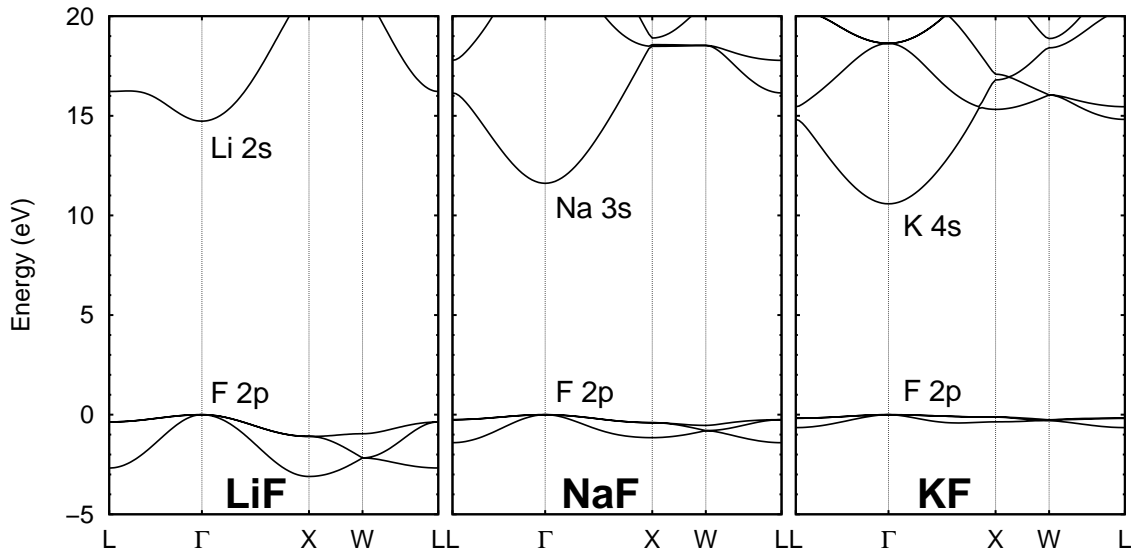


Figure 8.1: Electronic band-structures of LiF, NaF, KF as resulting from SIC calculations.

authors find a quasiparticle gap of 14.4, 14.3 and 14.3 eV, respectively, which is close to the calculated gap in this work of 14.7 eV.

An earlier SIC study [43] arrived at band gaps of 16.6, 13.3, and 12.5 eV for LiF, NaF and KF, respectively, overestimating the experimental values. In this study, an *ad-hoc* ansatz is made for corrective SIC potential terms and the single-particle charge densities are evaluated using approximate Wannier functions. The variational freedom of the single-particle orbitals is limited in this approach, however, which could be one reason for the slightly overestimated band gaps.

Along with the reduction of the gap energy from LiF to KF, one also finds a narrowing of the width of the F $2p$ valence bands from 3.1 eV in LiF over 1.4 eV in NaF to 0.6 eV in KF (see Fig. 8.1). They are mainly formed by F $_{2p}$ states. There is only a negligible admixture from cation s states. Therefore, the dispersion of the F $2p$ bands originates almost exclusively from direct interactions between the anions which are second-nearest neighbors in the lattice. The increasing size of the cations increases the anion-anion distance from 2.85 Å for LiF over 3.25 Å for NaF to 3.85 Å for KF so that the anion-anion interaction and the F $2p$ -band widths decrease accordingly. The same trend was also observed in UPS experiments [222]. Concerning absolute values, one has to note that Shirley *et al.* [207] found for LiF a corresponding band width of 3.5 and 3.6 eV from experiment and theory, respectively. For NaF, Wertheim *et al.* [223] observed a width of 1.6 ± 0.2 eV. The present results are in satisfactory agreement with these data.

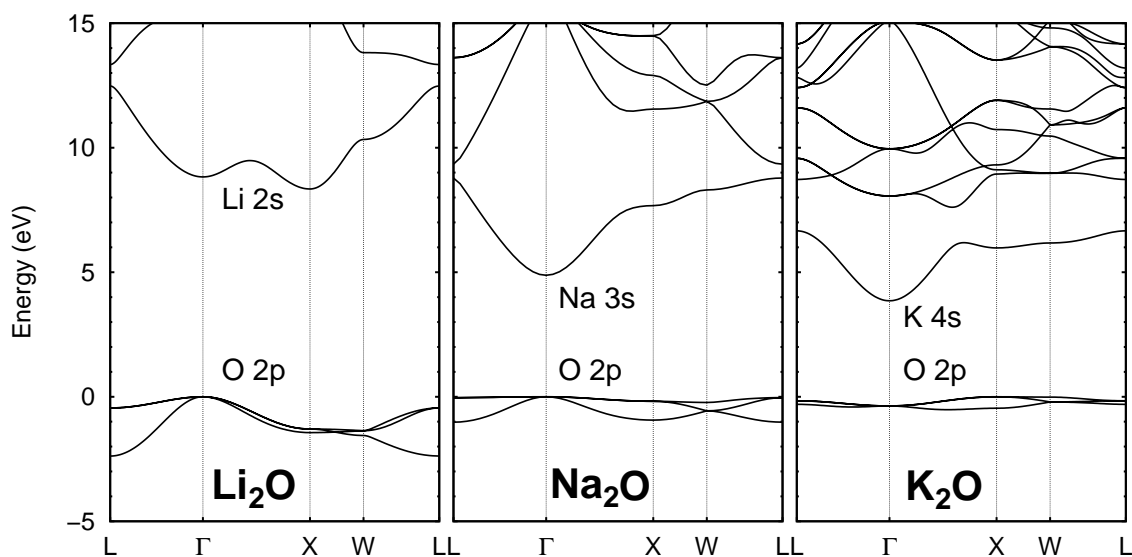


Figure 8.2: Electronic band-structures of Li_2O , Na_2O , K_2O as resulting from SIC calculations.

8.2.2. Oxides

Li_2O , Na_2O , and K_2O all crystallize in the cubic-antifluoride structure (belonging to the space group $\text{Fm}\bar{3}\text{m}$), which is antimorphous to CaF_2 . Positive alkali-metal ions are arranged on a simple cubic lattice with a spacing of $a/2$. Alternating cube centers are occupied by O^{2-} ions. The lattice constants are 4.62 Å, 5.56 Å and 6.45 Å, respectively [224]. As these lattices are comparatively open structures, additional slowly decaying s orbitals are included at $\frac{a}{2}(1, 1, 1)$ in order to appropriately represent extended cation-derived states in the solid. The resulting fundamental band gaps and oxide s -band positions are listed in Tab. 8.2, as well. Experimental data on the value of the band gap is relatively sparse. For Li_2O there is a more recent reflectivity study [213] in which the authors derived a fundamental band gap of 8.0 eV from excitonic spectra. The only reported equivalent for Na_2O and K_2O is a very early study of corresponding absorption spectra [214] showing transitions at 6.6, 4.4, and 4.0 eV for Li_2O , Na_2O and K_2O , respectively. These spectra, however, contain excitonic contributions which have not been accounted for in Ref. [214]. Considering that the result for Li_2O of 6.6 eV deviates from the more recent exciton-corrected value in Ref. [213] by 1.4 eV, a very rough estimate for the upper limit of the expected Na_2O and K_2O gaps can be made by adding this full difference to the reported values for Na_2O and K_2O in Ref. [214]. The resulting values of 5.8 eV (Na_2O) and 5.4 eV (K_2O) are given in Tab. 8.2 as upper limits, as well. Certainly, the true gaps in the two latter cases are smaller than the upper limits given in Table 8.2 since the exciton energies in Na_2O and K_2O are bound to be considerably smaller than in Li_2O because the oxides of sodium and potassium have significantly smaller energy gaps than Li_2O (see

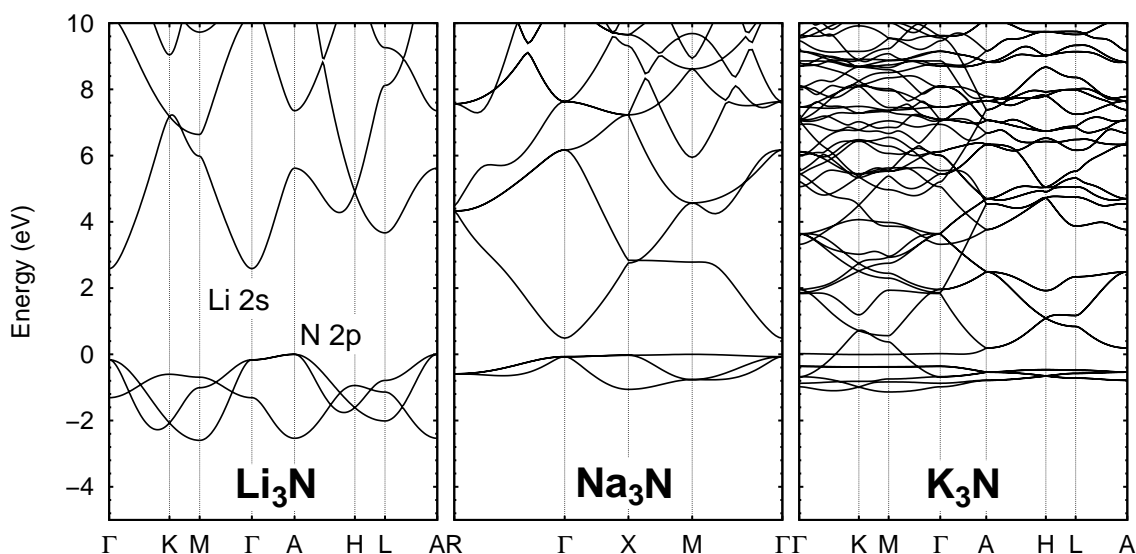


Figure 8.3: Electronic band-structures of Li_3N , Na_3N , K_3N as resulting from SIC calculations.

Fig. 8.2). So for Na_2O one would expect the gap to be considerably closer to the lower limit and for K_2O it ought to be very close to the lower limit. It is obvious (see Tab. 8.2) that for all three alkali-metal oxides, the band gaps calculated within DFT-LDA show the usual strong underestimation of the measured gap energies while the SIC gaps are opened up considerably being in much better agreement with experiment.

Fig. 8.2 shows the calculated SIC band structures for the three oxides. In all three cases, a low-lying O $2s$ band (not shown in the figures) occurs (see Table 8.2). Near the top of the valence bands a group of three O $2p$ bands whose widths decrease again from Li_2O to K_2O is visible. The bottom of the conduction bands originates in each case from cation ns states with $n=2, 3$ and 4 , respectively. For Li_2O , a band gap of 8.3 eV results in nice agreement with the experimental value [213] of 8.0 eV and the gap energy of 8.1 eV resulting from a hybrid-functional calculation [225]. The band gap is indirect, with the valence-band maximum located at Γ and the conduction-band minimum at X . In contrast, Na_2O has a direct gap at Γ , which is 4.9 eV wide according to the SIC results. The situation is different again for K_2O . Here the results show an indirect fundamental gap of 3.8 eV between X and Γ . Similar observations regarding the nature of the band gaps have recently been reported by Eithirjai *et al.* based on a TB-LMTO study [226]. Their calculated LDA band gaps of 5.8 eV for Li_2O , 2.4 eV for Na_2O and 1.8 eV for K_2O are considerably lower, however.

The valence electronic structure of the alkali-metal oxides has been studied experimentally by Mikajlo and coworkers using electron momentum spectroscopy [227–229]. In particular, the authors derived the width of the upper O $2p$ valence bands to be 1.6 eV for Li_2O , 0.6 eV for Na_2O and 0.3 eV for K_2O with an uncertainty of ± 0.2 eV each. The

respective values from the SIC calculations of 2.4 eV, 1.0 eV and 0.5 eV are in reasonable accord with the data.

8.2.3. Nitrides

Lithium nitride (Li_3N) crystallizes in a hexagonal structure with the space group $P6/mmm$. In this peculiar structure each N atom is surrounded by eight Li atoms in a layered configuration along the hexagonal axis consisting of one Li_2N layer and a layer of pure Li. The lattice constants [230] are $a = 3.65\text{\AA}$ and $c = 3.87\text{\AA}$. Accounting for the unique character of the atomic structure of Li_3N , additional slowly decaying Gaussian orbitals are placed at $(a/2, \pm a/2\sqrt{3}, c/2)$, i. e., at positions within the Li layer above and below Li atoms of the Li_2N layer, to accurately represent the more extended bulk states. From optical absorption experiments [215, 231] a gap energy of about 2.2 eV results. In contrast, the calculated LDA gap energy is only 1.1 eV (see Table 8.2) in agreement with the results of previous LDA studies [232, 233]. In earlier Hartree-Fock calculations [234], a gap energy of 7.8 eV was obtained.

In the left panel of Fig. 8.3 the band structure of Li_3N as resulting from SIC calculations is shown along the high symmetry lines of the hexagonal Brillouin zone. Also Li_3N has a low-lying anionic N $2s$ valence band (see Table 8.2) and three N $2p$ bands near the top of the valence bands. The lowest conduction band is mainly derived from Li_{2s} states. The band structure shows an indirect band gap between the A and Γ points. The gap is 2.6 eV wide and deviates only by 0.4 eV from the experimental value [215] of 2.2 eV. As a consequence of the hexagonal structure, a crystal field splitting occurs for the highest N $2p$ bands at the Γ point. While the components perpendicular to the hexagonal axis remain degenerate, the p_z -component is shifted down in energy showing an inverted dispersion. The crystal field splitting is rather large amounting to 1.2 eV.

Contrary to Li_3N , sodium nitride (Na_3N) was experimentally found to occur in a cubic anti- ReO_3 crystal structure (space group $\text{Pm}\bar{3}\text{m}$) with a lattice constant [25] of 4.73\AA . This structure (see Fig. 8.4) can be interpreted as a cubic perovskite (CaTiO_3) structure

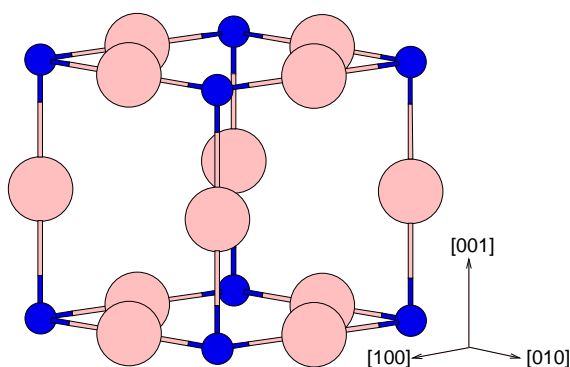


Figure 8.4: Lattice structure of Na_3N . Positions of the Na (N) atoms are indicated by large (small blue) circles.

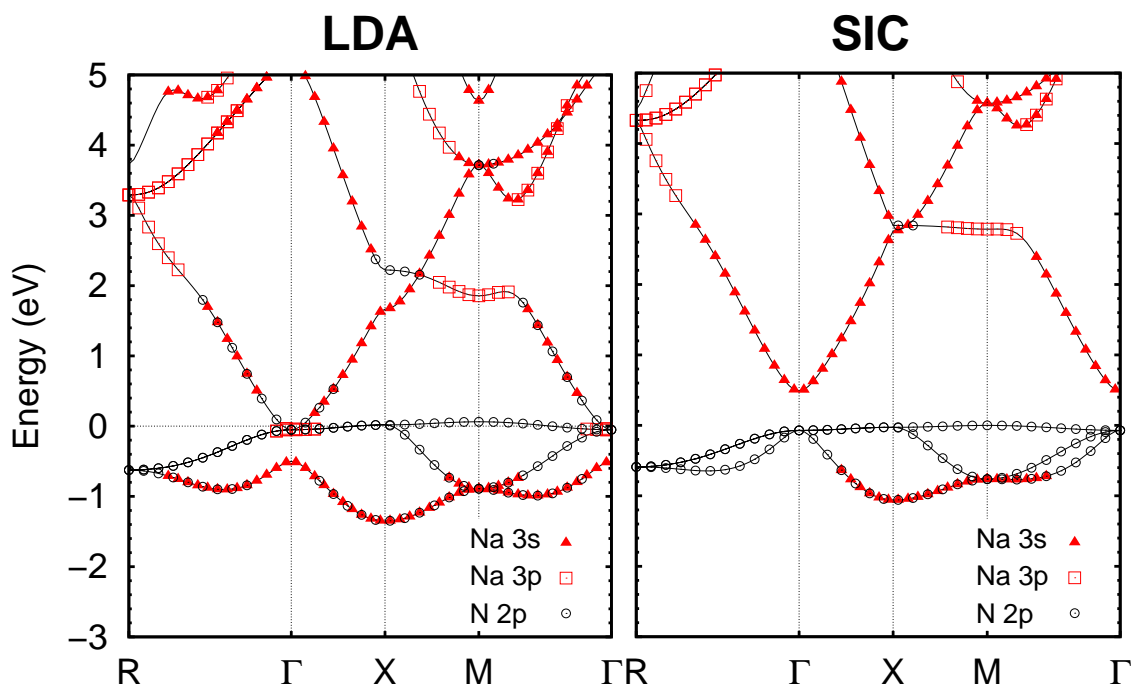


Figure 8.5: Band structure of Na_3N as resulting from LDA (left panel) and SIC calculations (right panel), respectively. Bands derived from N_{2p} states are marked by open circles. Red triangles and squares label bands that are derived from Na_{3s} and Na_{3p} states, respectively.

with a removed Ca atom so that the N atoms are located in the Ti sites while the Na atoms occupy the O sites. Slowly decaying Gaussian orbitals are placed on the cube centers. As noted before, standard LDA calculations yield an electronic structure with a negative gap of 0.6 eV for this crystal rendering Na_3N metallic. The band structure of Na_3N as resulting from SIC calculations is shown in the middle panel of Fig. 8.3.

Compared to the band structure of Li_3N , the energy separation between the top of the N $2p$ valence bands and the bottom of the Na $3s$ conduction band has decreased considerably. Yet, Na_3N clearly exhibits a band gap of 0.5 eV in the SIC results while it appears to be a metal within LDA. Nevertheless, it should be noted that the calculated SIC gap is significantly smaller than the measured gap (1.6 eV). The width of the three N $2p$ bands has strongly decreased, as compared to Li_3N . The reason appears to be more subtle than, e. g., for the respective fluorides. The anion-anion distance is as large as 4.73 Å, indeed, but the anion-cation interaction in the N-Na-N bridges (see Fig. 8.4) comes into play in Na_3N . This can happen, since the Na_{3s} bands at Γ are relatively close in energy to the N_{2p} bands allowing for a certain interaction.

In order to elucidate the origin of the metallicity resulting within LDA the respective band structure of Na_3N is shown in the left panel of Fig. 8.5. In the figure bands are marked

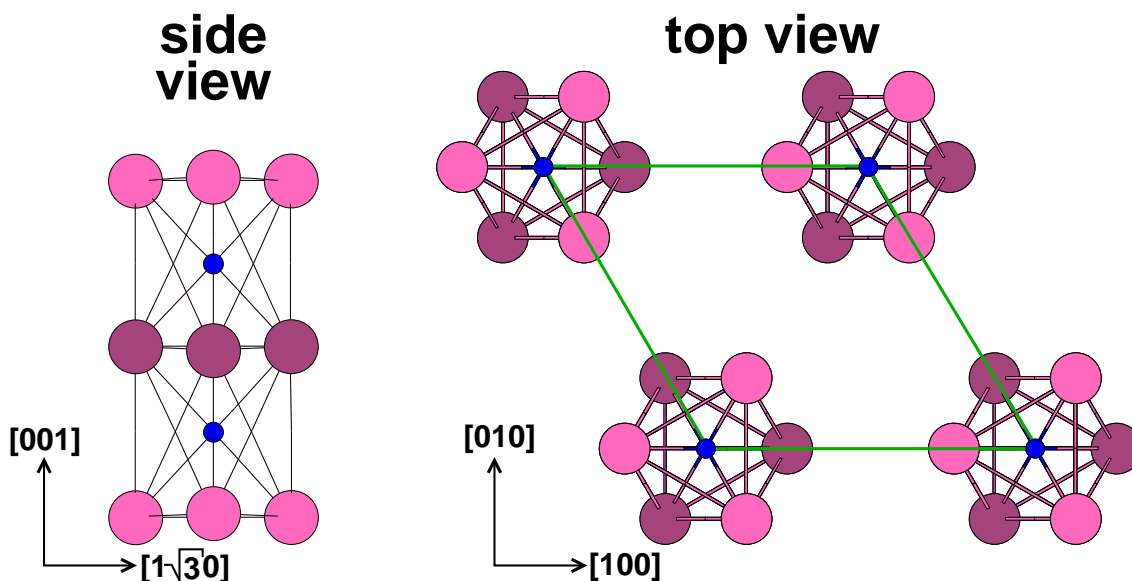


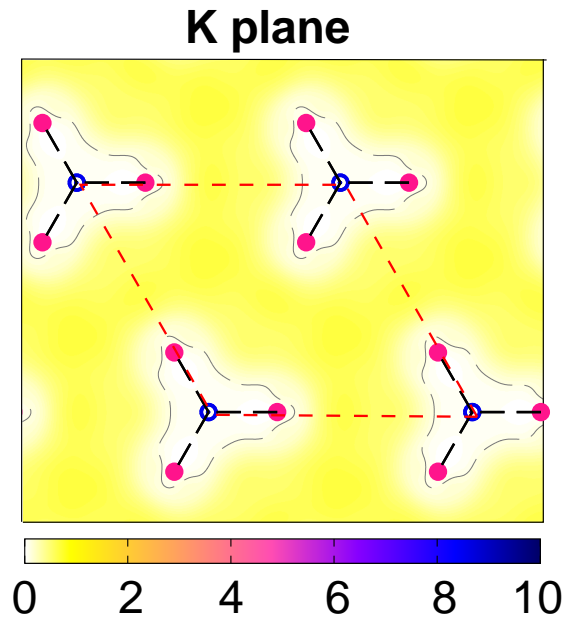
Figure 8.6: Side view of a single K_3N column and top view of the arrangement of the columns in the hexagonal anti- TiI_3 crystal structure. Positions of the K (N) atoms are indicated by light and dark red (blue) circles. The green line represents the boundary of the basal plane of the unit cell.

according to their orbital character, as resulting from a Mullikan analysis. Bands that can uniquely be identified as being derived from N_{2p} states are marked by open circles. Red filled triangles and open squares label bands that are derived from Na_{3s} and Na_{3p} states, respectively. It becomes clear that the metallic character of Na_3N resulting within LDA originates from an overlap of the Na $3s$ with the occupied N $2p$ bands occurring at the Γ point of the cubic Brillouin zone. This leads to a significant mixture of the two orbital contributions throughout the Brillouin zone. One of the three former N $2p$ bands is pushed down in energy due to non-vanishing contributions from Na_{3s} states. At the same time, the anionic $2p$ states also mix with the cationic $3s$ states for energies above the Fermi level, as can clearly be seen in the left panel of Fig. 8.5. This figure also indicates that Na_{3p} and Na_{3d} states do not play a significant role for the metallicity of Na_3N as resulting within LDA.

The right panel of Fig. 8.5 shows the orbital-resolved Na_3N band structure as resulting from SIC calculations. From the band markings according to the Mullikan orbital decomposition it becomes apparent that the inclusion of self-interaction corrections significantly reduces the previously discussed mixture of N_{2p} and Na_{3s} states around the Fermi level so that a gap opens.

Potassium nitride (K_3N) is the third compound in the row of alkali-metal nitrides addressed in this work. It exists in a low-density anti- TiI_3 crystal structure (space group $P6_3/mcm$) with lattice constants [235] of $a = 7.80\text{\AA}$ and $c = 7.59\text{\AA}$. A top and side

Figure 8.7: Charge density contours (in $10^{-2} a_B$) of the occupied K-derived state at the Γ point of the hexagonal Brillouin zone at $E = -0.81$ eV. The density is shown in a $[100]$ - $[010]$ plane containing one potassium layer. Filled rose and open blue circles represent positions of K atoms within and N atoms above and below the plotting plane.



view of the lattice is shown in Fig. 8.6. This structure can be considered as hexagonal columns consisting of K_3N , in which the K and N atoms are ionically bonded. The length of the K-N bond is 2.78 \AA . Within the potassium planes, the K atoms form trigonal arrays with a mutual distance of 3.51 \AA . To accurately represent the more extended bulk states in this fairly open structure, twenty slowly decaying s -type Gaussians are placed in the unit cell. They are located in the same four planes as the K and N atoms of the K_3N columns (see side view in Fig. 8.6) and are stacked on five respective columns of orbitals. These columns pierce the top view of the lattice in Fig. 8.6 in the middle between neighboring K_3N units (three of them) and in the middle of the two triangles formed by the K_3N units (the other two).

The band structure of K_3N is shown in the right panel of Fig. 8.3. Obviously, K_3N turns out to be metallic even after inclusion of self-interaction corrections. Also in this case, there is a low-lying N $2s$ band (see Table 8.2). The lowest bands shown in the figure can mainly be attributed to occupied N $2p$ states. They exhibit only a very small dispersion, which is due to the rather large unit cell. Above the Fermi level there is a group of bands that shows similarities to loosely bound, almost free electron-like s bands extending down in energy to -0.81 eV at Γ . They originate from K atoms. Thus SIC leads to a certain separation of the K $4s$ and N $2p$ bands but it is not as complete as the related separation of the Na $3s$ and N $2p$ bands in Na_3N (cf. right panel of Fig. 8.5). The situation resembles more the LDA result for Na_3N in the left panel of Fig. 8.5 where the Na $3s$ and N $2p$ bands overlap near Γ .

Along the high-symmetry lines on the $k_z = 0$ plane from Γ to K and from M to Γ of

the hexagonal Brillouin zone, the lowest of the free-electron-like bands is resonant in energy with the N $2p$ bands leading to the metallicity of K_3N according to the present calculations. The columns at the corners of the hexagonal base plane appear bonded together by metallic electrons between K atoms over a distance of 5.15\AA . This peculiar atomic structure has interesting consequences on the electronic structure. Fig. 8.7 shows charge density contours of the lowest occupied free-electron-like state at Γ . The density is rather delocalized and fills the empty space between the columns. The free-electron-like bands in the right panel of Fig. 8.3 can be attributed to this charge density and the associated metallic binding between the stacked K_3N columns on the hexagonal lattice. As this metallic contribution to the binding appears to be essential to keep the crystal together from a calculational point of view, the respective bands must be at least partially occupied. The mixture of the ionic intra-column binding and the metallic inter-column binding manifests itself in the overlap of the metallic and ionic bands near the Fermi energy. The SIC effects turn out to be less pronounced for K_3N than for Li_3N and Na_3N . Nevertheless, they have some influence on the band structure as can be exemplified for selected points in the hexagonal Brillouin zone. The direct gap, e. g., at the A point opens up from 0.35 eV in LDA to 0.72 eV in SIC. At present, there are no experimental band-structure data available on the highly fragile K_3N for comparison, as yet.

From a chemical point of view, K_3N is expected to be ionic in accord with the formulation $(K^+)_3N^{3-}$ and thus its electronic structure should feature a band gap between the filled N $2p$ and empty K $4s$ states. However, the self-interaction corrections alone, as employed in this work, appear to be not sufficient to open up such a gap, perhaps due to the remaining underestimation as also in the related Na_3N with the expected formulation $(Na^+)_3N^{3-}$. This aspect of the electronic structure remains to be resolved by further experiments and by more advanced calculations.

8.3. Bulk structural properties

In the previous section the electronic properties of alkali-metal fluorides, oxides and nitrides have been presented as calculated at the experimental lattice constants (a_{exp}), to allow for a most meaningful direct comparison of LDA and SIC results and a clear identification of the SIC effects on the band structures. In addition, the use of experimental lattice constants appears to be the most realistic for comparison with experiment. If one were to use theoretical lattice constants (a_{th}), which depend on the theoretical method employed, their differences would have an additional effect on the band structures obscuring the pure SIC effect to a certain extent.

To identify this combined effect the lattice constants of the investigated solids have been calculated within LDA and SIC. In Table 8.3 the optimized lattice constants and bulk

Table 8.3: Calculated lattice constants (in Å) and bulk moduli (in Mbar) as resulting from LDA and SIC calculations in comparison with other theoretical and experimental results.

		LDA	SIC	Other	Exp
LiF	<i>a</i>	3.97	3.91	3.91 ^a ,4.03 ^b	3.99 ^c
	<i>B</i>	0.80	0.95	0.87 ^a ,0.76 ^b	0.77 ^d
NaF	<i>a</i>	4.52	4.44	4.51 ^a ,4.63 ^b	4.57 ^c
	<i>B</i>	0.64	0.72	0.63 ^a ,0.51 ^b	0.54 ^d
KF	<i>a</i>	5.20	5.13	5.49 ^b	5.29 ^c
	<i>B</i>	0.50	0.65	0.30 ^b	0.36 ^d
Li₂O	<i>a</i>	4.52	4.50	4.53 ^e ,4.57 ^f	4.62 ^g
	<i>B</i>	0.88	0.91	0.95 ^e ,0.95 ^f	0.89 ^h
Na₂O	<i>a</i>	5.35	5.29	5.47 ^e ,5.48 ^f	5.56 ^g
	<i>B</i>	0.62	0.67	0.59 ^e ,0.61 ^f	
K₂O	<i>a</i>	6.46	6.42	6.36 ^e	6.45 ^g
	<i>B</i>	0.30	0.34	0.33 ^e	
Li₃N	<i>a</i>	3.56	3.55	3.51 ⁱ	3.65 ¹⁰
	<i>c</i>	3.80	3.79	3.75 ⁱ	3.87 ^j
	<i>B</i>	0.60	0.61		
Na₃N	<i>a</i>	4.57	4.56		4.73 ^k
	<i>B</i>	0.27	0.28		
K₃N	<i>a</i>	7.76	7.89	7.65 ^l	7.80 ^l
	<i>c</i>	7.29	7.10	7.50 ^l	7.59 ^l
	<i>B</i>	0.19	0.18		

^afrom Ref. [236], LDA

^bfrom Ref. [237], Hartree-Fock

^cfrom Ref. [216]

^dfrom Ref. [238]

^efrom Ref. [226], LDA

^ffrom Ref. [239], Hartree-Fock

^gfrom Ref. [224]

^hfrom Ref. [240]

ⁱfrom Ref. [241], LDA

^jfrom Ref. [230]

^kfrom Ref. [24]

^lfrom Ref. [235], LDA, Exp.

moduli are summarized for the nine bulk crystals studied. While LDA is known to underestimate lattice constants of common elemental, III-V and II-VI semiconductors only by roughly 1%, in the case of the alkali-metal fluorides, oxides and nitrides the respective underestimates span a range from 0.5 to about 4% (see Table 8.3). This can be viewed as an indication that the calculation of structural properties of the latter, partially much more ionic materials, is more intricate. This seems to apply to K_3N , in particular.

The lattice constants resulting within SIC are even somewhat smaller than those resulting from LDA. This appears to be related to the fact that both term values of the anions are drastically lowered relative to those of the cations due to SIC by similar amounts (see Table 8.1). As a consequence, the atomic $2s$ and $2p$ orbitals of the anions become more localized in SIC than in LDA and the lattice constants are reduced accordingly. The underestimate of the lattice constants in LDA and SIC results in respective overestimates of the bulk moduli, as compared to experiment.

One should note that the SIC approach yields larger lattice constants than LDA for IIB-VI semiconductor compounds [16], group III-nitrides [18], as well as silicon carbide polytypes and earth-alkali metal oxides studied in this work, which are in close agreement with experiment. In all of these cases, SIC also leads to a stronger localization of anionic orbitals. This does not give rise to smaller lattice constants, however, since the stronger orbital localization is accompanied by a partial weakening of the bonds in these materials giving rise to an increase in lattice constants. In the alkali-metal fluorides, oxides and nitrides, the valence bands are built up exclusively from anion orbitals while the cation orbitals give rise to the lower conduction bands. As a result, there is no reduction in ionic bonding and no increase in lattice constants involved when the anion orbitals become more localized.

One interesting notion in this regard is the fact that in these calculations pseudopotentials including non-linear core corrections have been employed. In the present pseudopotential approach, a self-interaction corrected treatment of the core charge density is conceptually not accounted for. Usually, the energetically deep core states are a truly atomic property even in the bulk crystal that does not influence its chemical characteristics. In terms of the self-consistent calculation of the structural properties of the solids, this means that any SIC for the core states will only lead to a constant shift of the total energy that does not contribute to any of the calculated properties which are based on derivatives of $E(V)$. In order to test this assumption, the structural properties of LiF have also been calculated using a pseudopotential for lithium based on the electronic configuration $1s^2$, i.e. like in the case of the alkaline earth metal oxides as sketched in Appendix B. The Li $1s$ core state is explicitly included in the pseudopotential as a valence state. A SIC calculation based on such a configuration yields a band structure with a band gap of 14.6 eV and a SIC induced downward shift of the Li $1s$ band comparable to that found in a GWA calculation [221]. This particular pseudopotential produces a reasonable electronic structure

and can therefore be expected to work reliably in terms of a total energy minimization. Just as in the case of the NLCC calculation, a lattice constant of bulk LiF results smaller in SIC (3.87 Å) than in LDA (3.91 Å). Hence, the above assumptions concerning the SIC treatment of the core charge appear to be justified and the smaller lattice constants for such highly ionic compounds seem to be an intrinsic feature of the SIC pseudopotentials. As is well-known, energy gaps are sensitive to the lattice constants and to the theoretical method used to calculate them. Very recently, for example, von Lilienfeld and Schultz [242] have investigated in great detail the sensitivity of the band gaps of GaAs, GaP, and GaN on pseudopotentials and lattice constants where the Ga 3*d* semicore states are of particular importance. Concerning the materials studied in this work, the band gaps vary linearly with the lattice constants around $E_g(a_{\text{exp}})$. The dependance of E_g on the lattice constant a can be described as

$$E_g(a) = E_g(a_{\text{exp}}) + (a_{\text{exp}} - a)S \quad (8.1)$$

where S is the slope. The resulting slopes are given in Table 8.4 in eV/Å. For the hexagonal Li_3N the slope is calculated at c_{exp} . Note that the differences between measured and calculated lattice constants are only in the order of 0.1 Å in most cases. The gap dependance on lattice constants turns out to be stronger in SIC than in LDA and it is largest for the most ionic solids in the studied material class. With the lattice constants in Table 8.3 and the slopes in Table 8.4 the band gaps for the LDA and SIC lattice constants can easily be calculated. For example, the largest effect of the lattice constants occurs for the gap of LiF. It results as 8.5 and 14.7 eV from LDA and SIC at a_{exp} , respectively, (see Table 8.2) while the LDA gap at $a_{\text{th}}^{\text{LDA}}$ is 8.6 eV and the SIC gap at $a_{\text{th}}^{\text{SIC}}$ is 15.3 eV. Thus in the former case the pure SIC-induced opening of the gap amounts to 6.2 eV while in the latter case the combined influence of the lattice constants and of SIC opens the gap by 6.7 eV seemingly increasing the SIC effect by 0.5 eV. Nevertheless, also the gap energies at the different theoretical lattice constants clearly reveal the superiority of SIC as compared to LDA. In any case, it is most realistic to use the experimental lattice constants when the results are to be compared with experiment, as has been done in the previous section.

8.4. Summary

The bulk electronic structure of alkali-metal fluorides, oxides and nitrides as resulting from density-functional theory including self-interaction corrections by employing corresponding pseudopotentials has been investigated in this chapter. Except for K_3N , all other alkali-metal fluorides (MF), oxides (M_2O) and nitrides (M_3N) with $\text{M} = \text{Li}, \text{Na}, \text{and K}$ turn out to be semiconductors or insulators. In particular, the band structure of Na_3N has been analyzed in more detail since this compound has been synthesized more recently

	LDA	SIC
LiF	6.21	7.10
NaF	3.53	4.49
KF	2.22	3.00
Li₂O	1.23	1.97
Na₂O	1.99	2.88
K₂O	0.97	1.70
Li₃N	0.97	1.22
Na₃N	no gap	0.38
K₃N	no gap	no gap

Table 8.4: Slope S of the variation of calculated band gaps with lattice constants (in eV/Å) according to Eq. (1).

and was shown to be a semiconductor much in contrast to the results of LDA calculations which find Na₃N to be metallic. On the contrary, the SIC results clearly corroborate that Na₃N is a semiconductor. In general, SIC results for all compounds studied are in good agreement with available experimental data and with the results of calculations going beyond LDA, such as correlation-corrected Hartree-Fock or *GW* quasiparticle calculations. The latter have been restricted so far to the fluorides, however. K₃N results as a metal both from LDA as well as from SIC calculations. According to the results, this appears to originate from the peculiar lattice structure of K₃N giving rise to a mixed metallic-ionic binding. More advanced calculations, such as many-body quasiparticle band-structure calculations, might be necessary to eventually clarify this point. They are however beyond the scope of this work.

Chapter 9.

Conclusions and Outlook

All in all, self-interaction corrected pseudopotentials have turned out to be an extremely useful and reliable tool in calculating the electronic structure of bulk solids, surfaces, and nanostructures like graphitic layers or nanotubes, with better qualitative and quantitative accuracy than standard LDA calculations. This is clearly shown by Fig. 9.1, in which the calculated energy gaps for the bulk systems studied in this work are plotted against their respective experimental values, if available. Compared to other beyond-LDA approaches, the SIC pseudopotential approach pragmatically treats the inherent problems of the local-density approximation in a way that is computationally undemanding. This fact is of particular importance when it comes to the study of systems that have to be described in large unit cells with a large number of atoms, as e.g. in the case of large surface reconstructions or nanotubes.

In the light of the remarkable success of the method as presented for the systems studied in this work, it must also be pointed out that there is still room for improvement as is exemplified by the two examples to follow.

SIC depending on the magnetic quantum number

Strongly localized electronic states often contribute significantly to the physical properties of condensed matter. A very important aspect has not been dealt with in the present work, namely magnetism. Recently, a system that is intimately related to substances studied in this work has come to the attention of scientific interest. Among others, doped oxides are expected to exhibit so called d^0 magnetism, i.e. magnetism that is not associated with narrow d -bands but instead with partially filled p -bands. In particular, MgO with substitutional nitrogen defects (N_O) has been studied theoretically using LSDA+U [243] and the so called ASIC method [244], which is related to the SIC method in this work.

In Fig. 9.2(a) the spin-resolved DOS of a system with one N impurity replacing one out of 16 oxygen atoms, i.e. a $Mg_{16}O_{15}N$ system, as resulting from a standard LSDA calculation [245] is shown. It turns out that the system is ferromagnetic with a half-metallic

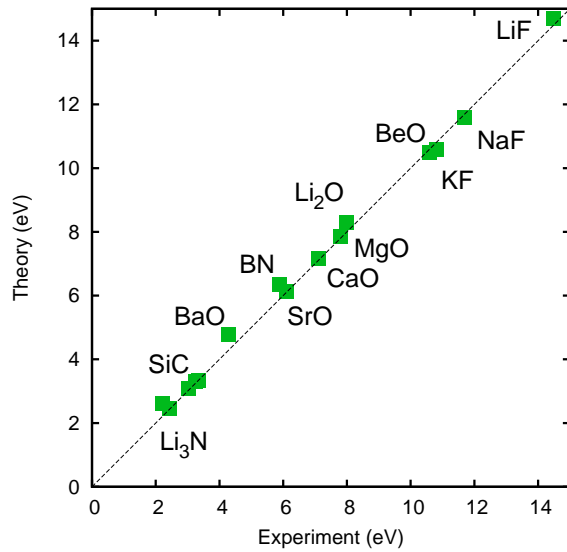


Figure 9.1: Calculated bulk band gap energies of materials studied in this work as resulting from SIC calculations compared to their respective experimental values.

ground state since the Fermi level cuts through the $2/3$ filled minority N $2p$ impurity band. Actually the magnetic moment is $\mu=1\mu_B$. In this case, the impurity hole is *delocalized* in the sense that it is equally distributed over p_x , p_y , and p_z states of the nitrogen atom. According to Ref. [244], this indicates that such a system exhibits large magnetic interactions between the impurities based on a *Zener mechanism*. However, as was discussed before, the use of the local-density approximation underestimates the attractive potential effecting localized charges. As was pointed out in both Refs. [243, 244], the better treatment of such localized contributions leads to a stronger localization of electrons and a splitting of the formerly degenerate N $2p$ level in a doubly occupied level (i.e. p_x and p_y) and an empty singlet (p_z) occurs. In such an insulating ground state, the magnetic coupling between the N_O impurities can only be explained by a weak *superexchange*. Obviously, the treatment of the localized charges is essential for predicting the fundamental aspects of d^0 -magnetism in such systems. When the SIC approach as used in this work is applied to this particular system, a spin-resolved density of states as in Fig. 9.2(b) results. Apparently, the fundamental half-metallic character of the ground state remains unchanged. This is due to the fact that the approach as of now does not explicitly discriminate between the different usually degenerate m -states of the atom. As the method contains no immediate "feedback" between occupancy in the solid and the atomic states used to construct the SIC pseudopotential, all three p -states equally experience self-interaction corrections. Without any additional external changes, i.e. an unusually large Jahn-Teller-like lattice distortion that would result in a crystal field split already in LSDA, there is no incentive for the electrons to prefer the doublet-singlet spin configuration as reported in Refs. [243, 244]. This indicates that it might be worthwhile to consider more intricate modifications to the SIC pseudopotentials. In particular, one should be able to treat states with different m for a fixed l independently. For the moment, one can assume a minority spin electron

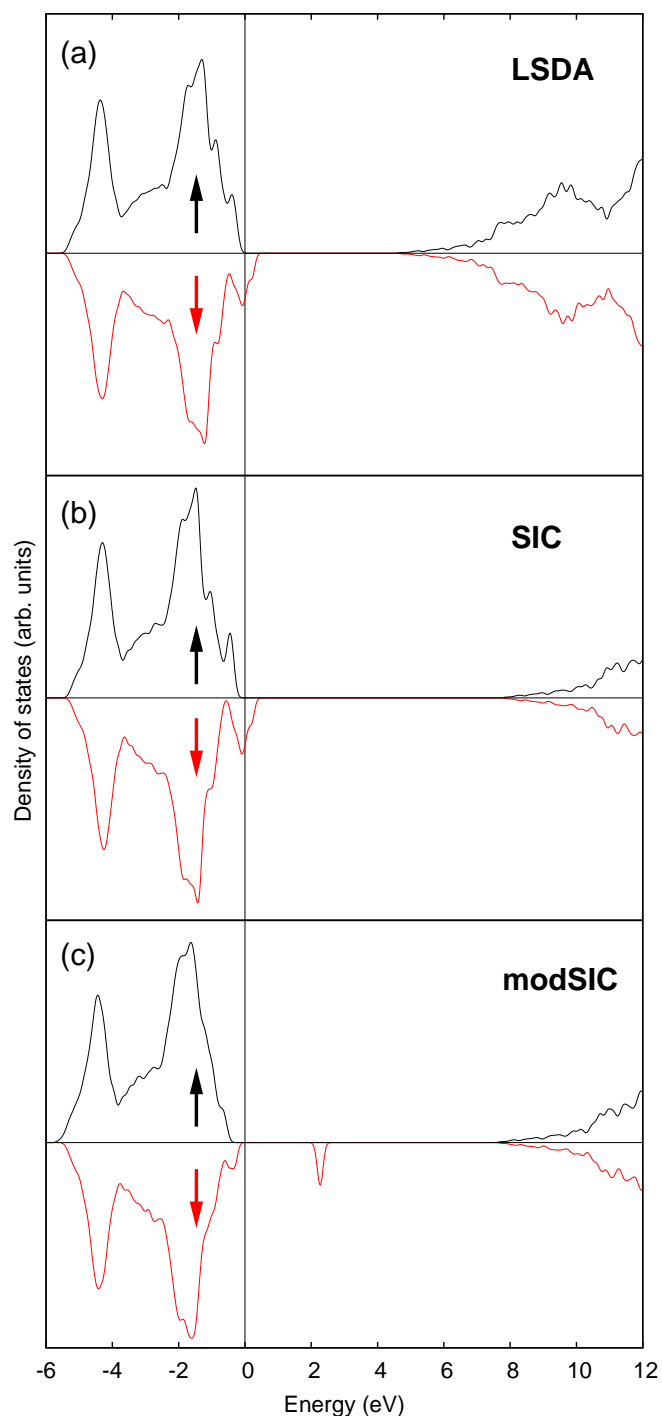


Figure 9.2: Spin-resolved density of states relative to the Fermi energy for $\text{Mg}_{16}\text{O}_{15}\text{N}$ as resulting from LSDA (a), SIC (b), and modified SIC (c) calculations, respectively. Majority and minority spins are represented by black and red lines, respectively, as indicated by the inset arrows.

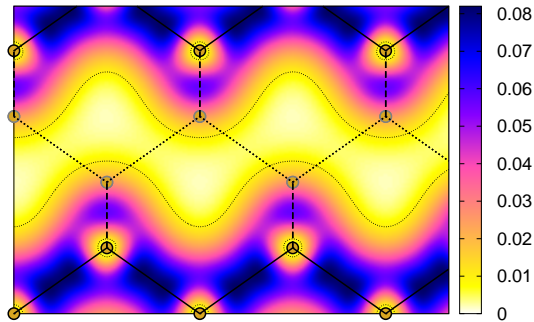


Figure 9.3: Valence charge density contours (in a_B^{-3}) of the silicon bulk crystal, shown in the $[011]$ - $[100]$ plane.

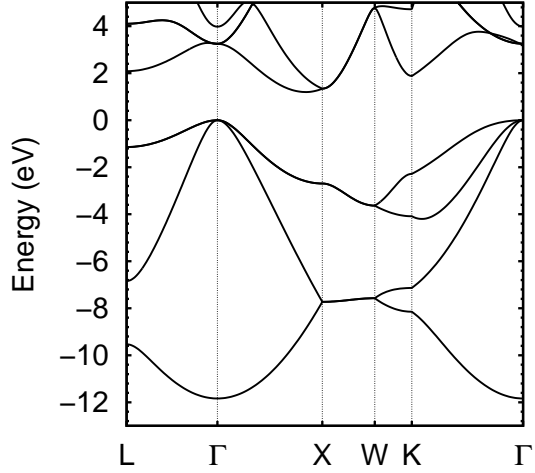
distribution as in Refs. [243, 244] and manually switch off the N $2p_z$ contribution to the minority spin Hamiltonian. For such a case the DOS as shown in Fig. 9.2(c) turns out to show the same features as reported, i.e. an insulating ground state and a level split by 2.2 eV, which is comparable to that found by LSDA+U (~ 1.8 eV) and ASIC (~ 3 eV). As the system does not automatically arrive at this electronic configuration, only a comparison of the total energies of the standard SIC and manually restricted calculations can serve to identify the true SIC ground state. Evaluating Eq. (3.25), the term $\sum_{\alpha}^{\text{occ}} E_{\text{HXC}}[\varrho_{\alpha}]$ has usually been omitted in the calculation because for the bulk solids investigated, the principally constant electronic configuration only leads to a constant term in the total energy. Now comparing the total energies of the degenerate and split configurations in the minority spin for $\text{Mg}_{16}\text{O}_{15}\text{N}$, one has to take the local orbital configuration of the nitrogen impurity explicitly into account. As it turns out, the split configuration results as 0.32 eV per unit cell more favorable than the degenerate one. This energy gain justifies the above modifications and makes it all the more evident that a modification of the SIC approach with regards to m -dependent self-interaction corrections is worth to be developed.

Purely covalent bonds: Silicon

Another aspect for which the simple SIC approach fails to deliver any improvement in the calculation of the electronic structure is the case of purely covalently bonded crystals, i.e. silicon, diamond, or germanium.

The reason why the atomic SIC pseudopotential approach cannot be successfully applied to these systems is evident. By construction these corrections largely affect the valence charge located at the ion cores. However as can be seen in Fig. 9.3, which shows a charge density contour plot for the silicon bulk crystal in the $[011]$ - $[100]$ plane, the bond charge is not located at these cores. Instead the fundamental nature of the covalent bond leads to maxima of charge density at the bond centers (BC) between the constituent atoms. In Ref. [246] it was shown that the description of phonons in covalently bonded crystals can

Figure 9.4: Band structure of the Si bulk crystal with a gap of 1.2 eV as resulting from an experimental bond-center SIC calculation. Note that the quantitative effect is coincidental because of the arbitrary nature of the used SIC potential.



be improved by adding additional force constants at these bond centers.

If one borrows this idea for the problem at hand, a first step is to add additional Gaussian orbitals at the bond centers. In fact in a simple LDA calculation, positioning a single shell of such additional only s -like orbitals with a decay constant of 0.18 (in atomic units) improves the total energy by 0.08 eV per unit cell. If one artificially attaches a simple very weak SIC pseudopotential to this s -orbital, a band structure of bulk silicon as depicted in Fig. 9.4 results. Astonishingly, the band structure contains all the usual features of the electronic structure of bulk silicon. Its gap, however, is not resulting as 0.6 eV showing the typical LDA underestimate. Instead one finds an indirect band gap of 1.2 eV, which is in excellent agreement with experimental reference values. The question arises whether there is any chance to uniquely define the self-interaction correction that should be associated with such an additional BC orbital. Actually the basis of Gaussian orbitals might be very helpful in this regard. If τ_{BC} defines the position of the additional orbital in the bulk unit cell one can use the associated expansion coefficients $c_{n,s,BC}(\mathbf{k})$ obtained during the diagonalization and constructs a \mathbf{k} -averaged pseudo-atomic bond-center s -wavefunction according to

$$\psi_{s,BC}(\mathbf{r}) = \sum_{n_{occ}} \sum_{\mathbf{k}} c_{n,s,BC}(\mathbf{k}) \chi_{s,BC}(\mathbf{k}, \mathbf{r}). \quad (9.1)$$

It could be possible to use the spherically defined atomic SIC for such a pseudo-atomic function and determine its corrective potential based on $\rho_{s,BC}(\mathbf{r})$. The resulting potential can possibly be employed in the next step of the calculation for the solid. In fact, this could be generalized for all angular momentum components and all atoms of the non-primitive basis, i.e. a natural partitioning of the total valence charge density in atomic contributions defined by the Gaussian basis. Further studies are needed to investigate whether such an approach is viable.

Summary

In this work, the structural and electronic properties of a multitude of materials in bulk configurations as well as with reduced periodicity has been investigated using an approximate self-interaction correction scheme that transfers well-defined atomic corrections to the solid.

As has been pointed out in the beginning, the calculation of the electronic structure within the framework of the standard local-density approximation of density-functional theory suffers from the systematic underestimate of fundamental energy gaps in semiconductors and insulators by roughly 50%. After introducing the methodology of self-interaction corrected pseudopotentials for the prototypical case of bulk silicon carbide polytypes, this pragmatic approach has at first been applied to the determination of the electronic structure of several selected surfaces of 3C-SiC and 4H-SiC. In the process it has turned out that the use of SIC pseudopotentials results in a reliably improved description of the surface band structure of the non-polar 3C-SiC(110)-(1×1) surface. Its surface characteristics are largely similar to that of the respective bulk crystal leading to a pronounced effect of the SIC pseudopotentials on the calculated surface band gap, which opens from 0.25 eV (LDA) to 1.17 eV (SIC). In contrast, 3C-SiC(001) is a polar surface which shows intricate surface reconstructions. In particular, for the Dimer Row Model of the (2×1) and the Bridging Dimer Model of the c(2×2) reconstructions studied in this work, carbon dimers form on the surface top-layer. Both bonding and anti-bonding dimer states are linear combinations of carbon *p*-like orbitals, which are equally affected by the C *2p* contribution to the SIC pseudopotential. An appropriate description requires a modification of the SIC approach. In order to accurately account for the fact that the empty anti-bonding states are not SI corrected, the SIC- Δ approach was introduced, which subtracts the spurious self-interaction correction from the calculated energies of unoccupied bands. For the Dimer Row Model of 3C-SiC(001)-(2×1) this approach yields a surface band gap of 0.99 eV – in contrast to the metallic character as determined by LDA – which is in very good agreement with the result of a quasiparticle calculation (0.94 eV) [79]. For the Bridging Dimer Model of the 3C-SiC(001)-c(2×2) surface, good agreement of calculated bands with experimental ARPES [80] and ARIPES [81] data is found. Experimentally and theoretically, the surfaces of 4H-SiC have been less intensively studied in the literature. In analogy to the 2H-SiC(10 $\bar{1}$ 0) surface [70], a so called relaxed Type A surface is favored from structure optimizations for 4H-SiC(10 $\bar{1}$ 0) in this work.

Four salient surface bands can be identified in this structure, two of which are occupied and two are empty. From an analysis of charge density distributions and localized Wannier functions, one pair of these bands (π_A , π_A^*) can be associated to the formation of a Si=C double bond on the outer surface layer. The second pair (π_B , π_B^*) contains more features of common occupied carbon and unoccupied silicon dangling bonds. The SIC- Δ band structure reveals that the fundamental surface gap is formed between π_B and π_B^* bands amounting to 1.74 eV. Very much in contrast to these findings, a preliminary photoemission study [85] alludes to the formation of only one occupied surface state. Comparing experimental and theoretical results, there is a good probability that the observed band corresponds to the π_A band. The attenuation or disappearance of the π_B band, however, cannot easily be resolved. Surface models with hydrogen adsorption and different surface stoichiometries have been investigated as well, all unable to reconcile theory and experiment.

In the case of the 4H-SiC($1\bar{1}02$)-c(2×2) surface, fourteen different reconstruction models have been investigated by total energy calculations, including the one originally proposed by Virojanadara *et al.* [90] on the basis of their experimental results. It turns out that this model, which features the formation of two staggered bridging triple-bonded carbon dimers in the surface unit cell accompanied by the adsorption of a single silicon atom in the so-called H3 position, is energetically unfavorable. While the H3 site for silicon adsorption is indeed favored over the alternative T4 site, the optimized model features the formation of a double-bonded carbon dimer pair (DP-H3). The calculation of the respective electronic structures reveals that this surface is semiconducting for all investigated models when using the SIC- Δ approach. In particular, the gap is formed between dispersion-less occupied carbon and empty silicon adatom dangling-bond bands. As a consequence all models result in a similarly large band gap of around 1.2 to 1.5 eV, which renders the electronic structure unsuitable to differentiate between the models in experiment. However, calculated empty state STM images at a simulated bias voltage of 3.7 V clearly reveal significant differences between the models as respective anti-bonding states of carbon dimers are mapped in one case and carbon as well as silicon dimers are mapped in the other case. Respective experiments should hence be able to identify the definite nature of the carbon dimers on the 4H-SiC($1\bar{1}02$)-c(2×2) surface.

The SIC pseudopotential approach has furthermore been used to study the electronic structure of alkaline-earth metal oxides in bulk as well as surface geometries. The calculated band gaps for bulk BeO, MgO, CaO, SrO, and BaO are in very good agreement with experimental and theoretical reference data. This enables a detailed and both qualitatively and quantitatively reliable investigation of the respective surface properties. In particular, the unoccupied electronic structure of the non-polar (001) surfaces of MgO, CaO, SrO, and BaO has been scrutinized for the occurrence of image potential states. Generally, the surface electronic structure is largely similar to that of the projected bulk band structure.

Due to the highly ionic character of the materials, no significant surface relaxations are encountered that could lead to notable changes in the electronic characteristics. In the case of MgO(001), the SIC band structure with a calculated surface gap of 6.5 eV agrees well with a quasiparticle calculation [164] (6.9 eV) and experimental evidence [150–152] (6.2 eV), highlighting the strong usefulness of the SIC pseudopotential approach for these surface systems. Moreover, at the (001) surfaces of MgO, CaO, and SrO the respective lowest unoccupied surface band could be identified as arising from image potential states, in which the electron density is nearly-free-electron-like parallel to the surface and resides in the vacuum. The related band on BaO(001), in contrast, turns out to originate from localized surface states bound to the surface cation. The nature of image potential states at alkaline-earth metal oxides has been compared to traditional IPS at metal surfaces and traditional bound empty surface states by an analysis of charge density contours and energy diagrams. The differences are interpreted in terms of the energetic accessibility of and potential coupling to bulk, surface, and vacuum states.

Based on these successes the SIC approach has been used to study structural, elastic, and electronic properties of SiC, BN, and BeO nanotubes with diameters ranging from 3 to 25 Å. The progression of the radial buckling, strain energy, Young's modulus, and energy gap with the diameter has been investigated. With the exception of the energy gap, all nanotube properties turn out to be largely independent of helicity for all three ionic materials. In case of SiC and BN nanotubes, a sensitive dependence of the energy gap is found. While for armchair nanotubes the calculated band gaps remain close to the limiting value of a single graphitic sheet (3.94 eV for SiC, 6.19 eV for BN, and 8.72 eV for BeO) with only small deviations for small diameters, their zigzag counterparts feature a strong breakdown of the energy gap. In contrast to usual LDA calculations, however, they remain semiconducting. The nanotubes of highly ionic BeO in contrast show a very different behavior. First of all, the progression of the band gap is virtually independent of helicity. Secondly, no narrowing of the band gap is found at small diameters but instead the gap reopens after running through a minimum at approx. 7 Å. The differences have been analyzed in terms of real space charge densities and can be attributed to the highly ionic character of BeO and the associated less directional bonding.

Finally the electronic structure of nine alkali-metal fluorides, oxides, and nitrides has been studied using the SIC approach. For such highly ionic systems, it is a well suited approach and has yielded electronic band structures that are in very good agreement with experimental and theoretical reference data. For instance the SIC band gap for LiF results as 14.7 eV, which compares favorably to the range of 13.6 eV to 14.5 eV measured in experiment [206–208] and 14.4 and 14.3 eV as resulting from quasiparticle calculations [207, 220, 221]. The investigation especially intended to scrutinize the electronic characteristics of the more recently synthesized Na₃N [24, 25]. Standard LDA calculations predict a metallic material with a negative gap of -0.6 eV resulting from an overlap

of Na $3s$ and N $2p$ bands near the Γ point of the Brillouin zone. This overlap vanishes within DFT-SIC and a band gap of 0.5 eV is obtained, clearly supporting the notion of sodium nitride being a semiconductor as is inferred from experiment [204].

All in all, it can be stated that the use of self-interaction corrected pseudopotentials in density-functional calculations has resulted in substantially improved description of the electronic properties for a number of different solids, surfaces, and nanotubes. Due to its low numerical demand, this method presents an efficient way to obtain reliable results even for comparatively large systems.

Appendix

A. Explicit forms of Pulay-, Hellmann-Feynman- and Madelung forces

In section 2.5, it was shown that the force \mathbf{F}_ν on the atom located at the position $\boldsymbol{\tau}_\nu$ consists of three different terms (2.40):

$$\mathbf{F}_\nu = -\nabla_\nu E_{\text{tot}} = \underbrace{-2\text{Re}\langle\Psi|\hat{H}|\nabla_\nu\Psi\rangle}_{:=\mathbf{F}_\nu^{\text{pul}}} - \underbrace{\langle\Psi|\nabla_\nu V_{\text{ext}}|\Psi\rangle}_{:=\mathbf{F}_\nu^{\text{HF}}} - \underbrace{\nabla_\nu E_{\text{Mad}}}_{:=\mathbf{F}_\nu^{\text{Mad}}} . \quad (\text{A.2})$$

The key to finding explicit expressions for the Pulay- and Hellmann-Feynman forces is the Hellmann-Feynman theorem. It deals with the derivatives of the single-particle energie ϵ_i with respect to an arbitrary parameter. In this case, we assume that this parameter is the j -th component of the position vector $\boldsymbol{\tau}_\nu$ of the ν -th atom and abbreviate

$$\partial := \frac{\partial}{\partial \tau_{\nu,j}} . \quad (\text{A.3})$$

Furthermore, let us expand the wave functions $|\psi_i\rangle$ in terms of a not necessarily orthonormal basis $\{|\chi_\alpha\rangle\}$

$$|\psi_i\rangle = \sum_\alpha c_\alpha^i |\chi_\alpha\rangle . \quad (\text{A.4})$$

Using the norm $\langle\psi_i|\psi_i\rangle = 1$ and the equation of the eigenvalue problem

$$\sum_{\alpha'} H_{\alpha\alpha'} c_{\alpha'}^i = \epsilon_i \sum_{\alpha'} S_{\alpha\alpha'} c_{\alpha'}^i \quad (\text{A.5})$$

yields in combination with eq. (2.36):

$$\partial\epsilon_i = \partial\langle\psi_i|\hat{H}|\psi_i\rangle = 2\text{Re} \sum_{\alpha\alpha'} c_\alpha^{i*} c_{\alpha'}^i \left(\tilde{\partial}H_{\alpha\alpha'} - \epsilon_i \tilde{\partial}S_{\alpha\alpha'} \right) + \langle\psi_i|\partial\hat{H}|\psi_i\rangle , \quad (\text{A.6})$$

where we have introduced

$$\tilde{\partial}H_{\alpha\alpha'} = \int \chi_\alpha^*(\mathbf{r}) \hat{H} \partial\chi_{\alpha'}(\mathbf{r}) d^3r \quad (\text{A.7})$$

and

$$\tilde{\delta}S_{\alpha\alpha'} = \int \chi_{\alpha}^*(\mathbf{r}) \partial \chi_{\alpha'}(\mathbf{r}) d^3r . \quad (\text{A.8})$$

Eq. (A.6) is a Hellmann-Feynman theorem for an incomplete basis. We can use it to derive an expression for the Pulay force:

$$\begin{aligned} \mathbf{F}_{\nu}^{\text{Pul}} &= -2\text{Re}\langle \Psi | \hat{H} | \nabla_{\nu} \Psi \rangle = -2\text{Re} \frac{2}{N_0} \sum_{n,\mathbf{k}}^{\text{occ}} \int_{V_0} \psi_{n,\mathbf{k}}^*(\mathbf{r}) \hat{H} [\nabla_{\nu} \psi_{n,\mathbf{k}}(\mathbf{r})] d^3r \\ &= -2\text{Re} \frac{2}{N_0} \sum_{n,\mathbf{k}}^{\text{occ}} \sum_{\alpha\mu} \sum_{\alpha'\mu'} c_{\alpha\mu}^{n,\mathbf{k}*} c_{\alpha'\mu'}^{n,\mathbf{k}} \left\{ \tilde{\nabla}_{\nu} H_{\alpha\mu,\alpha'\mu'}^{\mathbf{k}} - \epsilon_n^{\mathbf{k}} \tilde{\nabla}_{\nu} S_{\alpha\mu,\alpha'\mu'}^{\mathbf{k}} \right\} , \end{aligned} \quad (\text{A.9})$$

where we have defined

$$\begin{aligned} \tilde{\nabla}_{\nu} O_{\alpha\mu,\alpha'\mu'}^{\mathbf{k}} &:= \int_{V_0} \chi_{\alpha\mu}^*(\mathbf{k}, \mathbf{r}) \hat{O} \nabla_{\nu} \chi_{\alpha'\mu'}(\mathbf{k}, \mathbf{r}) d^3r \\ &= \delta_{\nu\mu'} \sum_j e^{i\mathbf{k}\mathbf{R}_{\mu\mu'}^j} \left\{ \tilde{\nabla}_{\nu} O_{\alpha\mu,\alpha'\mu'}^j + i\mathbf{k} O_{\alpha\mu,\alpha'\mu'}^j \right\} , \end{aligned} \quad (\text{A.10})$$

with

$$\tilde{\nabla}_{\nu} O_{\alpha\mu,\alpha'\mu'}^j = \int \phi_{\alpha\mu}(\mathbf{r} - \boldsymbol{\tau}_{\mu}) \hat{O} [\nabla_{\mu'} \phi_{\alpha'\mu'}(\mathbf{r} - \mathbf{R}_{\mu'}^j)] d^3r . \quad (\text{A.11})$$

As the terms linear in $i\mathbf{k}$ from the Hamilton and overlap matrices cancel each other (Kohn-Sham equation), the Pulay force is finally determined by

$$\mathbf{F}_{\nu}^{\text{Pul}} = -2\text{Re} \frac{2}{N_0} \sum_{n,\mathbf{k}}^{\text{occ}} \sum_{\alpha\mu} \sum_{\alpha'\mu'} c_{\alpha\mu}^{n,\mathbf{k}*} c_{\alpha'\mu'}^{n,\mathbf{k}} \sum_j e^{i\mathbf{k}\mathbf{R}_{\mu\mu'}^j} \left\{ \delta_{\nu\mu'} \tilde{\nabla}_{\nu} H_{\alpha\mu,\alpha'\mu'}^j - \epsilon_n^{\mathbf{k}} \tilde{\nabla}_{\nu} S_{\alpha\mu,\alpha'\mu'}^j \right\} . \quad (\text{A.12})$$

At this point it should be mentioned that based on the self-interaction correction scheme presented in Chapter 3.4, one could also try to calculate self-interaction corrected forces. However, the variational principle is not strictly fulfilled in this case rendering it impossible to make use of the Kohn-Sham equations as in the way above. No analytic expression equivalent to Eq. (A.12) can be derived. Instead, one would have to calculate the forces as derivatives of the total energy directly by a finite difference method. Since the structure parameters obtained by total energy minimization for bulk solids are in good agreement with those resulting in SIC, the somewhat more involved force calculations for surfaces within SIC is omitted in this work and the surface structure is determined within standard DFT-LDA framework.

	$r_{c,l}$	a	B	E_g	$\Delta_{\Gamma X}^{\text{CB}}$	$E_g(\Gamma)$	$E_g(X)$
A	$r_{c,s} = 1.6$						
	$r_{c,p} = 1.0$	5.02	1.09	2.90	0.53	3.43	2.98
	$r_{c,d} = 1.2$						
B	$r_{c,s} = 1.8$						
	$r_{c,p} = 1.0$	5.04	1.26	2.84	1.05	3.89	2.92
	$r_{c,d} = 1.2$						
C	$r_{c,s} = 1.9$						
	$r_{c,p} = 1.0$	5.09	1.09	2.80	0.71	4.23	2.90
	$r_{c,d} = 1.2$						
D	$r_{c,s} = 1.9$						
	$r_{c,p} = 1.1$	5.07	1.23	2.87	1.44	4.30	2.98
	$r_{c,d} = 1.5$						

Table B.1: Structural (lattice constant a in Å and bulk modulus B in Mbar) and selected electronic properties (band gap E_g , separation of the lowest conduction band $\Delta_{\Gamma X}^{\text{CB}}$ between Γ and X , direct gaps at Γ and X all in eV) of SrO resulting from different constructions of the strontium pseudopotential based on the ionic configuration $[\text{Ar}] 4s^2 4p^6$.

B. Pseudopotentials including semicore states

In Chapter 6.2, pseudopotentials for the alkaline-earth metals which explicitly include semicore states are used in the calculation of the electronic structure of the respective oxides. The procedure of how those pseudopotentials are generated shall be exemplified for the case of the strontium pseudopotential to be used for SrO in the following. Using the electron configuration $[\text{Ar}] 4s^2 4p^6$ guarantees the reliable calculation of structural properties, most importantly during structure optimization of the (001) surface. The explicit inclusion of the upper core states into the valence configuration reduces the error regarding the interaction of core and valence charge. During the construction process of the pseudopotentials, it is important to ensure its transferability by a suitable choice of the core radii $r_{c,l}$.

Table B.1 comparatively shows calculated structural and selected electronic properties of the SrO bulk crystal as resulting from four (A-D) choices of the core radii. It becomes immediately obvious that properties like the optimized lattice constant a and fundamental band gap E_g do not depend significantly on the core parameters. The dependence of the bulk modulus B as well as the energetic position of the lowest conduction band at the Γ -point of the Brillouin zone is by far more pronounced. The results for the bulk modulus obtained using potential B and D deviate strongly in comparison to experimental data

($B^{\text{exp}} = 0.91 \text{ Mbar}$). Potentials A and C seem more reliable. These two however yield a markedly different electronic structure. In particular, the electronic properties resulting from potential A depend substantially on the lattice constant. If the band structure is calculated at the experimental lattice constant, the formerly indirect Γ - X band gap becomes direct at Γ . There is no experimental indication at all, that SrO features such a direct gap. In contrast, calculations using potential C are consistent in this regard. The different behavior of potentials A and C can easily be understood. In the first case, a rather small core radius of 1.6 a.u. is used for the s -component of the pseudopotential. With this component which is based on the Sr $4s$ level, the $5s$ levels shall be suitably described, as well. A small core radius in this case leads to worse transferability which particularly influences the lowest conduction band state at Γ . A Mulliken analysis of the conduction bands reveals a dominant s^* contribution (Sr $5s$) to the lowest band at Γ while the higher ones are mostly derived from Sr $4d$. At X , this situation is inverted, visible by a band crossing along the Γ - X line. Due to the small core radius, the transferability of the pseudopotential, most notably its s -component, is compromised, which leads to the observed behavior of potential A.

C. Decay constants for Gaussian orbitals

In Table C.1, the decay constants (in atomic units) used for the elements in this work are listed. If not mentioned otherwise, s , p , d , and s^* functions are treated equally.

Element	shells	Element	shells
Si (bulk)	0.20, 0.60	Ba	0.10, 0.25, 0.42, 1.75
Si (surface)	0.18, 0.50, 1.00	O	0.30, 0.90, 3.50
C (bulk)	0.35, 1.70	B	0.20, 0.42, 1.90
C (surface)	0.25, 1.00, 2.86	N	0.31, 1.36, 6.00
H	0.35	Li	0.30, 1.34, 6.00
Be	0.18, 0.40, 0.90	Na	0.16, 0.30, 0.60
Mg	0.25, 0.55, 0.95	K	0.16, 0.37, 0.88
Ca	0.16, 0.38, 0.85, 1.30	F	0.20, 0.95, 4.50
Sr	0.18, 0.40, 0.90, 1.70	vacuum	0.14 (s), 0.18 (s,p,d,s*)

Table C.1: Decay constants (in atomic units) for the elements in this work. The sets for silicon and carbon atoms at surfaces are also referred to as extended sets in the text.

Bibliography

- [1] **P. Hohenberg and W. Kohn**, *Inhomogeneous electron gas*, Phys. Rev. **136**, B864 (1964).
- [2] **W. Kohn and L.J. Sham**, *Self-consistent Equations including Exchange and Correlation Effects*, Phys. Rev. **140**, A1133 (1965).
- [3] **L. Hedin**, *New Method for Calculating the One-Particle Green's Function with Application to the Electron-Gas Problem*, Phys. Rev. **139**, A796 (1965).
- [4] **L. Hedin and S. Lundqvist**, Solid State Physics **23** (1965) edited by F. Seitz, D. Turnbull, and H. Ehrenreich (Academic, New York, 1965).
- [5] **M. S. Hybertsen and S. G. Louie**, *Electron correlation and the band gap in ionic crystals*, Phys. Rev. B **32**, 7005 (1985).
- [6] **M. S. Hybertsen and S. G. Louie**, *Electron correlation in semiconductors and insulators: Band gaps and quasiparticle energies*, Phys. Rev. B **34**, 5390 (1986).
- [7] **M. Rohlfing, P. Krüger, and J. Pollmann**, *Quasiparticle band-structure calculations for C, Si, Ge, GaAs, and SiC using Gaussian-orbital basis sets*, Phys. Rev. B **48**, 17791 (1993).
- [8] **B. Wenzien, P. Käckell, and F. Bechstedt**, *Quasiparticle band structure of silicon carbide polytypes*, Phys. Rev. B **52**, 10897 (1995).
- [9] **O. Gunnarsson, M. Jonson, and B. I. Lundqvist**, *Descriptions of exchange and correlation effects in inhomogeneous electron systems*, Phys. Rev. B **20**, 3139 (1979).
- [10] **R. M. Martin**, *Electronic Structure: Basic Theory and Practical Methods*. Cambridge University Press (2004).
- [11] **M. Ernzerhof and G. E. Scuseria**, *Assessment of the Perdew-Burke-Ernzerhof exchange-correlation functional*, J. Chem. Phys. **110**, 5029 (1999).
- [12] **A. D. Becke**, *A new mixing of Hartree-Fock and local density-functional theories*, J. Chem. Phys. **98**, 1372 (1993).
- [13] **J. P. Perdew and A. Zunger**, *Self-interaction correction to density-functional approximations for many-electron systems*, Phys. Rev. B **23**, 5048 (1981).
- [14] **M. M. Rieger and P. Vogl**, *Self-interaction corrections in semiconductors*, Phys. Rev. B **52**, 16567 (1995).
- [15] **Dirk Vogel**, *Elektronische und strukturelle Eigenschaften von wide-band-gap Halbleitern und ihren Oberflächen: Konstruktion und Anwendung neuer Pseudopotentiale*, Diploma thesis, Westfälische Wilhelms-Universität Münster (1998).

- [16] **D. Vogel, P. Krüger, and J. Pollmann**, *Ab initio electronic-structure calculations for II-VI semiconductors using self-interaction-corrected pseudopotentials*, Phys. Rev. B **52**, R14316 (1995).
- [17] **D. Vogel, P. Krüger, and J. Pollmann**, *Self-interaction and relaxation-corrected pseudopotentials for II-VI semiconductors*, Phys. Rev. B **54**, 5495 (1996).
- [18] **D. Vogel, P. Krüger, and J. Pollmann**, *Structural and electronic properties of group-III nitrides*, Phys. Rev. B **55**, 12836 (1997).
- [19] **A. Filippetti and N. A. Spaldin**, *Self-interaction-corrected pseudopotential scheme for magnetic and strongly-correlated systems*, Phys. Rev. B **67**, 125109 (2003).
- [20] **B. Baumeier**, *Selbstwechselwirkungs- und relaxationskorrigierte Pseudopotentiale für die Volumenkristalle von SiC, MgO, LiF, Silizium und Diamant*, Diploma thesis, Westfälische Wilhelms-Universität Münster (2005).
- [21] **M. Rohlfing, N.-P. Wang, P. Krüger, and J. Pollmann**, *Image States and Excitons at Insulator Surfaces with Negative Electron Affinity*, Phys. Rev. Lett. **91**, 256802 (2003).
- [22] **S. Iijima**, *Helical microtubules of graphitic carbon*, Nature **354**, 56 (1991).
- [23] **M. Zhao, Y. Xia, F. Li, R. Q. Zhang, and S.-T. Lee**, *Strain energy and electronic structures of silicon carbide nanotubes: Density functional calculations*, Phys. Rev. B **71**, 85312 (2005).
- [24] **D. Fischer and M. Jansen**, *Synthese und Struktur von Na₃N*, Angew. Chem. **114**, 1831 (2002).
- [25] **G. V. Vajenine**, *Plasma-Assisted Synthesis and Properties of Na₃N*, Inorg. Chem. **46**, 5146 (2007).
- [26] **M. Born and R. Oppenheimer**, *Zur Quantentheorie der Molekeln*, Ann. Phys. **389**, 457 (1927).
- [27] **D. M. Ceperley and B. J. Alder**, *Ground State of the Electron Gas by a Stochastic Method*, Phys. Rev. Lett. **45**, 566 (1980).
- [28] **J. Wieferink, P. Krüger, and J. Pollmann**, *Improved hybrid algorithm with Gaussian basis sets and plane waves: First-principles calculations of ethylene adsorption on β -SiC(001)-(3x2)*, Phys. Rev. B **74**, 205311 (2006).
- [29] **D. J. Chadi and M. L. Cohen**, *Special Points in the Brillouin Zone*, Phys. Rev. B **8**, 5747 (1973).
- [30] **H. J. Monkhorst and J. D. Pack**, *Special points for Brillouin-zone integrations*, Phys. Rev. B **13**, 5188 (1976).
- [31] **L. Kleinman and D. M. Bylander**, *Efficacious Form for Model Pseudopotentials*, Phys. Rev. Lett. **48**, 1425 (1982).

-
- [32] **S. G. Louie, S. Froyen, and M. L. Cohen**, *Nonlinear ionic pseudopotentials in spin-density-functional calculations*, Phys. Rev. B **26**, 1738 (1982).
- [33] **M. Fuchs, M. Bockstedte, E. Pehlke, and M. Scheffler**, *Pseudopotential study of binding properties of solids within generalized gradient approximations: The role of core-valence exchange correlation*, Phys. Rev. B **57**, 2134 (1998).
- [34] **D. Pozerag, M. R. Pederson, and A. Y. Liu**, *Importance of nonlinear core corrections for density-functional based pseudopotential calculations*, Phys. Rev. B **60**, 14132 (1999).
- [35] **B. Stärk**, *Elektronische und magnetische Eigenschaften von Kobalt-Schichten auf der Diamant(111)-Oberfläche: Resultate von ab-initio-Rechnungen*, Diploma thesis, Westfälische Wilhelms-Universität Münster (2008).
- [36] **Guido Hirsch**, *Ab-initio Berechnung der strukturellen und elektronischen Eigenschaften von S:GaAs(001)-Oberflächen*, Diploma thesis, Westfälische Wilhelms-Universität Münster (1997).
- [37] **W. C. Martin, A. Musgrove, S. Kotochigova, and J. E. Sansonetti**, *Ground Levels and Ionization Energies for the Neutral Atoms*.
available online at <http://physics.nist.gov/IonEnergy>.
- [38] **M. Stengel and N. A. Spaldin**, *Self-interaction correction with Wannier functions*, Phys. Rev. B. **77**, 155106 (2008).
- [39] **A. Svane and O. Gunnarsson**, *Localization in the self-interaction-corrected density-functional formalism*, Phys. Rev. B **37**, 9919 (1988).
- [40] **Z. Szotek, W. M. Temmerman, and H. Winter**, *Application of the self-interaction correction to transition-metal oxides*, Phys. Rev. B **47**, 4029 (1993).
- [41] **M. Arai and T. Fujiwara**, *Electronic structures of transition-metal mono-oxides in the self-interaction-corrected local-spin-density approximation*, Phys. Rev. B **51**, 1477 (1995).
- [42] **R. A. Heaton, J. G. Harrison, and C. C. Lin**, *Self-interaction correction for density-functional theory of electronic energy bands of solids*, Phys. Rev. B **28**, 5992 (1983).
- [43] **S. C. Erwin and C. C. Lin**, *The self-interaction-corrected electronic band structure of six alkali fluoride and chloride crystals*, J. Phys. C: Solid State Phys. **21**, 4285 (1988).
- [44] **Eric Bylaska, Kiril Tsemekhman, and Hannes Jonsson**, *Self-Consistent Self-Interaction Corrected DFT: The Method and Applications to Extended and Confined Systems*, APS Meeting Abstracts page 38004 (2004).
- [45] **W. A. Harrison**, *Electronic Structure and the Properties of Solids*. W. H. Freeman and Company (1980).
- [46] **R. G. Humphreys, D. Bimberg, and W. J. Choyke**, *Wavelength modulated absorption in SiC*, Solid State Commun. **39**, 163 (1981).

- [47] **H. Hoehst, M. Tang, B. C. Johnson, J. M. Meese, G. W. Zajac, and T. H. Fleisch**, *The electronic structure of cubic SiC grown by chemical vapor deposition on Si(100)*, J. Vac. Sci. Technol. A **5**, 1640 (1987).
- [48] **C. E. Moore**, *Atomic energy levels*, Natl. Bur. Stand. (U.S.) Circ. No. 467 (U.S. GPO, Washington, DC, 1949) Vol. I; Vol. II; Vol. III.
- [49] **A. Svane and O. Gunnarsson**, *Transition-metal oxides in the self-interaction-corrected density-functional formalism*, Phys. Rev. Lett. **65**, 1148 (1990).
- [50] **A. Svane**, *Electronic structure of La₂CuO₄ in the self-interaction-corrected density-functional formalism*, Phys. Rev. Lett. **68**, 1900 (1992).
- [51] **A. Svane**, *Electronic structure of cerium in the self-interaction corrected local spin density approximation*, Phys. Rev. Lett. **72**, 1248 (1994).
- [52] **W. M. Temmerman, Z. Szotek, and H. Winter**, *Band-structure method for 4f electrons in elemental Pr metal*, Phys. Rev. B **47**, 1184 (1993).
- [53] **Z. Szotek, W. M. Temmerman, and H. Winter**, *Self-interaction corrected, local spin density description of the $\gamma \rightarrow \alpha$ transition in Ce*, Phys. Rev. Lett. **72**, 1244 (1994).
- [54] **W. R. L. Lambrecht, B. Segall, M. Suttrop, M. Yoganathan, R. P. Devaty, W. J. Choyke, J. A. Edmond, J. A. Powell, and M. Alouani**, *Optical reflectivity of 3C and 4H-SiC polytypes: Theory and experiment*, Appl. Phys. Lett. **63**, 1747 (1993).
- [55] **K.-H. Hellwege and O. Madelung**, *Semiconductors Physics of Group IV Elements and III-IV Compounds*. New Series (1982).
- [56] **W. Lambrecht, B. Sagall, M. Yoganathan, W. Suttrop, R. Devaty, W. Choyke, J. Edmond, J. Powell, and M. Alouani**, *Calculated and measured uv reflectivity of SiC polytypes*, Phys. Rev. B **50**, 10722 (1994).
- [57] **G. L. Harris**, editor *Properties of Silicon Carbide* EMIS Datareviews series Vol. **13**. INSPEC, London (1995).
- [58] **W. J. Choyke, D. R. Hamilton, and L. Patrick**, *Optical Properties of Cubic SiC: Luminescence of Nitrogen-Exciton Complexes, and Interband Absorption*, Phys. Rev. **133**, A1163 (1964).
- [59] **C. H. Park, B. Cheong, K. Lee, and K. J. Chang**, *Structural and electronic properties of cubic, 2H, 4H and 6H SiC*, Phys. Rev. B **49**, 4485 (1994).
- [60] **P. Käckell, B. Wenzien, and F. Bechstedt**, *Electronic properties of cubic and hexagonal SiC polytypes from ab initio calculations*, Phys. Rev. B **50**, 10761 (1994).
- [61] **S. King, M. C. Benjamin, R.J. Nemanich, R.F. Davis, and W. R. L. Lambrecht**, *XPS measurement of the SiC/AlN band-offset at the (0001) interface*, Mater. Res. Soc. Symp. Proc. **395**, 375 (1996).

-
- [62] **S. E. Saddow and A. Agrawal**, editors *Advances in Silicon Carbide Processing and Applications*. Artech House Publishers (2004).
- [63] **W. J. Choyke, H. Matsunami, and G. Pensl**, *Silicon Carbide, Fundamental Questions and Applications to Current Device Technology*. Springer, Berlin (2004).
- [64] **M. A. Capano and R. J. Trew**, *Silicon carbide electronic devices and materials*, Materials Research Society Bulletin vol. **22** (1997).
- [65] **H. M. Matsunami W. J. Choyke and G. Pensl**, editors *Silicon Carbide: A Review of Fundamental Questions and Applications to Current Device Technology* Vols. 1 and 2. Akademie Verlag, Berlin (1998).
- [66] **K. L. Smith and K. M. Black**, *Characterization of the treated surfaces of silicon alloyed pyrolytic carbon and SiC*, J. Vac. Sci. Technol. A **2**, 744 (1984).
- [67] **S. Santavirta, M. Takagi, L. Nordsletten, A. Anttila, R. Lappalainen, and Y. T. Kontinen**, *Biocompatibility of silicon carbide in colony formation test in vitro*, Arch. Orthop. Trauma Surg. **118**, 89 (1998).
- [68] **A. Catellani G. Cicero and G. Galli**, *Atomic Control of Water Interaction with Biocompatible Surfaces: The Case of SiC(001)*, Phys. Rev. Lett. **93**, 016102 (2004).
- [69] **V. M. Bermudez**, *Structure and Properties of Cubic Silicon Carbide (100) Surfaces: A Review*, Phys. Stat. Sol. b **202**, 447 (1997).
- [70] **J. Pollmann, P. Krüger, and M. Sabisch**, *Atomic and Electronic Structure of SiC Surfaces from ab-initio Calculations*, phys. stat. sol (b) **202**, 421 (1997).
- [71] **P. Soukiassian and H. B. Enriquez**, *Atomic scale control and understanding of cubic silicon carbide surface reconstructions, nanostructures and nanochemistry*, J. Phys.: Cond. Matt. **16**, S1611 (2004).
- [72] **K. Heinz, J. Bernhardt, J. Schardt, and U. Starke**, *Functional surface reconstructions of hexagonal SiC*, J. Phys.: Cond. Matt. **16**, S1705 (2004).
- [73] **T. Seyller**, *Passivation of hexagonal SiC surfaces by hydrogen termination*, J. Phys.: Cond. Matt. **16**, S1755 (2004).
- [74] **J. Pollmann and P. Krüger**, *Reconstruction models of cubic SiC surfaces*, J. Phys.: Condens. Matter **16**, S1659 (2004).
- [75] **M. Sabisch, P. Krüger, and J. Pollmann**, *Ab initio calculations of SiC(110) and GaAs(110) surfaces: A comparative study and the role of ionicity*, Phys. Rev. B **51**, 13367 (1995).
- [76] **M. Sabisch**, *Ab-initio Studien elektronischer und struktureller Eigenschaften von SiC-Kristallen und deren Oberflächen*, PhD thesis, Westfälische Wilhelms-Universität Münster (1996).

- [77] **B. Wenzien, P. Käckell, and F. Bechstedt**, *Ab initio calculation of the atomic and electronic structure for the clean 3C SiC(110) 1×1 surface*, Surf. Sci. **307**, 989 (1994).
- [78] **W. Mönch**, *Semiconductor Surfaces and Interfaces*. Springer, Berlin (1993).
- [79] **M. Sabisch, P. Krüger, A. Mazur, M. Rohlfing, and J. Pollmann**, *First-principles calculations of β -SiC(001) surfaces*, Phys. Rev. B **53**, 13121 (1996).
- [80] **H. W. Yeom, M. Shimomura, J. Kitamura, S. Hara, K. Tono, I. Matsuda, B. S. Mun, W. A. R. Huff, S. Kono, T. Ohta, S. Yoshida, H. Okushi, K. Kajimura, and C. S. Fadley**, *Atomic and Electronic-Band Structures of Anomalous Carbon Dimers on 3C-SiC(001)-c(2x2)*, Phys. Rev. Lett. **83**, 1640 (1999).
- [81] **R. Ostendorf, C. Benesch, M. Hagedorn, H. Merz, and H. Zacharias**, *Unoccupied surface states of the c(2x2)-reconstructed 3C-SiC(001) surface*, Phys. Rev. B **66**, 245401 (2002).
- [82] **F.-H. Wang, P. Krüger, and J. Pollmann**, *First principles investigation of the C-terminated β -SiC(001)-c(2x2) surface*, Phys. Rev. B **66**, 195335 (2002).
- [83] **Arash A. Mostofi, Jonathan R. Yates, Young-Su Lee, Ivo Souza, David Vanderbilt, and Nicola Marzari**, *Wannier90: A tool for obtaining maximally-localised Wannier functions*, Comput. Phys. Comm. **178**, 685 (2008).
- [84] **J. Pollmann, P. Krüger, M. Rohlfing, M. Sabisch, and D. Vogel**, *Ab initio calculations of structural and electronic properties of prototype surfaces of group IV, III-V and II-VI semiconductors*, Appl. Surf. Sci. **104/105**, 1 (1996).
- [85] **K. Emtsev**, private communication (2006).
- [86] **K. Hricovini, R. Günther, P. Thiry, A. Taleb-Ibrahimi, G. Indlekofer, J. E. Bonnet, P. Dumas, Y. Petroff, X. Blase, Xuejun Zhu, Steven G. Louie, Y. J. Chabal, and P. A. Thiry**, *Electronic structure and its dependence on local order for H/Si(111)-(1x1) surfaces*, Phys. Rev. Lett. **70**, 1992 (1993).
- [87] **X. Blase, X. Zhu, and S. G. Louie**, *Self-energy effects on the surface-state energies of H-Si(111)1x1*, Phys. Rev. B **49**, 4973 (1994).
- [88] **M. Rohlfing**, *Quasiteilchen-Bandstrukturen von Halbleitern und Halbleiter-Oberflächen*, PhD thesis, Westfälische Wilhelms-Universität Münster (1996).
- [89] **C. Virojanadara, M. Hetzel, and U. Starke**, *A diagonal cut through the SiC bulk unit cell: Structure and composition of the 4H-SiC($\bar{1}\bar{1}02$) surface*, Appl. Phys. Lett. **92**, 061902 (2008).
- [90] **C. Virojanadara, M. Hetzel, L. I. Johansson, W. J. Choyke, , and U. Starke**, *Electronic and atomic structure of the 4H-SiC($\bar{1}\bar{1}02$)-c(2×2) surface*, Surf. Sci. **602**, 525 (2008).
- [91] **Y. Shishkin, W. J. Choyke, and R. P. Devaty**, *Photoelectrochemical etching of n-type 4H silicon carbide*, J. Appl. Phys. **96**, 2311 (2004).

-
- [92] **U. Starke, W. Y. Lee, C. Coletti, S. E. Sadow, R. P. Devaty, and W. J. Choyke**, *SiC pore surfaces: Surface studies of 4H-SiC($\bar{1}\bar{1}02$) and 4H-SiC($\bar{1}10\bar{2}$)*, Appl. Phys. Lett. **88**, 031915 (2006).
- [93] **J. P. Perdew and Y. Wang**, *Accurate and simple analytic representation of the electron-gas correlation energy*, Phys. Rev. B **45**, 13244 (1992).
- [94] **D. R. Hamann**, *Generalized norm-conserving pseudopotentials*, Phys. Rev. B **40**, 2980 (1989).
- [95] **A. Seubert, J. Bernhardt, M. Nerdling, U. Starke, and K. Heinz**, *In situ surface phases and silicon-atom geometry of the $(2\times 2)_C$ structure on 6H-SiC($000\bar{1}$)*, Surf. Sci. **454-456**, 45 (2000).
- [96] **U. Starke, J. Schardt, J. Bernhardt, M. Franke, and K. Heinz**, *Stacking Transformation from Hexagonal to Cubic SiC Induced by Surface Reconstruction: A Seed for Heterostructure Growth*, Phys. Rev. Lett. **82**, 2107 (1999).
- [97] **J. M. Powers, A. Wander, P. J. Rous, M. A. Van Hove, and G. A. Somorjai**, *Structural analysis of the β -SiC(100)- $c(2\times 2)$ surface reconstruction by automated tensor low-energy electron diffraction*, Phys. Rev. B **44**, 11159 (1991).
- [98] **J. P. Long, V. M. Bermudez, and D. E. Ramaker**, *Structural Determination of β -SiC(100)- $c(2\times 2)$ from C-1s Surface-Core-Exciton and Si-2p Absorption*, Phys. Rev. Lett. **76**, 991 (1996).
- [99] **P. Käckell, J. Furthmüller, F. Bechstedt, G. Kresse, and J. Hafner**, *Characterization of carbon-carbon bonds on the SiC(001)- $c(2\times 2)$ surface*, Phys. Rev. B **54**, 10304 (1996).
- [100] **A. Catellani, G. Galli, and F. Gygi**, *Reconstruction and Thermal Stability of the Cubic SiC (001) Surfaces*, Phys. Rev. Lett. **77**, 5090 (1996).
- [101] **A. Catellani, G. Galli, , and P. L. Rigolli**, *Carbon lines on the cubic SiC(001) surface*, Phys. Rev. B **62**, R4797 (2000).
- [102] **S. K. Burger and W. Yang**, *Quadratic string method for determining the minimum-energy path based on multiobjective optimization*, J. Chem. Phys. **124**, 054109 (2006).
- [103] **G. Henkelman and H. Jónsson**, *Improved tangent estimate in the nudged elastic band method for finding minimum energy paths and saddle points*, J. Chem. Phys. **113**, 9978 (2000).
- [104] **J. Wierferink, P. Krüger, and J. Pollmann**, *First-principles study of benzene adsorption on the SiC(001)- (3×2) surface*, Phys. Rev. B **78**, 165315 (2008).
- [105] **J. Tersoff and D. R. Hamann**, *Theory of the scanning tunneling microscope*, Phys. Rev. B **31**, 805 (1985).
- [106] **V. E. Henrich**, *The surfaces of metal oxides*, Rep. Prog. Phys. **48**, 1481 (1985).

Bibliography

- [107] **V. E. Henrich and P. A. Cox**, *The Surface Science of Metal Oxides*. Cambridge University Press (1994).
- [108] **H.-J. Freund**, *Adsorption von Gasen an komplexen Festkörperoberflächen*, *Angew. Chem.* **109**, 444 (1997).
- [109] **C. L. Freeman, F. Claeysens, N. L. Allan, and J.H. Harding**, *Graphitic Nanofilms as Precursors to Wurtzite Films: Theory*, *Phys. Rev. Lett* **96**, 66102 (2006).
- [110] **P. B. Sorokin, A. S. Fedorov, and L. A. Chernozatonskii**, *Structure and properties of BeO nanotubes*, *Phys. Solid State* **48**, 398 (2006).
- [111] **K. J. Chang, S. Froyen, and M. L. Cohen**, *The electronic band structures for zinblend and wurtzite BeO*, *J. Phys. C: Solid State Phys.* **16**, 3475 (1983).
- [112] **B. Soulé de Bas, H. E. Dorsett, and M. J. Ford**, *The electronic structure of Be and BeO: benchmark EMS measurements and LCAO calculations*, *J. Phys. Chem. Sol.* **64**, 495 (2003).
- [113] **P. E. Van Camp and V. E. Van Doren**, *Ground-state properties and structural phase transformation of beryllium oxide*, *J. Phys.: Condens. Matter* **8**, 3385 (1996).
- [114] **J. E. Jaffe and P. Zapol**, *Atomic relaxation of the BeO (10 $\bar{1}$ 0) surface*, *Surf. Sci.* **381**, L563 (1997).
- [115] **R. M. Hazen and L. W. Finger**, *High-pressure and high-temperature crystal chemistry of beryllium oxide*, *J. Appl. Phys.* **59**, 3728 (1986).
- [116] **R. W. G. Wyckoff**, *Crystal structure*. John Wiley, New York (1963).
- [117] **G. G. Bentle**, *Elastic constants of single-crystal BeO at room temperature*, *J. Am. Ceram. Soc.* **49**, 125 (1966).
- [118] **C. F. Cline, H. L. Dunegan, and G. W. Henderson**, *Elastic Constants of Hexagonal BeO, ZnS, and CdSe*, *J. Appl. Phys.* **38**, 1944 (1967).
- [119] **W. R. L. Lambrecht and B. Segall**, *Electronic structure and total energy of diamond/BeO interfaces*, *J. Mater. Res.* **7**, 696 (1992).
- [120] **M. J. Weber**, editor *Handbook of Laser Science and Technology*. CRC, Cleveland (1986).
- [121] **D. M. Roessler, W. C. Walker, and E. Loh**, *Electronic spectrum of crystalline beryllium oxide*, *J. Phys. Chem. Solids* **30**, 157 (1969).
- [122] **B. E. Kulyabin, V. A. Lobach, and A. V. Kruzhalov**, *Band-structure and parameters of the ground-state of BeO*, *Sov. Phys. Solid State* **32**, 2138 (1990).
- [123] **A. P. Lukirskii and I. A. Brytov**, *Investigation of the energy structure of Be and BeO by ultra-soft x-ray spectroscopy*, *Sov. Phys. Solid State* **6**, 33 (1964).
- [124] **V. A. Fomichev**, *X-ray spectra and energy band schemes of BeO and BN*, *Sov. Phys. Solid State* **13**, 754 (1971).

-
- [125] **V. A. Sashin, M. A. Bolorizadeh, A. S. Kheifets, and M. J. Ford**, *Electronic band structure of beryllium oxide*, J. Phys.: Condens. Matter **15**, 3567 (2003).
- [126] **K. Hamrin, G. Johansson, U. Gelius, C. Nordling, and K. Siegbahn**, *Valence Bands and Core Levels of the Isoelectronic Series LiF, BeO, BN, and Graphite Studied by ESCA*, Physica Scripta **1**, 277 (1970).
- [127] **S. C. Erwin and C. C. Lin**, *The self-interaction-corrected electronic band structure of six alkali fluoride and chloride crystals*, J. Phys. C: Solid State Phys. **21**, 4285 (1988).
- [128] **P. Schröer, P. Krüger, and J. Pollmann**, *Self-consistent electronic-structure calculations of the (10 $\bar{1}$ 0) surfaces of the wurtzite compounds ZnO and CdS*, Phys. Rev. B **49**, 17092 (1994).
- [129] **B. Meyer and D. Marx**, *Density-functional study of the structure and stability of ZnO surfaces*, Phys. Rev. B **67**, 35403 (2003).
- [130] **J. E. Jaffe, N. M. Harrison, and A. C. Hess**, *Ab initio study of ZnO (10 $\bar{1}$ 0) surface relaxation*, Phys. Rev. B **49**, 11153 (1994).
- [131] **M. Rohlfing, P. Krüger, and J. Pollmann**, *Efficient scheme for GW quasiparticle band-structure calculations with applications to bulk Si and to the Si(001)-(2x1) surface*, Phys. Rev. B **52**, 1905 (1995).
- [132] **H.-J. Freund**, *Metal-supported ultrathin oxide film systems as designable catalysts and catalyst supports*, Surf. Sci. **601**, 1438 (2007).
- [133] **P. R. Son and R. A. Bartels**, *CaO and SrO single crystal elastic constants and their pressure derivatives*, J. Phys. Chem. Solids **33**, 819 (1972).
- [134] **V. A. Fomichev, T. M. Zimkina, and I. I. Zhukova**, *Investigation of energy structure of MgO by ultrasoft x-ray spectroscopy*, Sov. Phys. Solid State **10**, 2421 (1969).
- [135] **S. P. Kowalczyk, F. R. McFreely, L. Ley, V. T. Gritsyna, and D. A. Shirley**, *The electronic structure of SrTiO₃ and some simple related oxides (MgO, Al₂O₃, SrO, TiO₂)*, Solid State Commun. **23**, 161 (1977).
- [136] **H. van Doveren and J. A. T. Verhoeven**, *XPS spectra of Ca, Sr, Ba and their oxides*, J. Electron Spectrosc. Relat Phenom. **21**, 265 (1980).
- [137] **V. A. Shashin, H. E. Dorsett, M. A. Bolorizadeh, and M. J. Ford**, *The valence band structures of BeO, MgO, and CaO*, J. Chem. Phys. **113**, 8175 (2000).
- [138] **G. Jura and C. W. Garland**, *The Experimental Determination of the Surface Tension of Magnesium Oxide*, J. Am. Chem. Soc. **74**, 6033 (1952).
- [139] **C. G. Kinniburgh**, *A LEED study of MgO(100). II. Theory at normal incidence*, J. Phys. C: Solid State Phys. **8**, 2382 (1975).
- [140] **M. R. Welton-Cook and W. Berndt**, *A LEED study of the MgO (100) surface: identification of a finite rumple*, J. Phys. C: Solid State Phys. **15**, 5691 (1982).

Bibliography

- [141] **T. Urano, T. Kanaji, and M. Kaburagi**, *Surface structure of MgO(001) surface studied by LEED*, Surf. Sci. **134**, 109 (1983).
- [142] **D. L. Blanchard, D. L. Lessor, J. P. Lafemina, D. R. Baer, W. K. Ford, and T. Guo**, *A low-energy electron diffraction study of the MgO(001) surface structure*, J. Vac. Sci. Technol. A **9**, 1814 (1991).
- [143] **Y. Murata, S. Murakami, H. Namba, T. Gotoh, and K. Kinoshita**, in **R. Dobrozemski**, editor, *Proceedings of the 7th International Vacuum Congress*. Berger, Vienna (1977).
- [144] **P. A. Maksym**, *Analysis of intensity data for rheed by the MgO(001) surface*, Surf. Sci. **149**, 157 (1985).
- [145] **H. Nakamatsu, A. Sudo, and S. Kawai**, *Relaxation of the MgO(100) surface studied by ICISS*, Surf. Sci. **194**, 265 (1988).
- [146] **A. Santoni, D. B. T. Thoai, and J. Urban**, *MgO (100) surface topology determination by surface extended energy loss fine structure*, Solid State Commun. **68**, 1039 (1988).
- [147] **M. Prutton, J. A. Ramsey, J. A. Walker, and M. R. Welton-Cook**, *A LEED study of the structure of the (100) surface of CaO*, J. Phys. C: Solid State Phys. **12**, 5271 (1979).
- [148] **L. H. Tjeng, A. R. Vos, and G. A. Sawatzky**, *Electronic structure of MgO studied by angle-resolved ultraviolet photoelectron spectroscopy*, Surf. Sci. **235**, 269 (1990).
- [149] **D. Ochs, W. Maus-Freidrichs, M. Bause, J. Günster, V. Kempter, V. Puchin, A. Shluger, and L. Kantorovich**, *Study of the surface electronic structure of MgO bulk crystals and thin films*, Surf. Sci. **365**, 557 (1996).
- [150] **V. E. Henrich, G. Dresselhaus, and H. J. Zeiger**, *Energy-dependent electron-energy-loss spectroscopy: Application to the surface and bulk electronic structure of MgO*, Phys. Rev. B **22**, 4764 (1980).
- [151] **P. A. Cox and A. A. Williams**, *Surface excitons on ionic crystals*, Surf. Sci. **175**, L782 (1986).
- [152] **S. Schintke, S. Messerli, M. Pivetta, F. Patthey, L. Libioulle, M. Stengel, A. De Vita, and W.-D. Schneider**, *Insulator at the Ultrathin Limit: MgO on Ag(001)*, Phys. Rev. Lett. **87**, 276801 (2001).
- [153] **K. J. Chang and M. L. Cohen**, *High-pressure behavior of MgO: Structural and electronic properties*, Phys. Rev. B **30**, 4774 (1984).
- [154] **E. Taurian, M. Springborg, and N. E. Chirstensen**, *Self-consistent electronic structures of MgO and SrO*, Solid State Commun. **55**, 351 (1985).
- [155] **P. Cortona and A. V. Monteleone**, *Ab initio calculations of cohesive and structural properties of the alkali-earth oxides*, J. Phys.: Condens. Matter **8**, 8983 (1996).

-
- [156] **D. R. Alfonso, J. A. Snyder, J. E. Jaffe, and A. C. Hess**, *Opposite rumpling of the MgO and CaO (100) surfaces: A density-functional theory study*, Phys. Rev. B **62**, 8318 (2000).
- [157] **P. Broqvist, H. Grönbeck, and I. Panas**, *Surface properties of alkaline earth metal oxides*, Surf. Sci. **554**, 262 (2004).
- [158] **N. V. Skorodumova and K. Hermansson and B. Johansson**, *Structural and electronic properties of the (100) surface and bulk of alkaline-earth metal oxides*, Phys. Rev. B **72**, 125414 (2005).
- [159] **A. Schleife, F. Fuchs, J. Furthmüller, and F. Bechstedt**, *First-principles study of ground- and excited-state properties of MgO, ZnO, and CdO polymorphs*, Phys. Rev. B **73**, 245212 (2006).
- [160] **Y. Cho, Ch. Kim, H.-S. Ahn, E. Cho, T.-E. Kim, and S. Han**, *First-principles study on secondary electron emission of MgO surface*, J. Appl. Phys. **101**, 83710 (2007).
- [161] **U. Schöneberger and F. Aryasetiawan**, *Bulk and surface electronic structures of MgO*, Phys. Rev. B **52**, 8788 (1995).
- [162] **G. Cappellini, S. Bouette-Russo, B. Amadon, C. Noguera, and F. Finocchi**, *Structural properties and quasiparticle energies of cubic SrO, MgO and SrTiO₃*, J. Phys.: Condens. Matter **12**, 3671 (2000).
- [163] **A. Yamasaki and T. Fujiwara**, *Electronic structure of the MO oxides (M=Mg, Ca, Ti, V) in the GW approximation*, Phys. Rev. B **66**, 245108 (2002).
- [164] **N.-P. Wang, M. Rohlfing, P. Krüger, and J. Pollmann**, *Femtosecond dynamics of excited states of CO adsorbed on MgO(001)-(1x1)*, Phys. Rev. B **71**, 45407 (2005).
- [165] **T. Lv, D. Chen, and M. Huang**, *Quasiparticle band structures of BaO and BaS*, J. Appl. Phys. **100**, 86103 (2006).
- [166] **R. Pandey, J. E. Jaffe, and A. B. Kunz**, *Ab initio band-structure calculations for alkaline-earth oxides and sulfides*, Phys. Rev. B **43**, 9228 (1991).
- [167] **A. Zupan, I. Petek, M. Causa, and R. Dovesi**, *Elastic constants, phase transition, and electronic structure of strontium oxide SrO: An ab initio Hartree-Fock study*, Phys. Rev. B **48**, 799 (1993).
- [168] **J. Robertson, K. Xiong, and S. J. Clark**, *Band structure of functional oxides by screened exchange and the weighted density approximation*, phys. stat. sol. (b) **243**, 2054 (2006).
- [169] **T. Kotani**, *Exact exchange-potential band-structure calculations by the LMTO-ASA method: MgO and CaO*, Phys. Rev. B **50**, 14816 (1994).
- [170] **Z. P. Chang and G. R. Barsch**, *Pressure dependence of elastic constants of single-crystalline magnesium oxide*, J. Geophys. Res. **74**, 3291 (1969).
- [171] **Z. P. Chang and E. K. Graham**, *Elastic properties of oxides in the NaCl-structure*, J. Phys. Chem. Solids **38**, 1355 (1977).

Bibliography

- [172] **A. S. Rao and R. T. Keamey**, *Logarithmic derivative reflectance spectra of BaO and SrO*, *phys. stat. sol. (b)* **95**, 243 (1979).
- [173] **M. P. Tosi**, *Cohesion of ionic solids in the Born model*, *Solid State Phys.* **16**, 1 (1964).
- [174] **T. Fauster**, *Bildpotentialzustände – Elektronen nahe Metalloberflächen*, *Physik in unserer Zeit* **33**, 68 (2002).
- [175] **R. Saito, M. Fujita, G. Dresselhaus, and M. S. Dressenhaus**, *Electronic structure of chiral graphene tubules*, *Appl. Phys. Lett.* **60**, 2204 (1992).
- [176] **N. G. Chopra, R. J. Luyken, K. Cherry, V. H. Crespi, M. L. Cohen, S. G. Louie, and A. Zettl**, *Boron Nitride Nanotubes*, *Science* **269**, 966 (1995).
- [177] **X. H. Sun, C. P. Li, W. K. Wong, N. B. Wong, C. S. Lee, S. T. Lee, and B. K. Teo**, *Formation of Silicon Carbide Nanotubes and Nanowires via Reaction of Silicon (from Disproportionation of Silicon Monoxide) with Carbon Nanotubes*, *J. Am. Chem. Soc.* **124**, 14464 (2002).
- [178] **R. Tenne, L. Margulis, M. Genut, and G. Hodes**, *Polyhedral and cylindrical structures of tungsten disulphide*, *Nature* **360**, 444 (1992).
- [179] **R. Tenne, M. Homyonfer, and Y. Feldman**, *Nanoparticles of Layered Compounds with Hollow Cage Structures (Inorganic Fullerene-Like Structures)*, *Chem. Mater.* **10**, 3225 (1998).
- [180] **P. Zhang and V. H. Crespi**, *Theory of B₂O and BeB₂ Nanotubes: New Semiconductors and Metals in One Dimension*, *Phys. Rev. Lett.* **89**, 56403 (2002).
- [181] **N. Hamada, S. I. Sawada, and A. Oshiyama**, *New one-dimensional conductors: Graphitic microtubules*, *Phys. Rev. Lett.* **68**, 1579 (1992).
- [182] **X. Blase, L. X. Benedict, E. L. Shirley, and S. G. Louie**, *Hybridization effects and metallicity in small radius carbon nanotubes*, *Phys. Rev. Lett.* **72**, 1878 (1994).
- [183] **L. Vaccarini, C. Goze, L. Henrard, E. Hernández, P. Bernier, and A. Rubio**, *Mechanical and electronic properties of carbon and boron-nitride nanotubes*, *Carbon* **38**, 1681 (2000).
- [184] **A. Rubio, J. L. Corkill, and M. L. Cohen**, *Theory of graphitic boron nitride nanotubes*, *Phys. Rev. B* **49**, R5081 (1994).
- [185] **E. Hernández, C. Goze, P. Bernier, and A. Rubio**, *Elastic Properties of C and B_xC_yN_z Composite Nanotubes*, *Phys. Rev. Lett.* **80**, 4502 (1998).
- [186] **X. Blase, A. Rubio, S. G. Louie, and M. L. Cohen**, *Stability and Band Gap Constancy of Boron Nitride Nanotubes*, *Europhys. Lett.* **28**, 335 (1994).
- [187] **Y.-H. Kim, K. J. Chang, and S. G. Louie**, *Electronic structure of radially deformed BN and BC₃ nanotubes*, *Phys. Rev. B* **63**, 205408 (2001).
- [188] **S. Okada, S. Saito, and A. Oshiyama**, *Interwall interaction and electronic structure of double-walled BN nanotubes*, *Phys. Rev. B* **65**, 165410 (2002).

-
- [189] **S.-H. Jhi, D. J. Roundy, S. G. Louie, and M. L. Cohen**, *Formation and electronic properties of double-walled boron nitride nanotubes*, Sol. State Commun. **134**, 397 (2005).
- [190] **M. Menon, E. Richter, A. Mavrandonakis, and G. Froudakis and A. N. Andriotis**, *Structure and stability of SiC nanotubes*, Phys. Rev. B **69**, 115322 (2004).
- [191] **H. J. Xiang, J. Yang, J. G. Hou, and Q. Zhu**, *First-principles study of small-radius single-walled BN nanotubes*, Phys. Rev. B **68**, 35427 (2003).
- [192] **G. Y. Guo and J. C. Lin**, *Systematic ab initio study of the optical properties of BN nanotubes*, Phys. Rev. B **71**, 165402 (2005).
- [193] **H. J. Xiang, Z. Y. Chen, and J. Yang**, *Electronic and Piezoelectric Properties of BN Nanotubes from Hybrid Density Functional Method*, J. Comp. Theor. Nanosci. **3**, 838 (2006).
- [194] **A. Gali**, *Ab initio study of nitrogen and boron substitutional impurities in single-wall SiC nanotubes*, Phys. Rev. B **73**, 245415 (2006).
- [195] **R. J. Baierle, P. Piquini, L. P. Neves, and R. H. Miva**, *Ab initio study of native defects in SiC nanotubes*, Phys. Rev. B **74**, 155425 (2006).
- [196] **A. Gali**, *Ab initio theoretical study of hydrogen and its interaction with boron acceptors and nitrogen donors in single-wall silicon carbide nanotubes*, Phys. Rev. B **75**, 85416 (2007).
- [197] **C.-H. Park, C. D. Spataru, and S. G. Louie**, *Excitons and Many-Electron Effects in the Optical Response of Single-Walled Boron Nitride Nanotubes*, Phys. Rev. Lett. **96**, 126105 (2006).
- [198] **L. Wirtz, A. Marini, and A. Rubio**, *Excitons in Boron Nitride Nanotubes: Dimensionality Effects*, Phys. Rev. Lett. **96**, 126104 (2006).
- [199] **A. Mavrandonakis, G. E. Froudakis, A. Andriotis, and M. Menon**, *Silicon carbide nanotube tips: Promising materials for atomic force microscopy and/or scanning tunneling microscopy*, Appl. Phys. Lett. **89**, 123126 (1989).
- [200] **A. Catellani, M. Posternak, A. Baldereschi, H. J. F. Jansen, and A. J. Freeman**, *Electronic interlayer states in hexagonal boron nitride*, Phys. Rev. B **32**, 6997 (1985).
- [201] **X. Blase, A. Rubio, S. G. Louie, and M. L. Cohen**, *Quasiparticle band structure of bulk hexagonal boron nitride and related systems*, Phys. Rev. B **51**, 6868 (1995).
- [202] **W. R. L. Lambrecht and B. Segall**, in **J. H. Edgar**, editor, *Properties of Group III Nitrides*. EMIS Datareviews Series, London (1994).
- [203] **N. Miyata, K. Moriki, G. Mishima, and M. Fujisawa and T. Hattori**, *Optical constants of cubic boron nitride*, Phys. Rev. B **40**, 12028 (1989).
- [204] **G. V. Vajenine**, *On Reactions between Alkali Metals and Active Nitrogen*, Solid. State Sci. **10**, 450 (2008).
- [205] **S. G. Louie, S. Froyen, and M. L. Cohen**, *Nonlinear ionic pseudopotentials in spin-density-functional calculations*, Phys. Rev. B **26**, 1738 (1982).

Bibliography

- [206] **D. M. Roessler and W. C. Walker**, *Electronic spectrum of crystalline lithium fluoride*, J. Phys. Chem. Solids **28**, 1507 (1967).
- [207] **E. Shirley, L. J. Terminello, J. E. Klepeis, and F. J. Himpsel**, *Detailed theoretical photoelectron angular distributions for LiF(100)*, Phys. Rev. B **53**, 10296 (1996).
- [208] **M. Piacentini**, *A new interpretation of the fundamental exciton region in LiF*, Solid. State Commun. **17**, 697 (1975).
- [209] **S. Nakai and T. Sagawa**, *Na+ L_{2,3} Absorption Spectra of Sodium Halides*, J. Phys. Soc. Jpn. **26**, 1427 (1969).
- [210] **J. E. Eby, K. J. Teegarden, and D. B. Dutton**, *Ultraviolet Absorption of Alkali Halides*, Phys. Rev **116**, 1099 (1959).
- [211] **K. Teegarden and G. Baldini**, *Optical Absorption Spectra of the Alkali Halides at 10° K*, Phys. Rev **155**, 896 (1967).
- [212] **T. Tomiki and T. Miyata**, *Optical Studies of Alkali Fluorides and Alkaline Earth Fluorides in VUV region*, J. Phys. Soc. Jpn. **27**, 658 (1969).
- [213] **Y. Ishii, J. Murakami, and M. Itoh**, *Optical spectra of excitons in lithium oxide*, J. Phys. Soc. Jpn. **68**, 696 (1999).
- [214] **W. Rauch**, *Die ultravioletten Dispersionsfrequenzen der Alkalioxyde*, ZS f. Phys. **116**, 652 (1940).
- [215] **H. Brendecke and W. Bludau**, *Optical absorption of lithium nitride*, J. Appl. Phys. **50**, 4743 (1979).
- [216] **G. W. Wyckoff**, *Crystal Structures* volume 1. Wiley, New York 2nd edition (1968).
- [217] **F. Perrot**, *Hartree-Fock Band Structure of Alkali Fluorides and Chlorides*, phys. stat. sol. (b) **52**, 163 (1972).
- [218] **A.B. Kunz**, *Study of the electronic structure of twelve alkali halide crystals*, Phys. Rev. B **26**, 2056 (1982).
- [219] **M. Berrondo and J. F. Rivas-Silva**, *Cluster Models of Ionic Crystals: Band Gaps*, Int. J. of Quant. Chem. **57**, 1115 (1996).
- [220] **J. A. Soininen and E. Shirley**, *Effects of electron-hole interaction on the dynamic structure factor: Application to nonresonant inelastic x-ray scattering*, Phys. Rev. B **61**, 16423 (2000).
- [221] **N.-P. Wang, M. Rohlfing, P. Krüger, and J. Pollmann**, *Quasiparticle band structure and optical spectrum of LiF(001)*, Phys. Rev. B **67**, 115111 (2003).
- [222] **R. T. Poole, J. G. Jenkin, J. Liesegang, and R. C. G. Leckey**, *Electronic band structure of the alkali halides. I. Experimental parameters*, Phys. Rev. B **11**, 5179 (1975).

- [223] **G. K. Wertheim, J. E. Rowe, D. N. E. Buchanan, and P. H. Citrin**, *Valence-band structure of alkali halides determined from photoemission data*, Phys. Rev. B **51**, 13675 (1995).
- [224] **E. Zintl, A. Harder, and B. Dauth**, Z. Elektrochem. **40**, 588 (1934).
- [225] **M. M. Islam, T. Bredow, and C. Minot**, *Theoretical Analysis of Structural, Energetic, Electronic, and Defect Properties of Li_2O* , J. Phys. Chem. B **110**, 9413 (2006).
- [226] **R. D. Eithiraj, G. Jaiganesh, and G. Kalpana**, *Electronic and ground-state properties of alkali-metal oxides- Li_2O , Na_2O , K_2O and Rb_2O : A first-principles study*, J. Phys. Chem. B **110**, 9413 (2006).
- [227] **E. A. Mikajlo, K. L. Nixon, V. A. Coleman, and M. J. Ford**, *The electronic band structure of Li_2O : testing theoretical predictions using electron momentum spectroscopy*, J. Phys.: Condens. Matter **14**, 3587 (2002).
- [228] **E. A. Mikajlo, K. L. Nixon, and M. J. Ford**, *Electron momentum spectroscopy and linear combination of atomic orbitals calculation of bulk Na_2O* , J. Phys.: Condens. Matter **15**, 2155 (2003).
- [229] **E. A. Mikajlo and M. J. Ford**, *Energy and momentum resolved band structure of K_2O : electron momentum spectroscopy and linear combination of atomic orbitals calculation*, J. Phys.: Condens. Matter **15**, 6955 (2003).
- [230] **A. Rabenau and H. Schulz**, *Re-evaluation of the lithium nitride structure*, J. Less-Common Met. **50**, 155 (1976).
- [231] **H. J. Beister, S. Haag, R. Kniep, K. Strößner, and K. Syassen**, *Phasenumwandlungen von Lithiumnitrid unter Druck*, Angew. Chem. **100**, 1116 (1988).
- [232] **G. Kerker**, *Electronic structure of Li_3N* , Phys. Rev. B **23**, 6312 (1981).
- [233] **P. Blaha, J. Redinger, and K. Schwarz**, *Energy Bands and Electron Densities of Li_3N* , Z. Phys. B - Condensed Matter **57**, 273 (1984).
- [234] **M. Seel and R. Pandey**, *Comparative Ab initio Study of Electronic and Ionic Properties of Lithium Nitride (Li_3N), Lithium Phosphide (Li_3P), and Lithium Arsenide (Li_3As)*, Int. J. Quant. Chem. **25**, 461 (1991).
- [235] **D. Fischer, Z. Cancarevic, J. C. Schön, and M. Jansen**, *Zur Synthese und Struktur von K_3N* , Z. Anorg. Allg. Chem. **630**, 156 (2004).
- [236] **V. N. Staroverov, G. E. Scuseria, J. Tao, and J. P. Perdew**, *Tests of a ladder of density functionals for bulk solids and surfaces*, Phys. Rev. B **69**, 075103 (2004).
- [237] **M. Prencipe, A. Zupan, R. Dovesi, E. Apra, and V. R. Saunders**, *Ab initio study of the structural properties of LiF , NaF , KF , LiCl , NaCl , and KCl* , Phys. Rev. B **51**, 3391 (1995).
- [238] **S. Haussühl**, *Thermo-elastische Konstanten der Alkalihalogenide vom NaCl -Typ*, Z. Phys. **159**, 223 (1960).

- [239] **A. Shukla, M. Dolg, P. Fulde, and H. Stoll**, *Towards a quantum-mechanical description of crystalline insulators: A Wannier-function-based Hartree-Fock study of Li_2O and Na_2O* , J. Chem. Phys. **108**, 8521 (1998).
- [240] **S. Hull, T. W. D. Farley, W. Hayes, and M. T. Hutchings**, *The elastic properties of lithium oxide and their variation with temperature*, J. Nucl. Mater. **160**, 125 (1988).
- [241] **A. C. Ho, M. K. Granger, A. L. Ruoff, P. E. Van Camp, and V. E. Van Doren**, *Experimental and theoretical study of Li_3N at high pressure*, Phys. Rev. B **59**, 6083 (1999).
- [242] **O. A. von Lilienfeld and P. A. Schultz**, *Structure and band gaps of Ga-(V) semiconductors: The challenge of Ga pseudopotentials*, Phys. Rev. B **77**, 115202 (2008).
- [243] **V. Pardo and W. E. Pickett**, *Magnetism from 2p states in alkaline earth monoxides: Trends with varying N impurity concentration*, Phys. Rev. B **78**, 134427 (2008).
- [244] **A. Droghetti, C. D. Pemmaraju, and S. Sanvito**, *Predicting d^0 magnetism: Self-interaction correction scheme*, Phys. Rev. B **78**, 140404(R) (2008).
- [245] **B. Stärk**, private communication (2008).
- [246] **W. Weber**, *Adiabatic bond charge model for the phonons in diamond, Si, Ge, and α -Sn*, Phys. Rev. B **15**, 4789 (1977).

Zusammenfassung

In der vorliegenden Arbeit wurden die strukturellen und elektronischen Eigenschaften einer Vielzahl von Materialien sowohl in Volumenkristallkonfiguration als auch in reduzierten Dimensionen unter Verwendung einer näherungsweise Selbstwechselwirkungskorrektur, die für atomare Systeme wohldefinierte Korrekturen auf den Festkörper überträgt, untersucht.

Zu Beginn wurde bereits hervorgehoben, dass die im Rahmen der Dichtefunktionaltheorie unter der Standardnäherung der Lokalen Dichteanäherung berechnete elektronische Struktur eine systematische Unterschätzung der fundamentalen Bandlücke in Halbleiter- und Isolatormaterialien von ca. 50% aufweist. Nach der Vorstellung der Methode der selbstwechselwirkungskorrigierten Pseudopotentiale anhand der Beispiele der Volumenkristalle von Siliziumkarbid wurde dieser pragmatische Zugang zunächst auf einige ausgewählte Oberflächensysteme von 3C-SiC und 4H-SiC angewandt. Im Verlauf dieser Studien hat sich herausgestellt, dass die Verwendung von selbstwechselwirkungskorrigierten Pseudopotentialen in einer zuverlässig verbesserten Beschreibung der Bandstruktur der nicht-polaren 3C-SiC(110)-(1×1) Oberfläche resultiert. Die Charakteristika der Oberfläche sind sehr ähnlich zu denen des Volumenkristalls, was den deutlichen Effekt auf die Bandlücke, die sich von 0.25 eV (LDA) auf 1.17 eV (SIC) vergrößert, begründet. Im Gegensatz dazu ist die 3C-SiC(001) Oberfläche polar und weist kompliziertere Rekonstruktionen auf. Insbesondere bilden sich sowohl im „Dimer Row Model“ der (2×1) als auch im „Bridging Dimer Model“ der c(2×2) Rekonstruktion, die beide in dieser Arbeit untersucht wurden, Kohlenstoffdimere in der äußersten Oberflächenschicht aus. Sowohl bindende wie auch antibindende Dimerzustände sind Linearkombinationen Kohlenstoff 2p-artiger Zustände, die im Rahmen der hier vorgestellten SIC Pseudopotentialmethode gleichermaßen beeinflusst werden. Eine angemessene Beschreibung solcher Zustände erfordert eine Modifikation des SIC Zugangs. Um der Tatsache ausreichend Rechnung zu tragen, dass derartige unbesetzte, antibindende Zustände nicht selbstwechselwirkungskorrigiert werden, wurde der SIC- Δ Zugang eingeführt, in welchem die überschüssige Selbstwechselwirkungskorrektur wieder von den Energien der unbesetzten Bänder abgezogen wird. Für das „Dimer Row Model“ der 3C-SiC(001)-(2×1) Oberfläche liefert dieser Zugang eine Bandlücke von 0.99 eV – ganz im Gegensatz zu dem von der LDA vorhergesagten metallischen Verhalten – was in sehr guter Übereinstimmung mit den Ergebnissen einer Quasiteilchenrechnung (0.94 eV) [79] ist. Für das „Bridging Dimer Model“ der

3C-SiC(001)-c(2×2) Oberfläche wird eine ebenfalls gute Übereinstimmung der berechneten Bänder mit experimentellen ARPES [80] und ARIPES [81] Daten festgestellt.

Die Oberflächen von 4H-SiC sind im Vergleich zu denen von 3C-SiC bislang in der Literatur sowohl aus experimenteller, als auch aus theoretischer Sicht deutlich weniger intensiv untersucht worden. In Analogie zur 2H-SiC(10 $\bar{1}$ 0) Oberfläche [70] wird eine so genannte relaxierte Typ A Geometrie durch die Strukturoptimierungen in dieser Arbeit favorisiert. Vier lokalisierte Oberflächenzustände, von denen jeweils zwei besetzt und zwei unbesetzt sind, können für diese Struktur identifiziert werden. Durch eine Analyse der entsprechenden Ladungsdichteverteilungen sowie lokalisierter Wannierfunktionen kann ein Paar dieser Zustände (π_A , π_A^*) mit der Ausbildung einer Si=C Doppelbindung in der äußersten Oberflächenschicht in Verbindung gebracht werden. Das zweite Paar (π_B , π_B^*) weist im Vergleich dazu mehr Eigenschaften gewöhnlicher besetzter und unbesetzter dangling-bond Zustände auf. Eine SIC- Δ Bandstruktur für die optimierte Oberflächenstruktur zeigt, dass die fundamentale Bandlücke durch π_B und π_B^* Bänder gebildet wird und 1.74 eV groß ist. Im Gegensatz hierzu legt eine vorläufige Photoemissionsstudie [85] nahe, dass nur ein einzelner besetzter Oberflächenzustand gebildet wird. Eine Vergleich der experimentellen und theoretischen Ergebnisse lässt den Schluß zu, dass es sich bei dem im Experiment beobachteten Band um das π_A Band handelt. Die Abschwächung bzw. das Verschwinden des π_B Bandes ist jedoch nicht einfach erklärbar. Oberflächenmodelle mit adsorbiertem Wasserstoff sowie unterschiedlicher Stöchiometrie sind ebenfalls in dieser Arbeit untersucht worden. Keines dieser Modelle konnte allerdings erfolgreich eine Übereinstimmung zwischen Theorie und Experiment herstellen.

Im Fall der 4H-SiC(1 $\bar{1}$ 02)-c(2×2) Oberfläche wurden vierzehn verschiedenen Rekonstruktionsmodelle im Rahmen von Gesamtenergieminimierungen untersucht. Zu diesen Modellen gehört auch die ursprünglich von Virojanadara *et al.* [90] auf Basis ihrer experimentellen Daten vorgeschlagene Struktur. Es hat sich gezeigt, dass dieses Modell, welches auf der Bildung von versetzten, dreifach gebundenen Kohlenstoffdimeren in der Oberflächeneinheit zelle zusammen mit der Adsorption eines Siliziumatoms in einer so genannten H3 Position beruht, energetisch ungünstig ist. Während die H3 Position in der Tat energetisch gegenüber der alternativen T4 Position zu favorisieren ist, weist das optimierte Modell die Ausbildung eines Paares aus zweifach gebundenen Kohlenstoffdimeren (DP-H3) auf. Die Berechnung der jeweiligen Bandstrukturen verrät, dass im Rahmen des SIC- Δ Zugangs alle Modelle halbleitend sind. Insbesondere wird die Bandlücke in allen Fällen zwischen weitestgehend dispersionslosen dangling-bond Bändern gebildet. Dabei sind die Zustände des besetzten Bandes kohlenstoffartig, während die des unbesetzten Bandes am Siliziumatom lokalisiert sind. Als Folge davon liegt die Bandlücke in allen vierzehn Modellen zwischen 1.2 und 1.5 eV, wodurch diese Eigenschaft der elektronischen Struktur ungeeignet ist, im Experiment zwischen den Modellen zu unterscheiden. Jedoch zeigen berechnete STM Bilder unbesetzter Zustände bei einer Spannung von 3.7 V

signifikante Unterschiede, da in einem Fall (DP-H3) nur die jeweiligen antibindenden Zustände der Kohlenstoffdimere abgebildet werden, im anderen Fall aber auch die der Siliziumdimere in der zweiten Oberflächenschicht zu sehen sind. Entsprechende Experimente sollten daher in der Lage sein, die definitive Struktur der $4\text{H-SiC}(1\bar{1}02)\text{-c}(2\times 2)$ zu identifizieren.

Weiterhin wurde der SIC Pseudopotentialzugang benutzt, um die elektronische Struktur der Volumenkristalle und (001) Oberflächen der Erdalkalimetalloxide zu untersuchen. Die berechneten Bandlücken für BeO , MgO , CaO , SrO und BaO sind in guter Übereinstimmung mit Referenzdaten aus Theorie und Experiment. Dies ermöglicht eine detaillierte und zuverlässige Untersuchung der Eigenschaften der jeweiligen Oberflächen. Insbesondere wird die unbesetzte elektronische Struktur der nicht-polaren (001) Oberflächen auf das Vorkommen von Bildpotentialzuständen hin untersucht. Generell lässt sich feststellen, dass die Oberflächenbandstruktur in ihren wesentlichen Charakteristika größtenteils volumenartig ist. Aufgrund des stark ionischen Charakters der Materialien werden keine signifikanten Oberflächenrelaxationen, die zu einer bedeutsamen Änderung der elektronischen Struktur führen könnten, beobachtet. Für den Fall von $\text{MgO}(001)$ stimmt die SIC Bandstruktur gut mit dem Ergebnis einer Quasiteilchenrechnung [164] und experimentellen Hinweisen [152] überein, was die hohe Nützlichkeit des SIC Pseudopotentialzugangs noch einmal verdeutlicht. Desweiteren zeigt sich, dass an den (001) Oberflächen von MgO , CaO und SrO die jeweiligen tiefsten unbesetzten Oberflächenbänder von Bildpotentialzuständen abgeleitet sind, in denen die Ladungsdichteverteilung der fast-freier Elektronen entspricht und im Vakuumbereich über der Oberfläche zu finden ist. Das entsprechende Band an $\text{BaO}(001)$ ist im Gegensatz dazu von einem am Oberflächenkation lokalisierten gebundenen Zustand abgeleitet.

Auf Basis dieser Erfolge wurde der SIC Zugang in dieser Arbeit auch dazu benutzt, die strukturellen, elastischen und elektronischen Eigenschaften von SiC , BN , und BeO Nanoröhren mit einem Durchmesser von 3 bis 25 \AA zu studieren. Der Verlauf der radialen Verkrümmung, der Verzerrungsenergie, des Young-Moduls und der Bandlücke in Abhängigkeit des Durchmessers wurde untersucht. Es ergibt sich, dass für alle drei ionischen Materialien alle Eigenschaften mit Ausnahme der Bandlücke so gut wie unabhängig von der Helizität der Nanoröhren sind. Im Fall von SiC und BN Nanoröhren stellt man eine sensible Abhängigkeit der berechneten Bandlücke fest. Während bei den *armchair* Nanoröhren die Bandlücken nahe bei dem Grenzwert einer graphitartigen Monolage liegen, weisen ihre *zigzag* Gegenstücke ein starkes Einbrechen dieser Größe bei kleinen Durchmessern auf. Anders als bei LDA Rechnungen bleiben sie aber im Rahmen des SIC Zugangs selbst für die kleinsten betrachteten Durchmesser halbleitend. Die Nanoröhren des stark ionischen BeO verhalten sich grundlegend anders. Zunächst einmal ist der Verlauf der Bandlücke unabhängig von der Helizität. Weiterhin lässt sich kein Verkleinern der Bandlücke bei kleinen Durchmessern feststellen. Stattdessen weitet sie sich nach Durch-

schreiten eines leichten Minimums bei ca. 7 \AA wieder. Die grundsätzlich unterschiedlichen Verhaltensweisen wurden durch Analysen der Ladungsdichten im Realraum analysiert und können demnach auf die Unterschiede in der Ionizität der Bindungen und damit ihrem weniger gerichteten Charakter für BeO verglichen mit SiC und BN zurückgeführt werden.

Schließlich wurde im Rahmen dieser Arbeit noch die elektronische Struktur von neun Alkalimetallfluoriden, -oxiden und -nitriden mit Hilfe des SIC Zugangs untersucht. Für solch stark ionische Systeme ist dies eine sehr gut geeignete Methode, die Bandstrukturen in sehr guter Übereinstimmung mit experimentellen und theoretischen Referenzdaten, sofern vorhanden, liefert. Ziel dieser Untersuchungen war es insbesondere, die elektronischen Eigenschaften des erst kürzlich synthetisierten Na_3N [24, 25] zu klären. LDA Rechnungen sagen für dieses System einen metallischen Charakter mit einer negativen Bandlücke von -0.6 eV voraus, die aus einem Überlapp von Na $3s$ und N $2p$ Bändern in der Nähe des Γ -Punkts der Brillouin Zone resultiert. Dieser Überlapp verschwindet im Rahmen des SIC Zugangs und eine Bandlücke der Größe 0.5 eV wird berechnet, was deutlich die experimentelle Einordnung von Natriumnitrid als Halbleiter [204] stützt.

Alles in allem hat sich in dieser Arbeit herausgestellt, dass die Verwendung selbstwechselwirkungskorrigierter Pseudopotentiale in Dichtefunktionalrechnungen zu einer substantiellen Verbesserung der Beschreibung der strukturellen und elektronischen Eigenschaften einer Vielzahl von Volumenkristallen, Oberflächen und Nanoröhren geführt hat. Dank ihrer geringen numerischen Anforderungen erweist sich diese Methode als effiziente Möglichkeit, zuverlässige Ergebnisse auch für vergleichsweise große Systeme zu erzielen.

Keine Schuld ist dringender, als die, Dank zu sagen

Marcus Tullius Cicero

Eine Arbeit wie diese ist niemals das Ergebnis der Bemühungen eines Einzelnen, sondern vielmehr ein Produkt des Zusammenwirkens vieler Personen in unterschiedlichen Bereichen, die sowohl direkt als auch indirekt mit der Arbeit verknüpft sind.

In erster Linie habe ich *Prof. Dr. J. Pollmann* für die Betreuung meiner Dissertation zu danken. Seine thematischen Anregungen und tatkräftigen Hilfen – ganz besonders bei der Erstellung der Publikationen – haben entscheidend zum Erfolg meiner Arbeiten in den letzten drei Jahren beigetragen. Im gleichen Atemzug muss auch *Prof. Dr. P. Krüger* genannt werden, der mir mit vielen Ratschlägen und hilfreichen Diskussionen stets eine große Hilfe war.

Ohne die hervorragende Betreuung der Rechnersysteme durch *Dr. A. Mazur* wäre die Durchführung der Rechnungen, die zu den Ergebnissen in dieser Arbeit geführt haben, nicht möglich gewesen. Ganz besonders möchte ich mich bei meinem Zimmerkollegen *J. Wieferink* für das Zurverfügungstellen seines Programmcodes bedanken.

Im Übrigen gilt mein Dank allen Mitgliedern der Arbeitsgruppe und des Instituts für Festkörpertheorie für die immer angenehme und entspannte Arbeitsatmosphäre, nicht zuletzt durch die lockere nachmittägliche Kaffeerunde.

Die Zeit der Anfertigung dieser Arbeit wäre um einiges ärmer gewesen, wenn ich nicht auf einen besonders lieben Menschen gestoßen wäre, der – wie kein anderer – mich immer unterstützt und zu mir gestanden hat. Danke für alles!

Münster, im Dezember 2008

Lebenslauf

Name: Björn Baumeier
Geburtsdatum: 22.03.1979
Geburtsort: Münster
Staatsangehörigkeit: Deutsch
Eltern: Manfred Baumeier
Ingrid Schürmann, geb. Selker

Schulbildung

1985 – 1987 Grundschule Nottuln
1987 – 1989 Grundschule Havixbeck
1989 – 1998 Gymnasium Paulinum, Münster
09.06.1998 Allgemeine Hochschulreife

Wehrdienst

11/1998 – 08/1999 Grundwehrdienst beim Jagdgeschwader 72 „Westfalen“, Rheine

Studium

1999 – 2005 Studium der Physik an der Westfälischen Wilhelms-Universität
Münster
18.09.2001 Diplom-Vorprüfung
02/2004 – 02/2005 Diplomarbeit in Physik: Selbstwechselwirkungs- und relaxations-
korrigierte Pseudopotentiale für die Volumenkristalle von SiC, MgO,
LiF, Silizium und Diamant
15.03.2005 Diplomprüfung

Promotionsstudium

18.03.2005 Beginn der Dissertation am Institut für Festkörpertheorie unter der
Betreuung von Prof. Dr. Johannes Pollmann

Berufstätigkeit

09/2002 – 03/2005 Studentische Hilfskraft bei der Informationsverarbeitungs- Ver-
sorgungseinheit (IVV) Naturwissenschaften an der Westfälischen
Wilhelms-Universität Münster

-
- 04/2005 – 05/2005 Wissenschaftliche Hilfskraft bei der IVV Naturwissenschaften an der Westfälischen Wilhelms-Universität Münster
- 06/2005 – 09/2005 Junior Research Specialist am Institute of Surface and Interface Science an der University of California, Irvine, bei Prof. Alexei A. Maradudin
- seit 10/2005 Wissenschaftlicher Mitarbeiter am Institut für Festkörpertheorie an der Westfälischen Wilhelms-Universität Münster

Münster, 26. Januar 2009